

---

Dissertation zur Erlangung des Doktorgrades  
der Fakultät für Chemie und Pharmazie  
der Ludwig-Maximilians-Universität München

**Structural and biochemical  
characterization  
of the IFT-B proteins  
IFT22, IFT74 and IFT81**

STEFANIE MARINKA WACHTER

aus

Tübingen, Deutschland

2018

---



## **ERKLÄRUNG**

Diese Dissertation wurde im Sinne von § 7 der Promotionsordnung vom 28. November 2011 von Frau Prof. Dr. Elena Conti betreut.

## **EIDESSTATTLICHE VERSICHERUNG**

Diese Dissertation wurde eigenständig und ohne unerlaubte Hilfe erarbeitet.

München, 18. Mai 2018

Ort, Datum

Stefanie Wachter

Unterschrift

Dissertation eingereicht am: 29. März 2018

1. Gutachterin: Prof. Dr. Elena Conti

2. Gutachter: Prof. Dr. Karl-Peter Hopfner

Mündliche Prüfung am: 07. Mai 2018

# Acknowledgements

Finally, it is time to thank a great many people who helped and supported me during the last years.

First and foremost, I would like to thank my supervisor Esben for taking me as a PhD student and letting me work on this project. I benefited from his guidance and support as much as I appreciated the individual freedom he granted all of his group members.

I also want to thank Elena, not only for being the official thesis examiner and member of my TAC, but also for providing such an inspiring and top quality work environment. I could not imagine finding a better place to conduct a doctoral thesis. Besides, I felt cordially “adopted” by the Conti group for the last stage of my PhD research after the Lorentzen group moved to Aarhus.

Special thanks go to my dear lab mates who made work life so much more enjoyable: Taschi for sharing protocols and lab wisdom, for his patient explanations and help with anything protein-related, for teaching me insect cell expression and his semi-funny jokes; Sagar for introducing me to the lab and techniques and his amazingly charming character and bright smile; Krissy for all kinds of administrative and methodical help in the beginning and for her open and supportive personality; Mela for being the nicest office and bench neighbor I could imagine, for her constantly cheerful and motivating character and for some pleasant conference days in Amsterdam; Lisa for helping me a lot with insect cell cultures and for her extensive purification support in busy weeks; André, Marc, Mayanka and Qianmin for contributing to the good atmosphere in the group and valuable suggestions in internal meetings. This thank you expands to all the members of the Biertümpfel, Mizuno and Conti groups.

I benefited a lot both from the scientific resources of the department and the MPI of Biochemistry and from personal support of many people. Thanks go to Katharina, Deborah, Jerome, Christian, Shun-Hsiao and Sevim for nice company at successful SLS trips. I thank Claire and Fabien for introduction to new methods and assistance with data evaluation. I also would like to thank Karina, Sabine and Ariane from the crystallization facility for crystal screening and Stephan Uebel, Lissy, Naga, Antonio and Susanne from the biochemistry core facility for measurements and assistance with new methods. Thanks to Petra and Ulrike for dealing with administrative issues, Walter with all sort of technical problems and Peter for first aid with malfunctioning ÄKTAs. I also received a lot of support from Elfriede and Marc, who took care of our insect cells. I especially want to thank Jerome for advice and support on the crystallographic part of my project, including organization of beamtime and SLS trips and help with data collection and structure solving. Besides all the scientific assistance, I appreciated a lot the diverse chats with my “new” office neighbors Lisa S. and Mahesh (and that they granted me admission to their candy drawer). Similarly, I thank Wolfgang and Lisa N. for occasional relaxing coffee breaks. I also would like to acknowledge the general motivating scientific atmosphere in our department and the joyful non-scientific get-togethers at various Christmas and BBQ parties.

## Acknowledgements

---

Furthermore, I would like to thank Philippe Bastin at the Institut Pasteur in Paris for being part of my TAC and for the fruitful *in vivo* collaboration on this project.

I received generous financial and personal support from the Christiane Nüsslein-Volhard Foundation, for which I am very thankful.

Very special thanks go to Brone for little distractions and making working days much more pleasant (and for her cloning help with my last construct) and to Karo for always having an open ear, bearing complaints and her remote mental support. I am truly grateful for our friendship.

Big thanks go to my parents for their support and trust throughout my life.

Last but not least, I thank Jochen for tolerating my moods and impatience, for his extensive support with  $\LaTeX$ , for always being there for me – and most of all for being a real partner in every respect. And thanks to Jakob who brings so much joy into my life.

# Summary

Cilia (or flagella) are highly specialized hair-like organelles present on the surface of most eukaryotic cells. They feature a microtubule-based axonemal core structure surrounded by the ciliary membrane that is continuous with the plasma membrane. Cilia serve essential functions in sensing of environmental cues, several signaling pathways and cell motility and harbor a specific composition of proteins. Import of ciliary proteins through the diffusion barrier and transport to the ciliary tip and back relies on a conserved transport mechanism, termed intraflagellar transport (IFT). IFT is crucial for cilium formation and maintenance and depends on the multiprotein IFT complex and microtubule motor proteins. Extensive research in the past years tried to shed light on individual IFT protein functions, but *in vivo* knockout studies reach their limits due to the composite interaction network within the IFT complex. It is therefore of great importance to further investigate and characterize individual IFT proteins and subcomplexes *in vitro* by means of structural biology and biochemistry approaches. The 1.5 MDa IFT complex consists of 22 proteins identified to date and can be subdivided into several biochemically distinct subcomplexes. In this thesis, the structural and biochemical characterization of the three IFT-B1 subcomplex proteins IFT22, IFT74 and IFT81 will be described. IFT22 was classified as an atypical small GTPase of the Rab family based on sequence analysis, showing a high degree of variance especially in usually conserved sequences needed for proper nucleotide binding. Hence, due to the lack of biochemical analysis, it was not known if IFT22 is a functional GTPase and if it is specific for guanine nucleotides. Interestingly, IFT22 studies in different organisms revealed functional differences between species. Extensive complex reconstitution studies in the past years from our lab have mapped the binding site of IFT22 to a short sequence stretch on the IFT74/81 coiled-coil heterodimer, however no structural data regarding the binding mechanism was available. In this study, we present crystal structures of GDP- and GTP-loaded IFT22 and identify an unusual G nucleotide-binding mode, bypassing the usage of a highly conserved classical sequence motif. Nucleotide-titration and HPLC experiments detected specificity for G nucleotides and affinities for GDP/GTP in the low micromolar range. Furthermore, we show that IFT22 has a low, but measurable intrinsic GTPase activity similar to other small Rab GTPases. A third crystal structure obtained for the trimeric IFT22/74/81 complex reveals that IFT74/81 is a conserved effector of IFT22. The structure allows us to pinpoint critical residues for complex formation and shows that IFT22 binds IFT74/81 via its switch regions. In a collaboration project, we tested structure guided mutations in trypanosome parasites *in vivo* and demonstrate that association of IFT22 with IFT-B1, but not nucleotide-binding is essential for ciliogenesis in trypanosomes.

# Contents

<b>Acknowledgements</b>	<b>4</b>
<b>Summary</b>	<b>6</b>
<b>Preface</b>	<b>10</b>
<b>Publications &amp; Contributions</b>	<b>11</b>
<b>Introduction</b>	<b>12</b>
<b>1 The cilium: a ubiquitous eukaryotic organelle</b>	<b>12</b>
1.1 Overall architecture . . . . .	13
1.1.1 The ciliary axoneme . . . . .	14
1.1.2 The ciliary basal body and transition zone . . . . .	14
1.1.3 The ciliary membrane and ciliary pocket . . . . .	15
1.2 Ciliary functions: Sensoring, signaling & motility . . . . .	15
1.2.1 Sensory functions . . . . .	16
1.2.2 Signaling functions . . . . .	17
1.2.3 Cell motility . . . . .	19
1.3 Cilia in human disease . . . . .	19
1.4 <i>Trypanosoma brucei</i> as a model organism for cilium studies . . . . .	20
<b>2 Intraflagellar transport and its key players</b>	<b>21</b>
2.1 IFT motor proteins . . . . .	23
2.2 The IFT-A subcomplex . . . . .	24
2.3 The IFT-B subcomplex . . . . .	25
2.4 The BBSome . . . . .	27
2.5 IFT cargo proteins . . . . .	28
<b>3 Small GTPases in ciliary construction and maintenance</b>	<b>29</b>
3.1 General structure and features of (small) GTPases . . . . .	29
3.2 Cellular functions of small Rab GTPases . . . . .	31
3.3 Small GTPases involved in ciliary targeting . . . . .	32
3.4 IFT-associated Rab GTPases . . . . .	33
3.4.1 IFT27 (Rab14) . . . . .	33
3.4.2 IFT22 (Rab15) . . . . .	34
3.4.3 Rab12 . . . . .	35
<b>Aim of the thesis</b>	<b>37</b>

<b>Paper A: Crystal structure of the intraflagellar transport complex 22/74/81: IFT22 association with the IFT complex but not with nucleotides is essential for <i>Trypanosoma brucei</i> flagellum construction</b>	<b>40</b>
<b>1 Introduction</b>	<b>41</b>
<b>2 Results</b>	<b>43</b>
2.1 IFT22 is a specific guanine nucleotide-binding protein with a low hydrolysis rate . . . . .	43
2.2 The crystal structures of IFT22 reveal an unusual GTP/GDP-binding mode . . . . .	45
2.3 IFT22 exhibits unstructured switch regions in the GDP- and GTP-bound structure . . . . .	45
2.4 Structural characterization of the IFT22/74 <sub>79-401</sub> /81 <sub>1-450</sub> subcomplex . . . . .	46
2.5 <i>Tb</i> and <i>CrIFT81</i> CH domains show a similar organization of tubulin-binding residues . . . . .	48
2.6 IFT74/81 interacts via a conserved surface patch and is an effector of IFT22 . . . . .	49
2.7 Association of IFT22 to IFT-B1 is essential for flagellum assembly in <i>T. brucei</i> . . . . .	50
2.8 An inactive GTP-binding mutant shows significantly reduced affinity to IFT74/81, but does not cause a strong effect <i>in vivo</i> . . . . .	53
<b>3 Discussion</b>	<b>57</b>
3.1 IFT22 shares common features with IFT27 . . . . .	57
3.2 Is IFT22 a potential cargo-binding protein? . . . . .	58
3.3 IFT22 may be involved in causing Short-Rib Polydactyly Syndrome . . . . .	58
<b>4 Experimental Procedures</b>	<b>60</b>
4.1 Recombinant protein expression and purification from <i>E. coli</i> . . . . .	60
4.2 Expression of selenomethionine derivatives . . . . .	60
4.3 Recombinant protein expression and purification from insect cells . . . . .	60
4.4 Crystallization of GTP/GDP- <i>TbIFT22</i> and <i>TbIFT22/74<sub>79-401</sub>/81<sub>1-450</sub></i> . . . . .	61
4.5 Data collection and crystal structure determination . . . . .	61
4.6 Affinity pulldown experiments . . . . .	62
4.7 Protein denaturation by urea and refolding for nucleotide removal . . . . .	63
4.8 HPLC nucleotide analysis . . . . .	63
4.9 Nucleotide-binding experiments . . . . .	63
4.10 GTPase assay . . . . .	63
4.11 Isothermal titration calorimetry (ITC) . . . . .	64
4.12 Trypanosome cultures and transfection . . . . .	64
4.13 Immunofluorescence (IFA) . . . . .	64
4.14 Live Cell Imaging . . . . .	65
4.15 Western Blot . . . . .	65
4.16 Transmission electron microscopy . . . . .	66
<b>Paper B: Phosphoproteomics reveals that Parkinson's disease kinase LRRK2 regulates a subset of Rab GTPases</b>	<b>74</b>
<b>Introduction</b>	<b>74</b>
<b>Results</b>	<b>76</b>

<b>Discussion</b>	<b>87</b>
<b>Materials and methods</b>	<b>89</b>
<b>References</b>	<b>97</b>
<b>Figure supplements</b>	<b>102</b>
<b>Extended discussion and perspectives</b>	<b>114</b>
1 Towards a high-resolution structure of the IFT-B1 complex	114
2 IFT74 could interact with IFT-A via a conserved N-terminal surface patch	115
3 Analysis of the tubulin-binding CH domain	117
4 IFT22 – a functional GTPase or not?	118
5 The IFT74/81 heterodimer as a GTPase-binding platform	120
6 A potential role for IFT22 and the IFT74/81 effector complex in human disease	121
<b>Abbreviations</b>	<b>123</b>
<b>List of Figures</b>	<b>126</b>
<b>References</b>	<b>127</b>

# Preface

The present doctoral thesis is summarizing the research I did in the course of my PhD studies in the lab of Dr. Esben Lorentzen at the MPI of Biochemistry. During the past four years I have worked on one main project covering the structural and biochemical analysis of the ciliary IFT22/74/81 subcomplex, which I will focus on describing in this work. Besides, I contributed to a collaborative project on studies of a Parkinson's disease kinase resulting in a publication in eLIFE. The common ground of both projects lies in the biochemical analysis of small Rab GTPases and investigation of their effects on cellular processes. The first part of my thesis will give a detailed introduction to the field of ciliary research and an overview over the family of Rab GTPases based on available literature. The results section is subdivided into two parts containing the published research article and a manuscript of my main project that is currently being finalized for submission. Both documents build separate comprehensive entities regarding results, analyses and conclusions. An extended discussion on the findings of the IFT22/74/81 project followed by an outlook of potential future research directions completes this work.

# Publications & Contributions

## Paper A

**Wachter, S.**, Jung, J., Shafiq, S., Basquin, J., Fort, C., Bastin, P., Lorentzen, E. (2018). *Crystal structure of the intraflagellar transport complex 22/74/81: IFT22 association with the IFT complex but not with nucleotides is essential for Trypanosoma brucei flagellum construction.* (Manuscript in preparation)

For this study, I performed all biochemical and *in vitro* experiments including preparative work such as cloning, construct design, and protein purifications. I determined the crystal structures of IFT22 and IFT22/74/81. J.B. helped with data collection and structure solving of the IFT22/74/81 structure. J.J., C.F. and S.S. carried out structure-based *in vivo* experiments. I discussed the results, analyzed and interpreted generated data and assembled all figures except for the *in vivo* panels that were generated by J.J. I wrote the manuscript together with E.L. and P.B.

## Paper B

Steger, M., Tonelli, F., Ito, G., Davies, P., Trost, M., Vetter, M., **Wachter, S.**, Lorentzen, E., Duddy, G., Wilson, S., Baptista, M., Fiske, B., Fell, M., Morrow, J., Reith, A., Alessi, D., Mann, M. (2016). *Phosphoproteomics reveals that Parkinson's disease kinase LRRK2 regulates a subset of Rab GTPases.* eLIFE ((5), e12813)

This project was of contributive nature. I established and performed Rab8a (WT and T72E) nucleotide-binding experiments with fluorescently-labeled GDP and a non-hydrolysable GTP analog. I discussed the results, analyzed and interpreted generated data and provided Figure 5 Supplement 1.

# Introduction

## 1 The cilium: a ubiquitous eukaryotic organelle

The main feature distinguishing eukaryotic cells from their prokaryotic counterparts is their extensive intracellular compartmentalization. The membrane-enclosed nucleus contains the genetic information and the necessary machinery for basic DNA metabolism such as transcription, replication and recombination, and various other spatially separated organelles provide dedicated biochemical environments for processes such as protein folding and transport (e.g. endoplasmic reticulum, Golgi apparatus), protein degradation (lysosomes), or energy production (mitochondria). While functions of many of those organelles have been investigated for many decades and are well understood, the role of cilia was underestimated for a long time. Cilia (or flagella, the terms can be used interchangeably) are hair-like structures emerging from the cell surface of nearly every eukaryotic cell and have first been described 1677 by the Dutch microbiologist van Leeuwenhoek (van Leeuwenhoek 1677). They are highly evolutionarily conserved and were present on the last eukaryotic common ancestor (Satir et al. 2008). Cilia can be found on cells ranging from unicellular organisms like the green alga *Chlamydomonas reinhardtii* (Fig. 1A) or the sleeping sickness-causing parasite *Trypanosoma brucei* (Fig. 1B) (Morga & Bastin 2013) to nearly every cell in the mammalian body. They are highly variable with regards to their length (from several micrometers to few millimeters) and their copy-number (from one to thousands of copies) on a given cell type (Fig. 1).

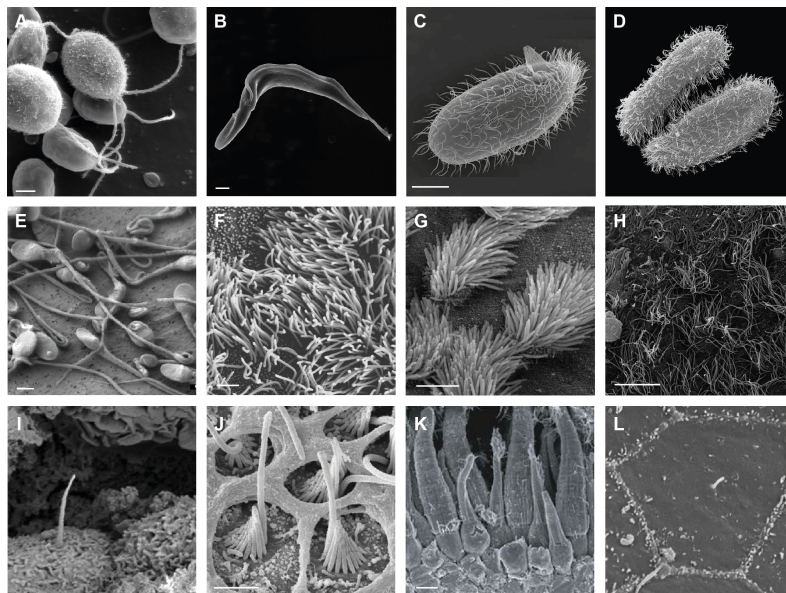


**Figure 1: Scanning electron microscopy images of different ciliated cell types**

First row: Ciliated unicellular organisms A. *C. reinhardtii* (2  $\mu\text{m}$ ) (EM facility, Dartmouth College), B. *T. brucei* (1  $\mu\text{m}$ ) (Morga & Bastin 2013), C. *T. thermophila* (10  $\mu\text{m}$ ) (Singer 2009) and D. *Paramecium* representative; Middle row: Ciliated mammalian cells (motile cilia) (Schipper 2017) E. Sperm cells (2  $\mu\text{m}$ ) (Nussdorfer et al. 2018), F. Fallopian tube epithelial cells (4  $\mu\text{m}$ ) (Baczynska et al. 2007), G. Respiratory epithelial cells (5  $\mu\text{m}$ ) (EM facility, Dartmouth College), H. Ependymal cells (1  $\mu\text{m}$ ); Bottom row: Ciliated mammalian cells (primary cilia) (EM facility, Duke University), I. Kidney cell (EM facility, UT Southwestern), J. Inner ear hair cells (2  $\mu\text{m}$ ) (Schwarz et al. 2011), K. Photoreceptor cells of the eye (10  $\mu\text{m}$ ) (Schietroma et al. 2017), L. Buccopharyngeal membrane cells (Benmerah et al. 2015).

However, cilia are absent in higher plants and fungi, such as *Arabidopsis thaliana* and *Saccharomyces cerevisiae*. Various functions of cilia have been described to date with the most prominent one being cellular locomotion using motile cilia. Another no less important type is the so-called immotile or primary cilium. The primary cilium was discovered 1898 by Zimmermann in human tissue cells (Zimmermann 1898) and for a long time it was considered to be a meaningless evolutionary remnant (similar to the human appendix) until its essential role in sensory reception and several signaling pathways was uncovered (section 1.2). Thus, it is not surprising that an increasing number of genetic disorders and developmental abnormalities, referred to as ciliopathies, could be linked to defective cilia (Badano et al. 2006; Waters & Beales 2011).

## 1.1 Overall architecture

The central shape-giving element in every cilium is a microtubule-based axoneme emerging from a centriole-like structure at the ciliary base, the basal body. The axoneme is surrounded by the ciliary membrane, which is continuous with the plasma membrane but contains a specific composition of lipids and membrane proteins. A diffusion barrier ensuring controlled entry, exit and retention of components in the organelle is provided by a section called transition zone. The different structural elements are described in detail in the following paragraphs and are depicted in Fig. 2.

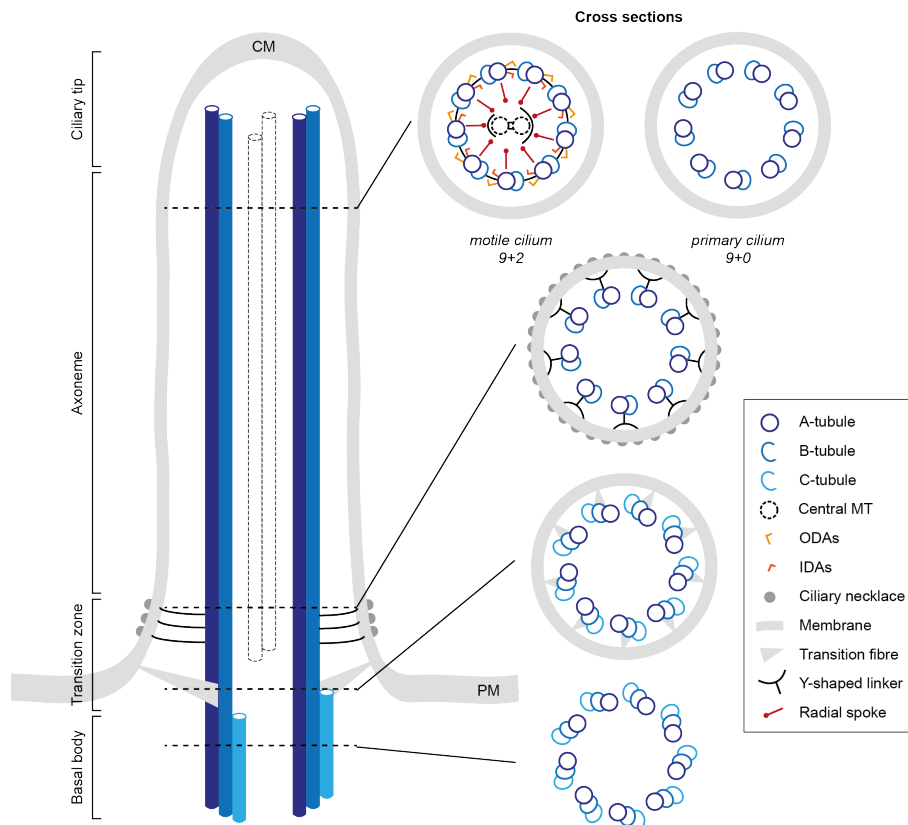


**Figure 2: Schematic overview of the ciliary ultrastructure**

Left: Schematic illustration of the cilium architecture depicting the different structural elements and functionally distinct zones. Right: Cross section from various regions within the cilium showing the respective inner organization. (CM = ciliary membrane, PM = plasma membrane)

### 1.1.1 The ciliary axoneme

The axoneme is the core structure of each cilium, providing the organelle with its characteristic elongated appearance and rigidity. It is composed of nine outer doublet microtubules (MTs) arranged in a ring-like manner (9 + 0 arrangement) with their growing plus-ends oriented towards the distal end of the cilium. Each MT doublet consists of a complete A-tubule with 13 protofilaments and an adjacent incomplete B-tubule with 10 protofilaments. The outer doublets are known to be subject to a diverse array of post-translational modifications (PTMs), such as tubulin acetylation, detyrosination and glutamylation. These PTMs are required for the correct assembly and maintenance of the axoneme and play an important role in the regulation of cilium stability (Wloga et al. 2017). While primary cilia are typically characterized by the aforementioned 9 + 0 arrangement of MTs, motile cilia typically feature an additional central pair of two complete MTs (9 + 2 arrangement) (see cross sections in Fig. 2). Examples of mammalian primary cilia can be found on cells of kidney tubules, pancreatic cells and photoreceptor cells of the eye, whereas prominent representatives of motile cilia are the sperm cell flagellum, cilia on the fallopian tube of the female reproductive apparatus and cilia protruding from the epithelium of the airway system (Fliegauf et al. 2007). However, exceptions to this general rule can be found. Embryonic nodal cells lack the central pair and thus exhibit a 9 + 0 structure, but are still able to perform ciliary beating due to the presence of the dynein motor machinery, thereby creating a flow of extra-embryonic fluid that is required for establishment of left-right asymmetry (Hirokawa et al. 2006). On the other hand, specialized cilia of the inner ear (kinocilia) hold a 9 + 2 arrangement of MTs, but lack components required for the movement process and are considered as immotile (Dabdoub & Kelley 2005).

Classical 9 + 2 motile cilia possess a number of additional MT-associated protein complexes to carry out their function in motility, amongst which are outer dynein arms (ODAs, linking outer doublet MTs and facing the ciliary membrane), inner dynein arms (IDAs, linking outer doublet MTs and pointing towards the central pair), radial spokes (RS, linking outer doublets with the central pair) and nexins (proteinaceous fibers connecting the individual outer MT doublets) (Warner & Satir 1974; Satir & Christensen 2007) (Fig. 2, cross sections).

The well-coordinated wave-like movement is the result of a sliding mechanism of neighboring MTs relative to each other that is driven by ATP hydrolysis of the heavy chains of dynein arms (Gibbons & Rowe 1965; Porter et al. 1999). In order to allow target-oriented locomotion or directed fluid flow, ciliary bending has to be tightly regulated regarding timing and spatial positioning of respective sliding MTs. Studies have linked an interplay of the dynein regulatory complex (DRC), radial spokes, the central pair and IDAs to be responsible for regulation of dynein activity (Heuser et al. 2009).

### 1.1.2 The ciliary basal body and transition zone

The basal body (BB) is a modified centriole-like structure and the most proximal element to the cell body. It forms the anchoring point for the axoneme and consists of an array of nine MT triplets, termed A-, B- and C-tubules (Sorokin 1968; Beisson & Wright 2003). While A- and B-tubules are continuous with the

axonemal structure, the 10-protofilament C-tubules terminate at the transition zone (TZ). In the case of 9 + 2 cilia, the TZ is the point of origin for the central pair of MTs. The TZ is an electron dense structure that is considered to be the selective entry gate to the cilium and builds the intersection between the ciliary compartment and cytoplasm. It is composed of transition fibers spanning the intermembrane space between MTs of the BB and the ciliary membrane and preventing the passive diffusion of particles larger than 9 nm through the barrier (Breslow et al. 2013). Distal to the transition fibers is an integral part of the TZ called the “ciliary necklace”, a series of parallel strands of intramembrane protein particles that are connected to the axoneme via so-called Y-shaped linkers (Gilula & Satir 1972; O’Toole et al. 2007; Reiter et al. 2012). The ciliary necklace marks the beginning of the ciliary membrane (Fig. 2).

It has been shown that proteins destined for the cilium are recruited to the region of the transition fibers, where they are thought to be assembled into larger transport particles (Deane et al. 2001). These particles then have to be guided through the diffusion barrier, however the mechanism of this entry process still remains unclear.

### **1.1.3 The ciliary membrane and ciliary pocket**

The ciliary membrane is a highly specialized outgrowth of the plasma membrane covering the axoneme and separating the ciliary compartment from the extracellular space. It hosts a unique composition of lipids and membrane proteins, such as specific ion channels and receptors. The membrane is enriched in raft-forming sterols, glycolipids, sphingolipids and phospholipids (Emmer et al. 2010; Serricchio et al. 2015). This is not surprising since lipid rafts are known to act as organizing centers for signaling molecules (Simons & Ehehalt 2002) and the cilium is considered an important sensing and signaling organelle (see section 1.2). It has also been demonstrated that the distal part of the ciliary membrane contains a condensed lipid zone that might prevent lateral diffusion between ciliary and plasma membrane compounds (Vieira et al. 2006; Rohatgi & Snell 2010).

Besides, several ciliated organisms exhibit a specialized membrane domain termed the ciliary pocket (Benmerah 2013), a membrane invagination at the ciliary base which may function in endocytosis and exocytosis, similar to the trypanosome flagellar pocket (Overath & Engstler 2004) (see section 1.4), and as a docking site for cilia-targeted vesicles (Benmerah 2013). Another suggested role for the ciliary pocket is the defined spatial positioning of the cilium since it was found to tightly interact with the actin cytoskeleton (Molla-Herman et al. 2010). However, given that not all ciliated cells contain a ciliary pocket, it does not necessarily seem to be essential for the described processes.

## **1.2 Ciliary functions: Sensoring, signaling & motility**

Cilia fulfill a wide spectrum of functions, dependent on their structure (motile or immotile) and their tissue-specific localization. Due to the exposed position at the cellular rim and their relatively large surface area, cilia are ideally suited for a role in sensing of extracellular cues and transmission of signals

into the cytoplasm and thus are often referred to as cellular antennas. The following section will give an overview of the most common functions of both motile and primary cilia.

### 1.2.1 Sensory functions

**Mechanosensation:** Sensing of fluid flow and extracellular movement is a key function of primary cilia. Epithelial cells in the kidney possess a single cilium facing the tubular lumen (Fig. 1I) that is able to sense urine flow through ciliary bending, which in turn mediates  $\text{Ca}^{2+}$  influx (Fliegauf et al. 2007). Primary cilia have been demonstrated to be important  $\text{Ca}^{2+}$  signaling organelles that contain a ~7-fold higher  $\text{Ca}^{2+}$  concentration than the cytoplasm (Delling et al. 2013). This is achieved by the action of the polycystin-1/polycystin-2 (PC1/PC2) heterodimer, a designated mechanosensory complex enriched in the ciliary membrane (Nauli et al. 2003). While PC1 is a G protein-coupled receptor (GPCR) acting as a flow-sensor, PC2 functions as a  $\text{Ca}^{2+}$  channel that opens upon signal transmission of PC1 (Pazour et al. 2002a; Parnell et al. 2002). The increased ciliary  $\text{Ca}^{2+}$  level can then induce downstream  $\text{Ca}^{2+}$  signaling cascades. Mutations in the genes encoding PC1 and PC2 have been linked to polycystic kidney disease (PKD) due to impaired sensing of extracellular flow, leading to interruption of  $\text{Ca}^{2+}$  signaling (Nagao et al. 2008).

A second example of flow-induced cellular signaling mediated by the cilium is described for the non-canonical Wingless pathway in section 1.2.2.

**Photoreception:** The retina of the eye contains two classes of photoreceptor cells, rods and cones (Fig. 1K). They are polarized sensory neurons consisting of an inner and outer segment. While the inner segment harbors cellular organelles and the protein synthesis machinery, the outer segment is composed of a stack of membrane discs obtained through invaginations of the plasma membrane (Hollyfield et al. 1977) (Fig. 3C). These discs represent the sensory part of the neuron, as the membranes are enriched with large amounts of the photosensitive GPCRs opsin and rhodopsin and signaling molecules. Inner and outer segment are bridged via a non-motile cilium that serves as a transport corridor and is referred to as connecting cilium (Horst et al. 1990). Since turnover rates of receptors in the outer segment are very high, an efficient transport machinery is needed to deliver components between the two compartments (Rosenbaum et al. 1999). Mutations leading to defects in the transport process and thus to accumulation of receptor proteins in the inner segment were shown to cause retinal degeneration (Pazour et al. 2002b; Marszalek et al. 2000). The nature of this conserved machinery will be discussed in section 2.

**Odorant and auditory reception:** Apart from the eye, cilia also serve important roles in other sensory organs. One example are cilia on the surface of the olfactory epithelium in the vertebrate nose. Specialized sensory cells, the olfactory sensory neurons, end in so-called dendritic knobs that exhibit a cluster of primary cilia (Buck & Axel 1991; McEwen et al. 2008) (Fig. 3D). These cilia protrude into the mucus covering the olfactory epithelium and sense odorants via olfactory GPCRs in their membranes. GPCR activation leads to induction of downstream signaling pathways that result in the sense of smell.

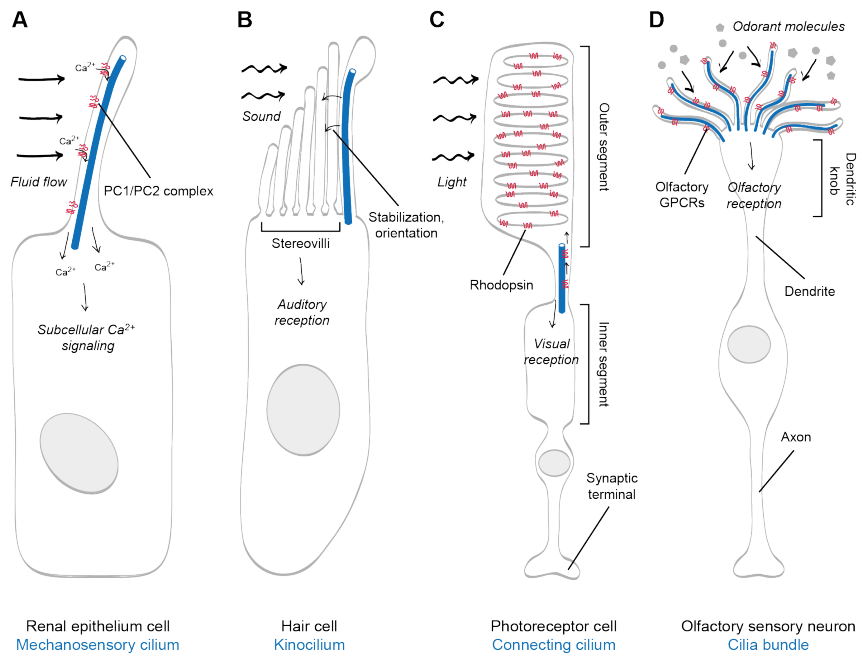


**Figure 3: Schematic illustration of various sensory cilia**

Axonemes are depicted in blue and sensory receptors in red. Incoming environmental cues are indicated by arrows. **A.** Cilia on renal epithelial cells serve as flow sensors mediating  $\text{Ca}^{2+}$  signaling via the PC1/PC2 complex. **B.** Kinocilia on hair cells orient and stabilize the actin-based stereovilli needed for auditory reception. **C.** The connecting cilium of photoreceptor cells links the inner and outer segment and is essential for rhodopsin receptor trafficking and visual reception. **D.** The ciliary bundle on olfactory sensory neurons harbors numerous olfactory receptors and mediates signal transduction leading to the sense of smell.

It is not surprising that olfactory cilia defects lead to reduction or loss of smell (Kulaga et al. 2004; McEwen et al. 2008).

A fundamentally different example is the specialized cilium on the inner ear hair cells, termed kinocilium. It is not directly involved in auditory reception, but required to orient and polarize the mechanosensory actin-based stereovilli correctly (Fig. 1J and Fig. 3B). Stereovilli arrange in bundles of tightly packed rows and are the sensing and signaling parts of the hearing process (Hudspeth 1985). The kinocilium is placed directly behind the stereovilli bundle and disruption of kinocilia leads to misoriented stereovilli bundles and morphology defects, making the kinocilium a crucial component for auditory reception (Fukuda et al. 2014; Grati et al. 2015).

### 1.2.2 Signaling functions

The fact that the ciliary membrane is enriched with receptor proteins and ion channels together with the results of various *in vivo* studies have led to the awareness that cilia are relevant organelles for several developmental signaling pathways, three of which will be described exemplarily here.

**Hedgehog (Hh) signaling:** Hh signaling is an important signal transduction pathway in embryonic development and required for body axis determination, but also plays a role in adult stem cells (McMahon et al. 2003; Pasca di Magliano & Hebrok 2003). Several components of the pathway

were found to be localized to cilia (Corbit et al. 2005; Haycraft et al. 2005). The pathway is induced by the secreted Hh protein ligand binding to the Patched-1 (Ptch1) receptor that is localized in the ciliary membrane (Rohatgi et al. 2007) (Fig. 4). This can occur in an autocrine or paracrine fashion. In unstimulated conditions, Ptch-1 inhibits Smoothed (Smo), another transmembrane protein, and blocks its entry to the cilium. Upon ligand binding to Ptch-1, this inhibitory effect is alleviated, Ptch-1 exits and Smo translocates to the cilium where it activates glioma (Gli) transcription factors in a stepwise process. Gli factors are then released at the ciliary base and enter the nucleus, where they regulate the expression of Hh target genes (Goetz & Anderson 2010).

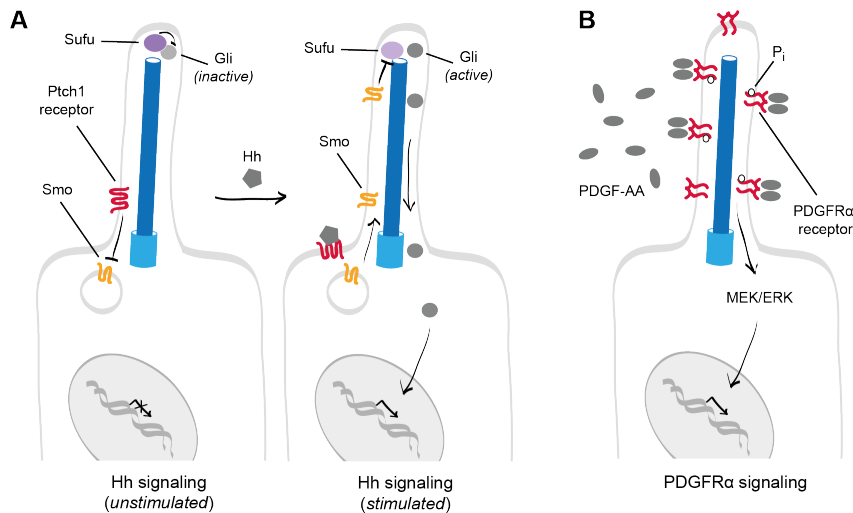


**Figure 4: The role of cilia in different signaling pathways**

**A. Hh signaling:** In the absence of ligand, the ciliary Ptch1 receptor inhibits and blocks entry of the Smo transmembrane protein, thus keeping the Gli transcription factor inactive (left image). Upon binding of Hh ligand to Ptch1, Ptch1 exits the cilium and allows entry of Smo. At the ciliary tip, Smo promotes the activation of Gli by inactivation of Sufu. The Gli transcription factor is transported to the cytoplasm and enters the nucleus to induce target gene expression. **B. PDGFR $\alpha$  signaling:** Binding of the PDGF-AA ligand to the PDGFR $\alpha$  receptor activates the kinase activity of the receptor, leading to autophosphorylation and initiation of the downstream MEK/ERK pathway. The MEK/ERK pathway regulates transcription of target genes for cell cycle entry.

**Wingless (Wnt) signaling:** Wnt signaling can be grouped into two separate pathways, the canonical and non-canonical route. While the canonical pathway includes the protein  $\beta$ -catenin, the non-canonical pathway is  $\beta$ -catenin independent (Clevers 2006). Both pathways serve important roles in embryonic development and adult tissue maintenance. In the canonical pathway, Wnt ligand binding to the Frizzled (Fz) receptor at the ciliary base induces a cascade that leads to stabilization of the cytoplasmic  $\beta$ -catenin protein which is otherwise targeted for ubiquitin-mediated degradation in the absence of a signal (Fig. 4). Subsequently,  $\beta$ -catenin is translocated to the nucleus where it acts as transcriptional coactivator of Wnt target genes (Logan & Nusse 2004). These genes control a set of processes related to cell fate determination and proliferation. The non-canonical pathway is initiated by flow-induced physical bending of the cilium that triggers  $\text{Ca}^{2+}$  influx into the organelle. Release of  $\text{Ca}^{2+}$  into the cytoplasm leads to increased Inversin (Inv) expression levels which in turn promotes degradation of cytoplasmic Dishevelled (Dsh) protein, a component of the canonical pathway, thus destabilizing  $\beta$ -catenin (Veeman et al. 2003). This pathway is required for regulation of the cytoskeleton and controls cell polarity (Christensen et al. 2008).

**Platelet-derived growth factor receptor- $\alpha$  (PDGFR $\alpha$ ) signaling:** PDGFR $\alpha$  is a homodimeric receptor localized in the ciliary membrane (Fredriksson et al. 2004; Schneider et al. 2005). Binding of the PDGF-AA ligand activates the receptor's kinase activity and induces autophosphorylation, followed by a phosphorylation cascade in the downstream AKT and MEK/ERK pathways at the ciliary base (Fig. 4). Activation of these pathways leads regulation of several transcription factors that induce cell cycle entry. Hence, PDGFR $\alpha$  signaling plays a crucial role in cell cycle control and therefore in cellular growth, differentiation and tissue maintenance (Andrae et al. 2008).

### 1.2.3 Cell motility

The first and most obvious function assigned to cilia was their necessity for locomotion of unicellular eukaryotes in aqueous environment (van Leeuwenhoek 1677). Since the motile cilium is an evolutionary conserved organelle, it can be found on many different types of protozoa (Lynn 2008), such as the green alga *Chlamydomonas reinhardtii* (Fig. 1A), a classical model organism used for cilia studies, *Tetrahymena thermophila* (Fig. 1C) or the parasite *Trypanosoma brucei* (Fig. 1B) that needs a cilium for its life cycle and pathogenesis (Foster 2009; Rajagopalan et al. 2009; Julkowska & Bastin 2009) (for an overview of the *T. brucei* flagellum see section 1.4). Apart from protozoa, multicellular organisms and mammalian cell types require motile cilia for locomotion as well. A widely known example is the male sperm cell (Fig. 1E) that needs its single long flagellum to move through the female reproductive system towards the egg (Munro et al. 1994).

Another important role of motile cilia in vertebrates is their ability to generate fluid flow. Cilia are not only needed for male fertility, but also line the female fallopian tubes (Fig. 1F) and transport the zygote from the ovary to the uterus through wave-like beating (Lyons et al. 2006). Thus, ciliary dysfunction can reduce both male and female fertility. In the airway system, motile cilia are present on the epithelial surface (Fig. 1G) where they are essential for mucus clearance (Duchateau et al. 1985). In addition, motile cilia protrude from cells lining the ventricular system of the brain (Fig. 1H) to produce circulation of cerebrospinal fluid (Banizs et al. 2005).

A special case of cilia-mediated fluid flow can be found on the surface of embryonic nodal cells during early embryonic development. The embryonic node harbors cells featuring a single 9 + 0 motile cilium on the ventral side. The absence of the central MTs creates a specific rotational movement generating a directed fluid flow that determines the left-right asymmetry of the human body (Nonaka et al. 2002). Consequently, defective cilia in the embryonic node can lead to different versions of *situs inversus*, a phenotype characterized by inverted positions of the internal organs (Okada et al. 1999).

## 1.3 Cilia in human disease

Given the diverse functions and implications of cilia and cilia-related processes, a wide range of human disorders arises from defects in cilia formation or function. These genetic disorders, commonly referred

to as ciliopathies, are a heterogeneous group characterized by mutations in cilia-associated genes (>180 % identified to date) (Reiter & Leroux 2017). Representatives of the disease spectrum are Bardet-Biedl syndrome (BBS), Usher syndrome, Joubert syndrome and Meckel-Gruber syndrome, to name just a few (Fliegau et al. 2007; Waters & Beales 2011). The first disease linked to ciliary defects was primary ciliary dyskinesia (PCD), a disease associated with malfunctioning motile cilia (Afzelius 1976). PCD patients carry cilia that are partially or totally lacking components of the motility machinery, such as ODAs, IDAs or radial spokes (see Fig. 2) (Olbrich et al. 2002; Ibañez-Tallon et al. 2002). Mutations leading to defects in motile cilia show typical phenotypes of infertility (due to immotile or inefficient sperm flagella or fallopian tube cilia), bronchiectasis (caused by defects of the airway cilia) and abnormal left-right asymmetry, called *situs inversus* (due to inability of the embryonic node cilia to generate a directed fluid flow) (Eliasson et al. 1977).

Ciliopathies generally exhibit a range of common phenotypes due to the widespread occurrence of cilia, including renal diseases, retinal degeneration, brain and skeletal abnormalities (Waters & Beales 2011). Further phenotypes include polydactyly, diabetes, obesity, hearing loss and fibrocystic diseases. Ciliary defects can in principle affect any organ, but are predominantly linked to kidney, eye, liver and brain. Mutation or deletion of genes resulting in severe universal cilium formation defects are often embryonic lethal (Veleri et al. 2014; Franco & Thauvin-Robinet 2016).

In most cases, the underlying molecular defects causing the different disease phenotypes are complex and not known to date. The majority of mutations causing ciliopathies are nonsense, frameshift or splice-site mutations in ciliary genes leading to complete loss of protein function. Additionally, many ciliary defect phenotypes are caused by aberrant cilia-related signal transduction pathways (Hh, Wnt) and are therefore not very informative in terms of specific protein functions. However, a previous study from our lab elucidated the structural basis of a point mutation in BBS1 found in 30 % of all BBS patients (Mourão et al. 2014). Further structural and biochemical investigations will be required to shed light on functions and molecular mechanisms of individual disease-causing proteins.

## 1.4 *Trypanosoma brucei* as a model organism for cilium studies

For many years, the prevalent model organism to study cilium function and protein composition has been the green alga *Chlamydomonas reinhardtii* with its two long flagella emerging from the apical end (Foster 2009) (Fig. 1A). However, the use of different model organisms with their individual biological features and experimental accessibility and limitations has revealed further insights for the field of cilium studies. These more recently used model organisms include, amongst others, *Caenorhabditis elegans*, *Tetrahymena thermophila* (Fig. 1C), *Trypanosoma brucei* (Fig. 1B) and mammalian cells (Rajagopalan et al. 2009; Müller et al. 2011; Morga & Bastin 2013; Ishikawa & Marshall 2015).

*Trypanosoma brucei* is the African parasite causing sleeping sickness. It proliferates in the bloodstream of mammalian hosts and is transmitted by the tsetse fly. In the fly, it resides in the gut and salivary glands and undergoes a complex series of developmental stages characterized by changes in biochemistry,

protein expression and cell morphology. Trypanosomes carry a single 9 + 2 motile cilium that is essential for their life cycle and pathology. The trypanosome flagellum exhibits several unique features (Fig. 5B) (Julkowska & Bastin 2009). It is attached alongside the cell body from its point of emergence to the end of the cell, with only the distal tip protruding into the extracellular environment and performing a pulling force to drag the cell forward. Yet, the beating-direction can be reversed, leading to backward motility of the parasite. The cilium includes a unique proteinaceous structure, the paraflagellar rod (PFR) that is attached to one side of the axoneme and is essential for locomotion. Its exact role in motility remains enigmatic (Bastin et al. 1996; Bastin et al. 1998). The cilium arises from the flagellar pocket (see also section 1.1.3, ciliary pocket), a special membrane invagination that represents the single site for endocytosis/exocytosis in trypanosomes (Overath & Engstler 2004). However, the most striking biological feature with respect to cilium biology is that before cell division, *T. brucei* assembles a second, new flagellum while keeping the old one intact, thus carrying two flagella at different assembly stages within one cell (Fig. 5A) (Sherwin & Gull 1989). This facilitates simultaneous investigation of a cilium under construction and a fully assembled one, which is a major advantage for studies on the role of individual ciliary proteins.

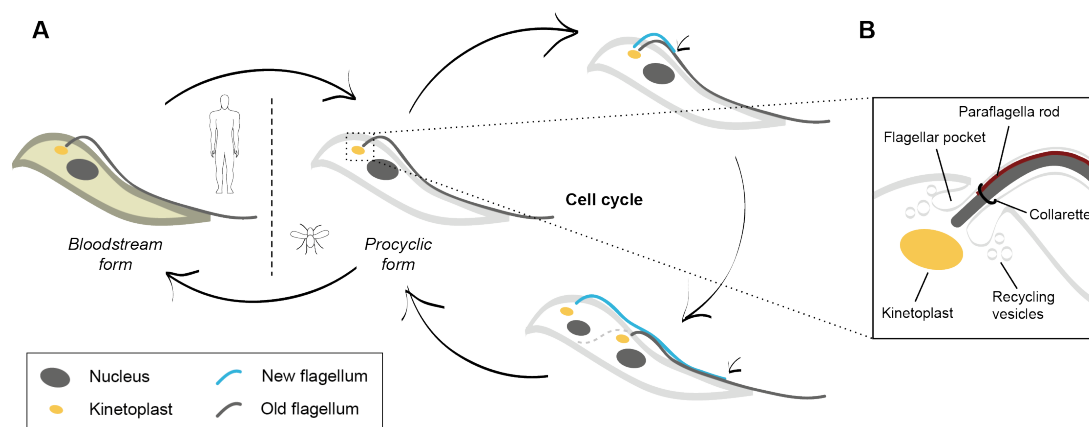


**Figure 5: Simplified overview of the trypanosome life cycle**

**A.** *Trypanosoma brucei* parasites proliferate in the bloodstream of mammalian hosts and are transmitted by the tsetse fly, where they undergo a complex series of different developmental stages. The most studied stage is the procyclic stage, in which they assemble a new flagellum before cytokinesis while keeping the old one intact, allowing simultaneous investigation of different flagellar assembly states in one cell. **B.** Schematic representation of characteristic features of the *T. brucei* flagellum.

A range of different techniques for cilium studies in *T. brucei* has been developed over the past years, including versatile tools for reverse genetics such as transient or tetracycline-inducible RNAi knockdown of individual genes (Julkowska & Bastin 2009).

## 2 Intraflagellar transport and its key players

The ciliary compartment harbors a unique composition of proteins including structural elements of the axoneme (e. g. tubulin, ODA and IDA subunits), signaling components and various membrane proteins. Proteomic analysis identified more than 600 protein candidates to reside in the organelle (Pazour et al. 2005), demonstrating the need of an elaborate and efficient transport machinery since proteins

synthesized in the cytoplasm cannot pass the TZ through passive diffusion (see section 1.1.2). Besides, assembly and elongation of the axoneme were shown to occur at the tip, thereby continuously moving further away from the cytoplasm during ciliogenesis (Johnson & Rosenbaum 1992). This intraflagellar transport (IFT) process was first discovered in *C. reinhardtii* flagella by differential interference contrast microscopy (Kozminski et al. 1993) and has since been observed in many other model organisms. The initial study determined different velocities for particles moving between the ciliary membrane and the axoneme from the base towards the tip (anterograde IFT,  $2 \mu\text{m s}^{-1}$ ) and particles moving in the opposite direction (retrograde IFT,  $3.5 \mu\text{m s}^{-1}$ ) (Kozminski et al. 1993). It is currently expected that anterograde IFT movement is performed on MT B-tubules, whereas retrograde IFT happens on A-tubules, thus preventing particle collision (Stepanek & Pigino 2016). Other studies identified the composition of the multisubunit IFT particles and showed the organization into biochemically and functionally distinct subcomplexes, termed IFT-A and IFT-B (Piperno & Mead 1997; D G Cole et al. 1998), which will be described in the following sections. Electron microscopic analyses showed that IFT particles arrange in a linear fashion forming train-like assemblies (so-called IFT trains) (Kozminski et al. 1995). To date, 22 proteins are known to assemble the roughly 1.5 MDa IFT complex (Taschner et al. 2016). They are highly conserved (Jékely & Arendt 2006) and typically named according to their apparent molecular weights in *C. reinhardtii*, a nomenclature that will be followed throughout this doctoral thesis for all homologs for the sake of consistency. Mutations in several IFT genes have been shown to contribute to the ciliopathy disease spectrum in humans caused by ciliary construction or signaling defects (Fliege et al. 2007). Bioinformatic analyses of IFT components predominantly identified protein-protein interaction domains such as coiled-coils,  $\beta$ -propeller or tetratricopeptide repeats (TPRs) (Taschner et al. 2012), which is in accordance with their function in binding and transport of diverse cargo proteins.

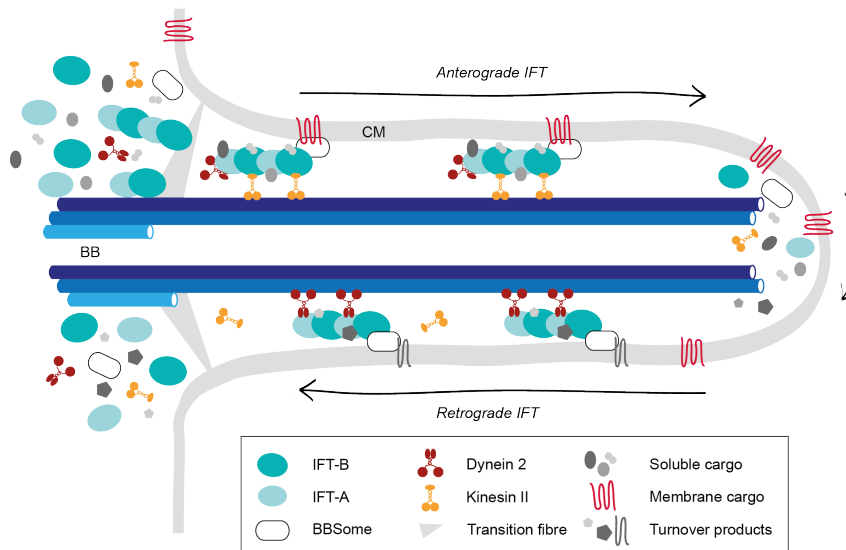


**Figure 6: Overview of the intraflagellar transport key steps**

IFT-A and IFT-B particles as well as ciliary cargo (both soluble and membrane-bound), the BBSome, and MT motor proteins enrich at the transition fibres, where they associate and assemble into IFT trains. Cargo- and inactive dynein-loaded trains enter the cilium and move towards the tip in a kinesin II-dependent manner (anterograde IFT). At the tip, cargo is released, IFT trains are remodeled and the anterograde motor is inactivated, while dynein 2 is activated. Kinesin II exits the cilium independent of IFT, while retrograde IFT trains loaded with ciliary turnover products are transported back to the base with help of the dynein motor (retrograde IFT). At the base, IFT trains exit the compartment and disassemble.

Apart from IFT proteins, IFT trains contain motor proteins required for transport along the MT filaments (see section 2.1). The conventional anterograde motor is heterotrimeric kinesin II, whereas retrograde transport has been assigned to cytoplasmic dynein 2 (Douglas G Cole et al. 1993; Walther et al. 1994; Pazour et al. 1998; Porter et al. 1999). Deletion of IFT-A and IFT-B proteins resulted in phenotypes similar to the ones observed for dynein 2 and kinesin II mutants, respectively, thus linking IFT-A proteins to retrograde and IFT-B components to anterograde IFT (see section 2.2 and 2.3).

IFT is a multi-step process (see Fig. 6) that starts with the enrichment of IFT and cargo proteins at the ciliary base, where the individual components have to assemble into cargo-loaded particles and trains. In the next step, trains move in the anterograde direction driven by the kinesin II motor, followed by cargo unloading and remodeling of IFT particles at the ciliary tip. There, turnover products have to be bound and motor activities have to be switched to activate dynein 2 for retrograde IFT. Finally, turnover products are released at the base and IFT particles are recycled for subsequent rounds of ciliary trafficking (Hao & Scholey 2009). This cycle has to be controlled and regulated at several steps, however the underlying molecular mechanisms are only poorly understood so far. Obtaining high-resolution protein structures could help to assign individual protein functions and explain mechanistic details of the key steps.

## **2.1 IFT motor proteins**

Trafficking of IFT particles along the axoneme in the anterograde direction mainly depends on the heterotrimeric kinesin II motor (Douglas G Cole et al. 1993; Walther et al. 1994), although an exception can be found in *C. elegans*, where homodimeric kinesin II acts as a second motor that works partially redundantly (Snow et al. 2004; Prevo et al. 2015). The energy driving the movement is derived from ATP hydrolysis in the kinesin head domain. Disruption of kinesin II leads to severe ciliogenesis defects (Kozminski et al. 1995), as can be observed for mutation of IFT-B proteins (Pazour et al. 2000; Tsao & Gorovsky 2008). It is therefore assumed that the kinesin motor binds to IFT particles via IFT-B during anterograde transport, which was supported by co-immunoprecipitation studies (Baker et al. 2003). Retrograde transport is then mediated via dynein 2 presumably bound to the IFT-A complex (Pazour et al. 1998; Porter et al. 1999; Perrone et al. 2003; Hou et al. 2004). Deletion mutants of either complex display a retrograde phenotype characterized by short bulbous cilia filled with IFT material at the tip (Piperno et al. 1998; Tsao & Gorovsky 2008; Iomini et al. 2009). In order to fulfill its function at the ciliary tip, the inactivated dynein motor has to be actively transported as a cargo by IFT and the kinesin motor to the distal end of the axoneme. A recent study detected a specific phosphorylation of kinesin II at the tip that leads to motor inactivation and dissociation from the IFT complex, thus providing a mechanism for regulation of the switch in motor activities (Liang et al. 2014). Return of the inactive kinesin motor to the ciliary base is likely carried out by diffusion in an IFT-independent manner (Engel et al. 2012).

## 2.2 The IFT-A subcomplex

IFT-A is a six-component IFT subcomplex comprising the proteins IFT144, IFT140, IFT139, IFT122, IFT121 and IFT43 (Fig. 7A). As described in the previous section, the IFT-A complex has been linked to dynein 2-mediated retrograde transport with mutants producing a typical retrograde IFT inactivation phenotype (Efimenko et al. 2006; Tran et al. 2008; Tsao & Gorovsky 2008; Absalon et al. 2008). It is therefore not surprising that several mutations in IFT-A encoding genes have been identified in ciliopathy patients (Gilissen et al. 2010; Arts et al. 2011; Bredrup et al. 2011).

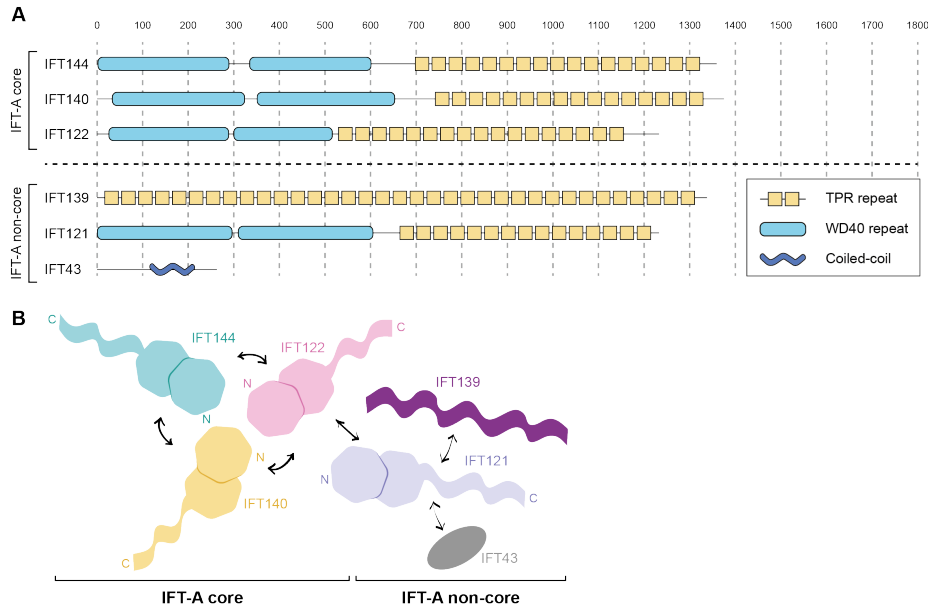


**Figure 7: Schematic overview of IFT-A complex components**

**A.** Domain architecture of currently identified IFT-A proteins. Depicted sizes and domain borders correspond to the *C. reinhardtii* proteins. **B.** Schematic interaction map of the IFT-A proteins.

To date, only little is known about structures and functions of individual IFT-A proteins as well as their interactions. It was shown that IFT122/140/144 build a stable, independent trimeric “core” complex (Mukhopadhyay et al. 2010) and recent (partly unpublished) data suggest that the remaining non-core proteins form an independent IFT43/121/139 complex as well (Behal et al. 2012; Taschner & Lorentzen, unpublished data). Identified interactions between IFT-A components are illustrated in Fig. 7B. Interestingly, four of the six IFT-A proteins have a predicted domain organization similar to membrane coat proteins with N-terminal  $\beta$ -propellers and C-terminal  $\alpha$ -solenoid structures (Fig. 7A) (Taschner et al. 2012). Apart from IFT121, these proteins involve all three components of the IFT-A core complex. Due to their similarity to coat protein complex I (COPI) proteins, it can be speculated that they could form a heterotrimeric complex mediated by their  $\beta$ -propeller head domains similar to COPI, although this hypothesis is lacking experimental confirmation (Taschner & Lorentzen 2016b). Despite the fact that IFT-A function is mainly associated with retrograde IFT, meaning return of turnover products and IFT components from the tip to the ciliary base, there is evidence that IFT-A is also needed for import of certain cargo proteins into the cilium see section 2.5.

One of the initial studies characterizing the IFT complex observed that IFT-A and IFT-B subcomplexes bind at low ionic strength, but dissociate when slightly increasing the salt concentration (D G Cole et al. 1998). Several follow-up studies could not detect direct interactions between IFT-A and IFT-B components (D G Cole et al. 1998; Follit et al. 2009), whereas others were able to (Qin et al. 2004; Pedersen et al. 2005), thus leading to contradictory results. A recent study in *C. reinhardtii* suggested that the N-terminal part of the IFT-B protein IFT74 might provide the attachment point for IFT-A, since deletion of this part prevented ciliary entry of IFT-A (Brown et al. 2015).

## 2.3 The IFT-B subcomplex

Initial analysis on IFT-B particle composition identified a salt-stable core complex consisting of six proteins (IFT88, IFT81, IFT74, IFT52, IFT46 and IFT27), as well as four other components (IFT172, IFT80, IFT57, IFT20) that dissociated at salt concentrations above 300 mM and were termed peripheral subunits (Lucker et al. 2005). Subsequent studies detected additional IFT-B proteins (Ou et al. 2005; Kunitomo & Iino 2008; Adhiambo et al. 2009; Zhaohui Wang et al. 2009; Lechtreck et al. 2009a; Fan et al. 2010; Ishikawa et al. 2014) and showed that the peripheral proteins actually form a stable complex on their own (Taschner et al. 2016; Katoh et al. 2016), suggesting the new nomenclature of IFT-B1 (previous IFT-B core) and IFT-B2 (previous IFT-B peripheral subunits). The currently assumed composition of the IFT-B complex consists of 10 proteins for IFT-B1 (IFT88, IFT81, IFT74, IFT70, IFT56, IFT52, IFT46, IFT27, IFT25, IFT22) and 6 proteins for IFT-B2 (IFT172, IFT80, IFT57, IFT54, IFT38, IFT20) and is schematically depicted in Fig. 8. As already mentioned, IFT-B is thought to bind the kinesin II motor for anterograde trafficking and disruption of IFT-B proteins strongly impairs cilium assembly (Pazour et al. 2000; Tsao & Gorovsky 2008).

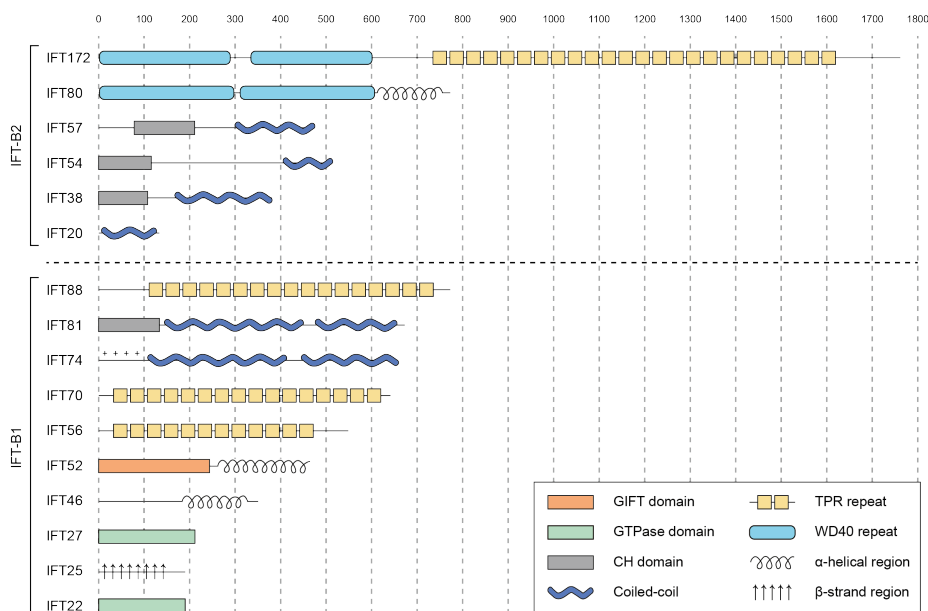


**Figure 8: Domain architecture of IFT-B complex components**

Depicted sizes and domain borders correspond to the *C. reinhardtii* proteins. The IFT-B complex can be subdivided into two stable subcomplexes, IFT-B1 and IFT-B2.

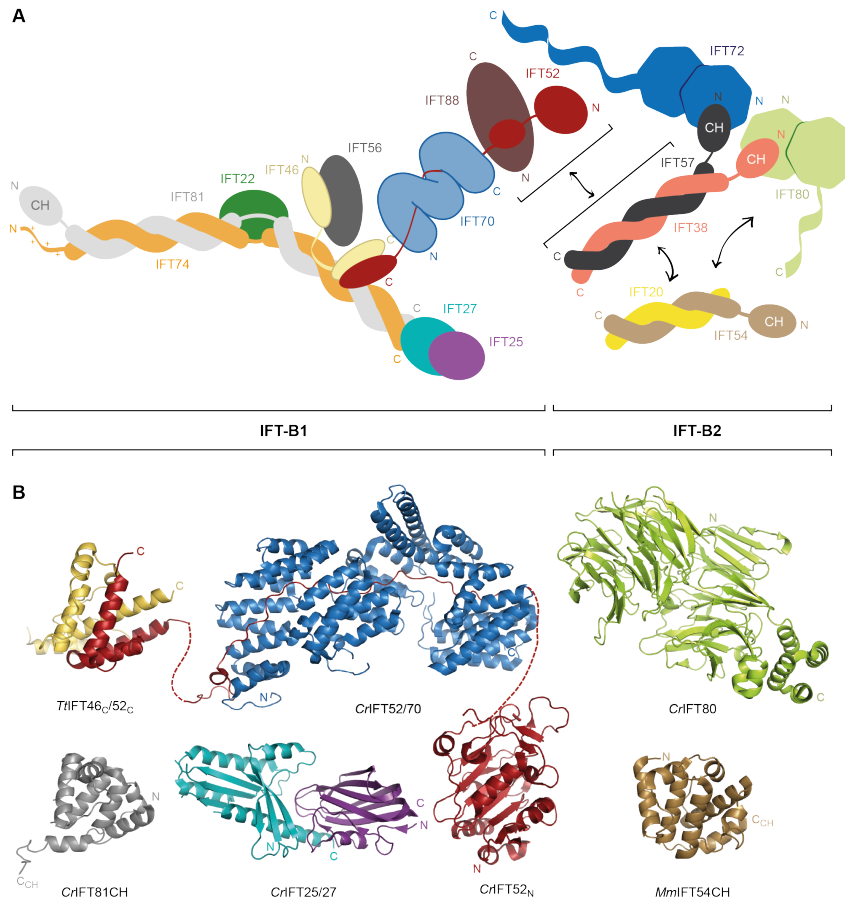


**Figure 9: Schematic overview of the IFT-B complex**

**A.** Interaction map of the IFT-B complex with all proteins identified to date. IFT-B1 and IFT-B2 interact via IFT52/88 and IFT38/57, respectively. Note that exact binding positions of IFT25/27 and IFT46/52 on the C-terminal part of IFT74/81, as well as the binding position of IFT56 on IFT46 are not known. **B.** Currently available crystal structures of IFT-B complex components and domain truncations. (PDB IDs: 4uzz, 4uzy, 5n4a, 4lvp, 2yc2, 5fmr, 5fmu)

Extensive *in vitro* studies using recombinant proteins have led to an advanced understanding of IFT-B complex architecture with mapped interactions between individual proteins or protein domains (Fig. 9A). In the past years, our lab made significant progress in the recombinant reconstitution of differently sized IFT-B subcomplexes with the biggest one being an almost complete 15-subunit IFT-B complex lacking only IFT56 (Taschner et al. 2011; Taschner et al. 2014; Taschner et al. 2016; Taschner & Lorentzen 2016a). The interaction between the two IFT-B complexes could recently be assigned to IFT88/52 on the IFT-B1 side and IFT57/38 on the IFT-B2 side. Contacts between IFT proteins are mainly mediated by hydrophobic interactions, which also explains IFT-B1 stability in salt concentrations above 2 M. A major challenge for studies on the IFT complex and for assigning specific functions to certain proteins is the composite interaction network of the individual components. For example, both IFT52 and IFT74 directly interact with five other IFT-B1 proteins each (Fig. 9A), so that depletion of either one results in severe complex destabilization and disassembly, leading to unspecific ciliogenesis phenotypes *in vivo* (Richey & Qin 2012; Brown et al. 2015). This problem is not only restricted to one subcomplex, but also expands to interactions linking IFT-B1 with IFT-B2 and the IFT-A complex and shows limitations of null mutant-based phenotypic analysis. A more targeted approach deleting only certain protein domains or

inserting point mutations *in vivo* that only disrupt specific interactions require detailed knowledge of the domain architecture and the three-dimensional structure of the protein of interest. Nevertheless, several functions of particular proteins could be identified as yet, amongst which are binding of some ciliary cargo proteins (for more information see section 2.5), sorting of ciliary membrane proteins at the Golgi apparatus by IFT20 (Follit et al. 2006) and regulation of the anterograde-retrograde switch at the tip of the cilium by IFT172 (Pedersen et al. 2005; Tsao & Gorovsky 2008).

Bioinformatic analysis of IFT-B proteins mostly revealed domains known to be involved in protein-protein interactions (for an overview, see Fig. 8) (Taschner et al. 2012). Four proteins contain predicted calponin homology (CH) domains of which two were experimentally shown to bind tubulin (IFT81 and IFT54, see section 2.5) whereas the other two (IFT57 and IFT38) function in mediating interactions between IFT proteins (Bhogaraju et al. 2013b; Taschner et al. 2016). Other proteins are composed of TPRs (IFT172, IFT88, IFT70, IFT56), coiled-coils (IFT81, IFT74, IFT57, IFT54, IFT38, IFT20) or WD40-repeats/ $\beta$ -propellers (IFT172, IFT80). Exceptional cases are the two small proteins IFT27 and IFT22 that show significant sequence similarity to small GTPases of the Rab family and are therefore the only proteins with potential enzymatic activity in the whole IFT complex. IFT27 and IFT22 are considered promising candidates for regulation of IFT or cilium-associated processes and will be described in detail in section 3.4.

High-resolution crystal structures of several IFT-B subunits are available to date and an overview of those is given in Fig. 9B. However, most crystal structures comprise only domain truncations or minimal interaction regions of complexes, and so far no structural information on larger assemblies could be obtained. Further structural investigations will be required using complementary approaches of both X-ray crystallography and single-particle cryo-EM for determination of three-dimensional structures of larger IFT assemblies in order to understand the underlying molecular details of the ciliary trafficking process.

## 2.4 The BBSome

In addition to the IFT complex, a second multiprotein complex was discovered to cycle in the cilium at the speed of IFT trains, and mutations in its components were found to cause a genetic disorder in humans, the Bardet-Biedl syndrome (Blacque & Leroux 2006). The BBSome complex consists of eight (or nine, dependent on the counting) individual proteins (BBS1, BBS2, (BBS3 = Arl6,) BBS4, BBS5, BBS7, BBS8, BBS9, BBS18) and associates with IFT particles and the ciliary membrane (Nachury et al. 2007; Mourão et al. 2014; Williams et al. 2014). Knockout experiments showed that the BBSome is not needed for cilium construction, but for establishing the correct composition of membrane proteins in the cilium (Lechtreck et al. 2009b; Zhang et al. 2013; Langousis et al. 2016). While several membrane proteins were found to accumulate, others were depleted from the cilium. Further studies led to the notion that the BBSome acts as an adaptor between the IFT complex and membrane proteins such as the Hh receptors Ptch1 and Smo (see section 1.2.2) and functions in trafficking of membrane proteins in

the cilium. Various interactions between individual BBSome proteins and signaling components have so far been identified (for an overview, see Mourão et al. 2016). Interestingly, IFT27 knockout mice showed a phenotype of accumulated BBSome material at the ciliary tip, leading to the conclusion that IFT27 is needed for ciliary export of the BBSome (Eguether et al. 2014), although the exact mechanism is still a matter of debate (Seo et al. 2011; Liew et al. 2014). Additionally, IFT27 mutations were found in BBS patients, supporting the functional connection between IFT27 and the BBSome (Aldahmesh et al. 2014). Besides, a second direct interaction between the IFT complex and the BBSome was detected between the IFT-A core protein IFT144 and BBS1 (Wei et al. 2012).

## 2.5 IFT cargo proteins

The ciliary organelle harbors several hundred proteins, most of which are considered to be actively transported across the diffusion barrier. The IFT complex represents an adaptor complex, linking ciliary cargo to molecular motor proteins for import into and export out of the cilium. Regarding the large number of (putative) cargo proteins, remarkably little is known about specific IFT-cargo interactions. In the previous section, the BBSome as a linker for membrane protein transport has been described. The few interactions between IFT proteins and cargo proteins that have been identified to date will be described here.

A study in mice found that the IFT-A core complex binds and imports Tubby-like protein 3 (TULP3), a protein that is needed for GPCR import into the cilium (Mukhopadhyay et al. 2010). However, it is still unclear which of the three proteins (IFT122, IFT140 and IFT144) mediates the interaction. Another direct interaction with an IFT-A protein was revealed between IFT144 and BBS1 and mutation of either protein resulted in BBSome exclusion from the cilium (Wei et al. 2012).

More direct interactions with ciliary cargo could be identified for IFT-B components, likely because this subcomplex underwent extensive investigations in the past decade. A breakthrough finding in ciliary cargo import was the detection of a direct interaction between the IFT81/74 N-termini and tubulin (Bhogaraju et al. 2013b), followed by identification of a second tubulin site in IFT54 (Taschner et al. 2016). For construction of a *C. reinhardtii* axoneme, approximately 350 000 tubulin dimers are required (Bhogaraju et al. 2014), making it the most abundant ciliary cargo protein. IFT81 contains an N-terminal CH domain that specifically binds the globular part of the  $\alpha/\beta$ -tubulin heterodimer, whereas the unstructured positively charged IFT74 N-terminus was shown to enhance the affinity by binding to the negatively charged tubulin E-hooks (Bhogaraju et al. 2013b).

ODAs and IDAs are large complexes and integral components of motile cilia responsible for ciliary bending (see also section 1.1.1). Import of ODAs was shown to depend on the adaptor protein ODA16 (Ahmed & Mitchell 2005), which in turn mediates binding to the IFT-B1 protein IFT46 (Hou et al. 2007). A recent study from our lab confirmed the direct interaction between IFT46 and ODA16 using recombinant proteins and mapped the binding interface to a region in the IFT46 N-terminal part (Taschner et al. 2017). IDAs on the other hand require IFT56 for ciliary trafficking, most likely also via an adaptor

protein (Ishikawa et al. 2014). As a potential candidate the HSP90-interacting protein TWI1 is under investigation (Ishikawa et al. 2014), but confirmation of a direct interaction is still missing.

Future research involving both *in vitro* studies with purified IFT proteins and *in vivo* analysis of domain deletion or point mutants will be required for identification of additional cargo proteins and mapping of interaction domains.

### 3 Small GTPases in ciliary construction and maintenance

GTP-binding proteins (G proteins) are a class of proteins that switch between an active and inactive state to regulate a diverse range of cellular processes. Their most prominent members are heterotrimeric G proteins that interact with GPCRs and regulate transmembrane signaling, and monomeric small G proteins that take over functions in signaling, cell shaping and motility and vesicular membrane transport. Since several small GTPases have been linked to cilium-related processes, the following sections will give an overview on their structures and functions.

#### 3.1 General structure and features of (small) GTPases

G proteins are characterized by altering between an active, GTP-bound state and an inactive, GDP-bound state, thereby acting as molecular switches. The conversion between the two states is achieved by GTP-hydrolysis and subsequent replacement of the GDP nucleotide and is facilitated by additional factors (Bos et al. 2007). A schematic representation of the GTPase cycle is depicted in Fig. 10A. Since intrinsic hydrolysis rates of small GTPases are usually very low, GTPase activating proteins (GAPs) stimulate GTP hydrolysis by insertion of a catalytic residue into the active site. This can accelerate the speed of reaction by several orders of magnitude (Wittinghofer & I. R. Vetter 2011). The inactive GTPase is then reactivated by a guanine nucleotide exchange factor (GEF) that catalyzes the replacement of GDP for GTP by increasing the dissociation rate of GDP (Cherfils & Zeghouf 2013). Due to the cytoplasmic excess of GTP over GDP, the protein gets GTP-loaded and reactivated. Downstream effector proteins preferably bind to the active GTP-bound form of small GTPases (I. R. Vetter & Wittinghofer 2001). Upon GAP-assisted GTP-hydrolysis, interaction with the effector becomes destabilized and disturbed. GEFs/GAPs usually are multidomain proteins that are selective for certain GTPases to guarantee signaling specificity (Bos et al. 2007).

The conserved approximately 20 kDa GTPase domain (G domain) is a common feature of all G proteins and consists of a central six-stranded  $\beta$ -sheet surrounded by five  $\alpha$ -helices (see Fig. 10A) (Wittinghofer 2014). Five conserved sequence motifs (G motifs G1-G5) are located in loop regions around the nucleotide-binding pocket and are required for stable binding of GTP/GDP and the  $Mg^{2+}$ -cofactor (I. R. Vetter & Wittinghofer 2001) (for consensus sequences and positions see Fig. 10A). G1 (also termed phosphate-binding (P) loop) ensures stable binding of the  $\beta$ -, and  $\gamma$ -phosphate. Residues in G2 and G3 interact

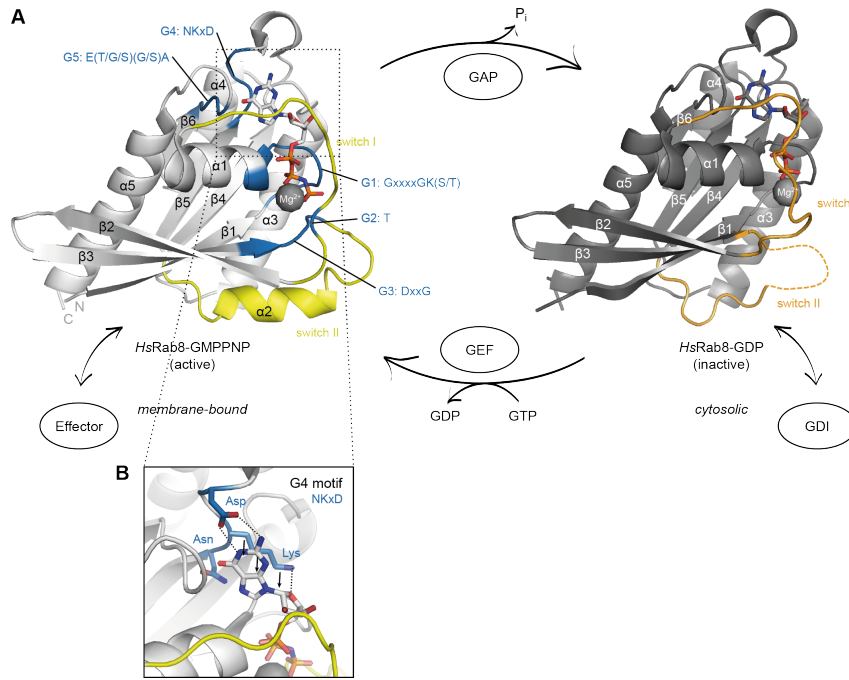


**Figure 10: Structure and features of small Rab GTPases**

**A.** Cartoon representations of *HsRab8* in its active, GTP-bound (left) and inactive, GDP-bound (right) form (PDB IDs: 4lhw,4lhv). Switch regions are shown in yellow/orange and undergo the biggest conformational changes upon nucleotide exchange. Conserved G motifs surrounding the nucleotide-binding pocket are depicted in blue and respective consensus sequences are indicated. The GTPase cycle is mediated by GEF and GAP proteins. **B.** Detailed view of the G4 motif residues interacting with the nucleotide. The highly conserved Asp residue is the major determinant of nucleotide specificity, forming a bifurcated hydrogen bond with the guanine base.

with the  $\gamma$ -phosphate of GTP and the  $Mg^{2+}$ -ion and are located in the so-called switch regions. Switch regions (switch I and switch II) undergo the most significant conformational changes during alternation of the nucleotide state (Fig. 10A), and are stabilized upon interaction with the GTP  $\gamma$ -phosphate (Milburn et al. 1990; Stroupe & Brunger 2000). This conformational change provides the structural basis for GTP-dependent effector binding, as well as for binding of nucleotide state-dependent regulators. In the GDP-bound state, switch I and II are less tightly bound and therefore often unstructured and invisible in crystal structures. G4 is the major determinant of nucleotide specificity, harboring a highly conserved Asp residue that forms hydrogen bonds with the guanine base and that precludes binding of ATP. Besides, the carbon chain of a Lys residue in G4 adjacent to Asp interacts with the purine ring system of the base via a stacking interaction and forms a hydrogen bond with the ribose (Paduch et al. 2001) (Fig. 10B). Part of the G5 motif also binds the guanine base, but it represents the least conserved sequence motif.

Small GTPases are monomeric proteins of 20 kDa to 25 kDa with most members (>150 in humans) found in the Ras superfamily. Based on sequence and functional similarities, the Ras superfamily can be further subdivided into Ras, Rho, Rab, Ran and Arf small GTPase families. Rab and Arf family members are the main regulators of vesicular transport and membrane trafficking and are involved in all key steps from cargo sorting and budding at the donor membrane to vesicle fusion with the acceptor membrane (Cooper 2000).

## 3.2 Cellular functions of small Rab GTPases

Rab GTPases comprise the largest family of small GTPases with approximately 70 known members in humans (Wandinger-Ness & Zerial 2014). They can be found in all eukaryotes and many of them are closely related, both in sequence and function. Rab GTPases are crucial for regulation of vesicular membrane trafficking and are characterized by distinct features: They contain five conserved Rab family sequence stretches clustering around the switch regions (F1-F5) and a variable cysteine motif at the C-terminus that serves as a prenylation signal used for membrane association (Pereira-Leal & Seabra 2000; Stenmark & Olkkonen 2001). They cycle between an active GTP- and membrane-bound state and an inactive GDP-bound cytosolic state, meaning that the nucleotide state determines their subcellular localization. In their GTP-bound form, they localize to the cytosolic side of different membrane-enclosed compartments (donor membranes) where they can recruit a specialized set of effectors. Like other GTPases, Rab proteins become inactivated by GAPs and upon inactivation they are released from the membrane. This process is mediated by so-called Rab GDP-dissociation inhibitors (GDIs) that stabilize the inactive state and shield the geranylgeranyl anchor from the aqueous solvent (Ullrich et al. 1993; Cherfils & Zeghouf 2013). GDIs on their part are considered to be regulated by GDI-displacement factors (GDFs) that promote RabGDI dissociation and thus allow for another round of GTP-loading and hydrolysis.

Vesicular membrane trafficking is needed for stable membrane and organelle homeostasis, cellular growth, cell proliferation and differentiation and intercellular signaling. Rab GTPases coordinate all steps associated with membrane trafficking, which are: 1) Recruitment of specific effectors and vesicle formation at the donor membrane, 2) Budding from the donor membrane, 3) Uncoating of vesicles, 4) Directed vesicle movement along actin filaments and microtubules, 5) Tethering at the acceptor membrane and 6) Membrane fusion (Stenmark 2009). Each of these processes has to be tightly regulated, both spatially and temporally, to ensure correct delivery of compounds between different subsets of membranes.

While different Rab GTPases show a high degree of structural similarity, their recruited effector proteins are very heterogeneous both structurally and functionally. Dependent on the different stage of the transport process, they range from adaptor proteins and kinases to tethering factors or motor proteins. Thus, distinct individual features have to be present in different Rab GTPases to facilitate selective effector binding. This specificity can be attributed to switch I, switch II and the interswitch region (a loop connecting  $\alpha 3$  with  $\beta 5$ ), sequence stretches that show the greatest variability in Rab GTPases (Eathiraj et al. 2005). Additionally, one Rab GTPase often binds several different effectors dependent on its current membrane localization. The mechanism of Rab targeting to their respective donor membranes is not yet clearly understood, but it is assumed that GDFs play an important role in this step (Sivars et al. 2003).

The degree to which different Rab proteins are dispensable is variable. While some Rab GTPases are crucial for proper cellular functions, others are dispensable or can be displaced by related family members. Knock-out studies and identification of patient mutations have revealed that disturbance of several Rab GTPase pathways can be linked to many genetic and pathogen-induced diseases, including

immunological or neurological defects and cancer (Stenmark 2009). These disruptions are not limited to Rab genes, but include mutations in genes encoding for effectors and regulatory proteins (Seabra et al. 1993; Pastural et al. 1997; Ménasché et al. 2000). A recent collaborative study linking common mutations in a Parkinson's disease kinase to Rab-regulated pathways by affecting the binding ability of certain Rabs to interaction partners is part of the results section of this thesis (see Paper B, starting on page 74).

### 3.3 Small GTPases involved in ciliary targeting

Proteins involved in cilium formation and maintenance have to be actively transported to the ciliary base prior to IFT/BBSome-mediated import and trafficking within the organelle. While not much is known about recruitment mechanisms and pathways of soluble ciliary proteins to the base, ciliary targeting of membrane proteins has been studied more extensively over the past years. Similar to other transmembrane proteins, receptors and channels destined for the ciliary compartment are synthesized at the endoplasmic reticulum (ER), subsequently processed in the Golgi apparatus, and then sorted and packaged into vesicles at the trans Golgi network (TGN). Membrane protein-enriched vesicles move along the cytoskeleton to the cilium, where they fuse with the periciliary membrane. Subsequent import of membrane proteins is likely mediated by the BBSome and the IFT machinery (Nachury et al. 2010) (see section 2).

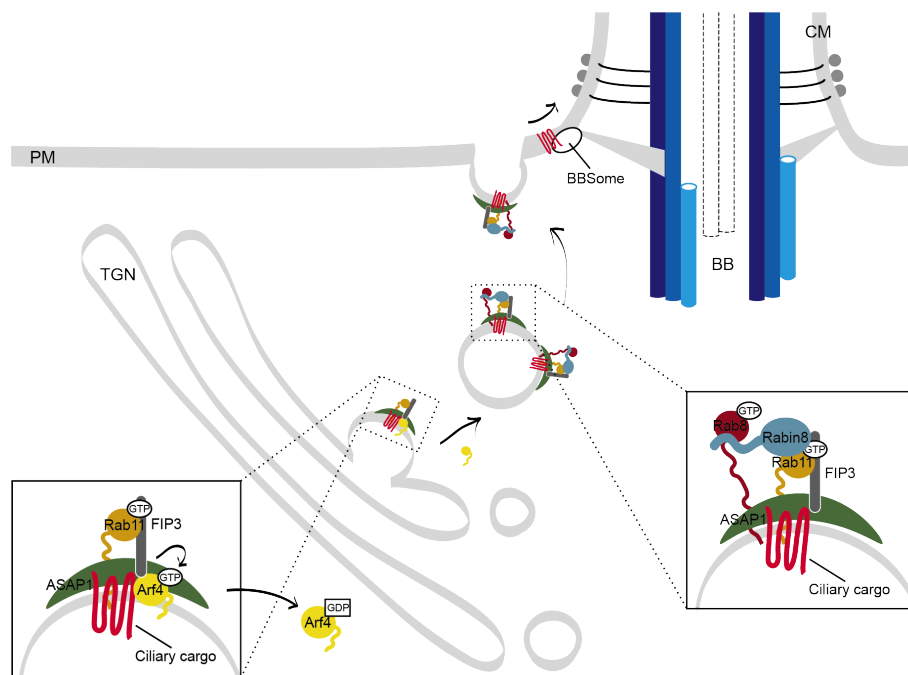


**Figure 11: Schematic representation of ciliary membrane trafficking**

Ciliary targeting complexes (detailed view) form on the TGN membrane. Active Arf4 recognizes ciliary targeting sequences of ciliary membrane cargo proteins and binds ASAP1, which in turn recruits the Arf4/Rab11 effector FIP3 and thus Rab11. ASAP1 acts as an Arf4-GAP and leads to dissociation of inactive Arf4 from the complex. Rab11 on budding vesicles recruits its effector Rabin8, which mediates binding and activation of Rab8. Active Rab8 regulates vesicle docking at the base of the cilium and facilitates association of ciliary membrane cargo with the BBSome machinery for ciliary import. (BB = basal body, CM = ciliary membrane, PM = plasma membrane, TGN = trans Golgi network)

Sorting of ciliary proteins at the TGN and correct targeting of vesicles requires recognition of ciliary targeting sequences (CTSs). Several different CTSs have been identified to date (Tam et al. 2000; Geng et al. 2006; Berbari et al. 2008), although they are not as conserved as the nuclear localization signal, for instance. It has also been suggested that apart from specific amino acid sequences, certain post-translational modifications contribute to the targeting signal (Follit et al. 2010). The first CTS was found in the GPCR rhodopsin (see section 1.2.1, *Photoreception*) (Tam et al. 2000), a ciliary cargo whose sorting machinery and ciliary trafficking has been studied most extensively over the past decades (Deretic 1998; Mazelova et al. 2009; M. Vetter et al. 2015).

Ciliary targeting of rhodopsin is accomplished by sequential binding of several factors, amongst them the small GTPases Arf4, Rab11 and Rab8, and formation of a targeting complex (for a schematic overview, see Fig. 11). The initial sorting machinery at the TGN consists of Arf4, the Arf4 GAP ASAP1, the small GTPase Rab11 and the Arf4/Rab11 effector FIP3. Activated membrane-bound Arf4 recognizes and binds the CTS of rhodopsin and recruits ASAP1 (Mazelova et al. 2009). ASAP1 is a large multidomain scaffold protein that binds both Arf4 and the rhodopsin receptor and is thought to induce the membrane curvature needed for vesicle formation through its BAR domain (J. Wang et al. 2012). Additionally, ASAP1 binds FIP3 that on the other hand interacts as an effector for active Rab11 and stimulates the GAP activity of ASAP1. Inactivated Arf4 dissociates from the complex and the transient ASAP1-Rab11-FIP3 complex subsequently recruits Rabin8 (J. Wang & Deretic 2015). Rabin8 is both an effector of Rab11 and a GEF for Rab8, facilitating association of Rab8 to the ciliary targeting complex and activating the GTPase. Instead of consecutively binding FIP3 and Rabin8, Rab11 simultaneously binds the two effectors, thus forming an unusual dual effector complex (M. Vetter et al. 2015). Rab8 is a known key regulator of vesicle docking and fusion at the ciliary base and has been shown to interact with the BBSome, thus providing a link between vesicular trafficking and ciliary transport (Nachury et al. 2007).

### 3.4 IFT-associated Rab GTPases

Two integral components of the 22-subunit IFT complex have strong predicted sequence similarity to small Rab GTPases: IFT22 (Rab15) and IFT27 (Rab14). Given the typical function of Rab family members in the regulation of transport processes, they are considered as potential candidates for regulating IFT or other cilium-related functions. Despite apparent similarities, IFT22 and IFT27 sequences differ from other Rabs as they do not contain a C-terminal prenylation motif required for membrane association.

#### 3.4.1 IFT27 (Rab14)

IFT27 contains well-conserved G-motif and Rab family sequences and has been shown to specifically bind guanine nucleotides (Qin et al. 2007; Bhogaraju et al. 2011). The crystal structure confirmed the overall Rab GTPase fold (Fig. 9B) and complementary biochemical analysis detected low micromolar affinities for GDP and GTP as well as low but measurable GTP hydrolysis rates (Bhogaraju et al. 2011). While low intrinsic GTPase activity is a common feature of small GTPases and is overcome by assistance

of GAP proteins (see section 3.1), Ras family GTPases normally exhibit nucleotide affinities in the picomolar to nanomolar range (Simon et al. 1996). It is therefore hypothesized that IFT27 nucleotide exchange might not require the presence of a GEF, similarly to some large GTPases (Uthaiyah et al. 2003; Bhogaraju et al. 2011). Structure-based similarity searches detected the most significant structural overlap with Rab8 and Rab11, two of the key players in ciliary targeting complexes (see section 3.1), suggesting their evolution from a common ciliary Rab ancestor.

In many organisms, IFT27 was found to directly interact with IFT25, a jelly-roll fold protein (Follit et al. 2009; Zhaohui Wang et al. 2009; Rual et al. 2005). Interestingly, organisms that lack homologs for IFT27 also lack IFT25, such as *C. elegans*, *D. melanogaster* and *G. intestinalis*, whereas *T. thermophila* does contain IFT27, but not IFT25. This is in stark contrast to the high degree of conservation of other IFT-B components and implicates that IFT25/27 serve functions other than cilium assembly. Biochemical *in vitro* experiments using recombinant proteins from different species showed that the IFT27 protein is unstable without IFT25, while IFT25 stability does not depend on IFT27 (Taschner et al. 2011; Bhogaraju et al. 2011; unpublished data from our lab). Consistently, IFT25 knockout in mice leads to depletion of IFT27 (Keady et al. 2012), suggesting that IFT25 is needed for IFT27 stabilization in most organisms.

Functional analysis of IFT27 revealed that association with the IFT-B complex and thereby IFT trafficking depends on the active GTP-bound state of IFT27 and that the inactive state is excluded from entry into the ciliary compartment (Eguether et al. 2014; Huet et al. 2014). Mouse knockout experiments of IFT25 and IFT27 showed formation of intact cilia, but severe birth defects due to abnormal Hh signaling. In agreement with this, BBSome components as well as Hh signaling molecules (Ptch1, Smo) were found to accumulate at the ciliary tip upon IFT25 or IFT27 depletion (Keady et al. 2012; Eguether et al. 2014). It is thus assumed that IFT27 is needed for BBSome and membrane protein export (see also section 2.4), although controversial models regarding the exact mechanism exist. While one study suggested a direct interaction between IFT27 and Arl6 (BBS3) (Liew et al. 2014), the authors of another study rather expected an additional linker protein to mediate the contact (Seo et al. 2011; Eguether et al. 2014). A special effect was reported for *T. brucei*, where knockdown of IFT27 led to a retrograde IFT depletion phenotype caused by the ciliary absence of IFT-A and the dynein motor (Huet et al. 2014). It is likely that IFT27 plays functionally different roles in unicellular species and in higher organisms.

Binding of IFT25/27 to the IFT-B1 complex was mapped to the C-terminal part of the IFT74/81 heterodimer (Taschner et al. 2014) and since it was shown to be GTP-dependent, IFT74/81 can be considered an effector of IFT27 that facilitates import of IFT27 into the cilium.

### 3.4.2 IFT22 (Rab15)

In contrast to IFT27, very little is known about structural and biochemical properties of IFT22. IFT22 shows a high degree of sequence deviation from classical Rab proteins affecting both the Rab sequence motifs and the G motifs. Since G4 is completely absent in IFT22 and G5 shows low conservation, IFT22 has been classified as an atypical small GTPase (Schafer et al. 2006; Adhiambo et al. 2009). These two

motifs are the major factors for guaranteeing guanine nucleotide specificity (see section 3.1) and it is unclear to date if IFT22 really is a functional nucleotide-binding protein, if it can bind ATP instead of GTP and if it can hydrolyze any nucleotides. IFT22 was shown to undergo IFT in different species (Schafer et al. 2006; Yoshimura et al. 2007; Adhiambo et al. 2009; Silva et al. 2012) and the binding site on IFT-B1 was mapped to a short and presumably  $\alpha$ -helical sequence stretch in the middle part of the IFT74/81 dimer (Taschner et al. 2014). Interestingly, neither the IFT81 nor IFT74 peptide alone was able to bind IFT22 and only their combination efficiently pulled down the small GTPase. Recombinant IFT complex reconstitution experiments demonstrated that IFT22 is not required for IFT-B complex stability (Taschner et al. 2014). Although IFT22 and IFT27 are both considered members of the Rab GTPase family and integral components of IFT-B1 interacting with IFT74/81, they share only low sequence similarity <15% (Adhiambo et al. 2009).

Studies on IFT22 cellular function detected species-dependent differences. Knockout of IFT22 (IFTA-2) in *C. elegans* did not impair cilium construction or IFT movement, but mutant worms showed phenotypes of a prolonged lifespan and defective dauer stage formation, an alternative developmental stage of nematodes (Schafer et al. 2006). Both effects are known to be associated with deficiencies in the DAF-2 (insulin-IGF-1-like) receptor signaling pathway, suggesting a role for IFT22 in the regulation of ciliary signaling cascades. In *C. reinhardtii*, IFT22 knockdown did not impair cilium morphology, but instead influenced the cellular levels of other IFT proteins thus regulating the availability of IFT particles for ciliary trafficking (Silva et al. 2012). In contrast, RNAi knockdown of IFT22 in *T. brucei* led to severe ciliogenesis defects and a phenotype linked to retrograde IFT inactivation, characterized by formation of short flagella filled with accumulated IFT material (Adhiambo et al. 2009).

Interestingly, IFT22 mutants mimicking the active GTP-bound and inactive GDP-bound state of the putative small GTPase in *C. elegans* showed clear differences in localization: While the potentially constitutively active mutant (D123L) localized to cilia and moved together with IFT particles similar to wild type (WT) IFT22, the inactive mutant (T42N) was excluded from the cilium and delocalized all over the cytoplasm, indicating that the nucleotide state could determine association with the IFT complex (Schafer et al. 2006). However, this interpretation awaits *in vitro* confirmation and biochemical analysis of the mutants to ensure their proper functionality (Nottingham & Pfeffer 2014).

Similar to IFT27, IFT22 is not ubiquitously conserved throughout ciliated organisms. Homologs are absent in the genomes of *G. intestinalis* and *T. thermophila* and both IFT22 and its IFT-B1 anchoring proteins IFT74/81 are missing in *D. melanogaster*.

### 3.4.3 Rabl2

Recent studies linked a third Rab-like GTPase to the IFT-B complex, Rabl2. First hints at a cilium-related function came from a study in mice, where mutations in Rabl2 led to male infertility due to reduced sperm cell motility (Lo et al. 2012). The authors also detected immunoprecipitation with other IFT proteins and proposed a potential role of Rabl2 in the import of several effector proteins into the sperm

cell flagellum. Follow-up sequence analysis and *in vivo* studies in *C. reinhardtii* and mammalian cells support the assumption that Rabl2 is indeed a ciliary protein transiently associating with the IFT-B1 complex (Eliáš et al. 2016; Nishijima et al. 2017; Kanie et al. 2017). Surprisingly, the interaction between IFT-B1 and the small GTPase was once more mapped to IFT74/81, making the coiled-coil heterodimer a binding platform for several Rab family GTPases (Nishijima et al. 2017; Kanie et al. 2017). Both studies detected GTP-dependent association of Rabl2 with IFT74/81 and suggest high intrinsic hydrolysis rates, although this notion still requires biochemical evidence.

In contrast to other IFT-B components, Rabl2 was not found to traffic in the cilium, but instead localized to the ciliary base. Disruption of Rabl2 however leads to cilium formation defects. The current model therefore implies that Rabl2 functions in controlling ciliary entry of the IFT complex at the base, although the exact mechanism remains to be discussed (Nishijima et al. 2017; Kanie et al. 2017).

# Aim of the thesis

Knowledge about ciliary functions as well as identification of key players involved in cilium-associated processes has tremendously increased over the past two decades. The view of cilia has long evolved from considering the organelle a useless remnant to appreciating its vital role in many developmental stages. IFT is the central process to ensure proper cilium formation and performance and is involved in almost all cilium-related functions. Current knowledge about IFT is predominantly based on knockout/knockdown *in vivo* studies in a series of model organisms, facing the issue of common phenotypes for many different IFT proteins through overall disruption of IFT complexes. More detailed information about individual protein functions, direct protein-protein interactions, protein domain organizations and potential cargo binding sites can be obtained by *in vitro* analysis of recombinant proteins and determination of high-resolution structures of single components and subcomplexes.

While the general outline of the IFT cycle is widely explained, not much is known to date about the regulation and molecular mechanisms of several key steps. Given their role in regulation of a variety of cellular processes, small GTPases are promising candidates to function in IFT regulation as well. Since two unusual small Rab-like GTPases are integral components of the IFT-B complex, they might be involved in regulation of ciliary trafficking. In my thesis project I focused on the structural and biochemical characterization of the putative small GTPase IFT22 and the interaction with its direct binding partners IFT74/81 to supplement previously published *in vivo* data on the topic. High-resolution structures and biochemical/biophysical analysis of the three proteins could help to shed light on the role of IFT22 and its association with IFT-B1 and point out possible future directions for research.



Paper

A

**Crystal structure of the intraflagellar transport complex 22/74/81: IFT22 association with the IFT complex but not with nucleotides is essential for *Trypanosoma brucei* flagellum construction**

Stefanie Wachter<sup>1</sup>, Jamin Jung<sup>2</sup>, Shahaan Shafiq<sup>2</sup>, Jérôme Basquin<sup>1</sup>, Cécile Fort<sup>2</sup>,  
Philippe Bastin<sup>2</sup> and Esben Lorentzen<sup>3</sup>

<sup>1</sup>Department of Structural Cell Biology, Max Planck Institute of Biochemistry, 82152 Martinsried, Germany

<sup>2</sup>Trypanosome Cell Biology Unit, Institut Pasteur & INSERM U1201, 75015 Paris, France

<sup>3</sup>Department of Molecular Biology and Genetics, Aarhus University, 8000 Aarhus C, Denmark

# **Crystal structure of the intraflagellar transport complex 22/74/81: IFT22 association with the IFT complex but not with nucleotides is essential for *Trypanosoma brucei* flagellum construction**

Stefanie Wachter, Jamin Jung, Shahaan Shafiq, Jerome Basquin, Cécile Fort, Philippe Bastin and Esben Lorentzen

Intraflagellar transport (IFT) is the bi-directional movement of proteins along the ciliary axoneme and is needed for construction and maintenance of the cilium organelle. IFT relies on motor proteins and the IFT complex that likely serves as a binding platform for ciliary cargo. IFT22 is an atypical small GTPase of the 22-subunit complex and exhibits functional differences between organisms. Here, we present the crystal structures of IFT22 in complex with GDP, GTP or GTP and IFT74/81. We detected a new G nucleotide-specific binding mode bypassing the classical G4 motif and show that IFT74/81 is a conserved effector of IFT22. Structure-based mutational analysis revealed that association of IFT22 to the IFT complex is essential for flagellum construction in *Trypanosoma brucei*. Furthermore, we investigated the impact of GTP-binding on IFT22 function and found that although binding to IFT74/81 is significantly reduced upon nucleotide exclusion *in vitro*, a nucleotide-binding mutant does not show a strong phenotype *in vivo*. We therefore conclude that IFT22 GTP-hydrolysis is not needed for ciliogenesis in trypanosomes.

## 1 Introduction

Cilia (or flagella) are important organelles needed for cell motility (San Agustin et al. 2015), morphogenesis (Kohl et al. 2003), sensory reception (Salinas et al. 2017) and several signaling pathways, such as sonic hedgehog and PDGFR $\alpha$  signaling (Huangfu et al. 2003; Schneider et al. 2005). Cilia are tail-like appendages protruding from the cell surface of nearly every eukaryotic cell type and are encountered on multiple unicellular organisms and on almost all cells in the mammalian body with variable length and number. For example, the protist *Trypanosoma brucei*, commonly known as the parasite causing sleeping sickness, carries a motile flagellum that is required for development and disease pathogenesis (Julkowska & Bastin 2009; Ralston et al. 2009; Langousis & Hill 2014). A microtubule-based axoneme extending from the centriole-like basal body at the ciliary base is the central shape-giving element in every cilium (Julkowska & Bastin 2009; Ishikawa & Marshall 2011; Langousis & Hill 2014; Ralston et al. 2009). The organelle is surrounded by the ciliary membrane, which is a continuous outgrowth of the plasma membrane, but hosts a unique composition of lipids and membrane proteins (Emmer et al. 2010; Serricchio et al. 2015). Cilia construction as well as maintenance of the organelle in almost all organisms relies on a conserved active transport process termed intraflagellar transport (IFT) (Kozminski et al. 1993; Rosenbaum & Witman 2002). To date, more than 600 different proteins have been identified to reside in the ciliary compartment (Pazour et al. 2005). IFT particles are thought to be responsible for the selective transfer of ciliary cargo proteins from the cytoplasm through the diffusion barrier at the transition zone. IFT is dependent on the motor proteins heterotrimeric kinesin II for anterograde (base to tip) (Douglas G Cole et al. 1993; D G Cole et al. 1998; Prevo et al. 2015) and dynein 2 for retrograde (tip to base) movement (Pazour et al. 1999; Porter et al. 1999; Signor et al. 1999) of cargo proteins and turnover products. The IFT particle is a multiprotein complex that bridges the contact between motors and ciliary cargo proteins (Bhogaraju et al. 2013a). It can be divided into biochemically distinct IFT-A and IFT-B subunits, consisting of at least 6 and 16 individual proteins, respectively (Piperno & Mead 1997; D G Cole et al. 1998; Taschner & Lorentzen 2016b). While inactivation of IFT-B complex components or the kinesin motor typically leads to defects in cilium construction due to disrupted anterograde IFT (Pazour et al. 2000; Absalon et al. 2008), IFT-A protein or dynein deletions produce phenotypes associated with malfunctioning retrograde transport (Pazour et al. 1999; Blacque et al. 2006). Mutations in IFT components and other ciliary proteins are the cause for a wide subset of genetic diseases and developmental abnormalities, known as ciliopathies (Reiter & Leroux 2017). The IFT-B complex is organized into two stable subcomplexes, the 10-subunit IFT-B1 (IFT22, IFT25, IFT27, IFT46, IFT52, IFT56, IFT70, IFT74, IFT81, IFT88) (Lucker et al. 2005; Follit et al. 2009; Taschner et al. 2014; Ishikawa et al. 2014) and the 6-subunit IFT-B2 complex (Taschner et al. 2016).

In order to be able to assemble into large complexes and bind diverse cargo proteins, the vast majority of IFT proteins are composed of protein-protein interaction domains such as coiled-coils,  $\beta$ -propeller and tetratricopeptide repeats (Taschner et al. 2012). Two members of the currently supposed 22-subunit IFT complex are predicted to be potential G-proteins, with Rab-like2 (Rab12) being a recently discovered possible third candidate (Lo et al. 2012; Kanie et al. 2017; Nishijima et al. 2017). IFT22 (Rab15) and IFT27

(Rabl4), both part of the B1-subcomplex, show significant sequence homology to small GTPases of the Rab family and are thus thought to play a regulatory role in IFT (Schafer et al. 2006; Adhiambo et al. 2009; Qin et al. 2007; Bhogaraju et al. 2011). Rab GTPases are key regulators of vesicular membrane-trafficking (Stenmark 2009; Itzen & Goody 2011) and are usually organelle-specific proteins that cycle between an active GTP-bound and inactive GDP-bound state. The crystal structure of IFT25/27 confirmed the overall Rab GTPase fold of IFT27 (Bhogaraju et al. 2011) and it was shown that association of IFT27 with IFT-B1 and therefore ciliary localization and IFT trafficking is dependent on GTP-binding (Eguether et al. 2014; Huet et al. 2014). Both IFT22 and IFT27 lack the C-terminal prenylation motif commonly found to associate Rab GTPases with membranes and associate with the IFT complex via different coiled-coil regions of the IFT74/81 heterodimer (Taschner et al. 2014). Despite these similarities, IFT22 and IFT27 share only low sequence identity (<15 %) (Adhiambo et al. 2009).

Previous studies have classified IFT22 as an atypical small GTPase with a high degree of sequence variance from classical Rab proteins, particularly in sequences assigned to the conserved nucleotide-binding pocket (Schafer et al. 2006; Adhiambo et al. 2009). IFT22 lacks the conventional G4 motif and contains a highly diverse G5 motif, consensus sequences that are key players for interaction with the guanine nucleotide base (Rensland et al. 1995; Itzen & Goody 2011; I. R. Vetter & Wittinghofer 2001). Hence, it is uncertain whether IFT22 really is a functional GTPase and whether it can specifically bind guanine nucleotides. Interestingly, *in vivo* studies in several ciliated organisms revealed functional differences of IFT22 between species. Disruption of the *Caenorhabditis elegans* (*Ce*) homolog IFTA-2 does not affect cilium formation or IFT, but worms show deficiencies in the DAF-2 (insulin-IGF-1-like) signaling pathway, leading to an extended lifespan and abnormalities in dauer stage formation (Schafer et al. 2006). In contrast, RNAi knockdown experiments of Rabl5 in *Trypanosoma brucei* (*Tb*) led to a retrograde IFT inactivation phenotype that is characterized by short flagella filled with IFT material thus assigning an essential role to Rabl5 in correct flagellum construction (Adhiambo et al. 2009). In *Chlamydomonas reinhardtii* (*Cr*), IFT22 was shown to control the cellular levels of both IFT-A and IFT-B proteins and to regulate availability of particles participating in IFT (Silva et al. 2012). Intriguingly, IFT22 homologs are missing in the genomes of *Giardia intestinalis* and *Tetrahymena thermophila*, although IFT is present in these ciliated organisms whereas *Drosophila melanogaster* lacks both IFT22 and IFT74/81 homologs (van Dam et al. 2013).

The diverse functions of IFT22 raise questions about the molecular structure and biochemical properties of the protein, how it interacts with the IFT-B1 complex and which roles nucleotide binding and hydrolysis play for IFT mediated cilium construction. In this study, we present the crystal structures of recombinantly expressed and purified GTP- and GDP-bound IFT22 and identify a new, unusual binding mode for G-nucleotides in the absence of the classical G4 motif. The crystal structure of the trimeric IFT22/74/81 complex allows us to determine residues critical for complex formation and reveals that the IFT74/81 subcomplex is an effector of IFT22 that however retains some residual binding capacity for the inactive nucleotide-free form of the small GTPase. *In vivo* experiments using structure-based IFT22 mutants in *T. brucei* demonstrate that association of IFT22 with IFT-B1 but not nucleotide-binding is essential for ciliogenesis.

## 2 Results

### 2.1 IFT22 is a specific guanine nucleotide-binding protein with a low intrinsic hydrolysis rate

Due to the unusual sequences in the G4/G5 regions, it is unclear if IFT22 is a selective guanine nucleotide-binding protein or may bind other purine nucleotides such as ATP (Taschner et al. 2012; Espinosa et al. 2009). We investigated this for IFT22 from either *T. brucei* (*Tb*) or *M. musculus* (*Mm*) alone and for IFT22 from *T. brucei*, *M. musculus* and *C. reinhardtii* (*Cr*) associated to helical fragments of two other IFT-B proteins, IFT74 and IFT81 (Fig. 14B and Supplements, Fig. 19A). The truncated trimeric IFT22/74/81 complex constitutes a minimal binding site for IFT22 (Taschner et al. 2014) and will be referred to as “IFT22/74/81 core”. The used constructs are: *TbIFT22/74*<sub>342-401</sub>/*81*<sub>397-450</sub> (see Fig. 13A), *CrIFT22/74*<sub>398-459</sub>/*81*<sub>390-442</sub> and *MmIFT22/74*<sub>352-406</sub>/*81*<sub>389-441</sub>).

We incubated IFT22 alone or the IFT22/74/81 core complex with excess of GTP and analyzed the content of bound nucleotides after size-exclusion chromatography (SEC) using an HPLC-based system (Fig. 12E). IFT22/74/81 core complexes from all three species bound GTP, albeit with different affinities. The core complex from *T. brucei* incorporated the highest percentage of GTP, followed by *C. reinhardtii* and last *M. musculus*. Notably, *TbIFT22* bound less GTP than the *TbIFT22/74/81* core complex and for *MmIFT22* no nucleotide could be detected, meaning that affinities for GTP in context of the complex increased and that this effect seems to be conserved. In order to confirm this hypothesis, we removed bound and co-purified nucleotides from the *T. brucei* proteins and performed nucleotide-binding experiments. Commonly used gentle methods for nucleotide removal such as EDTA- or SAP-treatment could not eliminate the nucleotide completely. Only after unfolding *TbIFT22* in 8 M urea, followed by protein re-folding and subsequent SEC, no GTP could be detected anymore via HPLC (Fig. 19C). We measured the affinities for GTP- and GDP-binding by titration experiments with fluorescently labeled non-hydrolysable GTP/ATP derivatives (mant-GMPPNP/mant-AMPPNP) or GDP (mant-GDP) using a fluorescence spectrophotometer. *TbIFT22* bound the GTP analog with a  $K_d$  of 2  $\mu$ M and GDP with a  $K_d$  of around 20  $\mu$ M (Fig. 12A, left and middle panel). These weak micromolar affinities are in the same range as reported for IFT27 (Bhogaraju et al. 2011) and might indicate that nucleotide exchange does not require a guanine nucleotide exchange factor (GEF), as it is the case for some large GTPases (Uthaiiah et al. 2003). No binding could be observed for the ATP analog (Fig. 12A, right panel). We therefore conclude that IFT22 is a specific guanine nucleotide-binding protein.

In addition to the small GTPase alone, we also measured the affinities for GDP/GTP in context of the *TbIFT22/74/81* core complex. We found that affinities for GTP and GDP in context of the complex increased by about two- and threefold, respectively (Fig. 12A, left and middle panel), supporting the described increase in affinity for nucleotides upon complex formation.

We also tested the intrinsic GTPase activity of *TbIFT22* and detected very low but measureable hydrolysis rates for both the protein alone and when associated to the core complex with IFT74/81, although the

latter showed an almost 3-fold increased rate ( $1.7 \times 10^{-3} \text{ min}^{-1}$  and  $4.7 \times 10^{-3} \text{ min}^{-1}$ , respectively) (Supplements, Fig. 19E). These values lie in the same order of magnitude as reported intrinsic hydrolysis rates of other small GTPases (Simon et al. 1996; Scheffzek & Ahmadian 2005; Bhogaraju et al. 2011). We assume that if cellular IFT22 function includes a classical GTPase cycle, a GTPase activating protein (GAP) is required to stimulate nucleotide turnover.

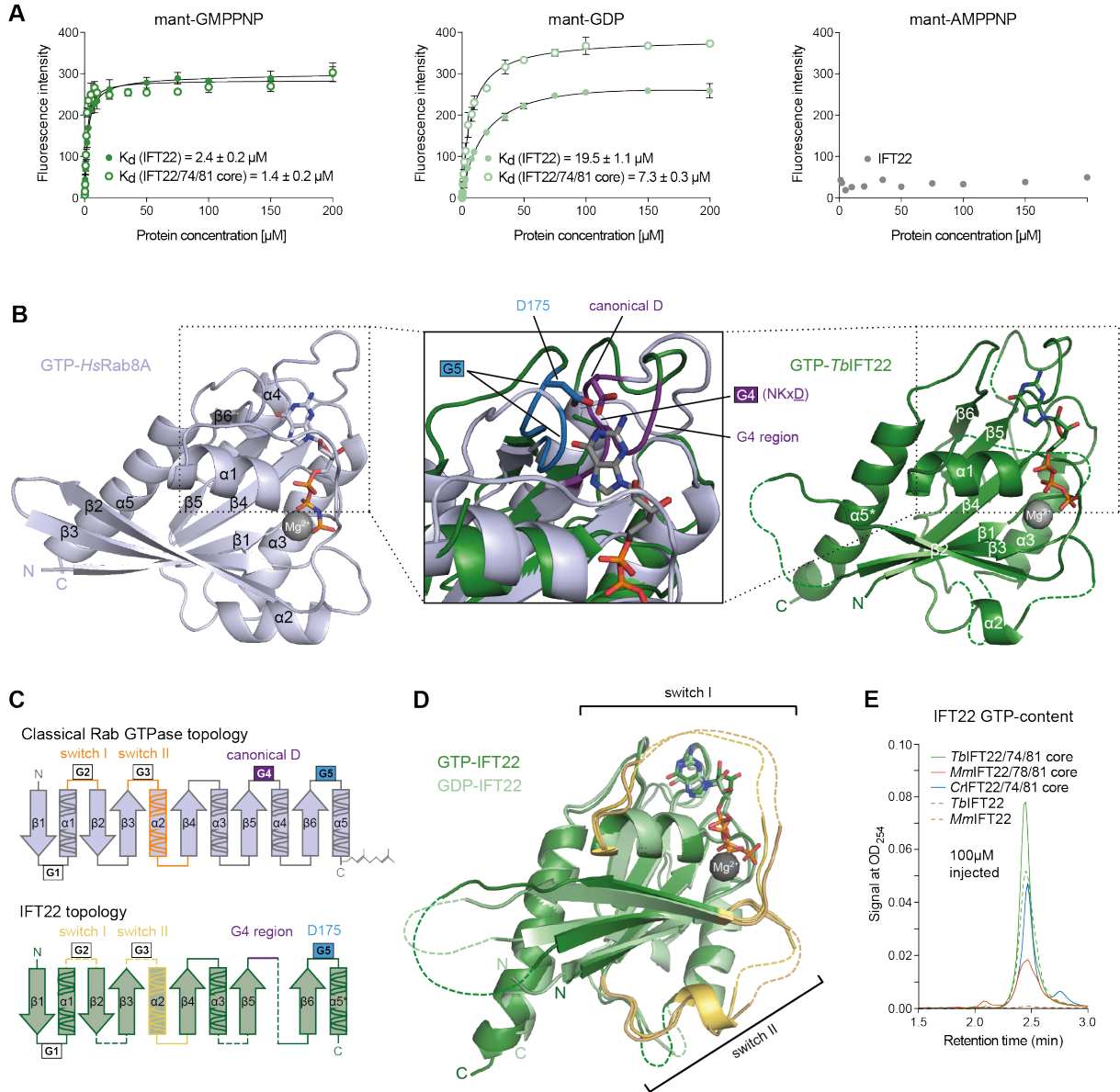


**Figure 12: IFT22 is an unusual guanine specific Rab GTPase**

**A.** IFT22 nucleotide-binding experiments. Fluorescence measurements using increasing amounts of IFT22 and IFT22/74<sub>342-401</sub>/81<sub>397-450</sub> incubated with mant-labeled GDP (mant-GDP) or non-hydrolysable GTP/ATP analogs (mant-GMPPNP/mant-AMPPNP). The fluorescence intensity is plotted as a function of protein concentration. Data were fitted to a single-site binding model equation for dissociation constant ( $K_d$ ) determination.  $K_d$ s and data points are indicated as means with standard deviations of three independent experiments. **B.** Structural comparison of GTP-bound *HsRab8A* (light purple, PDB ID: 4lhv) and *TbIFT22* (green) depicted in cartoon representation. Nucleotides are shown as sticks and  $\text{Mg}^{2+}$  as balls. IFT22 exhibits an overall Rab GTPase fold with a missing  $\alpha4$  helix. Unstructured regions in the crystal structure are represented with dotted lines. The zoomed-in view shows a superposition of the nucleotide-binding pocket. While classical GTPases form hydrogen bonds between a conserved Asp of the G4 motif (NKxD) and the guanine base, IFT22 instead utilizes D175 sitting in the sequence-wise remote G5 loop. **C.** Topology diagrams of classical Rab GTPases and IFT22. Positions of the conserved nucleotide-binding G-motifs (G1-G5) as well as switch regions are indicated. **D.** Superposition of GTP- (green) and GDP-bound (light green) *TbIFT22*. Switch regions are marked in yellow and dotted lines indicate disordered loops not modeled in the structures. **E.** HPLC GTP-elution profiles of purified IFT22 proteins and small IFT22/74/81 core complexes from different organisms. Same amounts of each protein (complex) were injected.

## 2.2 The crystal structures of IFT22 with nucleotides reveal an unusual GTP/GDP-binding mode

To address the molecular basis of nucleotide binding of IFT22 with its unusual G4/G5 sequence motifs, we over-expressed and purified *TbIFT22* and *MmIFT22*. Crystals were obtained for *TbIFT22* and the structure was determined by molecular replacement at a resolution of 2.3 Å. Data and refinement statistics are summarized in Table 1 on page 67. As expected, IFT22 exhibits the overall fold of a Rab GTPase, containing a mixed six-stranded  $\beta$ -sheet surrounded by  $\alpha$ -helices (Fig. 12B, right image). However, in contrast to classical GTPases that contain five  $\alpha$ -helices, IFT22 is missing the  $\alpha$ 4 helix between  $\beta$ 5 and  $\beta$ 6 (Fig. 12C). When comparing the IFT22 structure to 3D protein structures currently available in the protein data bank using the Dali server (Holm & Sander 1993), IFT22 is most similar to structures of other Rab family GTPases with the closest match being *HsRab8A* (PDB ID: 4lhw), superposing with a root mean square deviation (rmsd) of 2.4 Å (Fig. 12B). Curiously, the IFT22 structure shows a GTP-molecule bound in the nucleotide-binding pocket although no GTP was added to the crystallization setup (Supplements, Fig. 19F, left image). Therefore, GTP was co-purified from the *E. coli* extract. Previous sequence analyses have demonstrated that IFT22 features unusual sequences in regions of the so-called G motifs. G motifs are five conserved sequence motifs located in loop regions around the nucleotide-binding pocket that harbor the main nucleotide-interacting residues (see sequence alignment in Supplements, Fig. 18). IFT22 does not contain the conventional G4 sequence and shows high diversity in G5. These motifs contain amino acids interacting with the base and guaranteeing specificity for guanine over adenine (Rensland et al. 1995; Paduch et al. 2001). The structure reveals that *TbIFT22* bypasses the classical binding mode using Asp175 instead of the canonical Asp from the NKxD (G4) motif to form the bifurcated hydrogen bond with the guanine base (see detailed view in Fig. 12B). While the classical G4 motif is positioned in a loop connecting  $\beta$ 5 with  $\alpha$ 4, Asp175 is located between  $\beta$ 6 and  $\alpha$ 5\* (Fig. 12C), adjacent to the G5 sequence in *T. brucei*. Remarkably, IFT22 homologs from *D. rerio* (*Dr*) and mammals (*Mm*, *Hs*) possess a Glu residue in the same position (Supplements, Fig. 18) indicating a potentially similar binding mechanism in those species.

## 2.3 IFT22 exhibits unstructured switch regions in both the GDP- and GTP-bound structure

Next, we performed crystallization trials with nucleotide-free refolded *TbIFT22* with and without addition of GDP excess. While we could not obtain crystals for the Apo protein, IFT22 in presence of GDP crystallized and we could solve the structure of GDP-IFT22 at a resolution of 2.5 Å (see unbiased Fo-Fc map of the GDP-nucleotide in Supplements, Fig. 19F). Surprisingly, no major conformational change was observed between the GTP- and GDP-bound states of IFT22 (Fig. 12D) and both switch regions, regions that normally undergo major conformational changes between the active and inactive state of small GTPases (I. R. Vetter & Wittinghofer 2001; Mourão et al. 2014), are partially unstructured in both crystal structures. While switch I and II of inactive GDP-bound GTPases are known to be rather

flexible and thus likely to be invisible in crystal structures, active GTP-bound forms usually exhibit a rigid fold of their switch regions that provide a stable interaction surface for downstream effector binding. The aforementioned observation that the IFT22/74/81 core binds nucleotides stronger than IFT22 alone together with the fact that switch regions are not ordered in both *TbIFT22* structures suggest that interaction with IFT74/81 might occur via switch I/II, thereby stabilizing the nucleotide-binding pocket.

## 2.4 Structural characterization of the IFT22/74<sub>79-401</sub>/81<sub>1-450</sub> subcomplex

In order to further investigate the mode of interaction between IFT22 and the IFT-B1 complex components IFT74/81, we set out to obtain a structure of the trimeric complex. *TbIFT74* and *TbIFT81* are 68 kDa (602 residues) and 84 kDa (740 residues) proteins, respectively (Fig. 13A). It should be mentioned that we obtained an IFT74 sequence from extracted genomic trypanosome DNA that contains a 6 amino acid insertion compared to the published sequence in the TriTrypDB database (*Tb927.7.3370*, 596 residues) (Aslett et al. 2010) in the N-terminal part of the protein. This RPGSQM insertion is a repetitive sequence that is present in three consecutive copies in the annotated IFT74 sequence, but in four copies in our full-length (FL) construct. Since this part of the protein is predicted to be unstructured, we assume that this is a natural protein variant that does not affect IFT74 function. The IFT74 residue numbering in this publication will refer to the 602 aa protein version. Both IFT74 and IFT81 are predicted to be long coiled-coil proteins that are likely to be remote homologs (sequence identity 26 % for *Tb* proteins according to BLAST search (Altschul et al. 1990)). They were shown to directly interact with each other (Lucker et al. 2005; Kobayashi et al. 2007; Taschner et al. 2011) via their coiled-coil domains and build a binding platform for the IFT-B1 components IFT22, IFT25/27 and IFT46/52 (Taschner et al. 2014). Apart from their coiled-coil regions, IFT74/81 possess a heterodimeric tubulin-binding module at their N-termini. IFT81 harbors an N-terminal calponin homology (CH) domain that specifically recognizes the globular part of the  $\alpha/\beta$ -tubulin dimer, whereas IFT74 binds the acidic tubulin E-hooks with a basic sequence stretch, leading to increased affinity (Bhogaraju et al. 2013b).

Since IFT22/74/81 core complexes did not yield any crystals, we co-expressed and purified longer constructs of *TbIFT74/81* with *TbIFT22*, spanning the N-terminal predicted coiled-coil domains up to the IFT22 binding region. The positively charged IFT74 N-terminus is prone to degradation and was consequently removed (leading to *TbIFT74<sub>79-401</sub>*). We tested complexes with (*TbIFT81<sub>1-450</sub>*) and without (*TbIFT81<sub>143-450</sub>*) IFT81 CH domain (Supplements, Fig. 20A, B), however only the *TbIFT22/74/81* complex with CH domain crystalized (Supplements, Fig. 20C). The structure was solved at 3.2 Å resolution from a dataset derived from a selenomethionine substituted protein crystal (see Table 1 on page 67), because native crystals diffracted significantly worse.

The *TbIFT22/74<sub>79-401</sub>/81<sub>1-450</sub>* crystal structure reveals an elongated coiled-coil complex with compact side view packing and globular parts of the IFT81 CH domain and the IFT22 GTPase at its distal ends

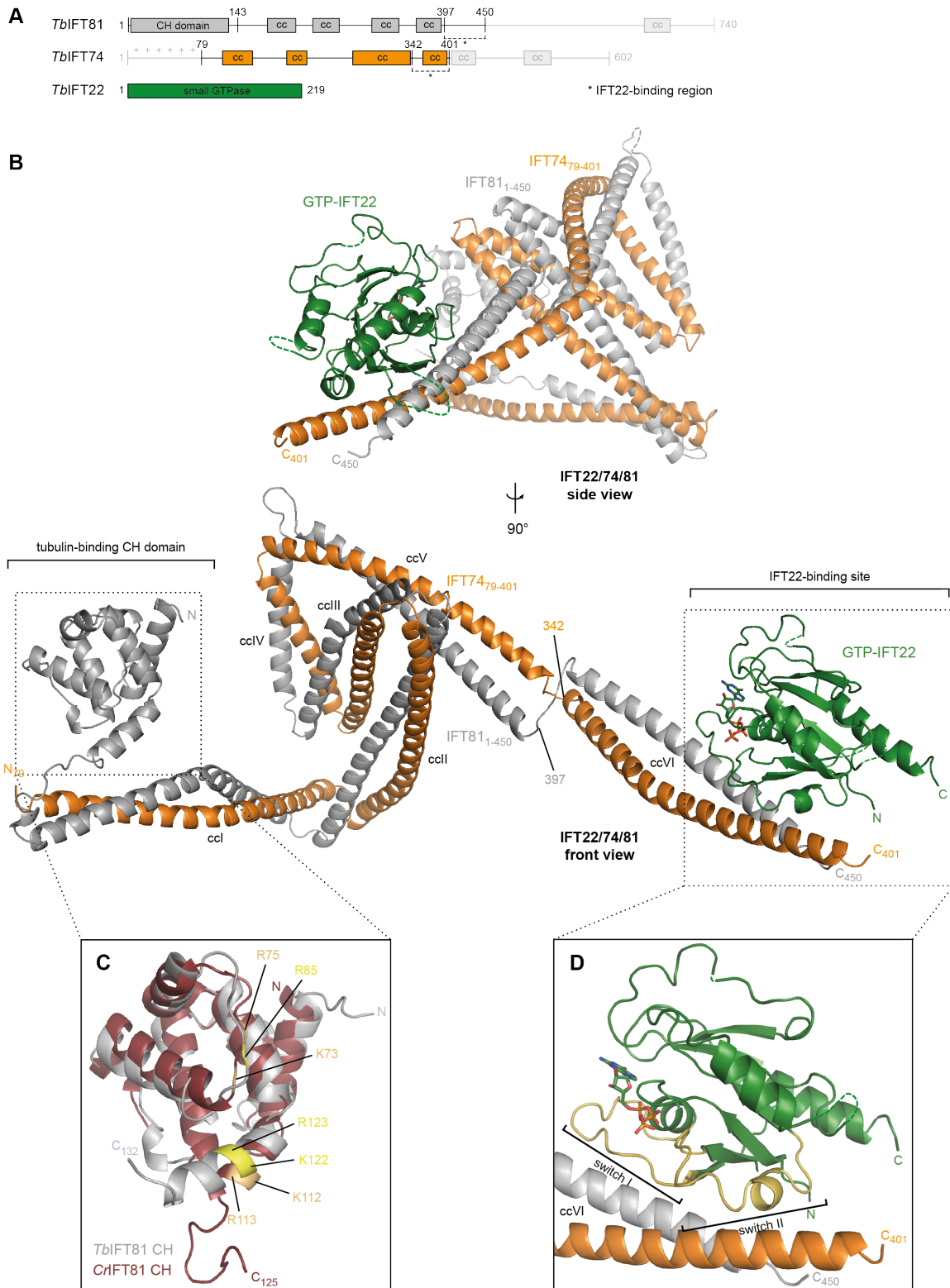


**Figure 13: Overall structure of the N-terminal IFT22/74/81 complex**

**A.** Domain organization of the small GTPase IFT22 and its IFT-B1 interaction partners IFT74 and IFT81. Numbers refer to the *Tb* proteins and indicate different constructs used in this study. The crystal structure constructs are highlighted in color. Coiled-coils positions are depicted based on prediction from the PCOILS webserver. (CH = calponin homology, cc = coiled-coil). **B.** Crystal structure of the *Tb*IFT22/74<sub>79-401</sub>/81<sub>1-450</sub> subcomplex in two orientations related by a 90° rotation and shown in cartoon representation. GTP is shown as sticks. IFT22 is depicted in green, IFT74 in orange and IFT81 in grey. Coiled-coils are numbered ccl to ccVI. **C.** Zoomed-in view of the N-terminal *Tb*IFT81 CH domain (grey) with superposed *Cr*IFT81 CH domain (brick-red). Basic tubulin-binding residues are highlighted in yellow and light orange, respectively. **D.** Zoomed-in view of the IFT22-binding site on IFT74/81 ccVI with ordered switch regions depicted in yellow.

(Fig. 13B). The oblonged IFT74/81 structure can be subdivided into six separate coiled-coils (ccI to ccVI), linked via sharp kinks. Boundaries of these coiled-coils do not match very well with previously predicted coiled-coils from the PCOILS webserver (as mapped in Fig. 13A) (Alva et al. 2016). Structural similarity search of IFT74/81 ccI to ccVI using the Dali server resulted in a list of coiled-coil but otherwise unrelated proteins, with the closest match being a short truncation of the mRNA localization machinery protein Bicaudal D1 superposing with an rmsd of 6.3 Å. The IFT81 CH domain is connected via a 15-residue linker to the coiled-coil scaffold of ccI and is fixed in its orientation by residue interactions between the last CH domain helix (Q118-Q131) and ccI. Besides, the N-terminal part of the CH domain is making crystal contacts to neighboring molecules in the lattice that are likely to be important for crystallization, since the complex with eliminated CH domain did not crystallize.

Interestingly, IFT22 switch regions are ordered in the IFT22/74/81 complex structure and mediate binding to ccVI of IFT74/81 (Fig. 13D), as hypothesized. This implies that complex formation stabilizes the conformation of switch I and II and explains why nucleotide-binding affinities as well as GTP hydrolysis rates are slightly enhanced in context of the IFT22/74/81 core complex when compared to IFT22 alone (Fig. 12E and Supplements, Fig. 19E). As already observed for the small core complex, the IFT22/74<sub>79-401</sub>/81<sub>1-450</sub> crystal structure complex was purified with IFT22 in a GTP-loaded state (confirmed by HPLC) and was set up for crystallization with additional excess of GTP at 4 °C. Although the nucleotide-base part does not exhibit a defined unbiased Fo-Fc difference electron density, the sugar and phosphate part of the nucleotide as well as the divalent Mg<sup>2+</sup>-ion are clearly visible in the map and provide evidence that the trimer structure contains IFT22 with unhydrolyzed GTP (Supplements, Fig. 19F, right image).

## 2.5 *Tb*IFT81 and *Cr*IFT81 CH domains show a similar organization of critical tubulin-binding residues

Previous studies from our group have identified two out of the four predicted CH domains present in the IFT-B complex to be tubulin-binding sites (Bhogaraju et al. 2013b; Taschner et al. 2016) that probably mediate IFT of  $\alpha/\beta$ -tubulin needed for construction and maintenance of the ciliary axoneme (Hao et al. 2011; Craft et al. 2015). The crystal structures of both *Cr*IFT81 CH and *Cr/Mm*IFT54 CH display basic Arg/Lys-rich patches on their surfaces and extensive reversed-charge mutations of these areas abolish tubulin-binding. In contrast, the CH domains of IFT57 and IFT38 do not contain basic residues in similar positions to either the IFT81 or IFT54 CH domain in sequence alignments and were shown to interact with other components of the IFT-B complex instead (Taschner et al. 2016).

The crystal structures of *Cr* and *Tb*IFT81 CH domains are very much alike and superpose with an rmsd of 1.9 Å (sequence identity 32%). Spatial arrangements of critical basic tubulin-binding residues are conserved (Fig. 13C), indicating a similar binding interface.

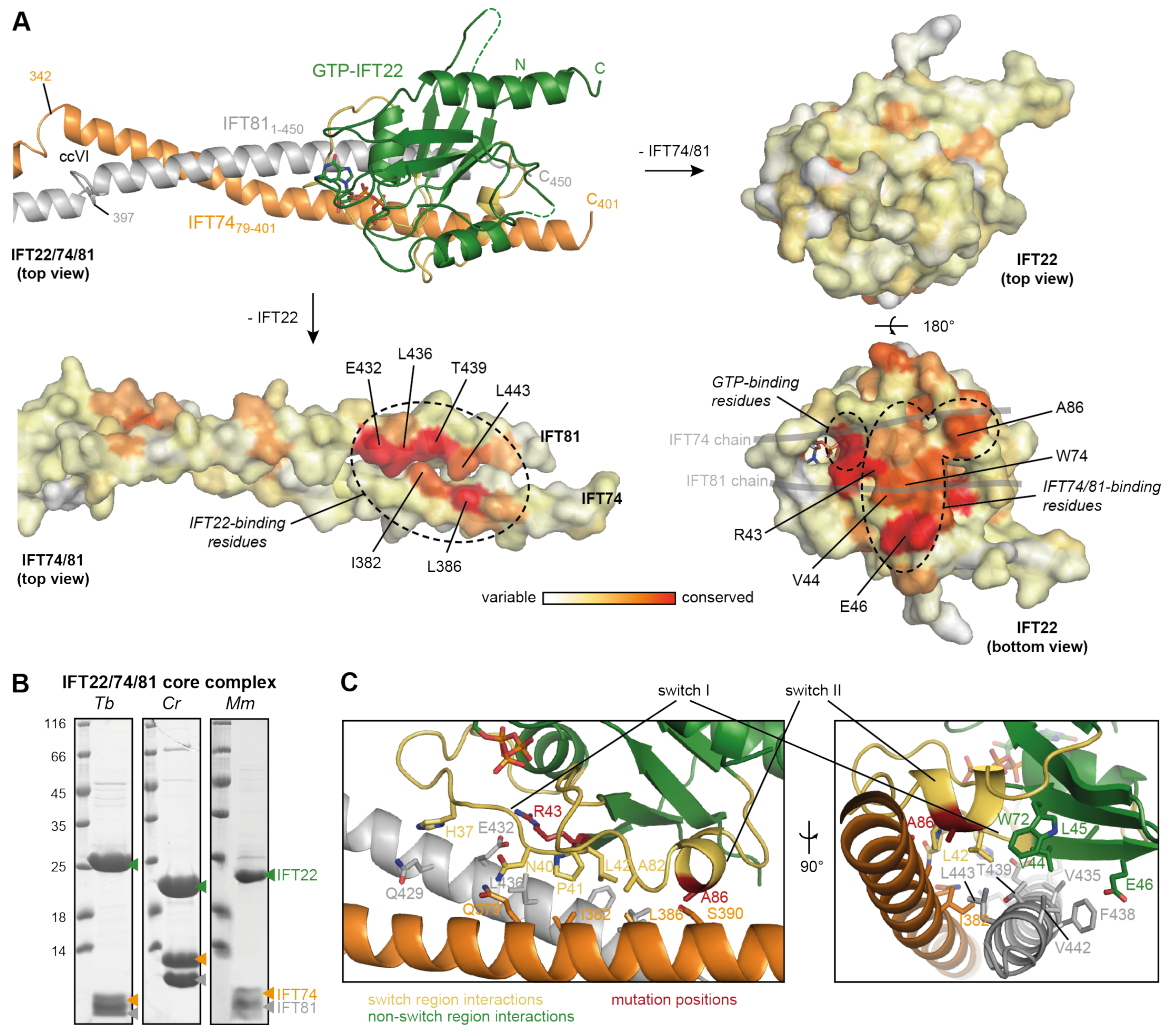


**Figure 14: IFT74/81 shows effector binding for IFT22**

**A.** Surface conservation of the IFT22-IFT74/81 binding site. The top left image shows the IFT22-binding site in cartoon representation from top view. Arrows point towards IFT22 (top right) and IFT74/81 (bottom left) structures in similar orientations in surface representation colored according to their sequence conservation. IFT74/81 ccVI displays a highly conserved patch at the IFT22-binding interface (black dashed circle). A 180° rotation of IFT22 (bottom right) exhibits a likewise conserved patch at the IFT74/81-binding interface (black dashed circle; position of the IFT74/81 helices are marked with light grey lines). Conserved residues are marked and labeled according to the *Tb* sequence. Conservation coloring is based on Clustal Omega multiple sequence alignments with *Hs*, *Mm*, *Dr*, *Tb*, *Cr* and *Ce* sequences (Fig. 18 and Fig. 20E) and ConSurf conservation grades. **B.** SDS-PAGE gels of purified IFT22/74/81 core complexes from different organisms. IFT74/81 constructs were designed based on sequence alignments (Fig. 20E) and resulting complexes are *Tb*IFT22/74<sub>342-401</sub>/81<sub>397-450</sub>, *Cr*IFT22/74<sub>398-459</sub>/81<sub>390-442</sub>, *Mm*IFT22/74<sub>352-406</sub>/81<sub>389-441</sub>. **C.** Detailed view of the IFT22-IFT74/81 binding site in two perpendicular orientations showing interacting residues in stick representation. Residues provided by IFT22 switch I and II are shown in yellow, whereas IFT22 non-switch region interactions are colored in green. The IFT74 helix is shown in orange and IFT81 in grey. Two residues chosen for mutational analysis are highlighted in red (R43 and A86). Most interactions are mediated by the switch regions of IFT22.

## 2.6 The IFT74/81 complex interacts via a conserved surface patch and is an effector of IFT22

We further analyzed the surface conservation of the IFT22/74/81 complex and found that both IFT22 and the IFT74/81 ccVI display a highly conserved patch right at the interaction surface between the two modules (Fig. 14A, based on Clustal Omega sequence alignments of *Hs*, *Mm*, *Dr*, *Tb*, *Cr*, *Ce* sequences and ConSurf conservation grades (Sievers et al. 2011; Landau et al. 2005)), suggesting that the binding site and

binding mode of IFT22 to the IFT-B1 complex are similar in different organisms. This was confirmed by expression and purification of stable *Tb*, *Cr* and *Mm* IFT22/74/81 core complexes that were designed based on sequence alignments (Fig. 14B and Supplements, Fig. 20E) (constructs: *Tb*IFT22/74<sub>342-401</sub>/81<sub>397-450</sub>, *Cr*IFT22/74<sub>398-459</sub>/81<sub>390-442</sub>, *Mm*IFT22/74<sub>352-406</sub>/81<sub>389-441</sub>). Moreover, we show that *Tb*IFT22 efficiently pulls down a purified *Cr*IFT25/27/74/81 complex (Supplements, Fig. 20G), thereby forming a stable pentameric IFT-B1 chimera.

Effectors are proteins that preferably interact with the switch regions of the active GTP-bound state of small GTPases (I. R. Vetter & Wittinghofer 2001), typically exhibiting changes in affinity of 500- to 1000-fold with nucleotide exchange (Leung & Rosen 2005). The crystal structure reveals that most of the IFT74/81-interacting residues of IFT22 are contributed by switch I and II (Fig. 14C) and IFT22 is bound to IFT74/81 in the GTP-loaded state, making the IFT74/81 subcomplex a classical effector of IFT22. Unfortunately, the IFT74/81 constructs used in the crystal structure as well as the constructs for the IFT22/74/81 core complex proved to be unstable when purified without IFT22 and had a strong tendency to degrade C-terminally, thus eliminating the IFT22-binding site. We therefore were unable to perform direct pulldown experiments with IFT74/81 and inactive GDP-loaded (or nucleotide-free) IFT22. However, we could obtain a nearly full-length *Tb*IFT25/27/74/81 complex (with the exception of IFT74 where the first 79 residues were truncated for stability reasons) upon expression in insect cells and determined the  $K_d$  of GTP-*Tb*IFT22 binding to the tetrameric complex by isothermal titration calorimetry (ITC) measurements to be in the low nanomolar range (Supplements, Fig. 20D), implying very strong binding.

## 2.7 Association of IFT22 to IFT-B1 (via IFT74/81) is essential for flagellum assembly in trypanosomes

To demonstrate the significance of the candidate interaction domain, we inserted two mutations in the conserved IFT74/81-interacting patch on IFT22, R43A or R43E adjacent to switch I and A86R in switch II (highlighted in red in Fig. 14C). A86R inserts a long, charged amino acid side chain that leads to steric clashes with the interacting IFT74 helix, R43A disrupts the salt bridge E432<sup>IFT81</sup>-R43<sup>IFT22</sup>, and R43E inserts a repulsive charge in the same position. Pulldowns of untagged mutant IFT22 proteins on the short His-tagged *Tb*IFT74/81 core peptides showed that while R43A is still pulled down from cell lysates (though in lower amounts than WT IFT22), R43E and A86R are obviously unable to bind to the short IFT74/81 core complex helices (Fig. 15A, third Ni pulldown lane, and Supplements, Fig. 20F). We also tested the *Tb*IFT22 A86R mutant in pulldowns with the longer *Tb*IFT74<sub>79-401</sub>/81<sub>1-450</sub> fragments (Fig. 15B, third Ni pulldown lane) and the purified *Tb*IFT25/27/74/81 complex expressed in insect cells (Fig. 15C), with similar results. Both the crystal structure and the full-length IFT74/81 constructs did not bind the A86R mutant.

We next investigated the consequences of the A86R mutation on the interaction between IFT22 and IFT74/81 *in vivo* in *T. brucei* cells. GFP::IFT22 was shown to traffic in the flagellum (Adhiambo et al.

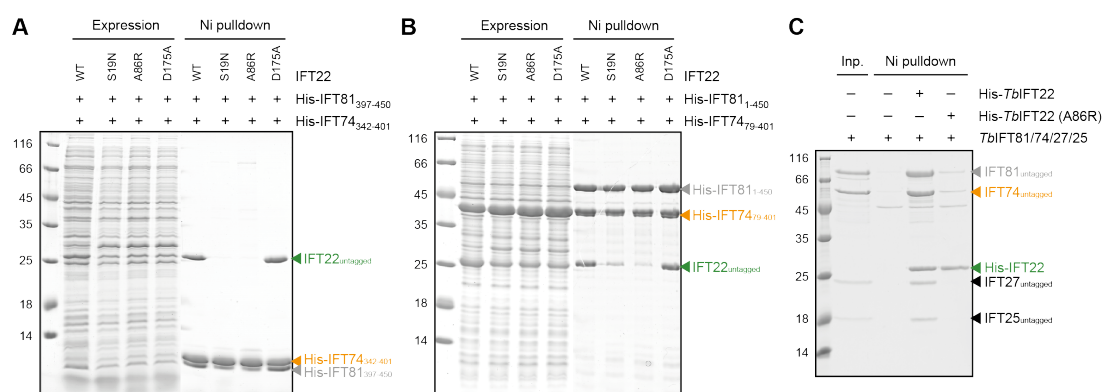


**Figure 15: Analysis of different IFT22 mutants**

**A.** SDS-PAGE gel of a Ni<sup>2+</sup>-NTA pulldown using His-tagged IFT74<sub>342-401</sub>/81<sub>397-450</sub> core complex peptides and untagged IFT22 (WT and mutants). Pulldowns were done from cell lysates of co-expressed proteins. Lanes 1-4 show similar total expression levels of the different co-expressed constructs (input samples). Lanes 5-8 show pulldown elutions. Both IFT22 S19N (inactive GTP-binding mutant) and A86R (IFT74/81-binding mutant) fail to bind to the IFT74/81 core complex peptides. **B.** SDS-PAGE gel of a Ni<sup>2+</sup>-NTA pulldown using the His-tagged IFT74<sub>79-401</sub>/81<sub>1-450</sub> crystal structure constructs and untagged IFT22 (WT and mutants). Pulldowns were done from cell lysates of co-expressed proteins. Lanes 1-4 show similar total expression levels of the different co-expressed constructs (input samples). Lanes 5-8 show pulldown elutions. Again, both IFT22 S19N (inactive GTPase mutant) and A86R (IFT74/81-binding mutant) are not pulled down by the IFT74/81 complex. **C.** SDS-PAGE gel of a Ni<sup>2+</sup>-NTA pulldown of the purified full-length IFT25/27/74/81 complex on His-tagged IFT22 (WT and A86R mutant). The IFT74/81-binding mutant IFT22 A86R fails to pull down the tetrameric complex. (WT = wild type)

2009), but conditions for proper quantification were not available at the time. We therefore acquired videos of GFP::IFT22 trafficking and quantified the movement by kymograph analysis (Buisson et al. 2013). Anterograde movement of GFP::IFT22 occurred at a frequency of 0.84 s<sup>-1</sup> and at an average speed of 2.73 ± 0.69 μm s<sup>-1</sup> (n = 218). These values are in the same range as observed for GFP::IFT27 (Huet et al. 2014) or GFP::IFT52 (Buisson et al. 2013). RNAi silencing of IFT22 resulted in a spectacular defect of retrograde transport (Adhiambo et al. 2009). To confirm this phenotype was specific and not due to an off-target effect, an RNAi-resistant version of IFT22 was fused to GFP to discriminate it from the product of the endogenous gene and expressed in the *IFT22<sup>RNAi</sup>* cell line (Fig. 16A). For the sake of simplicity, this *IFT22<sup>RNAi</sup>*+GFP::IFT22 RNAi resistant cell line will be called IFT22R. Western blot analysis using an anti-IFT22 demonstrated that the GFP::IFT22 fusion protein displayed the expected motility on gel (expected weight 52 kDa) and was detected alongside the endogenous protein (expected MW 24 kDa) (Fig. 16B). Video-microscopy on live cells demonstrated typical IFT trafficking (Video S1). Addition of tetracycline triggered RNAi knockdown of the endogenous IFT22 with the same efficiency as in the *IFT22<sup>RNAi</sup>* cell line alone (Fig. 16B). However, the GFP::IFT22R fusion protein was not affected (Fig. 16B, last lane). This was confirmed in live cells (Video S2). Of note, the signal-to-noise ratio for GFP::IFT22R in the flagellum was better in induced conditions, indicating a competition with the endogenous untagged IFT22 protein. Immunofluorescence assays (IFA) with an anti-IFT172 monoclonal antibody and a marker of the axoneme were used to further characterize the phenotypes (Fig. 16D). As expected, knockdown of IFT22 in the *IFT22<sup>RNAi</sup>* cell line led to the emergence of cells with tiny flagella usually filled with IFT material (Fig. 16D, second row), as previously reported (Adhiambo et al. 2009). By contrast, expression of the GFP::IFT22R rescued the phenotype as these cells displayed normal IFT distribution and possess flagella of normal length (Fig. 16D, third row). These results formally prove that the phenotype is indeed due to IFT22 knockdown and not to off-target effects and demonstrate that IFT22 is a *bona fide* IFT protein essential for retrograde transport.

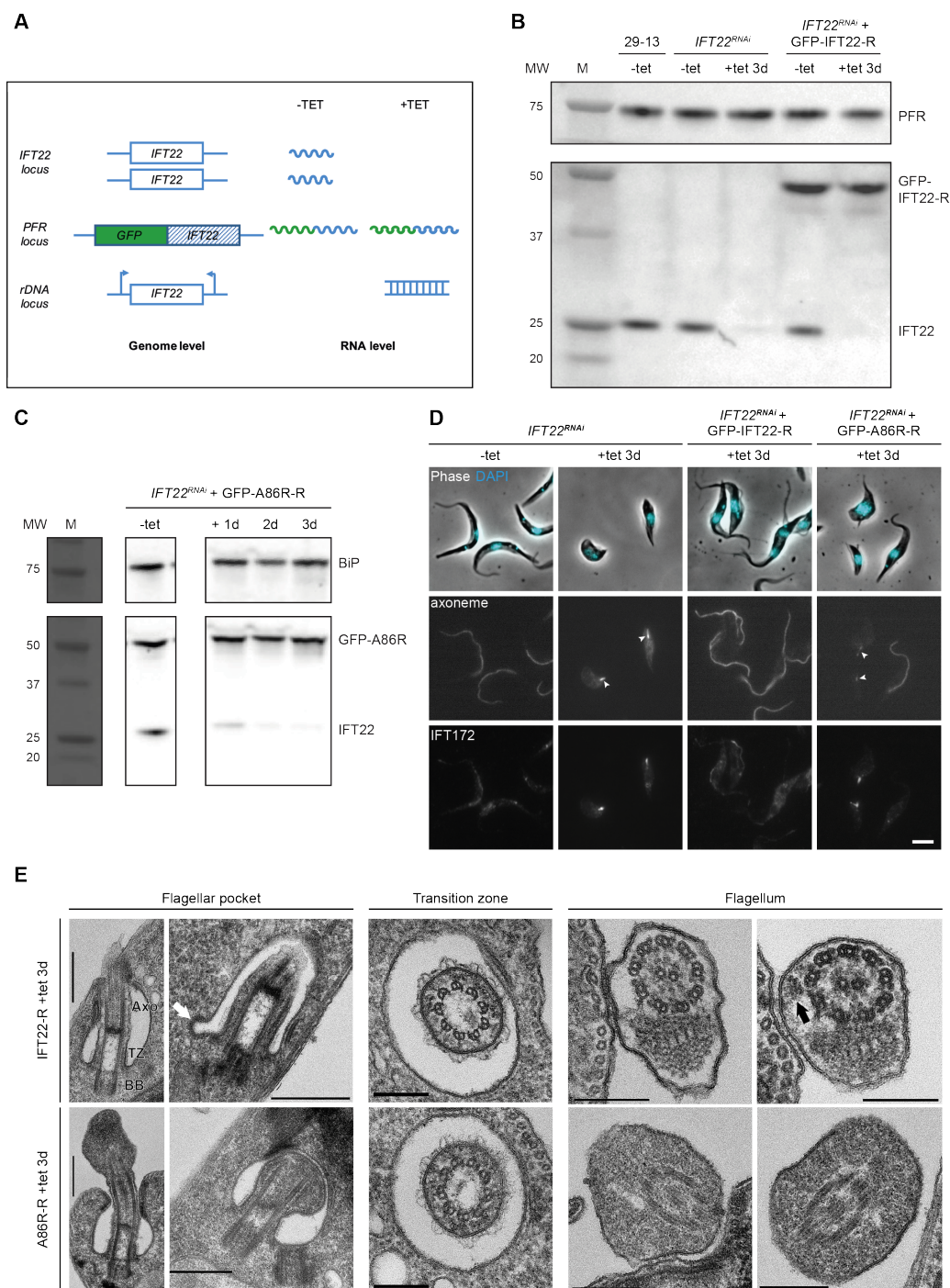


**Figure 16: The IFT22 A86R does not sustain IFT and cannot rescue the absence of IFT22**

**A.** Strategy used to evaluate the biological significance of IFT22 mutations. Boxes represent coding sequences and undulated lines correspond to mRNA. Cell lines used contain the two endogenous copies (trypanosomes are diploid) of IFT22, a single copy of an RNAi-resistant version (dashed blue) fused to GFP (green) expressed from the PFR locus and a construct for expression of double-stranded IFT22 RNA under the control of tetracycline-inducible promoters. In the absence of tetracycline, there is no dsRNA and mRNA originating from all three genes is present. However, addition of tetracycline triggers the production of dsRNA that result in degradation of transcripts from the endogenous genes but not from the recoded one. **B.** Western blot analysis of the indicated cell lines probed with the anti-IFT22 antibody (bottom) and with an anti-PFR as loading control (top). **C.** Western blot analysis of the IFT22<sup>RNAi</sup>+GFP::IFT22R A86R cell line probed with the anti-IFT22 antibody (bottom) and with an anti-BiP as loading control (top). **D.** IFAs with the indicated cell lines and conditions using the mAb25 (marker for the axoneme, central panels) and an anti-IFT172 antibody (marker for IFT, bottom panels). The top panels show the phase contrast image merged with DAPI (cyan) that stains nuclear and mitochondrial DNA. **E.** Sections of IFT22<sup>RNAi</sup>+GFP::IFT22R (top panels) or IFT22<sup>RNAi</sup>+GFP::IFT22R A86R (bottom panels) were analysed by transmission electron microscopy. Sections through the flagellar pocket and the flagellum are shown. Scale bars are 500 nm (flagellar pocket sections) or 200 nm (transition zone and flagellum sections). The white arrow indicates an endocytic vesicle budding off the flagellar pocket whereas the black one points at an IFT train. (Axo = axoneme, Bb = basal body, PFR = paraflagellar rod, TZ = transition zone)

An RNAi-resistant version of GFP::IFT22 carrying the A86R mutation was expressed in trypanosomes in the tetracycline-inducible *IFT22<sup>RNAi</sup>* cell line. This GFP::IFT22R A86R version will be referred to as A86R. Western blot analysis showed the expected motility for the fusion protein as well as efficient and specific silencing of the endogenous version of IFT22 (Fig. 16C). In both non-induced and induced conditions (leading to knock-down of the endogenous IFT22 protein), the A86R protein does not display IFT, fails to localize to the flagellum and accumulates throughout the cytoplasm (Video S3 and S4). Phase contrast observation showed the emergence of cells with tiny flagella filled with IFT172 protein or even no flagella (Fig. 16D, last row). Transmission electron microscopy (TEM) analysis was performed on tetracycline-induced IFT22R and A86R cell lines. It revealed that the base of the flagellum was properly inserted in the flagellar pocket but that the flagella were very short and contained excessive amount of electron-dense material (Fig. 16E, first two columns). The transition zone was properly assembled and displayed the normal morphology (Fig. 16E, third column) including the typical collarette that surrounds its proximal part (Trépot et al. 2018). By contrast, sections through the flagella revealed abnormal microtubule organisation and excessive IFT material (Fig. 16E, last two columns). This corresponds to the typical phenotype for IFT22 RNAi silencing (Fig. 16D, second row) and confirms that the A86R protein cannot rescue the phenotype.

Our results demonstrate that association of IFT22 to the IFT-B1 complex via IFT74/81 and localization of the small GTPase to IFT trains and the ciliary compartment is crucial for proper organelle assembly in trypanosomes.

## 2.8 An inactive GTP-binding mutant shows significantly reduced affinity to IFT74/81, but does not cause a strong effect *in vivo*

Because of previously mentioned difficulties regarding the analysis of GDP-loaded IFT22, we investigated different nucleotide-binding mutants (Fig. 17A) to evaluate the effect of nucleotide hydrolysis states and to assess the importance of the GTPase cycle for IFT22 function. First, we mutated the unusual Asp175 that binds the guanine base. A D to E conversion exhibits significantly reduced, though still clearly detectable nucleotide-binding abilities (approx. 10-fold reduction in  $K_d$  compared to WT, Fig. 17B, blue dots). This is in accordance with the fact that several IFT22 homologs have an E residue in the position of D175 of *TbIFT22* (Supplements, Fig. 18). Complete removal of the negatively charged side chain by a D to A mutation has a much stronger effect and *TbIFT22* D175A alone hardly shows any nucleotide-binding capacity in titration experiments (Fig. 17B, blue triangles, no curve fitting possible). However, when analyzing the D175A mutant in context of the small core complex, we found that the mutant core complex still co-purified with GTP (confirmed by HPLC) and titration experiments revealed a detectable nucleotide affinity for the GTP analog (approx. 70-fold reduction in  $K_d$  compared to WT IFT22/74/81 core complex) (Fig. 17B, dark blue outlined triangles).

The impact of the D175A mutation was tested in trypanosomes by expressing an RNAi-resistant version fused to GFP in the *IFT22<sup>RNAi</sup>* background as described above. Western blot analysis showed correct

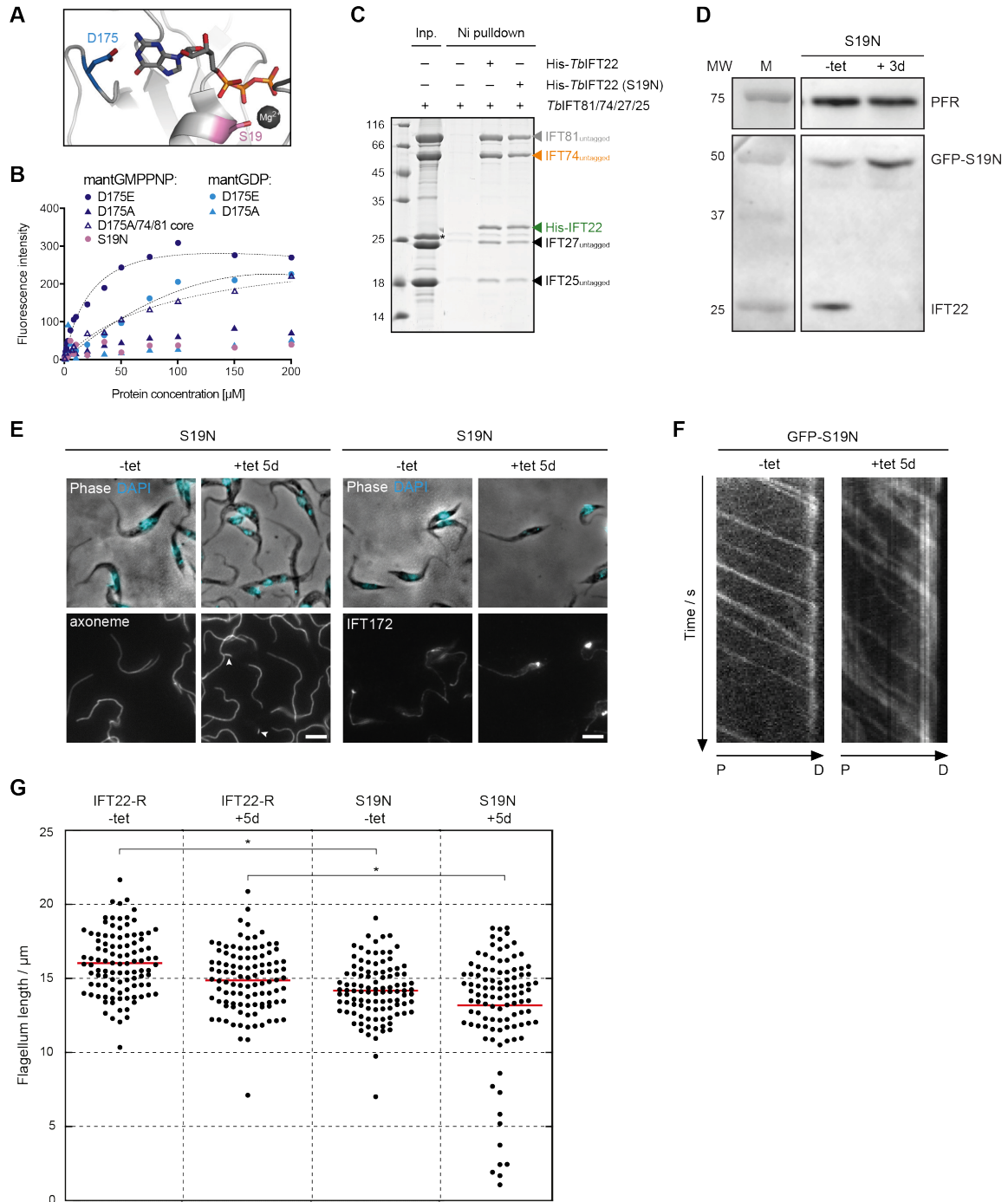


**Figure 17: The inactive GTPase mutant only shows a mild phenotype *in vivo***

**A.** Cartoon representation of IFT22 (grey) with positions of two nucleotide-binding mutants highlighted. GTP is shown in stick representation and  $Mg^{2+}$  as a ball. D175 (blue) is the unusual residue binding the guanine base (Fig. 12B), while S19 (pink) is a conserved residue needed for coordination of the  $Mg^{2+}$  cation. It is commonly point mutated in small GTPases to mimic an inactive GTPase state. **B.** Nucleotide-binding experiments of IFT22 nucleotide-binding mutants D175E, D175A and S19N with fluorescently labeled nucleotides. Only the S19N mutation (light pink) abolished IFT22 nucleotide-binding ability completely. **C.** SDS-PAGE gel of a  $Ni^{2+}$ -NTA pull-down of the purified full-length IFT25/27/74/81 on His-tagged IFT22 (WT and S19N mutant). In contrast to previous pull-downs on truncated IFT74/81 (Fig. 15A, B), the inactive GTP-binding mutant shows pull down of the full-length tetrameric complex. **D.** Western blot analysis of the  $IFT22^{RNAi} + GFP::IFT22R$  S19N cell line probed with the anti-IFT22 antibody (bottom) and with an anti-PFR as loading control (top). **E.** IFA in the indicated conditions using the mAb25 (marker for the axoneme, left panels) and an anti-IFT172 antibody (marker for IFT, right panels). The top panels show the phase contrast image merged with DAPI (cyan) that stains nuclear and mitochondrial DNA. **F.** Kymographs showing the movement of the GFP::IFT22R S19N in the presence (left) or the absence (right) of the IFT22 endogenous protein. Note the improved signal-to-noise ratio in the latter case. **G.** Dot plot representation of flagellum length in the indicated cell lines and conditions. Statistically significant differences are indicated by a star.

expression of the D175A protein and its resistance to silencing in contrast to the endogenous IFT22 protein (Supplements, Fig. 21A). The D175A protein traffics normally in the flagellum in the presence (Video S5) and the absence (Video S6) of the IFT22 endogenous protein. As mentioned above, the fluorescence signal in the flagellum was much better in induced conditions. This impression was confirmed by kymograph analysis (Supplements, Fig. 21D). Finally, IFA confirmed that these cells assemble normal length flagella and display the classic distribution of IFT proteins (Supplements, Fig. 21B, C).

We also tested a mutation classically introduced in small GTPases to impair GTP-binding. The S to N exchange inserts a long, polar amino acid in the position of the Mg<sup>2+</sup>-coordinating Ser residue, thereby preventing Mg<sup>2+</sup>-binding and thus locking the GTPase in a constitutively inactive state (Fig. 17A). The S19N mutant is unable to bind nucleotides in titration experiments (Fig. 17B, light pink) and both immobilized *Tb*IFT74/81 core complex peptides (Fig. 15A, second Ni pulldown lane) as well as the crystal structure *Tb*IFT74/81 constructs (Fig. 15B, second Ni pulldown lane) are incapable of pulling down untagged *Tb*IFT22 S19N efficiently. The fact that the latter pulldown retains a faint, but visible amount of S19N mutant bound, points to a drastic reduction in affinity towards IFT74/81 rather than a complete loss of binding. This is in agreement with formerly published results of affinities of GTPases for their effectors (Simon et al. 1996; Scheffzek & Ahmadian 2005; Bhogaraju et al. 2011). We further confirmed the decrease in affinity with a pulldown experiment using the *Tb*IFT25/27/74/81 complex. Here, immobilized *Tb*IFT22 S19N is able to pull down similar amounts of the tetrameric complex than WT *Tb*IFT22 (Fig. 17C). This may be explained by a more robust coiled-coil backbone in the full-length IFT74/81 complex compared to IFT74/81 constructs truncated directly after the IFT22-binding coiled-coil (ccVI), thus leading to tighter binding of the IFT22 switches. This change in complex stability leads to the effect that the reduced binding affinity of S19N for IFT74/81 is only detectable in pulldowns with truncated IFT74/81 versions, but not with the full-length proteins. Given that the K<sub>d</sub> of IFT22 for IFT74/81 lies in the low nanomolar range (Supplements, Fig. 20D), a 1000-fold reduction in affinity would still yield a complex strong enough to be traceable in pulldowns. We performed another supporting pulldown experiment using a chimeric *Tb/Cr* complex (Supplements, Fig. 20G). Whereas His-tagged *Tb*IFT22 firmly captures untagged *Cr*IFT25/27/74/81 complex on Ni beads (positive control), both the His-tagged A86R (negative control) and S19N mutant fail to bind the *Cr* complex. Unfortunately, we could not quantitatively determine the decrease in affinity for the inactive mutant, since the S19N protein was less stable and had a tendency to precipitate in ITC experiments due to the vigorous stirring.

In order to evaluate if the inactive nucleotide-binding mutant shows an effect *in vivo* and to address the question if the GTPase cycle plays a role in *T. brucei*, we introduced and expressed a GFP-tagged RNAi resistant version of *Tb*IFT22 S19N in the parasite. Western blot analysis confirmed efficient silencing of the endogenous IFT22 protein whereas the S19N protein remained present (Fig. 17D). The S19N protein is found at the base of the flagellum and traffics normally within the organelle in the presence (Video S7) or the absence (Video S8) of endogenous IFT22, as formally demonstrated by kymograph analysis (Fig. 17F). We noticed that trains tended to pause and change speed more frequently in the latter case, suggesting a mild disruption of IFT. Although at first sight most cells looked normal, a minority of them appeared to possess clearly shorter flagella. This was confirmed by IFA analysis with an axonemal

marker (Fig. 17E, second column) and some accumulation of IFT172 occurred in these cells (Fig. 17E, last column). The length of the flagellum was measured and revealed that ~10 % of the population had shorter flagella than normal (Fig. 17G). Moreover, statistical analysis (Anova test) revealed a significant difference ( $p < 0.001$ ) in the length of the flagellum between non-induced cells expressing the S19N protein or the non-mutated version (Fig. 17G). This indicates a dominant-negative effect of IFT22 S19N on the length of the flagellum. This was also observed in induced conditions when comparing with the IFT22R cell line that expresses the RNAi-resistant version without amino acid mutations.

From these results, we conclude that the reduced affinity of the inactive nucleotide-binding mutant for the IFT-B1 complex is still strong enough to facilitate ciliary trafficking in absence of the endogenous IFT22 protein in most cells. However, the S19N protein might be less efficient in its function, resulting in minor perturbations of IFT and the formation of shorter flagella.

### 3 Discussion

Small GTPases are involved in regulation of a large variety of cellular processes by acting as molecular switches and cycling between an active (GTP-) and inactive (GDP-bound) state. Members of the Rab family are usually associated with regulation of various membrane-trafficking pathways and over the past years an increasing number of Rab and Rab-like proteins were found to play a role in cilia-related processes (for a general review see (Blacque et al. 2017; Adhiambo et al. 2009)). However, still not much is known about the underlying molecular mechanisms and the exact cellular functions of these Rabs and their regulatory GEFs, GAPs and effector proteins. Small GTPases could function in several unresolved key steps of ciliogenesis and IFT that require tight regulation and are currently missing elaborate explanations: How are IFT complexes assembled into trains and loaded with cargo? How is the entry of proteins to the ciliary compartment regulated? What induces cargo release at the ciliary tip? What regulates the transition between anterograde and retrograde transport? And how are turnover products released at the ciliary base?

#### 3.1 IFT22 shares common features with IFT27

In this work we structurally demonstrate that the small GTPase IFT22 is an atypical Rab GTPase that specifically binds G nucleotides and has low intrinsic hydrolysis rates. GTP-hydrolysis rates and affinities for nucleotides are comparable to the ones reported for the other small GTPase of the IFT complex, IFT27 (Bhogaraju et al. 2011), and indicate the need for a GAP, but not a GEF protein for realization of a complete GTPase cycle. Studies of IFT27 in mouse and trypanosomes demonstrated that the GTP-bound state is needed for association with the IFT particle and that the inactive mutant is excluded from the cilium (Schafer et al. 2006; Huet et al. 2014; Eguether et al. 2014), making the direct interaction partners IFT74/81 an effector of IFT27. Interestingly, Eguether and colleagues found that the inactive *MmIFT27*<sup>T19N</sup> mutant retains some affinity for IFT-B in the absence of endogenous IFT27, can enter the cilium and partially rescues the IFT27 knockout phenotype. We made similar observations when investigating the effects of GTP/GDP states of IFT22: GTP-bound IFT22 shows clearly enhanced affinity for its effector complex IFT74/81 compared to the inactive *TbIFT22*<sup>S19N</sup> mutant *in vitro*. Localization of the inactive mutant has also been investigated in a previous study in *C. elegans* worms where the *CeIFT22*<sup>T24N</sup> mutant was detected in the cytoplasm and restricted from the cilium (Adhiambo et al. 2009; Schafer et al. 2006), even in the presence of endogenous IFT22 expression. Therefore, it is likely that IFT22, similar to IFT27, associates to the IFT-B complex in a GTP-bound state in the cell to ensure steady entry of the small GTPase into the cilium and to fulfill its ciliary function. The reported difference in localization and trafficking of the inactive mutant depends on the type of organism though and relies on the individual affinities of IFT22 homologs for the IFT74/81 effector complex.

IFT22 is purified with the IFT-B complex from trypanosomes (Franklin & Ullu 2010) and so the phenotypic defect in retrograde transport upon RNAi knockdown was rather unexpected (Adhiambo et al. 2009). Here, we formally demonstrate that the phenotype is specific because it can be rescued by the expression

of an RNAi-resistant version of the gene. Similar results were obtained for IFT27 that associates to the IFT-B complex and whose inhibition results in defects in entry of dynein and IFT-A proteins in the flagellum, possibly explaining the retrograde phenotype (Huet et al. 2014).

Noteworthy, both IFT22 and IFT27 GTPases are not globally conserved amongst ciliated organisms. While IFT27 is missing from the genome of *C. elegans*, no IFT22 homolog is identified in *T. thermophila* and both are missing in *G. intestinalis* (van Dam et al. 2013), leading to the hypothesis that other Rab GTPases might be able to take over their ciliary functions and that ciliary Rabs might share their yet to be identified regulatory proteins. Consistently, when analyzing sequences of IFT74 and IFT81, we found that the main residues interacting with IFT22 in other organisms are conserved in *G. intestinalis* and *T. thermophila*, too (Supplements, Fig. 20E). It can thus be speculated if those organisms do contain a yet unidentified homolog of IFT22 or if another small GTPase or more distantly related (cargo?) protein utilizes this patch as a connection point to the IFT complex instead.

### 3.2 Is IFT22 a potential cargo-binding protein?

Due to its association with the IFT complex it was hypothesized that IFT22 itself could act as an adaptor for IFT cargo proteins, such as signaling molecules in the case of *C. elegans* (Silva et al. 2012; Li & Hu 2011; Blacque et al. 2017). IFT22 displays one highly conserved surface patch harboring the IFT74/81 interacting residues and conserved residues in the GTP-binding pocket (Fig. 14A, IFT22 top and bottom view). Apart from that, the remaining surface conservation is rather variable. Thus, if IFT22 functions in cargo binding, it likely interacts with different types of cargo in different organisms rather than having one conserved interaction partner. This might also explain the observed functional differences between species.

### 3.3 IFT22 may be involved in causing Short-Rib Polydactyly Syndrome

Although no patient mutations in IFT22 have been reported to date, a recent study identified a series of mutations in IFT81 causing Short-Rib Polydactyly Syndrome (SRPS) (Duran et al. 2016). One of the disease mutations detected was an in-frame deletion of Leu435, which refers to Leu443 in trypanosomes and is a well-conserved residue directly interacting with IFT22 in the crystal structure (see sequence alignment in Supplements, Fig. 20E (L435 encircled in blue) and Fig. 14C for residue position). Unfortunately, no cultured cells were available for this particular mutation and the authors do not provide experimental data regarding expression levels and stability of this IFT81 mutant protein. However, two scenarios are conceivable: either the residue deletion leads to an overall IFT81 protein instability, affecting the whole IFT-B1 complex integrity, or the IFT74/81 scaffold stays intact but the deletion leads to dissociation or weakened binding of IFT22, causing an IFT22-mediated disease phenotype. Interestingly, many of the SRPS-causing mutations affect proteins required for retrograde IFT such as dynein-2 components

(Taylor et al. 2015; Dagonneau et al. 2009) or the IFT-A component IFT121 (Mill et al. 2011) and lead to typical retrograde IFT inactivation phenotypes. Knock-down of IFT22 in trypanosomes also causes a phenotype similar to inhibition of retrograde IFT (Adhiambo et al. 2009). IFT22 could therefore be a candidate gene for ciliopathies associated to skeletal defects.

## 4 Experimental Procedures

### 4.1 Recombinant protein expression and purification from *E. coli*

Wild type and mutant (A86R, S19N, D175A/E) IFT22 proteins from *Tb* and *Mm* were expressed as tobacco etch virus (TEV) cleavable N-terminal His<sub>6</sub> fusion proteins in *E. coli* BL21(DE3) grown in TB-medium at 37 °C. Overexpression was induced at 18 °C at an OD<sub>600</sub> of 1.8 with 0.5 mM IPTG. Cells were lysed by sonication in a buffer containing 50 mM Tris pH 7.5, 150 mM NaCl, 10 % (v/v) glycerol, 10 mM imidazole, 2 mM MgCl<sub>2</sub>, 5 mM β-mercaptoethanol, 1 mM PMSF and 25 μg ml<sup>-1</sup> DNaseI and the extract was cleared by centrifugation (4 °C, 75 000 × g, 30 min). In a first step, proteins were purified via a Ni<sup>2+</sup>-NTA affinity column (5 ml, Roche). In order to remove N-terminal His<sub>6</sub>-tags, proteins were incubated with TEV protease overnight at room temperature and dialysed against 50 mM NaCl buffer for subsequent ion-exchange chromatography (5 ml HiTrap Q sepharose, GE Healthcare). For further purification, proteins were subjected to size-exclusion chromatography (SEC) after concentrating to 20 mg ml<sup>-1</sup> to 30 mg ml<sup>-1</sup> in a buffer containing 10 mM HEPES pH 7.5, 150 mM NaCl, 2 mM MgCl<sub>2</sub> and 1 mM DTT using a HiLoad Superdex 75 column (GE Healthcare). In general, both *Tb* and *Mm*IFT22 were highly soluble and could be concentrated up to 2 mM (~50 mg ml<sup>-1</sup>). Proteins were stored at -80 °C in SEC buffer. IFT22/74/81 core complexes of *Tb*, *Mm* and *Cr* as well as the N-terminal *Tb*IFT22/74<sub>79-401</sub>/81<sub>1-450</sub> subcomplex were co-expressed in *E. coli* BL21(DE3) with each protein on a separate plasmid using N-terminal His<sub>6</sub>-tagged IFT74 and IFT81 constructs and untagged IFT22. The same purification procedure was followed. Expression and purification of *Cr*IFT25/27/74/81 was done as described previously (Taschner & Lorentzen 2016a).

### 4.2 Expression of selenomethionine derivatives

Selenomethionine derivative proteins were obtained from co-expression cultures of *Tb*IFT22/74<sub>79-401</sub>/81<sub>1-450</sub> grown in M9 minimal medium supplemented with 60 mg l<sup>-1</sup> selenomethionine. Overnight expression was induced at an OD<sub>600</sub> of 1.0 with 0.5 mM IPTG and the temperature was shifted to 20 °C. The purification procedure was followed as for the native proteins.

### 4.3 Recombinant protein expression and purification from insect cells

Coding sequences of *Tb* IFT25, IFT27, IFT74<sub>79-C</sub> and IFT81 were cloned as TEV-cleavable N-terminal His<sub>6</sub> fusion proteins into the multiple cloning sites of pFL vectors, with IFT25/27 and IFT74<sub>79-C</sub>/81 being located on the same vector, respectively (IFT27 into MCS1 via SmaI/SphI and IFT25 into MCS2 via EcoRI/XbaI; IFT81 into MCS1 via SmaI/SphI and IFT74 into MCS2 via EcoRI/XbaI). Recombinant baculoviruses were produced as described previously (Taschner et al. 2014). *Tb*IFT25/27 and *Tb*IFT74<sub>79-C</sub>/81

heterodimeric complexes were co-expressed at 26 °C in 6 l HighFive insect cells (Invitrogen) infected with pre-determined amounts of recombinant viruses. Cells were harvested after 72 h and lysed by dounce homogenization in a buffer containing 20 mM HEPES pH 7.5, 250 mM sucrose, 10 mM KCl, 1.5 mM MgCl<sub>2</sub>, 5 mM β-mercaptoethanol and one pill of protease inhibitor cocktail (complete, EDTA-free, Roche). Nuclei were removed as described in Taschner et al, 2016. Protein purification was done as outlined for proteins expressed in *E. coli*, except for using a HiLoad Superdex 200 or Superose 6 column in SEC.

#### 4.4 Crystallization of GTP/GDP-*TbIFT22* and *TbIFT22/74<sub>79-401</sub>/81<sub>1-450</sub>*

*TbIFT22* was set up for crystallization at 15.2 mg ml<sup>-1</sup> in SEC buffer by sitting-drop vapor diffusion in 0.2 μl drops obtained by mixture of equal volumes of protein and crystallization solution. Crystals appeared after 2 days at 4 °C as fine needle clusters after mixing with 20 % (w/v) PEG3350, 50 mM NaCacodylate pH 6.5 and 200 mM CaAcetate and turned into three-dimensional hexagons in the course of 10 days (Supplements, Fig. 19D). No excess of GTP was added to the protein or the crystallization solution since *TbIFT22* was purified bound to GTP from *E. coli*. For crystallization of the GDP-loaded state, refolded nucleotide-free *TbIFT22* was set up at 15.6 mg ml<sup>-1</sup> in SEC buffer supplemented with 7 mM GDP by sitting-drop vapor diffusion in 0.2 μl drops obtained by mixture of equal volumes of protein and crystallization solution. Crystals grew with a similar shape transition as described above at 4 °C after mixing with 15 % (w/v) PEG6000, 50 mM NaCacodylate pH 7.0 and 200 mM CaAcetate. Both GTP- and GDP-*TbIFT22* crystals were cryoprotected in mother liquor containing 15 % (v/v) glycerol prior to flash freezing in liquid nitrogen.

Crystals of the *TbIFT22/74/81* complex (native and selenomethionine derivate, Supplements, Fig. 20C) were obtained from protein concentrated to 25 mg ml<sup>-1</sup> by sitting-drop vapor diffusion at 4 °C in 0.2 μl drops (0.1 μl protein solution containing 2 mM GTP with 0.1 μl crystallization solution) supplemented with 40 nl freshly prepared microseeds. Crystals grew after mixing with 15 % (v/v) glycerol, 7.5 % (w/v) PEG4000, 100 mM HEPES pH 7.5 and were cryoprotected in reservoir solution containing 33 % (v/v) ethylene glycol prior to flash freezing in liquid nitrogen.

#### 4.5 Data collection and crystal structure determination

For the structures of the small GTPase, diffraction data were collected at the PXIII (for GTP-*TbIFT22*) and PXII (for GDP-*TbIFT22*) beamline at the Swiss Light Source (SLS) in Villigen, Switzerland, and were processed with XDS (Kabsch 2010) prior to scaling with Aimless of the CCP4 package (Winn et al. 2011). The structure of GTP-*TbIFT22* was solved at 2.3 Å resolution by molecular replacement (MR) with an ensemble of three different superposed Rab GTPases found by HHpred search (PDB IDs: 1vg8, 2y8e, 3oes) using the program Phaser (Storoni et al. 2004). The asymmetric unit contained two molecules of IFT22 and analysis with Xtriage detected twinned data. The model was completed by iterative cycles of

model building in COOT (Emsley et al. 2010), followed by refinement in PHENIX (Adams et al. 2010) using NCS restraints and applying the twin law  $h, -h-k, -l$ . The GDP-*TbIFT22* structure was determined at 2.5 Å resolution using the previously solved GTP-bound structure as a search model for MR.

X-ray diffraction data for the *TbIFT22/74/81* complex structure was collected at the PXII beamline at SLS, indexed with XDS and scaled with CCP4 Aimless. The structure was determined from selenomethionine substituted protein crystals. Single anomalous dispersion data were recorded at the Se peak wavelength, and AUTOSOL as part of the PHENIX package was used to locate Se sites and calculate experimental phases and electron density. The structure was solved at 3.2 Å resolution from a dataset derived from a selenomethionine substituted protein crystal, since native crystals diffracted significantly worse.

Two copies of the *TbIFT22/74<sub>79-401</sub>/81<sub>1-450</sub>* complex were located in the asymmetric unit. The 3.2 Å model was built in COOT and refined in PHENIX using NCS restraints, secondary structure restraints and optimized X-ray/stereochemistry weight. The two copies were very similar in most parts, but showed significant conformational differences in the C-terminal IFT22-binding coiled-coils of IFT74/81 (ccVI). While we could build IFT22 into the electron density map of one of the copies, we were unable to build the other IFT22 molecule with confidence into the electron density map, although the unbiased Fo-Fc map does show low quality difference density for the IFT22 GTPase. Data collection and refinement statistics are summarized in Table 1 on page 67.

## 4.6 Affinity pulldown experiments

For purified proteins, Ni<sup>2+</sup>-NTA affinity beads were pre-incubated with buffer containing 150 mM NaCl, 50 mM Tris pH 7.5, 2 mM MgCl<sub>2</sub> and 10 mM imidazole. 40 µg of purified His-tagged proteins were bound to 30 µl of beads in a total volume of 500 µl at 4 °C. After 1 h, beads were washed twice with 1 ml buffer to remove excess protein and were incubated with 400 µg of untagged interaction partner in 500 µl total volume for another hour. Beads were washed three times with 1 ml buffer to remove unbound protein. Bound proteins were eluted from the beads with 50 µl buffer containing 500 mM imidazole. In the case of Ni<sup>2+</sup> pulldowns from cell lysates, the proteins were co-expressed from separate plasmids in *E. coli* BL21(DE3) cells. 20 µl of each culture were taken and supplemented with SDS loading dye as total expression samples. Cell pellets from 10 ml overnight culture were resuspended in 1.5 ml lysis buffer (50 mM Tris pH 7.5, 150 mM NaCl, 10 % (v/v) glycerol, 10 mM imidazole, 2 mM MgCl<sub>2</sub>) and cells were lysed by sonication (1 min, 1 s pulse/1 s pause). Cell extracts were cleared by centrifugation (4 °C, 16 000 × g, 30 min) and the supernatant was incubated at 4 °C with 20 µl Ni<sup>2+</sup>-NTA affinity beads pre-incubated with lysis buffer. After 1h, beads were washed three times with 1 ml buffer and bound proteins were eluted with 50 µl buffer containing 500 mM imidazole. Eluate contents were analyzed by SDS-PAGE.

## 4.7 Protein denaturation by urea and refolding for nucleotide removal

*TbIFT22* and the *TbIFT22/74/81* core complex were refolded in order to remove bound GTP, since more gentle methods such as EDTA- or SAP-treatment were not successful (Supplements, Fig. 19C). Proteins were diluted to 0.5 mg ml<sup>-1</sup> and dialysed in a dialysis tube against buffer containing 50 mM Tris pH 7.5, 150 mM NaCl, 10 % (v/v) glycerol and 8 M urea overnight at 4 °C. After 18 h, dialysis tubes were transferred to fresh buffer without urea for protein refolding and dialysed for another 24 h. The buffer was exchanged twice to remove residual urea. After refolding, proteins were concentrated and subjected to SEC. Successful nucleotide-removal was verified by HPLC.

## 4.8 HPLC nucleotide analysis

Nucleotide species of purified proteins and their hydrolysis states were verified at 20 °C by reversed phase high-performance liquid chromatography (HPLC) using a Vydac 218TP C<sub>18</sub> column with a Securityguard filter cartridge system (Phenomenex) attached. Nucleotides were separated by isocratic elution at 20 °C with a buffer composed of 100 mM potassium phosphate pH 6.5, 10 mM tetrabutylammonium bromide and 7.5 % (v/v) acetonitrile and elution detected at 254 nm.

## 4.9 Nucleotide-binding experiments

Nucleotide-affinities of *TbIFT22* (WT, mutants and core complex) were determined by fluorescence spectrophotometric measurements (PerkinElmer LS50B) of 2'(3')-O-(N-methylanthraniloyl)-labeled (mant-labeled) nucleotides (Jena Bioscience). Increasing concentrations (2 µM to 200 µM) of HPLC-confirmed nucleotide-free protein were incubated with 1 µM mant-GDP/-GMPPNP/-ADP/-AMPPNP for 30 min in a buffer containing 50 mM Tris pH 7.5, 100 mM NaCl and 5 mM MgCl<sub>2</sub> in 60 µl volumes. Emission spectra of the samples were monitored at 20 °C in a quartz cuvette from 400 nm to 500 nm (excitation at 355 nm). Intrinsic protein fluorescence and mant-nucleotide background fluorescence were subtracted from the data. Emission maxima of the mant fluorophore at 448 nm were plotted against protein concentrations. Curve fitting and dissociation constant (K<sub>d</sub>) determination was done with GraphPad Prism 6.0 software using a binding equation that describes a single-site binding model.

## 4.10 GTPase assay

GTPase activities of *TbIFT22* and the *TbIFT22/74/81* core complex were measured at 20 °C with the EnzChek Phosphate Assay Kit (ThermoFisher). Reactions were initiated by adding 1 mM GTP to the protein mixed with kit solutions according to the manufacturer's recommendations. The release of inorganic phosphate (P<sub>i</sub>) upon GTP hydrolysis followed by an enzymatic reaction was monitored

over 20 min. The change in absorption at 360 nm was detected every minute using a PerkinElmer Lambda19 UV spectrometer. As a negative control, intrinsic GTP hydrolysis in buffer was followed. Rate quantifications were done with the help of a linear standard curve for P<sub>1</sub> generated with defined concentrations of KH<sub>2</sub>PO<sub>4</sub> from 10 μM to 200 μM after 20 min incubation.

#### 4.11 Isothermal titration calorimetry (ITC)

ITC experiments were carried out to determine the K<sub>d</sub> between *TbIFT22* and the *TbIFT25/27/74<sub>79-C</sub>/81* subcomplex using a MicroCal iTC200 instrument (Malvern). Proteins were buffered in identical solutions containing 10 mM HEPES pH 7.5, 150 mM NaCl and 2 mM MgCl<sub>2</sub>. For reasons of complex stabilization, IFT25/27/74/81 had to be supplemented with 2-fold molar excess of GTP. Experiments were performed with 15 μM to 20 μM *TbIFT25/27/74<sub>79-C</sub>/81* in the measurement cell and a 10-fold molar excess of *TbIFT22* in the syringe. *TbIFT22* was titrated in 20 injections of 0.8 μl under constant stirring (600 rpm) at 15 °C, with intervals of 180 s between injections. For all measurements, a background curve consisting of titration of *TbIFT22* into buffer was subtracted to account for heat dilution. Data analysis and K<sub>d</sub> calculations were done using the program Origin v7.0.

#### 4.12 Trypanosome cultures and transfection

Procyclic *T. brucei* cell lines were derivatives of the strain 427, grown in SDM79 medium containing 10 % foetal calf serum and hemin (Brun & Schönenberger 1979). Generation of the inducible *IFT22<sup>RNAi</sup>* (*RABL5<sup>RNAi</sup>*) cell line has been described previously (Adhiambo et al. 2009). In this cell line, a 447-nucleotide long fragment of IFT22 was cloned in the pZJM vector (Zefeng Wang et al. 2000). The two T7 promoters face each other and can be induced in the presence of tetracycline, leading to the production of double-stranded RNA (dsRNA). To express RNAi-resistant versions of IFT22, the entire nucleotide sequence of IFT22 was modified by substituting the last and when possible the second nucleotide of the codon to render the transcript insensitive to RNAi (Huet et al. 2014) hence retaining the original amino acid sequence. This was tagged with GFP and the resulting plasmid was called pPCPFR<sub>e</sub>GFPIFT22<sup>RNAiRes</sup>. GeneCust Europe carried out the chemical synthesis and additional point mutations were introduced to generate the S19N, A86R and D175A versions. The plasmids were linearized with NsiI to target integration in the *PFR2* locus (Adhiambo et al. 2009) following transfection using the Nucleofector Technology (Lonza, Italy) (Burkard et al. 2007).

#### 4.13 Immunofluorescence (IFA)

Cultured cells were spun at 580 × g and supernatant was removed and then washed in SDM79 medium without serum. Cells were spread onto poly-L-lysine coated slides, dehydrated and fixed in methanol at -20 °C for 5 min. Slides were rehydrated in 1× Phosphate-buffered saline (PBS) for 15 min. Primary

antibodies were diluted in PBS with 0.1 % Bovine serum albumin (BSA) and slides were incubated for 60 min at 37 °C. The mAb25 mouse monoclonal antibody recognises the *TbSAXO1* protein found along the entire length of the axoneme (Pradel et al. 2006) and was used as a flagellar marker. The anti-IFT22/RABL5 is a polyclonal mouse antiserum recognizing IFT22 (Adhiambo et al. 2009) and the monoclonal anti-IFT172 antibody is a classic marker for IFT-B proteins (Absalon et al. 2008). Slides were washed three times in PBS before being incubated with specific secondary antibodies, diluted in PBS with 0.1 % BSA, for 60 min at 37 °C. Sub-class specific secondary antibodies were used for double labelling and detection. Secondary antibodies were coupled to either Cy3 or Cy5 (Jackson ImmunoResearch Laboratories, West Grove, PA) or Alexa 488 (Invitrogen). Slides were washed again and stained with DAPI (2 µg µl<sup>-1</sup>; stains nucleus and kinetoplast) and mounted using ProLong (Invitrogen). Experiments were performed at least twice to confirm the results.

A DMI4000 Leica microscope equipped with a 100 × 1.4 lens (Leica, Germany) was used for observing slides, and images were captured using an ORCA-03G camera (Hamamatsu). Images were analysed using ImageJ v1.49 (National Institutes of Health, USA). Flagellum length was measured using the mAb25 signal and the measuring tool of ImageJ. Between 50 and 100 flagella were measured per experiment.

#### **4.14 Live Cell Imaging**

Cultured cells were spread onto a slide, covered with a coverslip and observed using the DMI4000 Leica Microscope. Videos were acquired using an Evolve 512 EMCCD Camera (Photometrics, AZ) driven by the Micro-Manager Acquisition software (Molecular Probes, CA) to record videos at 100 ms exposure. Analysis of acquired videos was performed using ImageJ v1.49. Kymograph extraction was performed using the KymographTracker plugin in Icy 1.9.5.1 (BioImage Analysis Unit, Institut Pasteur, France). Kymographs give a 2D graphical representation of the spatial position of IFT trains over time. The x-axis corresponds to the length of the region of interest (ROI) while the y-axis corresponds to the elapsed time. The ROI was traced semi-automatically as a path in a maximum intensity enhanced projection of a time lapse image sequence (200 frames at 10 fps) by clicking control points in the intensity projection such that the curve followed a high pixel-value trail. Vertical lines indicate no movement over time, corresponding to standing material. Moving material is represented by a slope of the line.

#### **4.15 Western Blot**

Cells were washed once in PBS. Laemmli loading buffer was added to the cells and samples were boiled for 5 min. 20 µg of protein were loaded onto each lane of a Criterion™ XT Bis-Tris Precast Gel 4 % to 12 % (Bio-Rad, UK) for SDS-Page separation. XT-Mops (1×) diluted in deionized water was used as a running buffer. Proteins were either transferred onto nitrocellulose membranes at 100 V over 1 h or by using the BioRad Trans-Blot Turbo™ blotting system (25 V over 7 min). The membrane was blocked with 5 % skimmed milk for one hour and then incubated with the anti-RABL5/IFT22 primary antibody diluted

in 0.05 % PBS-Tween (PBST). The anti-RABL5 polyclonal antibody was diluted 1/500. As a loading control, the anti-BiP (marker for an endoplasmic reticulum protein) (Bangs et al. 1993) diluted 1/1000 and anti-PFR (L13D6) (Kohl et al. 1999) diluted 1/50 were used. Both primary antibodies were diluted in 0.05 % PBST containing 1 % milk. After primary antibody incubation, three washes of 5 min each were performed in 0.05 % PBST followed by secondary antibody incubation. Anti-mouse secondary antibody coupled to horseradish peroxidase, diluted 1/20 000 in 0.05 % PBST containing 1 % milk, was used and the membrane was incubated for 60 min. The Amersham ECL Western Blotting Detection Reagent Kit (GE Healthcare Life Sciences, UK) was used for final detection of proteins on the membrane.

## **4.16 Transmission electron microscopy**

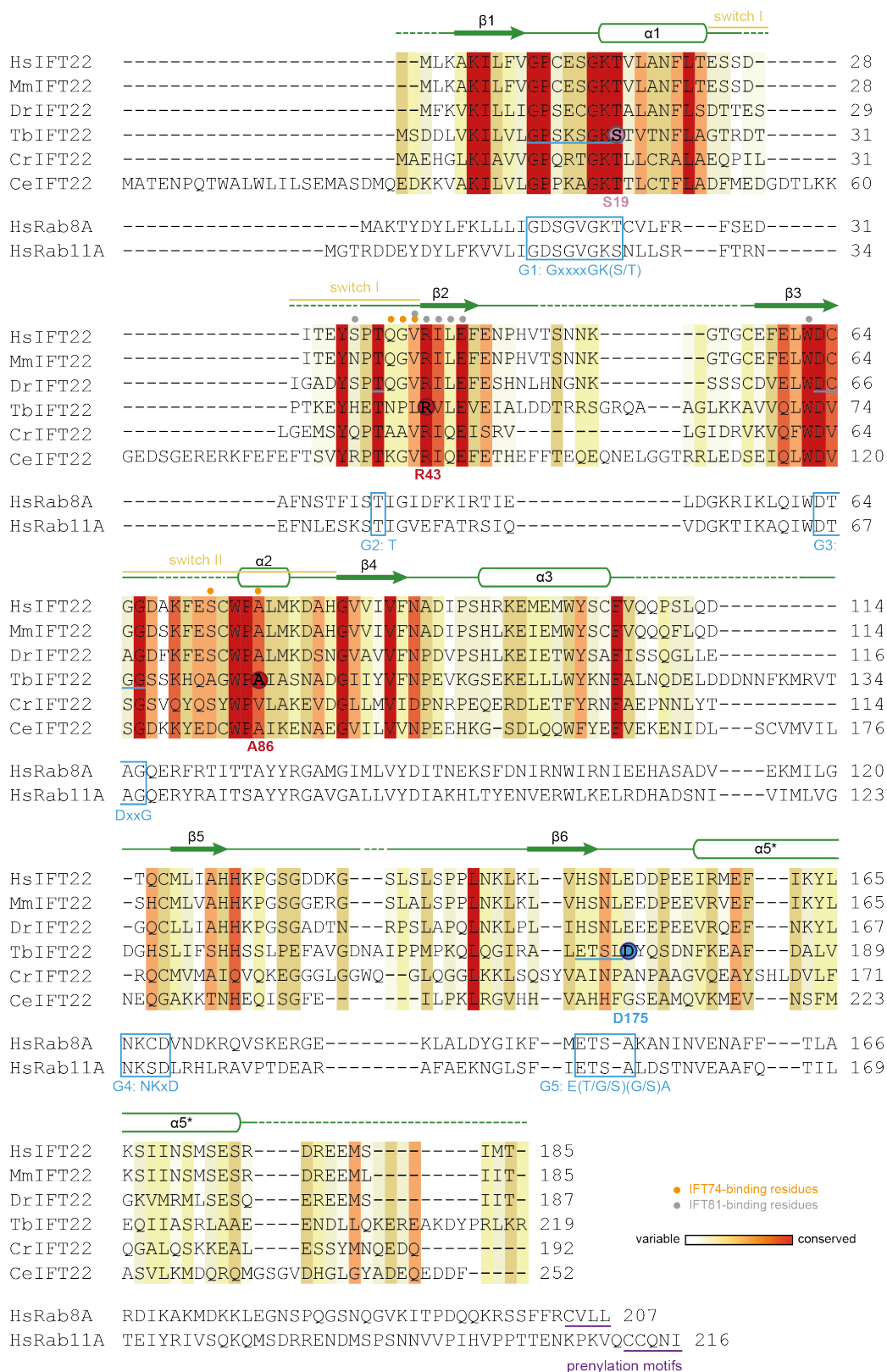
For electron microscopy, samples were treated as described in (Hughes et al. 2017) with a few modifications. Briefly, cells were fixed with 2.5 % glutaraldehyde directly in suspension in culture medium with gentle swirling. Cells were centrifuged for 5 min, washed in PBS and the pellet was re-suspended in a primary fixative containing 2.5 % glutaraldehyde, 2 % paraformaldehyde and 0.1 % tannic acid in 0.1 M phosphate buffer (pH 7.0) and incubated for 1 h. After three washes with 0.1 M phosphate buffer, the sample was post-fixed in 1 % osmium tetroxide for 60 min. The pellet was washed five times in water, stained overnight in 2 % aqueous uranyl acetate, dehydrated in increasing acetone series and finally embedded with progressive ascending concentrations of Agar-100 resin. Polymerisation was carried out for 120 min at 100 °C.

## Supplementary Figures &amp; Tables

Table 1: Data collection and refinement statistics

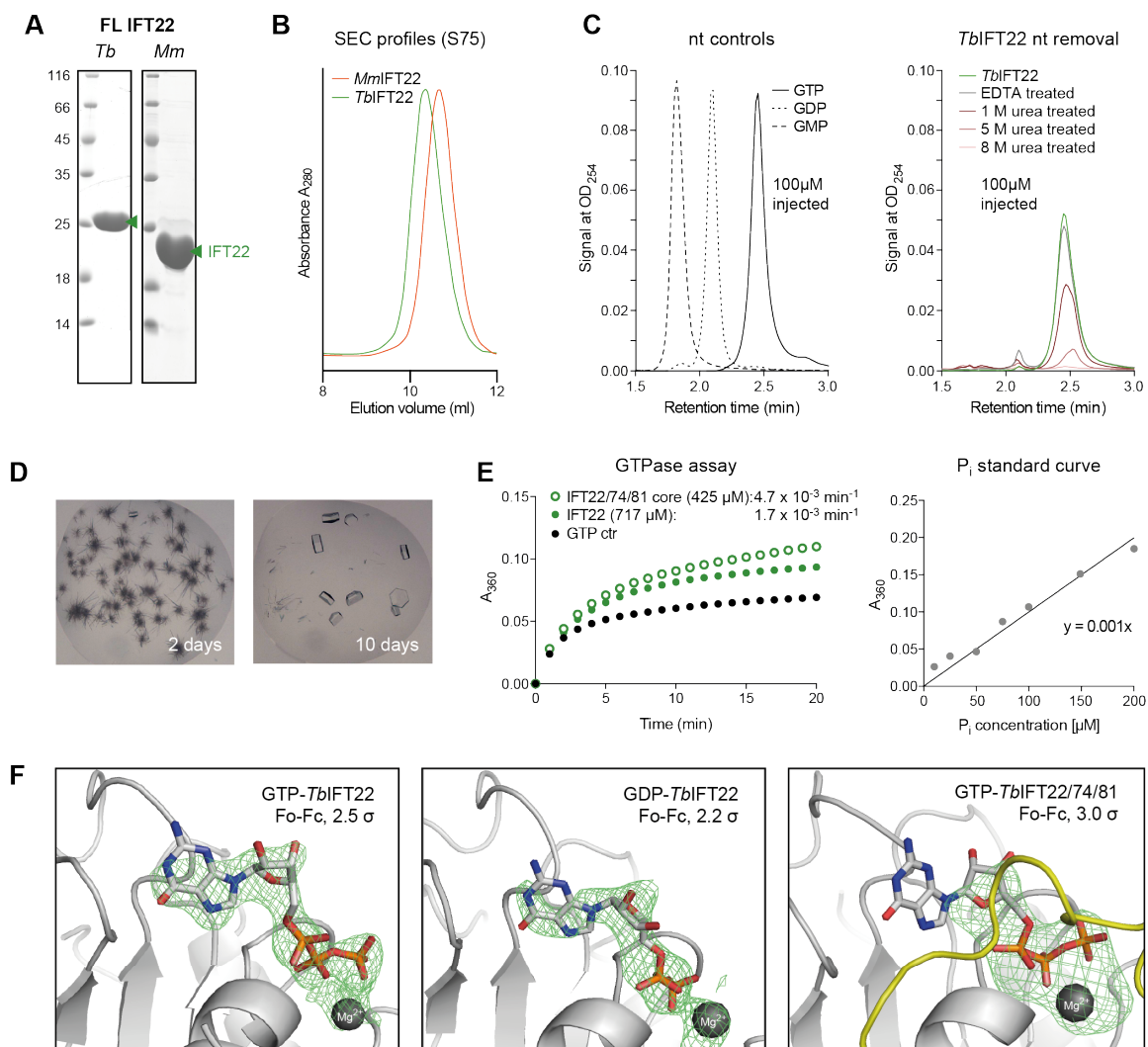
	GTP- <i>TbIFT22</i>	GDP- <i>TbIFT22</i>	<i>TbIFT22/74</i> <sub>79-401/81</sub> <sub>1-450</sub> SeMet
<b>Data collection</b>			
Wavelength (Å)	1.000 00	0.978 91	0.978 99
Resolution range (Å)	48.37 to 2.30 (2.38 to 2.30)	48.52 to 2.49 (2.57 to 2.49)	82.67 to 3.24 (3.37 to 3.24)
Space group	P 61 [169]	P 61 [169]	P 1 21 1 [4]
Unit cell (Å, °)	<i>a</i> = 55.84 <i>b</i> = 55.84 <i>c</i> = 263.43 $\alpha$ = 90 $\beta$ = 90 $\gamma$ = 120	<i>a</i> = 56.02 <i>b</i> = 56.02 <i>c</i> = 263.09 $\alpha$ = 90 $\beta$ = 90 $\gamma$ = 120	<i>a</i> = 68.56 <i>b</i> = 235.01 <i>c</i> = 116.50 $\alpha$ = 90 $\beta$ = 93.70 $\gamma$ = 90
Total reflections	205 477 (17 635)	321 430 (27 213)	2 195 989 (110 134)
Unique reflections	20 689 (1996)	16 300 (1558)	58 679 (5645)
Multiplicity	9.9 (8.8)	19.7 (17.5)	37.4 (19.5)
Completeness (%)	99.7 (96.7)	99.3 (96.1)	91.0 (88.0)
Mean I/ $\sigma$	16.7 (0.9)	18.5 (0.9)	15.8 (0.7)
R <sub>merge</sub>	0.102 (2.088)	0.111 (2.822)	0.21 (4.110)
CC1/2	0.999 (0.497)	0.998 (0.363)	1.000 (0.370)
<b>Refinement</b>			
Number of reflections	20 588	16 236	58 273
Protein residues	295	305	1637
Number of atoms	2311	2354	12 090
Protein	2208	2288	11 995
Ligands	67	58	33
Water (solvent)	36	8	62
R <sub>work</sub>	0.2690 (0.4716)	0.3007 (0.5127)	0.2869 (0.4559)
R <sub>free</sub>	0.2914 (0.4992)	0.2941 (0.5022)	0.3109 (0.4605)
Ramachandran favored (%)	95.5	94.39	96.53
Ramachandran outliers (%)	0.74	0.7	0.31
RMS bonds (Å)	0.01	0.00	0.00
RMS angles (°)	0.94	0.90	0.68
Average B-factors (Å <sup>2</sup> )	71.46	72.45	137.87

Statistics for the highest resolution shell are shown in parentheses.



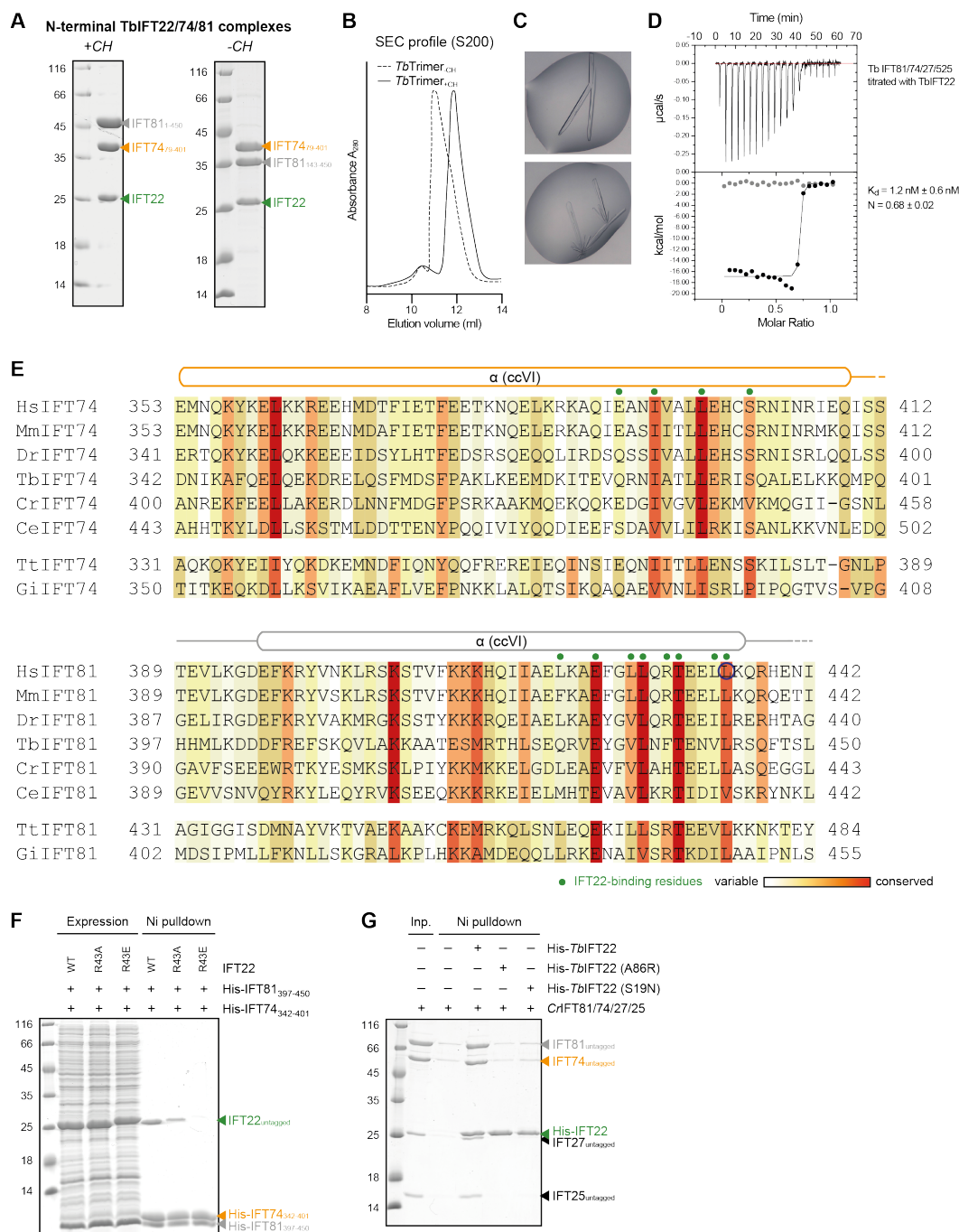
**Supplements, Figure 18: Multiple sequence alignment of IFT22 homologs**

Clustal Omega multiple sequence alignment of homologous IFT22 sequences from different organisms and the classical Rab GTPases Rab8A and Rab11A. Residue conservation is shown according to ConSurf grades (only for IFT22 sequences). Secondary structure elements from the GTP-*TbIFT22* crystal structure (green and yellow) are indicated above the sequence, as well as residues interacting with IFT74 (orange dots) and IFT81 (grey dots). Conserved sequence motifs of small GTPases are marked with blue boxes with consensus sequences inscribed below. Residues mutated in this study are circled. (*Hs* = *Homo sapiens*, *Mm* = *Mus musculus*, *Dr* = *Danio rerio*, *Tb* = *Trypanosoma brucei*, *Cr* = *Chlamydomonas reinhardtii* and *Ce* = *Caenorhabditis elegans*).



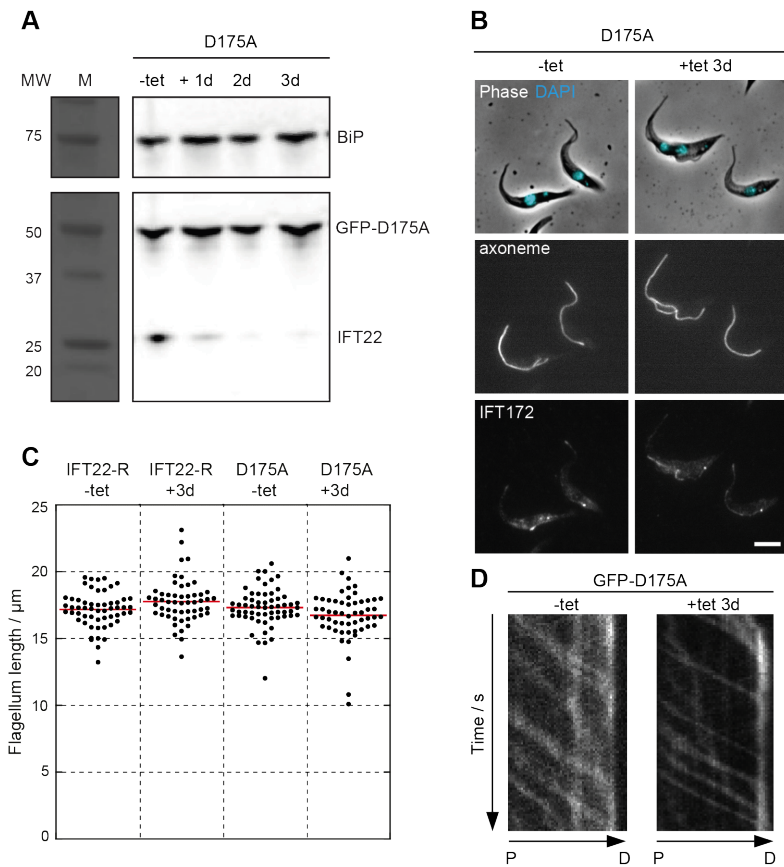
**Supplements, Figure 19: Additional IFT22 data**

**A.** SDS-PAGE gels of purified IFT22 from *T. brucei* and *M. musculus*. (FL = full-length) **B.** SEC profiles of *Tb* and *Mm*IFT22. **C.** HPLC nucleotide-elution profiles. Left: Nucleotide controls confirming resolution of different G-nucleotide hydrolysis states and showing their individual retention times. Right: Comparison of different procedures for nucleotide removal to obtain nucleotide-free IFT22. Only treatment with 8 M urea abolished bound GTP successfully. Same amounts of each nucleotide control or protein were injected (20  $\mu$ l, 100  $\mu$ M). **D.** *Tb*IFT22 crystallization. Needle-like clusters appeared 2 days after setup and turned into three-dimensional hexagonal crystals in the course of 10 days. Crystallization solution: 20 % (w/v) PEG3350, 50 mM NaCacodylate pH 6.5, 200 mM CaAcetate. **E.** GTPase activity assay for *Tb*IFT22 and the *Tb*IFT22/74/81 core complex. The release of inorganic Phosphate ( $P_i$ ) upon addition of 1 mM GTP to the proteins in buffer was followed for 20 min using an enzymatic reaction. As a negative control, hydrolysis of 1 mM GTP in buffer was monitored and subtracted from the protein curves for rate quantifications (left image). GTPase activity rates (*Tb*IFT22:  $1.7 \times 10^{-3} \text{ min}^{-1}$ ; *Tb*IFT22/74/81 core:  $4.7 \times 10^{-3} \text{ min}^{-1}$ ) were calculated based on a linear standard curve generated from different  $P_i$  concentrations (right image). **F.** Unbiased Fo-Fc electron density maps (green) of IFT22-bound nucleotides for structures solved in this study. IFT22 is shown in grey in cartoon representation in similar orientations for each structure, nucleotides are depicted as sticks and  $Mg^{2+}$  as a ball. Sigma levels and corresponding crystal structures are indicated on the images.



**Supplements, Figure 20: Additional IFT22/74/81 complex data**

**A.** SDS-PAGE gels of purified N-terminal *Tb*IFT22/74<sub>79-401</sub>/81<sub>x-450</sub> complexes with (left,  $x = 1$ ) and without (right,  $x = 143$ ) IFT81 CH domain. Only the complex with CH domain crystallized. **B.** SEC profiles of the *Tb*IFT22/74<sub>79-401</sub>/81<sub>1-450</sub> and *Tb*IFT22/74<sub>79-401</sub>/81<sub>143-450</sub> complex. **C.** *Tb*IFT22/74<sub>79-401</sub>/81<sub>1-450</sub> crystals. Selenomethionine derivative crystals diffracted best and were used for structure determination. Crystallization solution: 15% (v/v) glycerol, 7.5% (w/v) PEG4000, 100 mM HEPES pH 7.5. **D.** ITC experiment with purified *Tb*IFT25/27/74/81 titrated with *Tb*IFT22. Dissociation constant ( $K_d$ ) and standard deviation were calculated from three independent experiments. **E.** Clustal Omega multiple sequence alignment of the IFT22-binding region of homologous IFT74 and IFT81 sequences from different organisms. Residue conservation is shown according to ConSurf grades. Secondary structure elements from the IFT22/74/81 crystal structure are indicated above the sequence, as well as residues interacting with IFT22 (green dots). *Tt* and *Gi* are organisms lacking an IFT22 homolog. (*Hs* = *Homo sapiens*, *Mm* = *Mus musculus*, *Dr* = *Danio rerio*, *Tb* = *Trypanosoma brucei*, *Cr* = *Chlamydomonas reinhardtii* and *Ce* = *Caenorhabditis elegans*, *Tt* = *Tetrahymena thermophila*, *Gi* = *Giardia intestinalis*) **F.** SDS-PAGE gel of a Ni<sup>2+</sup>-NTA pulldown using His-tagged IFT74<sub>342-401</sub>/81<sub>397-450</sub> core complex peptides and untagged IFT22 (WT and mutants). Pulldowns were done from cell lysates of co-expressed proteins. Lanes 1-3 show similar total expression levels of the different co-expressed constructs (input samples). Lanes 4-6 show pulldown elutions. While IFT22 R43A still weakly binds to the IFT74/81 core complex, the R43E mutant fails to associate. (WT = wild type) **G.** SDS-PAGE gel of a chimeric Ni<sup>2+</sup>-NTA pulldown using His-tagged *Tb*IFT22 (WT and mutants) and untagged *Cr*IFT25/27/74/81. WT *Tb*IFT22 is able to pull down the *Cr* tetrameric complex, thus forming a chimeric IFT-B1 pentamer, while both the A86R and S19N mutant fail to bind the complex.



**Supplements, Figure 21: IFT22 D175A undergoes normal IFT and can rescue the absence of endogenous IFT22**

**A.** Western blot analysis of the *IFT22<sup>RNAi</sup>+GFP::IFT22R D175A* cell line probed with the anti-IFT22 antibody (bottom) and with an anti-BiP as loading control (top). **B.** IFA in the indicated conditions using the mAb25 (marker for the axoneme, middle panels) and an anti-IFT172 antibody (marker for IFT, bottom panels). The top panels show the phase contrast image merged with DAPI (cyan) that stains nuclear and mitochondrial DNA. **C.** Dot plot representation of flagellum length in the indicated cell lines and conditions. **D.** Kymographs showing the movement of the GFP::IFT22R D175A in the presence (left) or the absence (right) of the IFT22 endogenous protein. Note the improved signal-to-noise ratio in the latter case.



Paper

B

## **Phosphoproteomics reveals that Parkinson's disease kinase LRRK2 regulates a subset of Rab GTPases**

Martin Steger<sup>1</sup>, Francesca Tonelli<sup>2</sup>, Genta Ito<sup>2</sup>, Paul Davies<sup>2</sup>, Matthias Trost<sup>2</sup>, Melanie Vetter<sup>3</sup>, Stefanie Wachter<sup>3</sup>, Esben Lorentzen<sup>3</sup>, Graham Duddy<sup>4</sup>, Stephen Wilson<sup>5</sup>, Marco AS Baptista<sup>6</sup>, Brian K Fiske<sup>6</sup>, Matthew J Fell<sup>7</sup>, John A Morrow<sup>8</sup>, Alastair D Reith<sup>9</sup>, Dario R Alessi<sup>2</sup>, Matthias Mann<sup>1</sup>

<sup>1</sup>Department of Proteomics and Signal Transduction, Max Planck Institute of Biochemistry, Martinsried, Germany

<sup>2</sup>Medical Research Council Protein Phosphorylation and Ubiquitylation Unit, College of Life Sciences, University of Dundee, Dundee, United Kingdom

<sup>3</sup>Department of Structural Cell Biology, Max Planck Institute of Biochemistry, Martinsried, Germany

<sup>4</sup>Molecular Discovery Research, GlaxoSmithKline Pharmaceuticals R&D, Harlow, United Kingdom

<sup>5</sup>RD Platform Technology and Science, GlaxoSmithKline Pharmaceuticals R&D, Stevenage, United Kingdom

<sup>6</sup>The Michael J. Fox Foundation for Parkinson's Research, New York, United States

<sup>7</sup>Early Discovery Neuroscience, Merck Research Laboratories, Boston, United States

<sup>8</sup>Neuroscience, Merck Research Laboratories, Westpoint, United States

<sup>9</sup>Neurodegeneration Discovery Performance Unit, GlaxoSmithKline Pharmaceuticals R&D, Stevenage, United Kingdom



# Phosphoproteomics reveals that Parkinson's disease kinase LRRK2 regulates a subset of Rab GTPases

Martin Steger<sup>1</sup>, Francesca Tonelli<sup>2</sup>, Genta Ito<sup>2</sup>, Paul Davies<sup>2</sup>, Matthias Trost<sup>2</sup>, Melanie Vetter<sup>3</sup>, Stefanie Wachter<sup>3</sup>, Esben Lorentzen<sup>3</sup>, Graham Duddy<sup>4†</sup>, Stephen Wilson<sup>5</sup>, Marco AS Baptista<sup>6</sup>, Brian K Fiske<sup>6</sup>, Matthew J Fell<sup>7</sup>, John A Morrow<sup>8</sup>, Alastair D Reith<sup>9</sup>, Dario R Alessi<sup>2\*</sup>, Matthias Mann<sup>1\*</sup>

<sup>1</sup>Department of Proteomics and Signal Transduction, Max Planck Institute of Biochemistry, Martinsried, Germany; <sup>2</sup>Medical Research Council Protein Phosphorylation and Ubiquitylation Unit, College of Life Sciences, University of Dundee, Dundee, United Kingdom; <sup>3</sup>Department of Structural Cell Biology, Max Planck Institute of Biochemistry, Martinsried, Germany; <sup>4</sup>Molecular Discovery Research, GlaxoSmithKline Pharmaceuticals R&D, Harlow, United Kingdom; <sup>5</sup>RD Platform Technology and Science, GlaxoSmithKline Pharmaceuticals R&D, Stevenage, United Kingdom; <sup>6</sup>The Michael J. Fox Foundation for Parkinson's Research, New York, United States; <sup>7</sup>Early Discovery Neuroscience, Merck Research Laboratories, Boston, United States; <sup>8</sup>Neuroscience, Merck Research Laboratories, Westpoint, United States; <sup>9</sup>Neurodegeneration Discovery Performance Unit, GlaxoSmithKline Pharmaceuticals R&D, Stevenage, United Kingdom

\*For correspondence: d.r.alessi@dundee.ac.uk (DRA); mmann@biochem.mpg.de (MM)

Present address: <sup>†</sup>The Wellcome Trust Sanger Institute, Hinxton, United Kingdom

Competing interest: See page 23

Funding: See page 23

Received: 03 November 2015

Accepted: 21 January 2016

Published: 29 January 2016

Reviewing editor: Ivan Dikic, Goethe University Medical School, Germany

© Copyright Steger et al. This article is distributed under the terms of the [Creative Commons Attribution License](#), which permits unrestricted use and redistribution provided that the original author and source are credited.

**Abstract** Mutations in Park8, encoding for the multidomain Leucine-rich repeat kinase 2 (LRRK2) protein, comprise the predominant genetic cause of Parkinson's disease (PD). G2019S, the most common amino acid substitution activates the kinase two- to threefold. This has motivated the development of LRRK2 kinase inhibitors; however, poor consensus on physiological LRRK2 substrates has hampered clinical development of such therapeutics. We employ a combination of phosphoproteomics, genetics, and pharmacology to unambiguously identify a subset of Rab GTPases as key LRRK2 substrates. LRRK2 directly phosphorylates these both in vivo and in vitro on an evolutionary conserved residue in the switch II domain. Pathogenic LRRK2 variants mapping to different functional domains increase phosphorylation of Rabs and this strongly decreases their affinity to regulatory proteins including Rab GDP dissociation inhibitors (GDIs). Our findings uncover a key class of bona-fide LRRK2 substrates and a novel regulatory mechanism of Rabs that connects them to PD.

DOI: [10.7554/eLife.12813.001](https://doi.org/10.7554/eLife.12813.001)

## Introduction

Parkinson's disease (PD) is the second most common neurodegenerative disease, affecting 1–2% of the elderly population (Lees et al., 2009). Environmental and genetic factors contribute to the development of the disease, but its precise etiology still remains elusive (Burbulla and Krüger, 2011). Genome-wide association studies (GWAS) have related 28 genetic risk variants at 24 loci with nonfamilial PD (Nalls et al., 2014). Among those, mutations in LRRK2 (Park8) are also found in hereditary forms, pinpointing a shared molecular pathway driving pathogenesis in both familial and non-familial PD and comprising the most common cause of the disease (Simón-Sánchez et al.,

**eLife digest** Parkinson's disease is a degenerative disorder of the nervous system that affects approximately 1% of the elderly population. Mutations in the gene that encodes an enzyme known as LRRK2 are the most common causes of the inherited form of the disease. Such mutations generally increase the activity of LRRK2 and so drug companies have developed drugs that inhibit LRRK2 to prevent or delay the progression of Parkinson's disease. However, it was not known what role LRRK2 plays in cells, and why its over-activation is harmful.

Steger et al. used a 'proteomics' approach to find other proteins that are regulated by LRRK2. The experiments tested a set of newly developed LRRK2 inhibitors in cells and brain tissue from mice. The mice had mutations in the gene encoding LRRK2 that are often found in human patients with Parkinson's disease. The experiments show that LRRK2 targets some proteins belonging to the Rab GTPase family, which are involved in transporting molecules and other 'cargoes' around cells. Several Rab GTPases are less active in the mutant mice, which interferes with the ability of these proteins to correctly direct the movement of cargo around the cell.

Steger et al.'s findings will help to advance the development of new therapies for Parkinson's disease. The next challenges are to identify how altering the activity of Rab GTPases leads to degeneration of the nervous system and how LRRK2 inhibitors may slow down these processes.

DOI: [10.7554/eLife.12813.002](https://doi.org/10.7554/eLife.12813.002)

**2009; Satake et al., 2009**). LRRK2 encodes a large protein composed of central kinase and GTPase (ROC-COR) domains that are surrounded by multiple protein-protein interaction regions. PD pathogenic LRRK2 mutations map predominantly to the kinase (G2019S, I2020T) and the ROC-COR domains (R1441C/G/H, Y1699C), implying that these enzymatic activities are crucial for pathogenesis (**Rudenko and Cookson, 2014**). Presently, it is unclear how LRRK2 mutations occurring in different functional domains all predispose to PD. The most common PD-associated LRRK2 mutation is the G2019S amino acid substitution, which activates the kinase two- to threefold (**West et al., 2005; Khan, 2005; Jaleel et al., 2007**). Since protein kinases are attractive pharmacological targets, this finding has raised hopes that selective LRRK2 inhibition can prevent or delay the onset of PD (**Yao et al., 2013**).

Extensive studies of LRRK2 have associated it with diverse cellular processes such as Wnt signaling, mitochondrial disease, cytoskeleton remodeling, vesicular trafficking, autophagy, and protein translation (**Taymans et al., 2015; Cookson, 2015; Schapansky et al., 2014; Papkovskaia et al., 2012**). Moreover, several LRRK2 substrates have been reported previously; however, evidence that they are phosphorylated by LRRK2 in a physiological context is generally lacking and proofs are confined to in vitro approaches or to cellular systems using overexpressed kinase (**Jaleel et al., 2007; Kumar et al., 2010; Ohta et al., 2011; Kawakami et al., 2012; Bailey et al., 2013; Martin et al., 2014; Qing et al., 2009; Chen et al., 2012; Gloeckner et al., 2009; Imai et al., 2008; Gillardon, 2009; Kanao et al., 2010; Matta et al., 2012; Xiong et al., 2012; Yun et al., 2013; Yun et al., 2015; Krumova et al., 2015**). Significant off-target effects for LRRK2 compounds that have been used previously further complicate interpretation of the data (**Schapansky et al., 2015**). Overall, there is little consensus on the cellular roles of LRRK2; thus, identification of definitive and verifiable physiological LRRK2 substrates is considered to be one of the greatest challenges in the field (**Schapansky et al., 2015**).

Besides mutations in LRRK2, other genetic risk variants for PD map to the Park16 locus. Among the five genes within this locus is Rab7L1 (also known as Rab29), which together with LRRK2 increases nonfamilial PD risk. Depletion of Rab7L1 recapitulates the dopaminergic neuron loss observed with LRRK2-G2019S expression and its overexpression rescues mutant LRRK2 phenotypes (**MacLeod et al., 2013**). Rab GTPases comprise ~70 family members in humans, and they are key players in all forms of intracellular vesicular trafficking events (**Stenmark, 2009; Rivero-Rios et al., 2015**). Apart from Rab7L1, several other family members have been associated with PD pathogenesis. For example, mutations in Rab39b (Park21 locus) predispose to PD in humans (**Wilson et al., 2014; Mata et al., 2015**). Moreover, overexpression of Rab8a, Rab1, and Rab3a attenuate  $\alpha$ -synuclein-induced cytotoxicity in cellular and animal models of PD, suggesting a functional interplay

between Rab GTPases and known PD factors (Cooper, 2006; Gitler et al., 2008). Recently, another PD-connected protein kinase termed PTEN-Induce Kinase-1 (PINK1) has been reported to indirectly control the phosphorylation of a small group of Rabs including Rab8a at Ser111 (Lai et al., 2015). Despite these intriguing links, it is presently unclear whether LRRK2 directly or indirectly modulates Rab GTPases at the molecular level and if so, by which mechanism.

High-resolution quantitative mass spectrometry (MS) has become the method of choice for confident identification of in vitro and in vivo phosphorylation events (Roux and Thibault, 2013; Lemeer and Heck, 2009; Olsen et al., 2006). With current MS instrumentation, proteomics can identify tens of thousands of phosphosites (Sharma et al., 2014; Mallick and Kuster, 2010). However, challenges in the phosphoproteomic approaches are to determine functionally relevant residues from these large datasets and to establish direct kinase-substrate relationships.

As such, we complement the power of modern phosphoproteomics with parallel genetic, biochemical and pharmacological approaches to establish direct, in vivo LRRK2 substrates. Using fibroblasts derived from two different LRRK2 knock-in mouse lines we identify a subset of Rab GTPases as bona-fide LRRK2 targets. LRRK2 phosphorylates these substrates on an evolutionarily conserved residue situated in their switch II domain both in human and murine cells and in mouse brain. The phosphorylation of Rabs by LRRK2 is direct and strikingly all LRRK2 missense mutations that contribute to PD pathogenesis increase the phosphorylation of at least three Rab GTPases. Further, we establish that different PD pathogenic mutations modulate the interaction with a number of regulatory proteins including guanine dissociation inhibitors (GDI1/2). In this way, LRRK2 regulates the specific insertion of Rab GTPases into target membranes thereby altering their membrane-cytosol equilibrium.

## Results

### Identification of LRRK2 substrates in mouse embryonic fibroblasts (MEFs)

To search for bona-fide physiological LRRK2 substrates, we performed a dual-phosphoproteomic screening approach using knock-in lines harboring either hyperactive LRRK2 or a LRRK2 variant with wild-type activity but insensitive to a highly selective, newly developed LRRK2 compound. For our first screen (PS1), we generated a mouse model harboring the LRRK2-G2019S substitution that increases kinase activity two- to threefold (Figure 1B). We derived fibroblasts from these animals and treated them with two structurally different LRRK2 inhibitors, GSK2578215A (Reith et al., 2012) or HG-10-102-01 (Choi et al., 2012) (Figure 1A and Figure 1—figure supplement 1A). This screening modality offers three major advantages; first, increased activity of the G2019S-LRRK2 kinase amplifies the chance of finding bona-fide substrates, second, using an isogenic system excludes that measured phosphoproteome changes are due to differences in the genetic background and third, considering only the overlapping population of significantly modulated phosphopeptides of two structurally distinct inhibitors constitutes a very stringent criterion for specifically pinpointing LRRK2 substrates.

The second screen (PS2) added another layer of specificity by combining phosphoproteomics with genetics and chemical biology. For this, we used fibroblasts derived from either wt or A2016T-LRRK2 knock-in mice and treated them with the newly developed, highly potent and selective LRRK2 compound MLI-2 (Fell et al., 2015). The A2016T substitution does not change basal LRRK2 activity but decreases sensitivity to MLI-2 ~10-fold (Figure 1C,D and Figure 1—figure supplement 1B). At a dose of 10 nM, we observed a substantial decrease in phosphorylation of LRRK2-pS935, which is associated with LRRK2 kinase activity (Dzamko et al., 2010), in wt but not in A2016T cells (Figure 1E and Figure 1—figure supplement 1C). Under these conditions, the phosphoproteome of wt MEFs includes both LRRK2-specific and off-target sites, whereas A2016T (which is resistant to MLI-2) only includes off-targets. Therefore, direct quantitative comparison should reveal true LRRK2 substrates (Figure 1C).

Using a state-of-the-art workflow for phosphopeptide enrichment, label-free LC-MS/MS and the MaxQuant environment for stringent statistical data evaluation (Humphrey et al., 2015; Cox and Mann, 2008; Cox et al., 2011), we quantified over 9000 high-confidence phosphosites in each replicate in both screens (median R=0.80 and 0.89 in PS1 and PS2, respectively), (Figure 1—figure

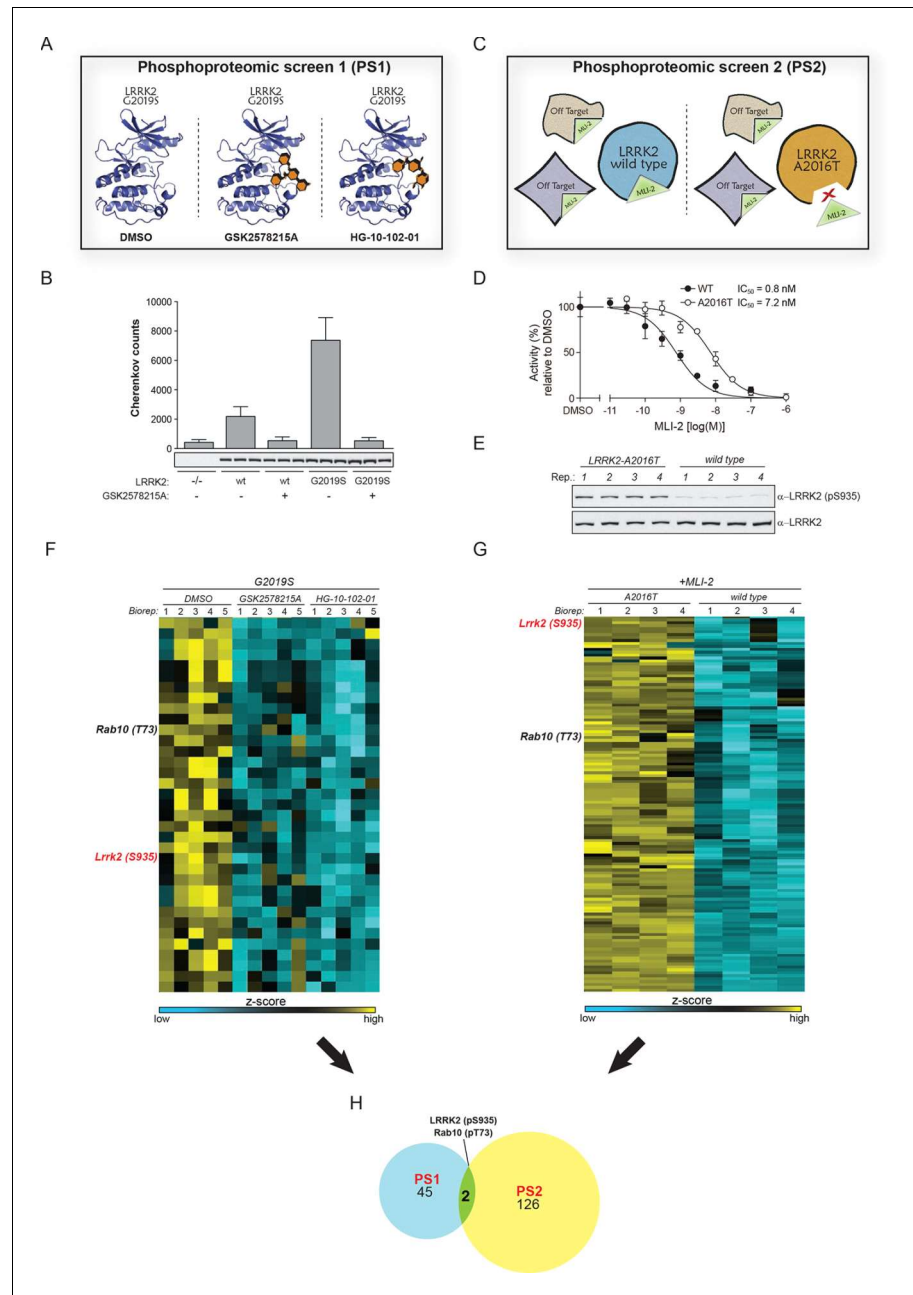


**Figure 1.** Two unbiased phosphoproteomic screens identify physiological LRRK2 targets. (A) Experimental setup of PS1. LRRK2-G2019S<sup>GSK</sup> mouse embryonic fibroblasts (MEFs, n=5) were treated with DMSO or each of two structurally distinct LRRK2 inhibitors GSK2578215A or HG-10-102-01 (1  $\mu$ M for 90 min). (B) LRRK2 immunoprecipitated from either knockout (-/-), wild-type (wt) or LRRK2-G2019S<sup>GSK</sup> (G2019S) knock-in MEFs was assessed for phosphorylation of Nictide (*Nichols et al., 2009*) peptide substrate in absence or presence of GSK2578215A (2  $\mu$ M). Western blot below shows that similar levels of LRRK2 were immunoprecipitated. Error bars are mean  $\pm$  SD (n=3). (C) Scheme of PS2. The higher affinity of MLI-2 toward wt-LRRK2 allows specific pinpointing of LRRK2 substrates when comparing the phosphoproteomes of wt and A2016T MEFs. (D) Kinase activities of wt (closed circles) and A2016T (open circles) GST-LRRK2 [1326-2527] purified from HEK293 cells were assayed in the presence of the indicated concentration of MLI-2 (n=3). (E) Decreased levels of pS935-LRRK2 in wt MEFs after *Figure 1 continued on next page*

Figure 1 continued

treatment with 10 nM MLI-2. (F) Heat map cluster of phosphopeptides in PS1 ( $p < 0.005$ ) which are downregulated after treatment with both GSK2578215A and HG-10-102-01. (G) Heat map cluster of downregulated (FDR=0.01,  $S_0=0.2$ ) phosphopeptides in PS2. (H) Venn diagram of overlapping downregulated phosphosites in PS1 and PS2. (Biorep= biological replicate). SD, standard deviation.

DOI: [10.7554/eLife.12813.003](https://doi.org/10.7554/eLife.12813.003)

The following figure supplements are available for figure 1:

**Figure supplement 1.** Two unbiased phosphoproteomic screens identify physiological LRRK2 targets.

DOI: [10.7554/eLife.12813.004](https://doi.org/10.7554/eLife.12813.004)

**Figure supplement 2.** Two unbiased phosphoproteomic screens identify physiological LRRK2 targets.

DOI: [10.7554/eLife.12813.005](https://doi.org/10.7554/eLife.12813.005)

**supplement 1D–G and Supplementary file 1).** Independently acquired proteome measurements verified that the detected phosphorylation changes in PS2 were not due to altered protein abundances (changes as determined by label-free quantification in MaxQuant (Cox et al., 2014) were less than twofold [Supplementary file 2]).

Next, we determined how many of the identified sites were significantly and robustly modulated. As we were interested in capturing the most strongly regulated sites, we required that the fold change had to be at least as strong as pS935-LRRK2. In PS1, we thus found 234 significantly regulated sites after treatment with each of the two LRRK2 compounds GSK2578215A and HG-10-102-01 (ANOVA,  $p < 0.005$ ), with 78 sites regulated by both (Figure 1—figure supplement 2A). Hierarchical clustering divided them into several subgroups (Figure 1—figure supplement 2B–C and Supplementary file 3A). Besides revealing potential off-target sites of the two LRRK2 inhibitors, this identified a particularly interesting cluster containing 47 sites that were downregulated after treatment with both compounds (Figure 1—figure supplement 2C, cluster 5).

In PS2, we identified 204 significantly regulated sites (two sample t-test, FDR=0.01,  $S_0=0.3$ ), when comparing wild-type and inhibitor-resistant LRRK2 fibroblasts, with 128 sites specifically downregulated in the wild type, thus excluding off-target effects (Figure 1G, Figure 1—figure supplement 2D and Supplementary file 3B).

Finally, to stringently define LRRK2 substrates, we overlapped the results of the two orthogonal screens. Remarkably, only two phosphosites passed these stringent filtering criteria, our positive control pS935-LRRK2 and the conserved T73 residue of the small GTPase Rab10 (Figure 1H).

## Direct in vitro phosphorylation of Rab isoforms by LRRK2

Rab10 belongs to the Ras family of small GTPases that regulate intracellular vesicular transport, with ~70 members in human. They function as molecular switches in the tethering, docking, fusion, and motion of intracellular membranes (Stenmark, 2009; Wandinger-Ness and Zerial, 2014). The T73 residue of Rab10 is located in the switch II domain, which is characteristic of Rab GTPases (Figure 2A). This region changes conformation upon nucleotide binding and regulates the interaction with multiple regulatory proteins (Pfeffer, 2005). Sequence alignment revealed that the equivalent site to T73-Rab10 is highly conserved in more than 40 human Rab-family members, indicating strong functional relevance (Figure 2B). Moreover, superposing the crystal structures of multiple Rab GTPases localizes the equivalent residues to T73-Rab10 in nearly the same position (Figure 2—figure supplement 1A). To investigate whether the phosphorylation of Rab10 by LRRK2 is direct, we performed an in vitro kinase assay using recombinant components. Notably, we found that both wt and LRRK2-G2019S, but neither kinase inactive D1994A mutant nor small molecule-inhibited LRRK2, efficiently phosphorylated Rab10, proving a direct kinase-substrate relationship (Figure 2C). Furthermore, incubation of Rab10 with LRRK2 followed by tryptic digestion and MS analysis unambiguously identified T73 as the major phosphorylation site (Figure 2—figure supplement 1B). Given the high conservation of T73-Rab10, we investigated whether other Rab GTPases were also phosphorylated by LRRK2 in vitro. Therefore, we first measured LRRK2-mediated phosphorylation of Rab8a, Rab1a, and Rab1b, all of which contain a Thr at the site equivalent to T73-Rab10, by MS or  $^{32}\text{P}$  incorporation followed by Edman sequencing. Remarkably, all proteins were rapidly phosphorylated on the predicted LRRK2 phosphorylation site in the switch II domain (Figure 2D–F and Figure 2—figure supplement 1C–E). Next, we compared Rab family members containing Thr sites in



Figure 2 continued

The following figure supplement is available for figure 2:

**Figure supplement 1.** Phosphorylation of Rab GTPases by LRRK2 in vitro.

DOI: [10.7554/eLife.12813.007](https://doi.org/10.7554/eLife.12813.007)

the switch II region with those containing a Ser in the equivalent position. Interestingly, while Rabs with threonines (Rab1b, Rab8a, and Rab10) were efficiently phosphorylated, those with the equivalent serine sites (Rab5b, Rab7a, Rab7L1, Rab12, and Rab39b) were phosphorylated to a drastically lower extent (**Figure 2G**). This confirms the previously reported in vitro preference for threonines by LRRK2 (**Nichols et al., 2009**). Finally, we performed a side by side comparison of the phosphorylation efficiencies of recombinant Rab8a and Rab7L1 against two previously reported substrates, moesin (Msn) and Rps15 (**Jaleel et al., 2007; Martin et al., 2014**). Msn is a cytoskeletal protein and a well-known in vitro LRRK2 substrate, whereas Rps15 is part of the 40S ribosomal subunit and its phosphorylation on Thr136 has been reported to regulate protein translation in *D. melanogaster* (**Martin et al., 2014**). In accordance with our previous observations (**Figure 2G**), phosphorylation levels of RAB7L1 were barely detectable, and even lower than those of Msn and Rps15. Strikingly, levels of pRab8a were about ten times higher as compared to Rps15 and Msn, two of the best in vitro LRRK2 substrates known to date, demonstrating that Rabs with Thr sites in the switch II domain are primary LRRK2 targets (**Figure 2H,I**).

### A subset of Rabs are physiological LRRK2 substrates

Because of the high conservation of T73-Rab10 (**Figure 2B**) and the ability of LRRK2 to phosphorylate multiple Rabs in vitro, we inspected our quantitative MS data further to determine whether all sequence and structurally equivalent sites are targets of LRRK2. This turned out not to be the case as pS72-Rab7a was not regulated in either of our screens. LRRK2 thus phosphorylates only a subset of Rab GTPases in mouse fibroblasts. Surprisingly, we noticed that pS105-Rab12, which is not phosphorylated by LRRK2 in vitro (**Figure 2G**), was among the significantly modulated sites in PS1 and also downregulated upon MLI-2 treatment in wt cells as compared to the inhibitor-resistant A2016T mutant in PS2 (**Figure 3A,B**). However, because of elevated intergroup variability and stringent FDR cut-offs, it was not selected in our first analysis. LRRK2 is found also in lower eukaryotes such as *C. elegans* and *D. melanogaster* (**Liu et al., 2011**) and T73-Rab10 is conserved in these organisms as well. Also, S105-Rab12 is present throughout the vertebrates (**Figure 3A,B**). We identified both pT73-Rab10 and pS105-Rab12 multiple times with high identification and phosphosite localization scores (**Supplementary file 1**) and the MS/MS fragmentation spectra of the corresponding synthetic peptides independently validated the MS results (**Figure 3—figure supplement 1A,B**). Total protein levels of Rab10 and Rab12 did not change appreciably in the A2016T knock-in model as judged by quantitative MS analysis, ruling out that the observed phospho-level changes are due to differential protein expression (**Figure 3—figure supplement 2A**).

To extend the analysis of LRRK2-mediated phosphorylation of Rab10, we used human embryonic kidney cells harboring doxycycline-dependent gene expression of LRRK2-G2019S (HEK293-t-rex-flpIn). Expression of the kinase, treatment with either GSK2578215A or HG-10-102-01 and enrichment of Rab10 by immunoprecipitation followed by quantitative MS analysis confirmed a strong, LRRK2-dependent decrease of pT73-Rab10 peptide levels (**Figure 3—figure supplement 2B**). Polyclonal antibodies recognizing pT73-Rab10 and pS106-Rab12 (note that the equivalent site is S105 in mouse) independently verified LRRK2-dependent phosphorylation of both Rab isoforms in HEK293 cells (**Figure 3C,D**).

Next, we evaluated whether more Rab isoforms can be phosphorylated in a LRRK2-dependent manner in human cells, focusing on Rab1a, Rab3a, and Rab8a, all of which contain Thr as predicted LRRK2 phosphorylation site (**Figure 2B**). Therefore, we first ectopically expressed LRRK2 along with either Rab1a or Rab3a, in presence or absence of HG-10-102-01 and quantified pT75-Rab1a and pT86-Rab3a peptide levels by MS. Whereas T86-Rab3a is clearly a LRRK2 target, Rab1a is not, indicating that overexpression of LRRK2 is not sufficient to phosphorylate all Rabs in cells (**Figure 3—figure supplement 2C,D**). Next, we inhibited LRRK2 in HEK293-t-rex-flpIn cells expressing LRRK2-G2019S and quantified pT72-Rab8. Again, we found a strong decrease of pT72 peptide levels upon

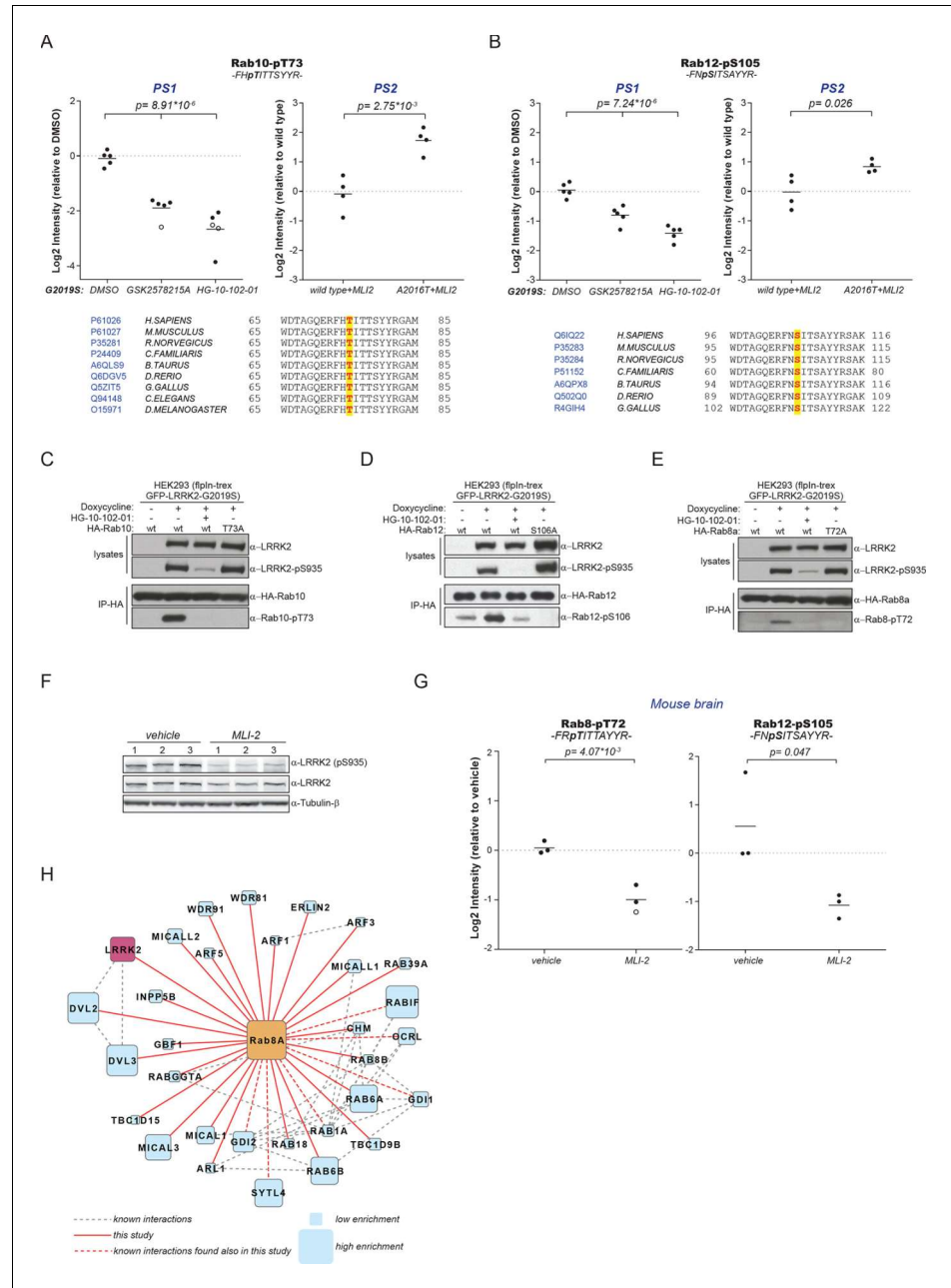


**Figure 3.** A number of Rab GTPases are physiological LRRK2 substrates. (A) MS-quantified pT73-Rab10 peptide intensities in PS1 and PS2. Sequence alignment of the T73-Rab10 region is shown below. (B) Same as (A) with pS106-Rab12. Western blots illustrating phosphorylation of T73-HA-Rab10 (C), S106-HA-Rab12 (D), and T72-Rab8 (E) after induction of LRRK2 expression by doxycycline (1 μg/ml). HG-10-102-01 (1 μM) was added prior to lysis. (F) Western blot of homogenized brain lysates from LRRK2-G2019S<sup>Lilly</sup> mice injected with vehicle (40% HPβCD) or with 3 mg/kg MLI-2 (Biorep= biological replicate) and (G) MS-based quantification of pT72-Rab8 and pS105-Rab12 peptides. (H) Cytoscape network analysis of Rab8a interacting proteins determined by affinity-purification mass spectrometry (AP-MS). LRRK2 is in purple and dashed lines in grey show experimentally determined interactions from string database (<http://string-db.org/>).

DOI: 10.7554/eLife.12813.008

Figure 3 continued on next page

Figure 3 continued

The following figure supplements are available for figure 3:

**Figure supplement 1.** HCD MS/MS spectra of synthetic Rab peptides

DOI: [10.7554/eLife.12813.009](https://doi.org/10.7554/eLife.12813.009)

**Figure supplement 2.** Quantification of Rab phosphorylation by mass spectrometry (MS).

DOI: [10.7554/eLife.12813.010](https://doi.org/10.7554/eLife.12813.010)

**Figure supplement 3.** Several Rabs stably associate with LRRK2 in cells.

DOI: [10.7554/eLife.12813.011](https://doi.org/10.7554/eLife.12813.011)

LRRK2 inhibition with both GSK2578215A and HG-10-102-01 (**Figure 3—figure supplement 2E**). An antibody raised for specific detection for pT72-Rab8 confirmed these results further (**Figure 2E**).

To analyze LRRK2-dependent phosphorylation of Rabs in an endogenous context, we quantified pT72-Rab8 and pT73-Rab10 peptide levels in MEFs derived from LRRK2 knockout, wt, or G2019S<sup>GSK</sup> animals. In the knock-out, the decrease was only about twofold compared to wt, implying a very low intrinsic LRRK2 activity in cells. Consistent with the two- to threefold increased in vitro activity of MEFs-extracted LRRK2-G2019S<sup>GSK</sup> (**Figure 1B**), our quantitative MS analysis revealed a threefold increase in both pT72-Rab8 and pT73-Rab10, which was restored to near wt levels by selective LRRK2 kinase inhibition (**Figure 3—figure supplement 2F–I**). Finally, we globally measured the brain phosphoproteome of LRRK2-G2019S<sup>Lilly</sup> mice injected with vehicle (40% HPβCD) or with MLI-2 (3 mg/kg). Levels of pT72-Rab8 and pS105-Rab12 were decreased more than twofold upon LRRK2 inhibition, validating our findings in the context of a LRRK2 pathogenic mouse model (**Figure 3F,G**).

Having identified Rabs as physiological substrates of LRRK2, we next asked if kinase and substrate also stably interact. Indeed, affinity-purification mass-spectrometry (AP-MS) showed that transiently expressed epitope-tagged LRRK2 and Rab8a efficiently associated with each other, demonstrating that LRRK2 is able to form stable complexes with Rab GTPases in cells (**Figure 3H** and **Figure 3—figure supplement 3A,B**). Similarly, Rab10 as well as Rab12 associate with LRRK2 when transiently overexpressed in HEK293 cells (**Figure 3—figure supplement 3C–E**).

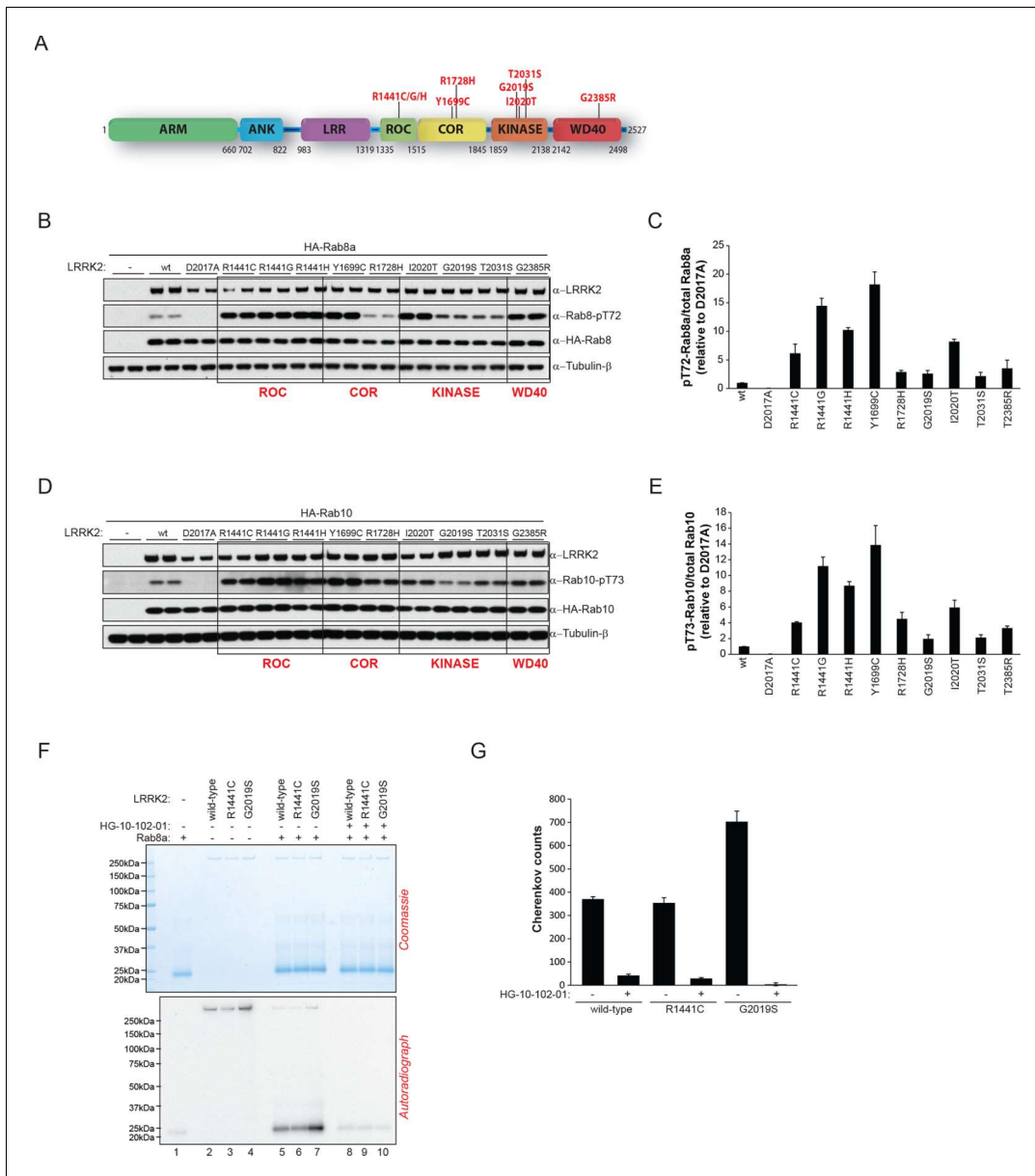
### Parkinson's disease-associated pathogenic mutations modulate Rab GTPase phosphorylation levels

Pathogenic PD LRRK2 mutations predominantly map to the kinase and the ROC-COR (GTPase) domains and a PD risk factor coding mutation is also found in the WD-40 domain (**Martin et al., 2014; Farrer et al., 2007**) (**Figure 4A**). Because it is presently unclear how mutations occurring in distinct LRRK2 functional domains lead to similar disease phenotypes, we decided to investigate if different LRRK2 pathogenic mutations might impact on the phosphorylation status of Rab GTPases. For this, we expressed different disease causing LRRK2 variants along with either Rab8a or Rab10 in HEK293 cells. This revealed that besides PD-associated mutations located in the kinase domain that augment LRRK2 kinase activity, those occurring in the GTPase (ROC-COR) or the WD-40 domains also increased pT72-Rab8a and pT73-Rab10 levels in cells (**Figure 4B–E**).

To determine whether this interplay between different functional domains was direct, we next tested whether pathogenic LRRK2 mutations which lie outside the kinase domain also increase Rab phosphorylation in vitro. As expected, compared to wt, the G2019S mutation resulted in a two- to threefold increase in Rab8a phosphorylation. However, the ROC-COR domain R1441C mutation failed to do so, which is consistent with previous data suggesting that these mutations do not directly enhance LRRK2 kinase activity (**Nichols et al., 2010**), indicating that its effect on Rab8a phosphorylation levels is mediated by accessory factors in cells (**Figure 4F,G**).

### LRRK2 controls the interaction of Rabs with regulatory proteins

Rab GTPases consist of a similar core structure comprising highly conserved P-loop, switch I and switch II regions (**Pfeffer, 2005**). They cycle between the cytosol, in which they are GDP bound and inactive and specific membrane compartments, where they are activated by GDP/GTP exchange (**Hutagalung and Novick, 2011**). In the crystal structure of Rab8a (**Guo et al., 2013**), the LRRK2-mediated phosphorylation site is in the switch II region (**Figure 2A**), which regulates hydrolysis of GTP and coordinates the binding to various regulatory proteins (**Pfeffer, 2005**). We therefore tested



whether the phosphomimetic T72E substitution would modulate GDP/GTP binding or interfere with Rab8a protein interactions. Binding affinities of wt and the TE mutant, determined with fluorescently labeled (N-Methylanthraniloyl, mant) GDP and non-hydrolysable GTP analogue GMPPNP, did not differ (Figure 5—figure supplement 1). In contrast, AP-MS revealed that a number of proteins preferentially bind to non-phosphorylatable T72A-Rab8a compared to the T72E

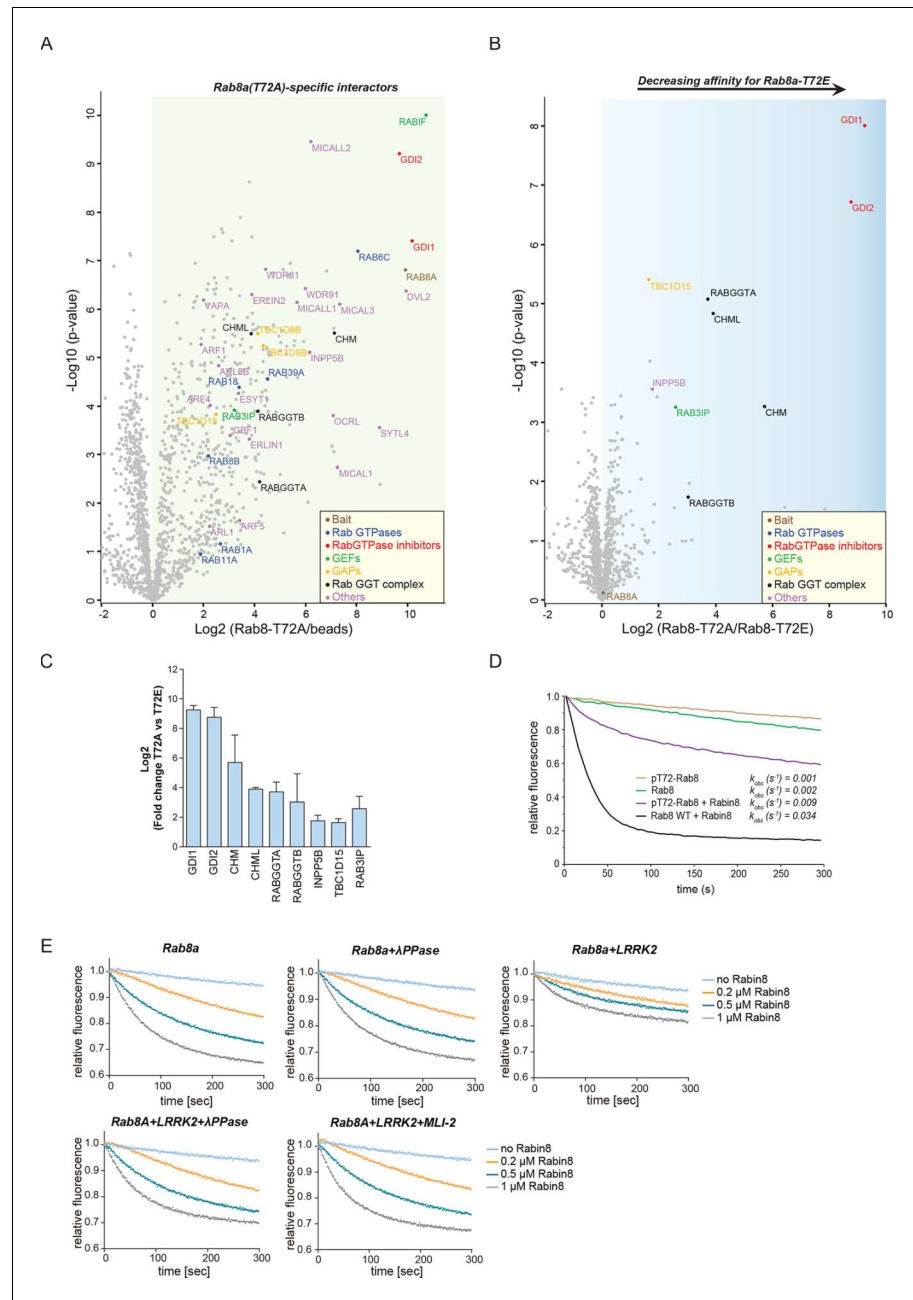


**Figure 5.** LRRK2 controls the interaction of Rabs with regulatory proteins. (A) Volcano plots showing interactors of GFP-Rab8a (T72A) transiently expressed in HEK293 cells and (B) Proteins differentially binding to T72A as compared to T72E. (C) Fold changes (T72A/T72E, n=4) of regulated proteins shown in (B). (D) Kinetic measurements of the dissociation of mant-GDP from non-phosphorylated and T72 phosphorylated Rab8a by Rabin8. Observed rate constants ( $k_{obs}$ ) are indicated for each reaction and data points represent mean (n=3). (E) Measurements of mant-GDP dissociation from LRRK2 phosphorylated Rab8a by Rabin8 in absence or presence of  $\lambda$ -phosphatase ( $\lambda$ -PPase) or MLI-2 (1  $\mu$ M). Error bars are mean  $\pm$  SD of replicates. DOI: 10.7554/eLife.12813.013

The following figure supplements are available for figure 5:

Figure 5 continued on next page

Figure 5 continued

**Figure supplement 1.** Rab8a nucleotide binding experiments.DOI: [10.7554/eLife.12813.014](https://doi.org/10.7554/eLife.12813.014)**Figure supplement 2.** Rab8a guanine nucleotide exchange assays.DOI: [10.7554/eLife.12813.015](https://doi.org/10.7554/eLife.12813.015)

phosphomimetic protein (**Figure 5A,B**). These were Rab GDP dissociation inhibitors  $\alpha$  and  $\beta$  (GDI1 and GDI2), Rab geranyltransferase complex members (CHM, CHML, and RabGGTA/RabGGTB), the Rab8a guanine nucleotide exchange factor (GEF) Rabin8 (Rab3IP), a guanine nucleotide activating protein TBC1D15 and the inositol phosphatase INPP5B (**Figure 5C**).

Rabin8 interacts with membrane-bound Rab8a and activates it by catalyzing the exchange of GDP to GTP (**Westlake et al., 2011**). This in turn triggers retention of Rab effector proteins that mediate downstream vesicular trafficking events. Rabin8 binds to the switch II domain of Rab8a and contacts the conserved, phosphorylatable T72 residue (**Figure 5—figure supplement 2A**) (**Guo et al., 2013**). We found that compared to wt, the T72E phosphomimetic substitution decreased the level of Rabin8-catalyzed mant-GDP displacement from a Rab8-GDP complex (**Figure 5—figure supplement 2B–D**). To further substantiate this finding, we phosphorylated purified Rab8a using LRRK2, which resulted in ~60% of T72-phosphorylated protein as determined by total protein MS and LC-MS/MS after tryptic digestion (**Figure 5—figure supplement 2E,F**). Further enrichment by ion-exchange chromatography yielded a highly enriched (~100%) fraction of pT72-Rab8a (**Figure 5—figure supplement 2E**). Loading of non-phosphorylated and phosphorylated Rab8a with mant-GDP following incubation with Rabin8 revealed that LRRK2-induced phosphorylation of T72-Rab8a inhibits rates of Rabin8-catalyzed GDP exchange fourfold and decreases Rab8a-Rabin8 interaction (**Figures 5D** and **Figure 5—figure supplement 2G**). Both  $\lambda$ -phosphatase treatment of LRRK2-phosphorylated Rab8a and pharmacological inhibition of LRRK2 prevented the decreased GEF activity of Rabin8 toward pT72-Rab8a (**Figure 5E** and **Figure 5—figure supplement 2H**). Thus, phosphorylation of Rab8a by LRRK2 can limit its activation by Rabin8.

### PD pathogenic LRRK2 mutations interfere with Rab-GDI1/2 association

GDI1 and GDI2, along with CHM and CHML (also known as Rab escorting proteins REP1 and REP2) form the GDI superfamily and are essential regulators of the Rab cycle. GDIs extract inactive, prenylated Rabs from membranes and bind them with high affinity in the cytosol (**Pylypenko et al., 2003**). The regulatory mechanism by which Rabs are displaced from GDIs to facilitate their insertion into specific target membranes is unknown. The co-crystal structure of GDI1 with the yeast Rab homologue Ypt1 shows that GDIs closely contact the switch II region (**Rak, 2003**), which explains why phosphorylation in this domain interferes with the Rab-GDI interaction. Since GDIs are not specific to one Rab isoform (**Seabra and Wasmeier, 2004**), we reasoned that phosphorylation of the switch II domain could be a general mechanism of Rab-GDI dissociation. We therefore substituted S106-Rab12 and T73-Rab10 with non-phosphorylatable Ala or phosphomimetic Glu residues and tested their capacity to form complexes with GDIs by immunoprecipitation followed by MS or western blotting. As compared to non-phosphorylatable Rab10 and Rab12, neither S106E-Rab12 nor T73E-Rab10 was able to bind GDIs, demonstrating the functional importance of these residues (**Figure 6A,B** and **Figure 6—figure supplement 1A,B**).

To further analyze the effect of Rab phosphorylation and GDI dissociation in the context of PD, we expressed LRRK2 variants harboring various pathogenic mutations along with Rab8a in cells and assessed Rab-GDI complex formation by immunoprecipitation. Strikingly, the level of Rab8a-GDI interaction closely correlated with the degree of T72-Rab8a phosphorylation (**Figure 6C,D**). Similarly, LRRK2-mediated phosphorylation of S106-Rab12 diminished the interaction with GDIs, confirming that the effect is not specific to one Rab isoform (**Figure 6E,F**). All tested LRRK2 pathogenic mutations that affect kinase activity thus control the interaction of Rabs with GDIs. Finally, to directly test whether disruption of the Rab-GDI interaction results in an altered subcellular distribution of Rabs, we quantitatively determined T72A-Rab8 and T72E-Rab8 protein abundances in SILAC (**Ong, 2002**) labeled HEK293 cells. This revealed a twofold increase of non-phosphorylatable T72A mutant in the cytosol. Consistently, we detected a significant ( $p = 2.58 \times 10^{-3}$ ) increase of T72E-Rab8 protein levels

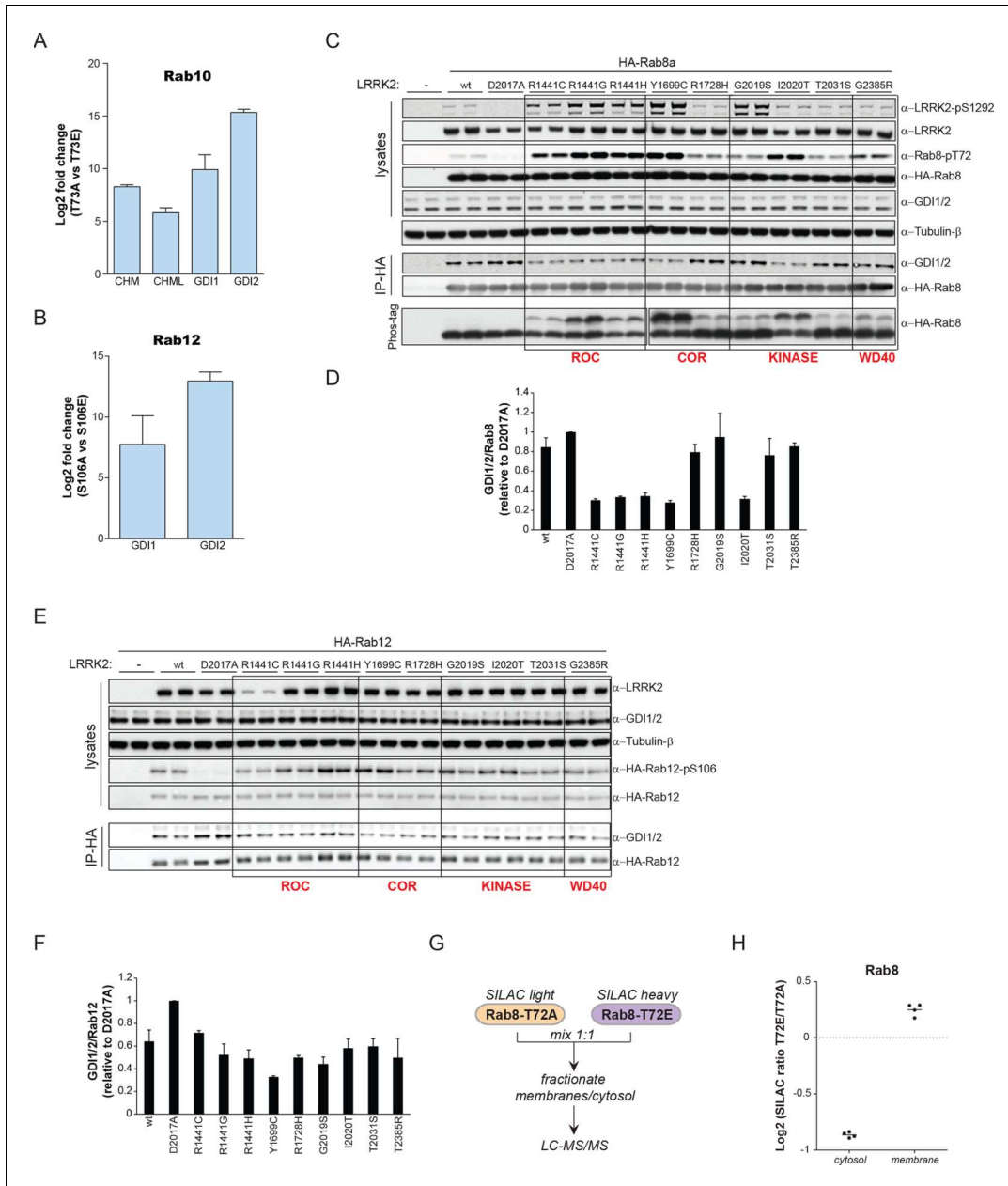


**Figure 6.** PD pathogenic LRRK2 mutations interfere with Rab-GDI/2 association. (A) Fold changes (T73A/T73E, n=3) of indicated MS-quantified Rab10 interactors. (B) Same as (A) but S106A-Rab12 and S106E-Rab12 (n=4). (C) Different LRRK2 versions were co-expressed with Rab8a in HEK293 cells, lysates subjected to immunoblot analysis or immunoprecipitation using  $\alpha$ -HA antibodies and indicated signals quantified (D). (E) and (F) Same as (C) with Rab12 expression. (G) Scheme for analyzing T72A-Rab8a and T72E-Rab8a subcellular protein distributions in a SILAC experiment. (H) SILAC ratios (Log<sub>2</sub>) of T72E-Rab8a/T72A-Rab8a proteins in the cytosolic and membrane fraction of HEK293 cells. PD, Parkinson's disease.

DOI: 10.7554/eLife.12813.016

The following figure supplement is available for figure 6:

**Figure supplement 1.** Rab10/12-GDI interactions.

DOI: 10.7554/eLife.12813.017

in the membrane fraction, demonstrating that interference with the Rab-GDI interaction results in an unbalanced membrane-cytosol distribution of Rabs (**Figure 6G,H**).

## Discussion

Here, we used a state of art MS-based phosphoproteomics workflow in combination with cells of two genetically engineered mouse models as well as a mixture of selective LRRK2 compounds to define LRRK2 targets with high stringency. Starting with almost 30,000 identified phosphosites, our screens rapidly narrowed down the candidates to a small number that were consistently and strongly regulated with all tested compounds and genetic models. Only the known phosphorylation site pS935 on LRRK2 itself and a specific residue in the Rab10 GTPase (T73) fulfilled our most specific criteria. LRRK2 kinase is conserved also in flies and worms and this is true of the T73-Rab10 substrate site as well. Further experiments with diverse model systems and techniques all verified the T73-Rab10 site as well as the equivalent sites on many but not all other Rab family members. These include the threonine sites on Rab8a and Rab3a (T72 and T86, respectively), as well as S106-Rab12. Rab7a is an important component of the endocytic pathway (**Wandinger-Ness and Zerial, 2014**) and phosphorylation on S72 has recently been shown to play a functional role in B-cell signaling (**Satpathy et al., 2015**). While our data clearly show that this site is not regulated by LRRK2 in mouse fibroblasts, its regulation by LRRK2 in B cells remains possible, given the high expression levels of LRRK2 in those cell types (**Gardet et al., 2010**). In vitro experiments proved that LRRK2 directly phosphorylates Thr but not the Ser sites in Rab isoforms, in line with its well-established in vitro preference (**Jaleel et al., 2007; Martin et al., 2014; Nichols et al., 2009**). We found that Ser sites on Rabs were hardly phosphorylated in vitro but S105-Rab12 (S106 in human) was clearly regulated in cells and brain tissue, establishing that accessory factors are required in this case. Consistent with this finding, the major characterized in vivo LRRK2 autophosphorylation site is a Ser residue (Ser1292) (**Sheng et al., 2012**). Our observation of residual Thr72-Rab8 phosphorylation in LRRK2<sup>-/-</sup> mice implies that one or more other kinase(s) are able to act upon this residue.

Besides defining Rab GTPases as LRRK2 targets, our screens identified a number of phosphosites as potential LRRK2 targets. However, these were validated by only one of the screens, their regulation was weaker and for many of them regulation may reflect indirect modulation by the LRRK2 kinase. This is likely to account for the difficulty in identifying substrates of this kinase. In a direct comparison of threonine Rab phosphorylation it was much stronger than the known in vitro LRRK2 targets we tested. Overall, the relatively small number of regulated sites in our screens, suggest that LRRK2 is a very specific or low activity kinase. LRRK2 is ubiquitously expressed, but highly abundant in the kidney, lungs, pancreas, and certain cell types of the immune system (**Schapansky et al., 2015**). Therefore, it is possible that different LRRK2 substrates, including Rab isoforms, are phosphorylated in a cell- or tissue-specific manner. Further phosphoproteomic research should shed more light on this open question. We conclude that the threonine sites on Rab family members identified here may not be the only functional ones in the context of LRRK2, but that they are the most prominent ones.

In searching for a functional role for LRRK2-mediated Rab phosphorylation, we noted that it maps onto the switch II region, which is known to mediate GDP/GTP exchange as well as interaction with regulatory proteins. Results from nucleotide affinity measurements make the former mechanism unlikely but AP-MS established phosphorylation-dependent binding of several proteins involved in regulating their cycling between cytosol and membrane compartments. This indicates that direct phosphorylation of Rabs on a conserved residue situated in the switch II domain regulates their movement by controlling the interaction with numerous regulatory proteins. The affinities of GDIs for Rabs are vastly decreased in a manner correlating with the phosphorylation levels induced by different LRRK2 pathogenic variants. Our data thus establish that LRRK2 is an important regulator of Rab homeostasis which is likely contributing to PD development (**Figure 7A**). Overactive LRRK2, which results in increased Rab phosphorylation, promotes dissociation from GDIs in the cytosol with concomitant membrane insertion (**Figure 7B**). In this way, the relative pool of membrane bound and cytosolic Rab is altered, disturbing intracellular trafficking. In particular, PD-associated LRRK2 mutations would shift the membrane-cytosol balance of Rabs toward the membrane compartment, thereby causing accumulation of inactive Rabs in the membranes (**Figure 7B**). The subtle increase in

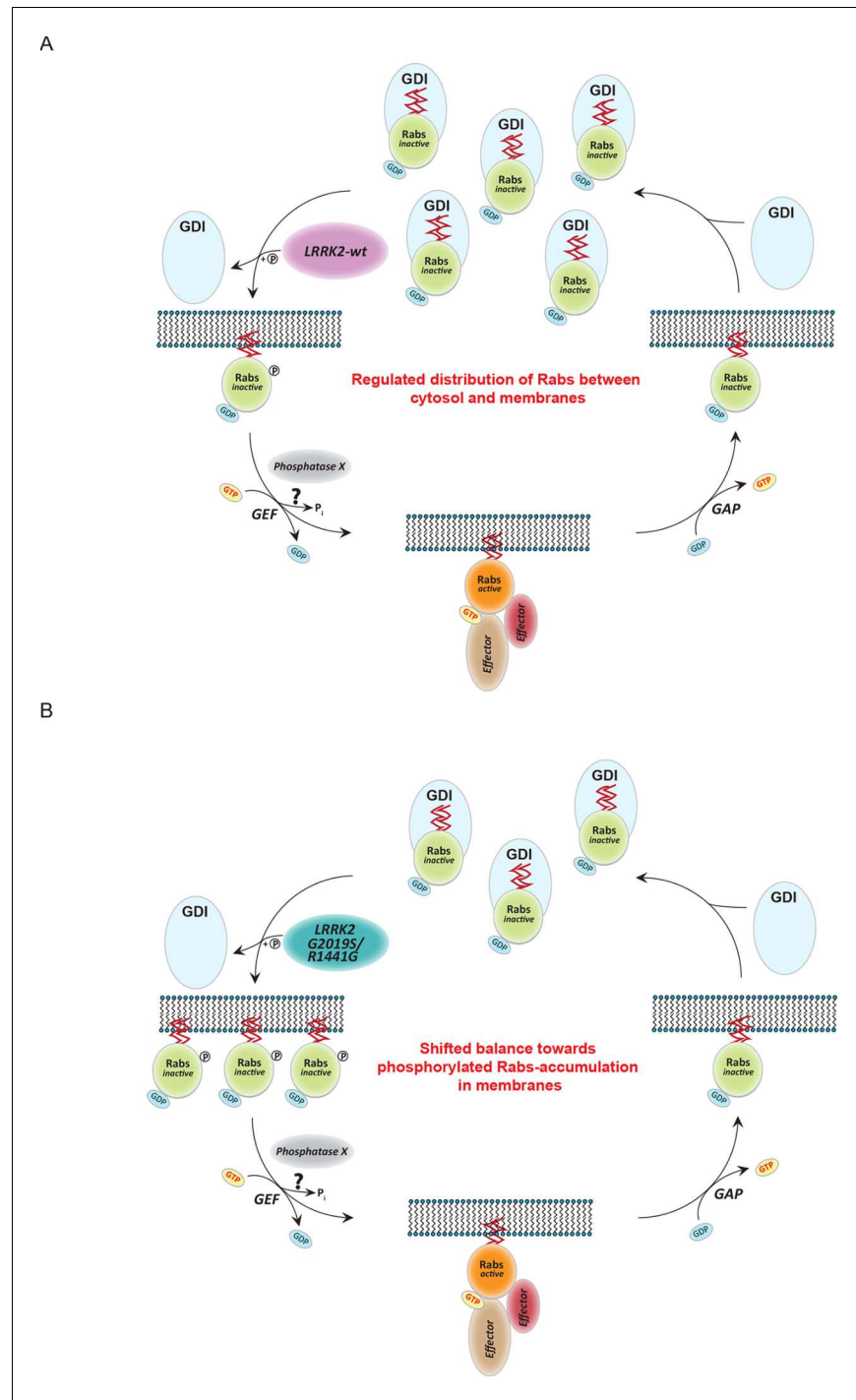


**Figure 7.** Model of Rab GTPase phosphorylation by LRRK2 and its outcome. (A) Rab GTPases (Rabs) cycle between an inactive (GDP-bound) and an active state (GTP-bound) between cytosol and membranes, respectively. Geranyl-geranyl-modified Rab GTPases in their GDP-bound state are tightly bound by guanine dissociation inhibitors (GDIs) in the cytosol. LRRK2 aids the insertion of Rabs in their specific target membrane. After removal of the LRRK2 phosphorylation site, guanine exchange factors (GEFs) facilitate exchange of GDP to GTP. This in Figure 7 continued on next page

Figure 7 continued

turn allows binding to effector proteins and membrane trafficking events. Next, a Rab-specific GTPase-activating protein (GAP) assists in the hydrolysis of GTP followed by removal of the Rab GTPase from the target membrane by GDIs. (B) In pathogenic conditions, in which LRRK2 is hyperactive, RabGTPases have strongly diminished affinities for GDIs. As a result, the equilibrium between membrane-bound and cytosolic Rabs is disturbed, which may contribute to LRRK2 mutant carrier disease phenotypes. Model adapted and modified from (Hutagalung and Novick, 2011).

DOI: 10.7554/eLife.12813.018

Rab phosphorylation in cells derived from LRRK2-G2019S knock-in mice is consistent with the long time needed for PD to manifest in humans.

Intriguingly, our results show that pathogenic LRRK2 mutations outside the kinase domain can also increase Rab phosphorylation. Although our in vitro data clearly shows that this mechanism is indirect, they will still act on the same pathway as kinase domain mutants. Therefore, the same model would also be applicable in this case.

Independent evidence that Rabs are likely to be primary LRRK2 substrates comes from LRRK2 knockout animal studies. LRRK2<sup>-/-</sup> mice and rats have deformed kidneys and lungs, indicative of defects in the autophagosome/lysosome pathway, which depend on properly tuned Rab activity (Herzig et al., 2011; Hinkle et al., 2012; Baptista et al., 2013). Moreover, it was recently reported that LRRK2 and Rab2a regulate Paneth cell function, which is compromised in Crohn's disease (Zhang et al., 2015). In this context, it is interesting that we found pS70-Rab2a/b to be regulated in our second screen, although it's very low abundance impedes meaningful statistical interpretation. Taken together these observations make it plausible that LRRK2 regulates Rab2a by direct phosphorylation of S70 in specialized cell types.

In conclusion, we prove that LRRK2 induces phosphorylation of Rabs and provide evidence that it deregulates cycling between cytosol and target membrane compartments. It will be interesting to investigate whether the Rab regulatory mechanism uncovered here is of key importance in vesicular trafficking in general. Discovery of a key physiological LRRK2 substrate should inform and accelerate research into PD, including monitoring the efficacy of therapeutic intervention.

## Materials and methods

### Reagents

MLI-2 (Fell et al., 2015) was obtained from Merck, GSK2578215A (Reith et al., 2012) from Tocris or GlaxoSmithKline. HG-10-102-01 was custom synthesized by Natalia Shapiro (University of Dundee) as described previously (Choi et al., 2012). Doxycycline, ATP, and trypsin were from Sigma. LysC was obtained from Wako. <sup>32</sup>P-γATP was from PerkinElmer. GST-LRRK2 (residues 960-2527 wild type, G2019S, D1994A), full-length wild type flag-LRRK2 from Invitrogen and MANT-GDP (2'-(or-3')-O-(N-Methylanthraniloyl) Guanosine 5'-Diphosphate, Disodium Salt) and MANT-GMPPNP from Jena Bioscience. GFP beads for affinity purification were from Chromotek. Recombinant Rab10 and Rab1a (Figure 3A and 3C) were purchased from mybiosource.

### Antibodies

Anti-Rab10 and Rab8 were from Cell Signaling Technologies, anti-GFP from Invitrogen, anti-HA high affinity from Roche, anti-GDI1/2 from Sigma, and anti-pS1292-LRRK2 from Abcam. Rabbit monoclonal antibodies for total LRRK2 and pS935-LRRK2 were purified at the University of Dundee (Dzamko et al., 2012). Antibodies against Rab8a phospho-Thr72 (S874D), Rab10 phospho-Thr73 (S873D) and Rab12 phospho-Ser106 (S876D) were generated by injection of the KLH (keyhole limpet hemocyanin)-conjugated phospho-peptides AGQERFRpTITTAYR (Rab8a), AGQERFHpTITTSYR (Rab10), AGQERFNpSITSAYR (Rab12) and IAGQERFpTSMTRLYR (where pS/T is phospho-serine/threonine) into sheep and affinity purified using the phosphopeptides. Antibodies were used at final concentrations of 1 μg/ml in the presence of 10 μg/ml of non-phosphorylated peptide.

## Plasmids

The following constructs were used: 6His-SUMO-Rab8a wt/T72A/T72E (DU47363, DU47433, DU47436), HA-Rab8 wt/T72A/T72E (DU35414, DU47360), 6His-SUMO-Rab5b (DU26116), 6-His-SUMO-Rab7a (DU24781), 6-His-SUMO-Rab7L1 (DU50261), 6-HIS-SUMO-Rab10 (DU51062), HA-Rab10 wt/T73A/T73E (DU44250, DU51006, DU51007), 6-His-SUMO-Rab12 (DU52221), HA-Rab12 wt/S106A/S106E (DU48963, DU48966, DU48967), and 6-His-SUMO-Rab39b (DU43869). Full data-sheets are available on <https://mrcppureagents.dundee.ac.uk/>.

## Protein purification

Purification of Rabs and Rabin8 (**Figures 2D, 2G, and 5E**)

Buffer A: 50 mM HEPES pH 8.0, 500 mM LiCl, 1 mM MgCl<sub>2</sub>, 10 μM GDP, 2 mM beta-mercaptoethanol; Elution buffer: buffer A + 500 mM imidazole; Lysis buffer: buffer A + 1 mM PMSF and Roche Complete protease inhibitor cocktail (EDTA-free); Gel-filtration buffer: 20 mM HEPES pH 8.0, 50 mM NaCl, 1 mM MgCl<sub>2</sub>, 10 μM GDP, 25 μM ATP, 2 mM DTT.

Rab isoforms and Rabin8 (153-237) were expressed as N-terminal His-Sumo fusion proteins in *E. coli* as described previously ([Bleimling et al., 2009](#)). The His-Sumo tag was removed using SENP1 protease ([Chaugule et al., 2011](#)). Transformed BL21 (DE3) harboring the GroEL/S plasmid ([Bleimling et al., 2009](#)) were grown at 37°C to an OD 600 of 0.8, then shifted to 19°C and protein expression induced with Isopropyl β-D-1-thiogalactopyranoside (0.5 mM) for 16 hr. Cells were pelleted at 5000 g (4°C for 20 min) and lysed by sonication (45% amplitude, 20 s pulse, 1 min pause, total of 10 min pulse) in lysis buffer. Lysates were clarified by centrifugation at 30,000 g for 20 min at 4°C followed by incubation with 1 ml of Nickel-NTA agarose/l culture for 1 hr at 4°C. The resin was equilibrated on an AKTA FPLC with buffer A, and bound proteins eluted with imidazole gradient (25 mM-500 mM). Fractions containing the protein of interest were identified by SDS-PAGE and pooled; 10 μg/ml His-SENP1 catalytic domain (residues 415–643) was used to cleave the His tag (16 hr at 4°C). Imidazole was removed by buffer exchange gel filtration on a G25 column equilibrated in Buffer A plus 20 mM Imidazole. His-SENP1 protease was removed using Nickel-NTA agarose. Proteins were concentrated to a maximum of 10 mg/ml using a Vivaspin 10 kDa cut centricon and 0.5 ml samples were resolved on a high-resolution Superdex 200, 24 ml gel-filtration column equilibrated with gel filtration buffer and 0.2 ml fractions were collected. Peak fractions containing recombinant protein were pooled. Identity and purity of proteins were assessed by MalDI-TOF MS and SDS-PAGE.

Purification of Rab8a and Rabin8 (**Figures 5D**)

Human Rab8a (wt, T72E, T72A, residues 1-183) and human Rabin8 constructs (144-460 and 144-245) containing tobacco etch virus (TEV) cleavable N-terminal 6-HIS tag were expressed in *E. coli* BL21 (DE3). Cells were lysed by sonication in a buffer containing 50 mM phosphate pH 7.5, 150 mM NaCl, 10% glycerol. For Rab8a proteins 5 mM MgCl<sub>2</sub> was added. Proteins were purified by Ni-NTA affinity chromatography. To remove the N-terminal HIS tag, proteins were incubated with TEV protease overnight. Further purification was done by ion-exchange chromatography (Q-Sepharose) followed by size exclusion chromatography (SEC) in a buffer of 10 mM HEPES pH 7.5, 150 mM NaCl, and 2 mM DTT using a HiLoad Superdex 75 column. For Rab8a proteins 5 mM MgCl<sub>2</sub> was added to the SEC buffer.

## Mice

Mice were maintained under specific pathogen-free conditions at the University of Dundee (UK). All animal studies were ethically reviewed and carried out in accordance with Animals (Scientific Procedures) Act 1986, the GSK Policy on the Care, Welfare and Treatment of Animals, regulations set by the University of Dundee and the U.K. Home Office. Animal studies and breeding were approved by the University of Dundee ethical committee and performed under a U.K. Home Office project license.

The LRRK2-G2019S<sup>GSK</sup> knock-in mouse line was generated by a targeting strategy devised to introduce the point mutation G2019S into exon 41 of the LRRK2 gene by homologous recombination in mouse embryonic stem (ES) cells. 5' and 3' homology arms (approximately 4.8 and 3.8 kb, respectively) flanking exon 41 were generated using Phusion High-Fidelity DNA Polymerase (New England Biolabs) on a C57BL/6J genomic DNA template. Similarly a 739 bp fragment carrying exon

41 lying between these two homology arms was isolated and subjected to site-directed mutagenesis with the QuickChange site-directed mutagenesis kit (Stratagene) to introduce the appropriate point mutation (GG to TC mutation at bps 107/8). The 5' and 3' homology arms and the mutated exon 41 fragments were subcloned into a parental targeting vector to achieve the positioning of the loxP and FRT sites and PGKneo cassette. Gene targeting was performed in de novo generated C57BL/6J-derived ES cells. The targeting construct was linearized and electroporated into ES cells according to standard methods. ES cells correctly targeted at the 3' end were identified by Southern blot analysis of EcoRV digested genomic DNA using a PCR-derived external probe. Correct gene targeting at the 5' end and presence of the point mutation was confirmed by sequencing of a ~6 kb PCR product. High-fidelity PCR of ES cell clone-derived genomic DNA using primers spanning the 5' homology arm generated the latter. Correctly targeted ES cell clones were injected into BALB/c blastocysts and implanted into foster mothers according to standard procedures. Male chimaeras resulting from the G2019S targeted ES cells were bred with C57BL/6J female mice, and germline transmission of the targeted allele was confirmed by PCR. The PGKneo cassette was subsequently removed by breeding germline mice to FLPeR (Farley et al., 2000) mice expressing Flp recombinase from the Rosa26 locus (C57BL/6J genetic background). Absence of the PGKneo cassette in offspring was confirmed by PCR and subsequent breeding to C57BL/6J mice removed the Flp locus (confirmed by PCR). The line was maintained by breeding with C57BL/6J, and crossing mice heterozygous for the point mutation generated homozygous mice. Standard genotyping which distinguishes wild type from point mutation knock-in alleles was used throughout. Requests for LRRK2-G2019SGSK mice should be directed to: [alastair.d.reith@gsk.com](mailto:alastair.d.reith@gsk.com).

The Michael J. Fox Foundation for Parkinson's Research generated the A2016T knock-in mice. A targeting vector was designed to introduce an alanine to threonine (A2016T) substitution at codon 2016 in exon 41 of the endogenous locus. In addition, an FRT-flanked neomycin resistance (neo) cassette was introduced 400 bp downstream of exon 41. The construct was electroporated into C57BL/6N-derived JM8 ES cells. Correctly targeted ES cells were injected into blastocysts and chimeric mice were bred to B6.Cg-Tg (ACTFLPe)9205Dym/J (JAX stock No. 005703) to remove the neo cassette and leave a silent FRT site. The resulting animals were crossed to C57BL/6NJ inbred mice (JAX stock No. 005304) for one generation. These mice are available from The Jackson Laboratory and for further information see <http://jaxmice.jax.org/strain/021828.html>. The LRRK2-G2019S<sup>Lilly</sup> were generated by Ely Lilly and maintained on a C57BL/6J background.

Genotyping of mice was performed by PCR using genomic DNA isolated from ear biopsies. For LRRK2-G2019S<sup>GSK</sup> knock-in mice, Primer 1 (5'-CCGAGCCAAAACTAAGCTC-3') and Primer 2 (5'-CATCTTGGGTACTTGACC-3') were used to detect the wild-type and knock-in alleles. For LRRK2-G2019S<sup>Lilly</sup> knock-in mice Primer 1 (5'-CATTGCGAAGATTGCGGACTACTCAATT-3') and Primer 2 (5'-AAACAGTAACTATTTCCGTCGTGATCCG-3') were used to detect the wild-type and knock-in alleles. For LRRK2-A2016T Primer 1 (5'-TTGCCTGTGAGTGTCTCTGG-3') and Primer 2 (5'-AGGAAA-TGTGGTCCGACAC-3') were used to detect the wild-type and knock-in alleles. The PCR program consisted of 5 min at 95°C, then 35 cycles of 30 s at 95°C, 30 s at 60°C and 30 s at 72°C, and 5 min at 72°C. DNA sequencing was used to confirm the knock-in mutation and performed by DNA Sequencing & Services (MRC-PPU; <http://www.dnaseq.co.uk>) using Applied Biosystems Big-Dye version 3.1 chemistry on an Applied Biosystems model 3730 automated capillary DNA sequencer.

For experiments shown in **Figure 3F–G**, homozygous LRRK2-G2019S<sup>Lilly</sup> mice (3 months of age) were injected subcutaneously with vehicle (40% Hydroxypropyl- $\beta$ -Cyclodextran) or MLI-2 (3 mg/kg of body mass dissolved in 40% Hydroxypropyl- $\beta$ -Cyclodextran) and euthanized by cervical dislocation 1 hr after treatment. Brains were rapidly isolated and snap frozen in liquid nitrogen. No specific randomization method or blinding was applied to experiments.

### Generation of MEFs

Littermate matched wild type and homozygous LRRK2-A2016T mouse embryonic fibroblasts (MEFs) were isolated from mouse embryos at day E12.5 resulting from crosses between heterozygous LRRK2-A2016T/WT mice using a previously described protocol (Wiggin et al., 2002). Cells were genotyped as described above for mice and wild type and homozygous A2016T knock-in cells generated from the same littermate selected for subsequent experiments. Cells cultured in parallel at passage 4 were used for MS and immunoblotting experiments.

Littermate matched wild type and homozygous LRRK2-G2019S<sup>GSK</sup> MEFs were isolated from mouse embryos at day E12.5 resulting from crosses between heterozygous LRRK2-G2019S<sup>GSK</sup>/WT mice as described previously (Wiggin *et al.*, 2002). Wild-type and homozygous LRRK2-G2019S<sup>GSK</sup>/G2019S<sup>GSK</sup> MEFs were continuously passaged in parallel for at least 15 passages before being used for MS and immunoblotting experiments. All cells were cultured in DMEM containing 10% FBS, 2 mM L-glutamine, 50 units/ml penicillin, 50 µg/ml streptomycin, and non-essential amino acids (Life Technologies). Littermate matched wild type and homozygous knock-out MEFs were isolated from LRRK2 knock-out mice (Dzamko *et al.*, 2012) as described previously (Davies *et al.*, 2013). All knock-in and knock-out cell lines were verified by allelic sequencing.

### Culture and transfection of cells

HEK293 were purchased from ATCC and cultured in Dulbecco's modified Eagle medium (Glutamax, Gibco) supplemented with 10% fetal calf serum, 100 U/ml penicillin, and 100 µg/ml streptomycin. The HEK293-t-rax-flpIn stable cell lines with doxycycline-inducible wild type and mutant forms of LRRK2 have been described previously (Nichols *et al.*, 2010). Transient transfections were performed 36-48 hr prior to cell lysis using Lipofectamine 2000 (Life Technologies) or FuGene HD (Promega). LRRK2 expression in HEK293-t-rax-flpIn was induced by doxycycline (1 µg/ml, 24 hr). All cells were tested for mycoplasma contamination and overexpressing lines were verified by Western blot analysis.

### Immunoprecipitations, pull-downs, and subcellular fractionation

For HA-Rab immunoprecipitations, HA-agarose (Sigma) was washed 3 times with PBS and incubated with lysates at a concentration of 25 µl of resin/mg lysate for 1 hr. Beads were then washed twice with 1 ml PBS and samples eluted in 2 x LDS (50 µl per 25 µl of resin) and centrifuged through a 0.22 µm Spinex filter, 2-mercaptoethanol added to 2% (v/v) and heated to 70°C for 5 min prior to SDS-PAGE. For GFP pull-downs and immunoprecipitations, cells were lysed in ice-cold NP-40 extraction buffer (50 mM Tris-HCl, pH 7.5, 120 mM NaCl, 1 mM EDTA, 6 mM EGTA, 15 mM sodium pyrophosphate and 1% NP-40 supplemented with protease and phosphatase inhibitors (Roche) and clarified by centrifugation at 14,000 rpm. Supernatants were incubated over night with Rab8 or Rab10 antibodies and bound complexes recovered using agarose protein A/G beads (Pierce). For GFP pull-downs, lysates were incubated with GFP beads for 2 hr (Chromotek). On bead digestion of protein complexes used for MS analysis was performed as described previously (Hubner *et al.*, 2010).

For subcellular fractionation, SILAC (Ong, 2002) labeled HEK293 cells were counted and mixed in a 1:1 ratio after harvesting in PBS, spun at 1000 rpm at 4°C for 5 min and then resuspended in subcellular fractionation buffer (250 mM sucrose, 20 mM HEPES pH 7.4, 10 mM KCl, 1.5 mM MgCl<sub>2</sub>, 1 mM EDTA, 1 mM EGTA and protease/phosphatase inhibitor cocktail [Roche]). Cells were then Dounce homogenized, left on ice for 20 min and spun at 750 g for 5 min. The supernatant spun in an ultracentrifuge (100,000 g) for 45 min to obtain cytosolic (supernatant) and membrane (pellet) fractions.

### Phos-tag SDS-PAGE

Phos-tag acrylamide and MnCl<sub>2</sub> were added to a standard gel solution at a final concentration of 50 µM and 100 µM, respectively. After degassing for 10 min, gels were polymerized by ammonium persulfate and TEMED. Cell lysates used for Phos-tag SDS-PAGE were supplemented with MnCl<sub>2</sub> at 10 mM to mask the effect of EDTA in the lysates. After SDS-PAGE, gels were washed 3 times with transfer buffer containing 10 mM EDTA followed by a wash with transfer buffer (10 min each). Blotting to nitrocellulose membranes was carried out according to a standard protocol.

### Total proteome and phosphoproteome sample preparation and MS analyses

All samples were lysed in SDS lysis buffer (4% SDS, 10 mM DTT, 10 mM Tris pH 7.5), boiled and sonicated, and precipitated overnight using ice-cold acetone (v/v= 80%). After centrifugation (4000 g), the pellet was washed at least twice with 80% ice-cold acetone before air drying and resuspension (sonication) in either urea (6 M urea, 2 M thiourea, 50 mM Tris pH 8) or TFE buffer (10% 2-2-2-

trifluoroethanol, 100 mM ammonium bicarbonate [ABC]). Proteins were digested using LysC and trypsin (1:100), overnight at 37°C. Peptides for total proteome measurements were desalted on C18 StageTips and phosphopeptides were enriched as described previously (Humphrey *et al.*, 2015).

### LC-MS/MS measurements

Peptides were loaded on a 50 cm reversed phase column (75  $\mu$ m inner diameter, packed in-house with ReproSil-Pur C18-AQ 1.9  $\mu$ m resin [Dr. Maisch GmbH]). Column temperature was maintained at 50°C using a homemade column oven. An EASY-nLC 1000 system (Thermo Fisher Scientific) was directly coupled online with a mass spectrometer (Q Exactive, Q Exactive Plus, Q Exactive HF, LTQ Orbitrap, Thermo Fisher Scientific) via a nano-electrospray source, and peptides were separated with a binary buffer system of buffer A (0.1% formic acid [FA]) and buffer B (80% acetonitrile plus 0.1% FA), at a flow rate of 250nl/min. Peptides were eluted with a gradient of 5-30% buffer B over 30, 95, 155, or 240 min followed by 30-95% buffer B over 10 min, resulting in approximately 1, 2, 3, or 4 hr gradients, respectively. The mass spectrometer was programmed to acquire in a data-dependent mode (Top5–Top15) using a fixed ion injection time strategy. Full scans were acquired in the Orbitrap mass analyzer with resolution 60,000 at 200 m/z (3E6 ions were accumulated with a maximum injection time of 25 ms). The top intense ions (N for TopN) with charge states  $\geq 2$  were sequentially isolated to a target value of 1E5 (maximum injection time of 120 ms, 20% underfill), fragmented by HCD (NCE 25%, Q Exactive) or CID (NCE 35%, LTQ Orbitrap) and detected in the Orbitrap (Q Exactive, R= 15,000 at m/z 200) or the Ion trap detector (LTQ Orbitrap).

### Data processing and analysis

Raw MS data were processed using MaxQuant version 1.5.1.6 or 1.5.3.15 (Cox and Mann, 2008; Cox *et al.*, 2011) with an FDR < 0.01 at the level of proteins, peptides and modifications. Searches were performed against the Mouse or Human UniProt FASTA database (September 2014). Enzyme specificity was set to trypsin, and the search included cysteine carbamidomethylation as a fixed modification and N-acetylation of protein, oxidation of methionine, and/or phosphorylation of Ser, Thr, Tyr residue (PhosphoSTY) as variable modifications. Up to two missed cleavages were allowed for protease digestion, and peptides had to be fully tryptic. Quantification was performed by MaxQuant, 'match between runs' was enabled, with a matching time window of 0.5-0.7 min. Bioinformatic analyses were performed with Perseus ([www.perseus-framework.org](http://www.perseus-framework.org)) and Microsoft Excel and data visualized using Graph Prism (GraphPad Software) or R studio (<https://www.rstudio.com/>). Hierarchical clustering of phosphosites was performed on logarithmized (Log2) intensities. Significance was assessed using one sample t-test, two-sample student's t-test, and ANOVA analysis, for which replicates were grouped, and statistical tests performed with permutation-based FDR correction for multiple hypothesis testing. Missing data points were replaced by data imputation after filtering for valid values (all valid values in at least one experimental group). Error bars are mean  $\pm$  SEM or mean  $\pm$  SD. Proteomics raw data have been deposited to the ProteomeXchange Consortium (<http://proteomecentral.proteomexchange.org>) via the PRIDE partner repository with the data set identifier PXD003071.

### LRRK2 inhibitor IC50 LRRK2 kinase assay

LRRK2 kinase activity was assessed in an in vitro kinase reaction performed as described previously (Nichols *et al.*, 2009). For IC<sub>50</sub> determination of LRRK2 inhibitor, peptide kinase assays were set up in a total volume of 30  $\mu$ l with recombinant wild type GST-LRRK2-(1326-2527) or mutant GST-LRRK2 [A2016T]-(1326-2527) (6 nM) in 50 mM Tris-HCl pH 7.5, 0.1 mM EGTA, 10 mM MgCl<sub>2</sub>, 0.1 mM [ $\gamma$ -32P]ATP (~300-600 cpm/pmol), and 20  $\mu$ M Nictide LRRK2 substrate peptide substrate, in the presence of indicated concentration of MLI-2. After incubation for 20 min at 30°C, reactions were terminated by applying 25  $\mu$ l of the reaction mixture onto P81 phosphocellulose papers and immersion in 50 mM phosphoric acid. After extensive washing, reaction products were quantified by Cerenkov counting. IC<sub>50</sub> values were calculated using non-linear regression analysis using GraphPad Prism (GraphPad Software). The IC<sub>50</sub>s for GSK2578215A (Reith *et al.*, 2012) against wild type GST-LRRK2-(1326-2527) or mutant GST-LRRK2[A2016T]-(1326-2527) are 10.9 nM and 81.1 nM, respectively, and the IC<sub>50</sub>s for HG-10-102-01 (Choi *et al.*, 2012) vs LRRK2 WT and A2016T are 20.3 nM and 153.7 nM, respectively. The IC<sub>50</sub> of MLI-2 against wild type GST-LRRK2-(1326-2527) or mutant GST-LRRK2

[A2016T]-(1326-2527) are 0.8 nM and 7.2 nM (see Extended Data **Figure 1A**). As MLI-2 displayed greater potency as well as a higher degree of resistance between wild type and A2016T mutation (9-fold compared to 7.4-fold for GSK2578215A and 7.6-fold for HG-10-102-01), we used MLI-2 for MS studies employing LRRK2[A2016T] knock-in MEFs.

### In vitro kinase assays

#### Phosphorylation of Rab isoforms (**Figures 2D, 2G, 2H and 4F**)

LRRK2 kinase assays were performed using purified recombinant GST-tagged LRRK2 (960-2527, wt, D1994A, G2019S, Invitrogen) incubated with recombinant Rab isoform (1  $\mu$ M). Proteins were incubated in kinase assay buffer (20 mM Tris pH 7.5, 1 mM EGTA, 5 mM  $\beta$ -glycerophosphate, 5 mM NaF, 10 mM  $MgCl_2$ , 2 mM DTT, 10  $\mu$ M ATP, and 0.5  $\mu$ Ci of  $\gamma$ - $^{32}P$ -ATP) at a combined volume of 30  $\mu$ L. The reaction mixture was incubated at 30°C for 30 min, or as indicated. Reactions were quenched by the addition of SDS-sample loading buffer, heated to 70°C for 10 min and then separated on SDS-PAGE. Following electrophoresis, gels were fixed (50% (v/v) methanol, 10% (v/v) acetic acid), stained in Coomassie brilliant blue, dried and exposed to a phospho-imaging screen for assessing radioactive  $^{32}P$  incorporation. For MS analysis, 100  $\mu$ M of ATP was used and the reaction was stopped by addition of 2 M urea buffer (2 M urea in 50 mM Tris pH 7.5) containing LRRK2 inhibitor HG-10-102-01 (2  $\mu$ M).

#### Phosphorylation of Rab isoforms (**Figures 2C and 2F**)

Assays were set up in a total volume of 25  $\mu$ L with recombinant full-length Flag-LRRK2 (100 ng, Invitrogen) in 50 mM Tris-HCl pH 7.5, 0.1 mM EGTA, 10 mM  $MgCl_2$ , 0.1 mM [ $\gamma$ - $^{32}P$ ]ATP (~300-600 cpm/pmol), with recombinant Rab isoform (1.5  $\mu$ g) in the presence or absence of the LRRK2 inhibitor HG-10-102-01 (2  $\mu$ M). After incubation for 30 min at 30°C, reactions were stopped by the addition of Laemmli sample buffer and reaction products resolved on SDS-PAGE. The incorporation of phosphate into protein substrates was determined by autoradiography. For phosphorylation of Rab8a or Nictide (**Figure 1B**) LRRK2 was immunoprecipitated from MEFs and kinase activity was assessed in an in vitro kinase reaction as described previously (**Davies et al., 2013**).

### Phosphosite identification by MS and Edman sequencing (**Figure 2—figure supplement 1**)

Purified Rab1b and Rab8a (5  $\mu$ g) were phosphorylated using recombinant full-length wild type Flag-LRRK2 (0.2  $\mu$ g; Invitrogen) in a buffer containing 50 mM Tris-HCl pH 7.5, 0.1 mM EGTA, 10 mM  $MgCl_2$ , 0.1 mM [ $\gamma$ - $^{32}P$ ]ATP (~3000 Ci/pmol) for 1 hr at 30°C. The reactions were stopped by the addition of SDS sample buffer, and reaction products were resolved by electrophoresis on SDS-PAGE gels that were stained with Coomassie blue. The band corresponding to Rab1b/Rab8a was excised and digested overnight with trypsin at 30°C, and the peptides were separated on a reverse-phase HPLC Vydac C18 column (Separations Group) equilibrated in 0.1% (v/v) trifluoroacetic acid, and the column developed with a linear acetonitrile gradient at a flow rate of 0.2 ml/min. Fractions (0.1 ml each) were collected and analyzed for  $^{32}P$  radioactivity by Cerenkov counting. Phosphopeptides were analyzed by liquid chromatography (LC)-MS/MS using a Thermo U3000 RSLC nano liquid chromatography system (Thermo Fisher Scientific) coupled to a Thermo LTQ-Orbitrap Velos mass spectrometer (Thermo Fisher Scientific). Data files were searched using Mascot ([www.matrixscience.com](http://www.matrixscience.com)) run on an in-house system against a database containing the appropriate Rab sequences, with a 10 ppm mass accuracy for precursor ions, a 0.6 Da tolerance for fragment ions, and allowing for Phospho (ST), Phospho (Y), Oxidation (M), and Dioxidation (M) as variable modifications. Individual MS/MS spectra were inspected using Xcalibur 2.2 (Thermo Fisher Scientific), and Proteome Discoverer with phosphoRS 3.1 (Thermo Fisher Scientific) was used to assist with phosphosite assignment. The site of phosphorylation of  $^{32}P$ -labeled peptides was determined by solid-phase Edman degradation on a Shimadzu PPSQ33A Sequencer of the peptide coupled to Sequelon-AA membrane (Applied Biosystems) as described previously (**Campbell and Morrice, 2002**).

### Phosphorylation of Rab8a (**Figure 5D**)

Rab8a was phosphorylated using LRRK2-G2019S (see 'in vitro kinase assays' section). Non-phosphorylated and phosphorylated Rab8a proteins were separated using ion-exchange chromatography

(Mono S 4.6/100; GE Healthcare) with a linear salt gradient from buffer A (20 mM Tris/HCl pH 7.5, 50 mM NaCl, 10% (v/v) glycerol) to buffer B (as buffer A, but with 1000 mM NaCl). The successful enrichment of phosphorylated Rab8a was confirmed by ESI-TOF MS.

### Rab8a nucleotide binding experiments

Rab8a (1-183, wt and T72E) were subjected to HPLC revealing that the purified proteins were (>90%) in the nucleotide-free form. To determine affinities for G-nucleotides, fluorescence measurements were carried out at 20°C in a buffer containing 50 mM Tris pH 7.5, 100 mM NaCl, and 5 mM MgCl<sub>2</sub>. Spectra were measured with a PerkinElmer LS50B fluorescence spectrophotometer; 1 μM of methylanthraniloyl (mant) labeled GMPPNP and GDP was incubated with increasing concentrations of wild type and T72E Rab8a in 60 μl volumes. Fluorescence of mant-nucleotides was excited at 355 nm and emission spectra monitored from 400 to 500 nm, with emission maxima detected at 448 nm. Intrinsic protein fluorescence and mant-nucleotide background fluorescence was subtracted from the curves. Data collection was performed with the program FL WinLab (PerkinElmer), while further analysis, curve fitting and dissociation constant (K<sub>d</sub>) determination was done using GraphPad Prism (GraphPad Software).

### Guanine exchange factor (GEF) assays

**Figure 5E:** Purified Rab8a (100 μg) was phosphorylated using LRRK2 G2019S (1.5 μg) in a buffer containing 50 mM Tris-HCl pH 7.5, 0.1 mM EGTA, 10 mM MgCl<sub>2</sub>, 2 mM DTT, 1 mM ATP (18 hr, room temperature [RT]) in a Dispo-Biodialyzer MWCO 1 kDa (Sigma-Aldrich) and incubated in 2 l of the same Buffer to allow for ADP exchange. The buffer was subsequently exchanged to a GDP dissociation assay buffer containing 20 mM HEPES-NaOH pH 7.5, 50 mM NaCl, 2 mM DTT, 1 mM MnCl<sub>2</sub>, 0.01% (w/v) Brij-35 using Zeba Spin desalting columns (Invitrogen). Phosphorylated Rab8a (50 μg) was treated with lambda phosphatase (5 μg) for 30 min at 30°C where indicated. To load mant-GDP, Rab8a was incubated with 40 μM mant-GDP in the presence of 5 mM EDTA at 30°C for 30 min. After adding MgCl<sub>2</sub> at 10 mM, in order to remove unbound mant-GDP, the buffer was exchanged to a buffer containing 10 mM HEPES-NaOH pH 7.5, 50 mM NaCl, 5 mM DTT, 1 mM MgCl<sub>2</sub> using Zeba Spin desalting columns. GDP dissociation reactions were set up in a total volume of 50 μl with 1 μM Rab8a:mant-GDP in 20 mM HEPES-NaOH pH 7.5, 50 mM NaCl, 2 mM DTT, 1 mM MgCl<sub>2</sub>, and 0.1 mM GDP, and the reaction was started by adding the indicated concentration of Rabin8 (residues 153-237) (Guo et al., 2013). Kinetic measurement of the mant fluorescence was carried out in a black half-area 96-well plate with PHERAStar FS (BMG Labtech) at RT using a set of filters (excitation: 350 nm, emission: 460 nm). The observed rate constant (k<sub>obs</sub>) and the catalytic efficiency (k<sub>cat</sub>/K<sub>m</sub>) were calculated as described previously (Delprato et al., 2004). Phosphorylation stoichiometry (63%) was calculated by digestion of the protein with trypsin and analyzing the fragments by Orbitrap MS.

**Figure 5D:** Phosphorylated Rab8a was obtained as described in section 'Phosphorylation of Rab8a'. GEF assays were performed as described previously (Eberth and Ahmadian, 2009). Loading of purified nucleotide-free (both phosphorylated and non-phosphorylated) Rab8a (1-183) with 2'(3')-O-(N-methylanthraniloyl)-GDP (mantGDP) was achieved by incubation with an 1.5 molar excess of mantGDP for 2 hr at RT. Unbound mantGDP was removed using a size-exclusion chromatography column. (Micro Bio-Spin column, Bio-RAD). The nucleotide exchange reactions were set up in a total volume of 50 μl in a quartz-glass cuvette (Hellma Analytics) with 0.5 μM mantGDP-bound Rab8a (non-phosphorylated or phosphorylated) using a GEF buffer containing 30 mM Tris pH 7.5, 5 mM MgCl<sub>2</sub>, 3 mM DTT and 10 mM KH<sub>2</sub>PO<sub>4</sub>, pH 7.4. Purified Rabin8 (144-245, GEF domain) was subjected to size exclusion chromatography prior to GEF activity assay to ensure no loss of GEF activity due to storage. Rabin8 was added to a final concentration of 2 μM and incubated for 30 min at 20°C. The reactions were initiated by addition of GTP (1 mM c<sub>i</sub>). The dissociation of mant-GDP from Rab8a was monitored every 2 s for a total of 300 s at 20°C using a fluorescence spectrometer (PerkinElmer, 366 nm excitation and 450 nm emission). The observed rate constants (k<sub>obs</sub>) were calculated by fitting the data into a one-phase exponential decay equation without constraints using nonlinear regression in GraphPad Prism (GraphPad Software Inc).

### Ni<sup>2+</sup>-NTA Rabin8 pull-down

Ni<sup>2+</sup>-NTA beads were pre-equilibrated with buffer containing PBS pH 7.4, 30 mM imidazole and 5 mM MgCl<sub>2</sub>. Purified HIS-tagged Rabin8 (residues 144-460) and untagged Rab8a (1-183) WT or quantitatively phosphorylated pT72 were mixed at equal molar ratios. Individual proteins and a mixture of the proteins were incubated with Ni<sup>2+</sup>-NTA beads for 1.5 hr at 4°C. Beads were washed 3 times with PBS, bound proteins eluted with 500 mM imidazole followed by SDS-PAGE and western blot analysis.

### Acknowledgements

This work was supported by the Max-Planck Society for the Advancement of Science, The Michael J. Fox Foundation for Parkinson's Research (grant ID 6986), the Swiss National Science Foundation (to M.S., P2ZHP3\_151580) and the Medical Research Council (to D.R.A.). We thank S. Suppmann, S. Uebel and E. Weyher-Stingl from the MPIB Biochemistry Core Facility and G. Sowa, S. Kroiss, K. Mayr and I. Paron from the department of Proteomics and Signal Transduction for providing technical assistance. M. Raeschle, F. Sacco, J. Liu and M. Murgia for critical reading and commenting on the manuscript. A. Itzen (TUM Munich) provided GroEL/ES chaperone plasmids. H. Cai (NIH Bethesda) provided LRRK2<sup>-/-</sup> mice. We thank T. Hochdorfer for protein purification as well as R. Gourlay and D. Campbell for technical support in the MRC-Protein Phosphorylation and Ubiquitylation Unit, the management of mouse colony service, genotyping and DNA Sequencing Service (coordinated by Nicholas Helps), the tissue culture team (coordinated by K. Airey and J. Stark) and the protein production and antibody purification teams (coordinated by H. McLauchlan and J. Hastie). Eli Lilly provided the LRRK2-G2019S<sup>Lilly</sup> knock-in mice. We acknowledge K. Basu, M. Miller and J. Scott from the chemistry department at Merck Research Laboratories and the Merck LRRK2 program team for their contributions leading to the discovery of MLI-2.

### Additional information

#### Competing interests

SWi: Employee of GlaxoSmithKline, a global healthcare company that may conceivably benefit financially through this publication. MJF: Employee of Merck Research Laboratories. JAM: Employee of GlaxoSmithKline, a global healthcare company that may conceivably benefit financially through this publication. ADR: Employee of Merck Research Laboratories, Contributed unpublished essential data or reagents. The other authors declare that no competing interests exist.

#### Funding

Funder	Grant reference number	Author
Schweizerischer Nationalfonds zur Förderung der Wissenschaftlichen Forschung	P2ZHP3_151580	Martin Steger
Michael J. Fox Foundation for Parkinson's Research	6986	Matthias Trost Dario R Alessi Matthias Mann Alastair D Reith
Max-Planck-Gesellschaft		Esben Lorentzen Matthias Mann
Medical Research Council	MC_UU_12016/3	Dario R Alessi

The funders had no role in study design, data collection and interpretation, or the decision to submit the work for publication.

#### Author contributions

MS, Designed the experiments, Performed the experiments, Conducted all global MS experiments and bioinformatic analyses of MS data and discovered the regulated Rab phosphorylation, Conception and design, Acquisition of data, Analysis and interpretation of data, Drafting or revising the article; FT, GI, Designed the experiments, Performed the experiments, Discussed the results and

approved the manuscript, Acquisition of data, Analysis and interpretation of data; PD, Designed the experiments, Discussed the results and approved the manuscript, Analysis and interpretation of data, Drafting or revising the article; MT, Performed the experiments, Discussed the results and approved the manuscript, Analysis and interpretation of data; MV, SWa, Performed the experiments, Discussed the results and approved the manuscript, Acquisition of data, Analysis and interpretation of data; EL, Designed the experiments, Discussed the results and approved the manuscript, Conception and design, Analysis and interpretation of data; GD, SWi, Contributed essential reagents, Generated the G2019SGSK knock-in mouse line, Discussed the results and approved the manuscript, Contributed unpublished essential data or reagents; MASB, BKF, Generated A2016T knock-in mice and supported the project, Discussed the results and approved the manuscript, Conception and design, Contributed unpublished essential data or reagents; MJF, Employees of Merck Research Laboratories, Contributed unpublished essential data or reagents; JAM, Contributed essential reagents, Provided MLI-2, Discussed the results and approved the manuscript, Contributed unpublished essential data or reagents; ADR, Contributed essential reagents, Generated the G2019SGSK knock-in mouse line, Provided GSK2578215A and supported the project from conception, Discussed the results and approved the manuscript, Contributed unpublished essential data or reagents; DRA, Designed the experiments, Wrote the manuscript, Discussed the results and approved the manuscript, Conception and design, Analysis and interpretation of data, Drafting or revising the article; MM, Conception and design, Analysis and interpretation of data, Drafting or revising the article

### Ethics

Animal experimentation: All animal studies were ethically reviewed and carried out in accordance with Animals (Scientific Procedures) Act 1986, the GSK Policy on the Care, Welfare and Treatment of Animals, regulations set by the University of Dundee and the U.K. Home Office. Animal studies and breeding were approved by the University of Dundee ethical committee and performed under a U.K. Home Office project license.

## Additional files

### Supplementary files

- Supplementary file 1. All phosphosites quantified in the phosphoproteomic screens one (PS1, LRRK2-G2019S<sup>GSK</sup> MEFs and two (PS2, wt and LRRK2-A2016T MEFs).  
DOI: [10.7554/eLife.12813.019](https://doi.org/10.7554/eLife.12813.019)
- Supplementary file 2. All quantified proteins of wt and LRRK2-A2016T MEFs.  
DOI: [10.7554/eLife.12813.020](https://doi.org/10.7554/eLife.12813.020)
- Supplementary file 3. (A) Significantly modulated sites of PS1. (B) Significantly modulated sites of PS2.  
DOI: [10.7554/eLife.12813.021](https://doi.org/10.7554/eLife.12813.021)

## References

- Bailey RM, Covy JP, Melrose HL, Rousseau L, Watkinson R, Knight J, Miles S, Farrer MJ, Dickson DW, Giasson BI, Lewis J. 2013. LRRK2 phosphorylates novel tau epitopes and promotes tauopathy. *Acta Neuropathologica* **126**: 809–827. doi: [10.1007/s00401-013-1188-4](https://doi.org/10.1007/s00401-013-1188-4)
- Baptista MAS, Dave KD, Frasier MA, Sherer TB, Greeley M, Beck MJ, Varsho JS, Parker GA, Moore C, Churchill MJ, Meshul CK, Fiske BK. 2013. Loss of leucine-rich repeat kinase 2 (LRRK2) in rats leads to progressive abnormal phenotypes in peripheral organs. *PLoS One* **8**:e80705. doi: [10.1371/journal.pone.0080705](https://doi.org/10.1371/journal.pone.0080705)
- Bleimling N, Alexandrov K, Goody R, Itzen A. 2009. Chaperone-assisted production of active human Rab8A GTPase in escherichia coli. *Protein Expression and Purification* **65**:190–195. doi: [10.1016/j.pep.2008.12.002](https://doi.org/10.1016/j.pep.2008.12.002)
- Burbulla LF, Krüger R. 2011. Converging environmental and genetic pathways in the pathogenesis of parkinson's disease. *Journal of the Neurological Sciences* **306**:1–8. doi: [10.1016/j.jns.2011.04.005](https://doi.org/10.1016/j.jns.2011.04.005)
- Campbell DG, Morrice NA. 2002. Identification of protein phosphorylation sites by a combination of mass spectrometry and solid phase edman sequencing. *Journal of Biomolecular Techniques* **13**:119–130.
- Chaugule VK, Burchell L, Barber KR, Sidhu A, Leslie SJ, Shaw GS, Walden H. 2011. Autoregulation of parkin activity through its ubiquitin-like domain. *The EMBO Journal* **30**:2853–2867. doi: [10.1038/emboj.2011.204](https://doi.org/10.1038/emboj.2011.204)

- Chen C-Y**, Weng Y-H, Chien K-Y, Lin K-J, Yeh T-H, Cheng Y-P, Lu C-S, Wang H-L. 2012. (G2019S) LRRK2 activates MKK4-JNK pathway and causes degeneration of SN dopaminergic neurons in a transgenic mouse model of PD. *Cell Death and Differentiation* **19**:1623–1633. doi: [10.1038/cdd.2012.42](https://doi.org/10.1038/cdd.2012.42)
- Choi HG**, Zhang J, Deng X, Hatcher JM, Patricelli MP, Zhao Z, Alessi DR, Gray NS. 2012. Brain penetrant LRRK2 inhibitor. *ACS Medicinal Chemistry Letters* **3**:658–662. doi: [10.1021/ml300123a](https://doi.org/10.1021/ml300123a)
- Cookson MR**. 2015. LRRK2 pathways leading to neurodegeneration. *Current Neurology and Neuroscience Reports* **15**:42. doi: [10.1007/s11910-015-0564-y](https://doi.org/10.1007/s11910-015-0564-y)
- Cooper AA**, Gitler AD, Cashikar A, Haynes CM, Hill KJ, Bhullar B, Liu K, Xu K, Strathearn KE, Liu F, Cao S, Caldwell KA, Caldwell GA, Marsischky G, Kolodner RD, Labaer J, Rochet JC, Bonini NM, Lindquist S. 2006. Alpha-synuclein blocks ER-golgi traffic and Rab1 rescues neuron loss in parkinson's models. *Science* **313**:324–328. doi: [10.1126/science.1129462](https://doi.org/10.1126/science.1129462)
- Cox J**, Hein MY, Luber CA, Paron I, Nagaraj N, Mann M. 2014. Accurate proteome-wide label-free quantification by delayed normalization and maximal peptide ratio extraction, termed MaxLFO. *Molecular & Cellular Proteomics* **13**:2513–2526. doi: [10.1074/mcp.M113.031591](https://doi.org/10.1074/mcp.M113.031591)
- Cox J**, Mann M. 2008. MaxQuant enables high peptide identification rates, individualized p.p.b.-range mass accuracies and proteome-wide protein quantification. *Nature Biotechnology* **26**:1367–1372. doi: [10.1038/nbt.1511](https://doi.org/10.1038/nbt.1511)
- Cox J**, Neuhauser N, Michalski A, Scheltema RA, Olsen JV, Mann M. 2011. Andromeda: a peptide search engine integrated into the MaxQuant environment. *Journal of Proteome Research* **10**:1794–1805. doi: [10.1021/pr101065j](https://doi.org/10.1021/pr101065j)
- Davies P**, Hinkle KM, Sukar NN, Sepulveda B, Mesias R, Serrano G, Alessi DR, Beach TG, Benson DL, White CL, Cowell RM, Das SS, West AB, Melrose HL. 2013. Comprehensive characterization and optimization of anti-LRRK2 (leucine-rich repeat kinase 2) monoclonal antibodies. *Biochemical Journal* **453**:101–113. doi: [10.1042/BJ20121742](https://doi.org/10.1042/BJ20121742)
- Delprato A**, Merithew E, Lambright DG. 2004. Structure, exchange determinants, and family-wide rab specificity of the tandem helical bundle and Vps9 domains of rabex-5. *Cell* **118**:607–617. doi: [10.1016/j.cell.2004.08.009](https://doi.org/10.1016/j.cell.2004.08.009)
- Dzamko N**, Deak M, Hentati F, Reith AD, Prescott AR, Alessi DR, Nichols RJ. 2010. Inhibition of LRRK2 kinase activity leads to dephosphorylation of Ser<sup>910</sup>/Ser<sup>935</sup>, disruption of 14-3-3 binding and altered cytoplasmic localization. *Biochemical Journal* **430**:405–413. doi: [10.1042/BJ20100784](https://doi.org/10.1042/BJ20100784)
- Dzamko N**, Inesta-Vaquera F, Zhang J, Xie C, Cai H, Arthur S, Tan L, Choi H, Gray N, Cohen P, Pedrioli P, Clark K, Alessi DR. 2012. The IkkappaB kinase family phosphorylates the parkinson's disease kinase LRRK2 at Ser935 and Ser910 during toll-like receptor signaling. *PLoS One* **7**:e39132. doi: [10.1371/journal.pone.0039132](https://doi.org/10.1371/journal.pone.0039132)
- Eberth A**, Ahmadian MR. 2009. In vitro GEF and GAP assays. *Current Protocols in Cell Biology / Editorial Board, Juan S Bonifacino [Et Al]* **14**. doi: [10.1002/0471143030.cb1409s43](https://doi.org/10.1002/0471143030.cb1409s43)
- Farley FW**, Soriano P, Steffen LS, Dymecki SM. 2000. Widespread recombinase expression using FLPeR (flipper) mice. *Genesis* **28**:106–110. doi: [10.1002/1526-968X\(200011/12\)28:3/4<106::AID-GENE30>3.0.CO;2-T](https://doi.org/10.1002/1526-968X(200011/12)28:3/4<106::AID-GENE30>3.0.CO;2-T)
- Farrer MJ**, Stone JT, Lin C-H, Dächsel JC, Hulihan MM, Haugarvoll K, Ross OA, Wu R-M. 2007. Lrrk2 G2385R is an ancestral risk factor for parkinson's disease in asia. *Parkinsonism & Related Disorders* **13**:89–92. doi: [10.1016/j.parkreldis.2006.12.001](https://doi.org/10.1016/j.parkreldis.2006.12.001)
- Fell MJ**, Mirescu C, Basu K, Cheewatrakoolpong B, DeMong DE, Ellis JM, Hyde LA, Lin Y, Markgraf CG, Mei H, Miller M, Poulet FM, Scott JD, Smith MD, Yin Z, Zhou X, Parker EM, Kennedy ME, Morrow JA. 2015. MLI-2, a potent, selective, and centrally active compound for exploring the therapeutic potential and safety of LRRK2 kinase inhibition. *Journal of Pharmacology and Experimental Therapeutics* **355**:397–409. doi: [10.1124/jpet.115.227587](https://doi.org/10.1124/jpet.115.227587)
- Gardet A**, Benita Y, Li C, Sands BE, Ballester I, Stevens C, Korzenik JR, Rioux JD, Daly MJ, Xavier RJ, Podolsky DK. 2010. LRRK2 is involved in the IFN- response and host response to pathogens. *The Journal of Immunology* **185**:5577–5585. doi: [10.4049/jimmunol.1000548](https://doi.org/10.4049/jimmunol.1000548)
- Gillardon F**. 2009. Leucine-rich repeat kinase 2 phosphorylates brain tubulin-beta isoforms and modulates microtubule stability - a point of convergence in parkinsonian neurodegeneration? *Journal of Neurochemistry* **110**:1514–1522. doi: [10.1111/j.1471-4159.2009.06235.x](https://doi.org/10.1111/j.1471-4159.2009.06235.x)
- Gitler AD**, Bevis BJ, Shorter J, Strathearn KE, Hamamichi S, Su LJ, Caldwell KA, Caldwell GA, Rochet J-C, McCaffery JM, Barlowe C, Lindquist S. 2008. The parkinson's disease protein -synuclein disrupts cellular rab homeostasis. *Proceedings of the National Academy of Sciences of the United States of America* **105**:145–150. doi: [10.1073/pnas.0710685105](https://doi.org/10.1073/pnas.0710685105)
- Gloeckner CJ**, Schumacher A, Boldt K, Ueffing M. 2009. The parkinson disease-associated protein kinase LRRK2 exhibits MAPKKK activity and phosphorylates MKK3/6 and MKK4/7, *in vitro*. *Journal of Neurochemistry* **109**:959–968. doi: [10.1111/j.1471-4159.2009.06024.x](https://doi.org/10.1111/j.1471-4159.2009.06024.x)
- Guo Z**, Hou X, Goody RS, Itzen A. 2013. Intermediates in the guanine nucleotide exchange reaction of Rab8 protein catalyzed by guanine nucleotide exchange factors Rabin8 and GRAB. *Journal of Biological Chemistry* **288**:32466–32474. doi: [10.1074/jbc.M113.498329](https://doi.org/10.1074/jbc.M113.498329)
- Herzig MC**, Köllly C, Persohn E, Theil D, Schweizer T, Hafner T, Stemmelen C, Troxler TJ, Schmid P, Danner S, Schnell CR, Mueller M, Kinzel B, Grevot A, Bolognani F, Stirn M, Kuhn RR, Kaupmann K, van der Putten PH, Rovelli G, Shimshek DR. 2011. LRRK2 protein levels are determined by kinase function and are crucial for kidney and lung homeostasis in mice. *Human Molecular Genetics* **20**:4209–4223. doi: [10.1093/hmg/ddr348](https://doi.org/10.1093/hmg/ddr348)
- Hinkle KM**, Yue M, Behrouz B, Dächsel JC, Lincoln SJ, Bowles EE, Beevers JE, Dugger B, Winner B, Prots I, Kent CB, Nishioka K, Lin W-L, Dickson DW, Janus CJ, Farrer MJ, Melrose HL. 2012. LRRK2 knockout mice have an

- intact dopaminergic system but display alterations in exploratory and motor co-ordination behaviors. *Molecular Neurodegeneration* **7**:25. doi: [10.1186/1750-1326-7-25](https://doi.org/10.1186/1750-1326-7-25)
- Hubner NC, Bird AW, Cox J, Spletstoesser B, Bandilla P, Poser I, Hyman A, Mann M. 2010. Quantitative proteomics combined with BAC TransgeneOmics reveals in vivo protein interactions. *The Journal of Cell Biology* **189**:739–754. doi: [10.1083/jcb.200911091](https://doi.org/10.1083/jcb.200911091)
- Humphrey SJ, Azimifar SB, Mann M. 2015. High-throughput phosphoproteomics reveals in vivo insulin signaling dynamics. *Nature Biotechnology* **33**:990–995. doi: [10.1038/nbt.3327](https://doi.org/10.1038/nbt.3327)
- Hutagalung AH, Novick PJ. 2011. Role of rab GTPases in membrane traffic and cell physiology. *Physiological Reviews* **91**:119–149. doi: [10.1152/physrev.00059.2009](https://doi.org/10.1152/physrev.00059.2009)
- Imai Y, Gehrke S, Wang H-Q, Takahashi R, Hasegawa K, Oota E, Lu B. 2008. Phosphorylation of 4E-BP by LRRK2 affects the maintenance of dopaminergic neurons in drosophila. *The EMBO Journal* **27**:2432–2443. doi: [10.1038/emboj.2008.163](https://doi.org/10.1038/emboj.2008.163)
- Jaleel M, Nichols RJ, Deak M, Campbell DG, Gillardon F, Knebel A, Alessi DR. 2007. LRRK2 phosphorylates moesin at threonine-558: characterization of how parkinson's disease mutants affect kinase activity. *Biochemical Journal* **405**:307–317. doi: [10.1042/BJ20070209](https://doi.org/10.1042/BJ20070209)
- Kanao T, Venderova K, Park DS, Unterman T, Lu B, Imai Y. 2010. Activation of FoxO by LRRK2 induces expression of proapoptotic proteins and alters survival of postmitotic dopaminergic neuron in drosophila. *Human Molecular Genetics* **19**:3747–3758. doi: [10.1093/hmg/ddq289](https://doi.org/10.1093/hmg/ddq289)
- Kawakami F, Yabata T, Ohta E, Maekawa T, Shimada N, Suzuki M, Maruyama H, Ichikawa T, Obata F. 2012. LRRK2 phosphorylates tubulin-associated tau but not the free molecule: LRRK2-mediated regulation of the tau-tubulin association and neurite outgrowth. *PLoS ONE* **7**:e30834. doi: [10.1371/journal.pone.0030834](https://doi.org/10.1371/journal.pone.0030834)
- Khan NL, Jain S, Lynch JM, Pavese N, Abou-Sleiman P, Holton JL, Healy DG, Gilks WP, Sweeney MG, Ganguly M, Gibbons V, Gandhi S, Vaughan J, Eunson LH, Katzenschlager R, Gayton J, Lennox G, Revesz T, Nicholl D, Bhatia KP, Quinn N, Brooks D, Lees AJ, Davis MB, Piccini P, Singleton AB, Wood NW. 2005. Mutations in the gene LRRK2 encoding dardarin (pARK8) cause familial parkinson's disease: clinical, pathological, olfactory and functional imaging and genetic data. *Brain* **128**:2786–2796. doi: [10.1093/brain/awh667](https://doi.org/10.1093/brain/awh667)
- Krumova P, Reyniers L, Meyer M, Lobbstaël E, Stauffer D, Gerrits B, Müller L, Hoving S, Kaupmann K, Voshol J, Fabbro D, Bauer A, Rovelli G, Taymans J-M, Bouwmeester T, Baekelandt V. 2015. Chemical genetic approach identifies microtubule affinity-regulating kinase 1 as a leucine-rich repeat kinase 2 substrate. *The FASEB Journal* **29**:2980–2992. doi: [10.1096/fj.14-262329](https://doi.org/10.1096/fj.14-262329)
- Kumar A, Greggio E, Beilina A, Kaganovich A, Chan D, Taymans J-M, Wolozin B, Cookson MR. 2010. The parkinson's disease associated LRRK2 exhibits weaker in vitro phosphorylation of 4E-BP compared to autophosphorylation. *PLoS One* **5**:e8730. doi: [10.1371/journal.pone.0008730](https://doi.org/10.1371/journal.pone.0008730)
- Lai Y-C, Kondapalli C, Lehneck R, Procter JB, Dill BD, Woodroof HI, Gourlay R, Peggie M, Macartney TJ, Corti O, Corvol J-C, Campbell DG, Itzen A, Trost M, Muqit MM. 2015. Phosphoproteomic screening identifies rab GTPases as novel downstream targets of PINK1. *The EMBO Journal* **34**:2840–2861. doi: [10.15252/emboj.201591593](https://doi.org/10.15252/emboj.201591593)
- Lees AJ, Hardy J, Revesz T. 2009. Parkinson's disease. *The Lancet* **373**:2055–2066. doi: [10.1016/S0140-6736\(09\)60492-X](https://doi.org/10.1016/S0140-6736(09)60492-X)
- Lemeer S, Heck AJR. 2009. The phosphoproteomics data explosion. *Current Opinion in Chemical Biology* **13**:414–420. doi: [10.1016/j.cbpa.2009.06.022](https://doi.org/10.1016/j.cbpa.2009.06.022)
- Liu Z, Hamamichi S, Dae Lee B, Yang D, Ray A, Caldwell GA, Caldwell KA, Dawson TM, Dawson VL. 2011. Inhibitors of LRRK2 kinase attenuate neurodegeneration and parkinson-like phenotypes in caenorhabditis elegans and drosophila parkinson's disease models. *Human Molecular Genetics* **20**:3933–3942. doi: [10.1093/hmg/ddr312](https://doi.org/10.1093/hmg/ddr312)
- MacLeod DA, Rhinn H, Kuwahara T, Zolin A, Di Paolo G, McCabe BD, MacCabe BD, Marder KS, Honig LS, Clark LN, Small SA, Abeliovich A. 2013. RAB7L1 interacts with LRRK2 to modify intraneuronal protein sorting and parkinson's disease risk. *Neuron* **77**:425–439. doi: [10.1016/j.neuron.2012.11.033](https://doi.org/10.1016/j.neuron.2012.11.033)
- Mallick P, Kuster B. 2010. Proteomics: a pragmatic perspective. *Nature Biotechnology* **28**:695–709. doi: [10.1038/nbt.1658](https://doi.org/10.1038/nbt.1658)
- Martin I, Kim JW, Dawson VL, Dawson TM. 2014. LRRK2 pathobiology in parkinson's disease. *Journal of Neurochemistry* **131**:554–565. doi: [10.1111/jnc.12949](https://doi.org/10.1111/jnc.12949)
- Martin I, Kim JW, Lee BD, Kang HC, Xu J-C, Jia H, Stankowski J, Kim M-S, Zhong J, Kumar M, Andrabi SA, Xiong Y, Dickson DW, Wszolek ZK, Pandey A, Dawson TM, Dawson VL. 2014. Ribosomal protein s15 phosphorylation mediates LRRK2 neurodegeneration in parkinson's disease. *Cell* **157**:472–485. doi: [10.1016/j.cell.2014.01.064](https://doi.org/10.1016/j.cell.2014.01.064)
- Mata IF, Jang Y, Kim C-H, Hanna DS, Dorschner MO, Samii A, Agarwal P, Roberts JW, Klepitskaya O, Shprecher DR, Chung KA, Factor SA, Espay AJ, Revilla FJ, Higgins DS, Litvan I, Leverenz JB, Yearout D, Inca-Martinez M, Martinez E, Thompson TR, Cholerton BA, Hu S-C, Edwards KL, Kim K-S, Zabetian CP. 2015. The RAB39B p.G192R mutation causes x-linked dominant parkinson's disease. *Molecular Neurodegeneration* **10**:50. doi: [10.1186/s13024-015-0045-4](https://doi.org/10.1186/s13024-015-0045-4)
- Matta S, Van Kolen K, da Cunha R, van den Bogaart G, Mandemakers W, Miskiewicz K, De Bock P-J, Morais VA, Vilain S, Haddad D, Delbroek L, Swerts J, Chávez-Gutiérrez L, Esposito G, Daneels G, Karran E, Holt M, Gevaert K, Moechars DW, De Strooper B, Verstreken P. 2012. LRRK2 controls an EndoA phosphorylation cycle in synaptic endocytosis. *Neuron* **75**:1008–1021. doi: [10.1016/j.neuron.2012.08.022](https://doi.org/10.1016/j.neuron.2012.08.022)
- Nalls MA, Pankratz N, Lill CM, Do CB, Hernandez DG, Saad M, DeStefano AL, Kara E, Bras J, Sharma M, Schulte C, Keller MF, Arepalli S, Letson C, Edsall C, Stefansson H, Liu X, Pliner H, Lee JH, Cheng R, Ikram MA, Ioannidis JP, Hadjigeorgiou GM, Bis JC, Martinez M, Perlmutter JS, Goate A, Marder K, Fiske B, Sutherland M,

- Xiomerisiou G, Myers RH, Clark LN, Stefansson K, Hardy JA, Heutink P, Chen H, Wood NW, Houlden H, Payami H, Brice A, Scott WK, Gasser T, Bertram L, Eriksson N, Foroud T, Singleton AB. International Parkinson's Disease Genomics Consortium (IPDGC); Parkinson's Study Group (PSG) Parkinson's Research: The Organized GENetics Initiative (PROGENI); 23andMe; GenePD; NeuroGenetics Research Consortium (NGRC); Hussman Institute of Human Genomics (HIHG); Ashkenazi Jewish Dataset Investigator; Cohorts for Health and Aging Research in Genetic Epidemiology (CHARGE); North American Brain Expression Consortium (NABEC); United Kingdom Brain Expression Consortium (UKBEC); Greek Parkinson's Disease Consortium; Alzheimer Genetic Analysis Group. 2014. Large-scale meta-analysis of genome-wide association data identifies six new risk loci for parkinson's disease. *Nature Genetics* **46**:989–993. doi: [10.1038/ng.3043](https://doi.org/10.1038/ng.3043)
- Nichols RJ, Dzakmo N, Hutti JE, Cantley LC, Deak M, Moran J, Bamborough P, Reith AD, Alessi DR. 2009. Substrate specificity and inhibitors of LRRK2, a protein kinase mutated in parkinson's disease. *Biochemical Journal* **424**:47–60. doi: [10.1042/BJ20091035](https://doi.org/10.1042/BJ20091035)
- Nichols RJ, Dzakmo N, Morrice NA, Campbell DG, Deak M, Ordureau A, Macartney T, Tong Y, Shen J, Prescott AR, Alessi DR. 2010. 14-3-3 binding to LRRK2 is disrupted by multiple parkinson's disease-associated mutations and regulates cytoplasmic localization. *Biochemical Journal* **430**:393–404. doi: [10.1042/BJ20100483](https://doi.org/10.1042/BJ20100483)
- Ohta E, Kawakami F, Kubo M, Obata F. 2011. LRRK2 directly phosphorylates Akt1 as a possible physiological substrate: impairment of the kinase activity by parkinson's disease-associated mutations. *FEBS Letters* **585**: 2165–2170. doi: [10.1016/j.febslet.2011.05.044](https://doi.org/10.1016/j.febslet.2011.05.044)
- Olsen JV, Blagoev B, Gnad F, Macek B, Kumar C, Mortensen P, Mann M. 2006. Global, in vivo, and site-specific phosphorylation dynamics in signaling networks. *Cell* **127**:635–648. doi: [10.1016/j.cell.2006.09.026](https://doi.org/10.1016/j.cell.2006.09.026)
- Ong SE, Blagoev B, Kratchmarova I, Kristensen DB, Steen H, Pandey A, Mann M. 2002. Stable isotope labeling by amino acids in cell culture, SILAC, as a simple and accurate approach to expression proteomics. *Molecular & Cellular Proteomics* **1**:376–386. doi: [10.1074/mcp.M200025-MCP200](https://doi.org/10.1074/mcp.M200025-MCP200)
- Papkovskaia TD, Chau K-Y, Inesta-Vaquera F, Papkovsky DB, Healy DG, Nishio K, Staddon J, Duchon MR, Hardy J, Schapira AHV, Cooper JM. 2012. G2019S leucine-rich repeat kinase 2 causes uncoupling protein-mediated mitochondrial depolarization. *Human Molecular Genetics* **21**:4201–4213. doi: [10.1093/hmg/dds244](https://doi.org/10.1093/hmg/dds244)
- Pfeffer SR. 2005. Structural clues to rab GTPase functional diversity. *Journal of Biological Chemistry* **280**:15485–15488. doi: [10.1074/jbc.R500003200](https://doi.org/10.1074/jbc.R500003200)
- Pylypenko O, Rak A, Reents R, Niculae A, Sidorovitch V, Cioaca M-D, Bessolitsyna E, Thomä NH, Waldmann H, Schlichting I, Goody RS, Alexandrov K. 2003. Structure of rab escort protein-1 in complex with rab geranylgeranyltransferase. *Molecular Cell* **11**:483–494. doi: [10.1016/S1097-2765\(03\)00044-3](https://doi.org/10.1016/S1097-2765(03)00044-3)
- Qing H, Wong W, McGeer EG, McGeer PL. 2009. Lrrk2 phosphorylates alpha synuclein at serine 129: parkinson disease implications. *Biochemical and Biophysical Research Communications* **387**:149–152. doi: [10.1016/j.bbrc.2009.06.142](https://doi.org/10.1016/j.bbrc.2009.06.142)
- Rak A, Pylypenko O, Durek T, Watzke A, Kushnir S, Brunsvelde L, Waldmann H, Goody RS, Alexandrov K. 2003. Structure of rab GDP-dissociation inhibitor in complex with prenylated YPT1 GTPase. *Science* **302**:646–650. doi: [10.1126/science.1087761](https://doi.org/10.1126/science.1087761)
- Reith AD, Bamborough P, Jandu K, Andreotti D, Mensah L, Dossang P, Choi HG, Deng X, Zhang J, Alessi DR, Gray NS. 2012. GSK2578215A; a potent and highly selective 2-arylmethoxy-5-substituent-n-arylbenzamide LRRK2 kinase inhibitor. *Bioorganic & Medicinal Chemistry Letters* **22**:5625–5629. doi: [10.1016/j.bmcl.2012.06.104](https://doi.org/10.1016/j.bmcl.2012.06.104)
- Rivero-Ríos P, Gómez-Suaga P, Fernández B, Madero-Pérez J, Schwab AJ, Ebert AD, Hilfiker S. 2015. Alterations in late endocytic trafficking related to the pathobiology of LRRK2-linked parkinson's disease. *Biochemical Society Transactions* **43**:390–395. doi: [10.1042/BST20140301](https://doi.org/10.1042/BST20140301)
- Roux PP, Thibault P. 2013. The coming of age of phosphoproteomics—from large data sets to inference of protein functions. *Molecular & Cellular Proteomics* **12**:3453–3464. doi: [10.1074/mcp.R113.032862](https://doi.org/10.1074/mcp.R113.032862)
- Rudenko IN, Cookson MR. 2014. Heterogeneity of leucine-rich repeat kinase 2 mutations: genetics, mechanisms and therapeutic implications. *Neurotherapeutics* **11**:738–750. doi: [10.1007/s13311-014-0284-z](https://doi.org/10.1007/s13311-014-0284-z)
- Satake W, Nakabayashi Y, Mizuta I, Hirota Y, Ito C, Kubo M, Kawaguchi T, Tsunoda T, Watanabe M, Takeda A, Tomiyama H, Nakashima K, Hasegawa K, Obata F, Yoshikawa T, Kawakami H, Sakoda S, Yamamoto M, Hattori N, Murata M, Nakamura Y, Toda T. 2009. Genome-wide association study identifies common variants at four loci as genetic risk factors for parkinson's disease. *Nature Genetics* **41**:1303–1307. doi: [10.1038/ng.485](https://doi.org/10.1038/ng.485)
- Satpathy S, Wagner SA, Beli P, Gupta R, Kristiansen TA, Malinova D, Francavilla C, Tolar P, Bishop GA, Hostager BS, Choudhary C. 2015. Systems-wide analysis of BCR signalosomes and downstream phosphorylation and ubiquitylation. *Molecular Systems Biology* **11**:810. doi: [10.15252/msb.20145880](https://doi.org/10.15252/msb.20145880)
- Schapansky J, Nardozi JD, Felizia F, LaVoie MJ. 2014. Membrane recruitment of endogenous LRRK2 precedes its potent regulation of autophagy. *Human Molecular Genetics* **23**:4201–4214. doi: [10.1093/hmg/ddu138](https://doi.org/10.1093/hmg/ddu138)
- Schapansky J, Nardozi JD, LaVoie MJ. 2015. The complex relationships between microglia, alpha-synuclein, and LRRK2 in parkinson's disease. *Neuroscience* **302**:74–88. doi: [10.1016/j.neuroscience.2014.09.049](https://doi.org/10.1016/j.neuroscience.2014.09.049)
- Seabra MC, Wasmeier C. 2004. Controlling the location and activation of rab GTPases. *Current Opinion in Cell Biology* **16**:451–457. doi: [10.1016/j.ceb.2004.06.014](https://doi.org/10.1016/j.ceb.2004.06.014)
- Sharma K, D'Souza RCJ, Tyanova S, Schaab C, Wiśniewski JR, Cox J, Mann M. 2014. Ultradeep human phosphoproteome reveals a distinct regulatory nature of tyr and Ser/Thr-based signaling. *Cell Reports* **8**:1583–1594. doi: [10.1016/j.celrep.2014.07.036](https://doi.org/10.1016/j.celrep.2014.07.036)
- Sheng Z, Zhang S, Bustos D, Kleinheinz T, Le Pichon CE, Dominguez SL, Solanoy HO, Drummond J, Zhang X, Ding X, Cai F, Song Q, Li X, Yue Z, van der Brug MP, Burdick DJ, Gunzner-Toste J, Chen H, Liu X, Estrada AA, Sweeney ZK, Scarce-Levie K, Moffat JG, Kirkpatrick DS, Zhu H. 2012. Ser1292 autophosphorylation is an

- indicator of LRRK2 kinase activity and contributes to the cellular effects of PD mutations. *Science Translational Medicine* **4**:164ra161. doi: [10.1126/scitranslmed.3004485](https://doi.org/10.1126/scitranslmed.3004485)
- Simón-Sánchez J, Schulte C, Bras JM, Sharma M, Gibbs JR, Berg D, Paisan-Ruiz C, Lichtner P, Scholz SW, Hernandez DG, Krüger R, Federoff M, Klein C, Goate A, Perlmutter J, Bonin M, Nalls MA, Illig T, Gieger C, Houlden H, Steffens M, Okun MS, Racette BA, Cookson MR, Foote KD, Fernandez HH, Traynor BJ, Schreiber S, Arepalli S, Zonozi R, Gwinn K, van der Brug M, Lopez G, Chanock SJ, Schatzkin A, Park Y, Hollenbeck A, Gao J, Huang X, Wood NW, Lorenz D, Deuschl G, Chen H, Riess O, Hardy JA, Singleton AB, Gasser T. 2009. Genome-wide association study reveals genetic risk underlying parkinson's disease. *Nature Genetics* **41**:1308–1312. doi: [10.1038/ng.487](https://doi.org/10.1038/ng.487)
- Stenmark H. 2009. Rab GTPases as coordinators of vesicle traffic. *Nature Reviews Molecular Cell Biology* **10**: 513–525. doi: [10.1038/nrm2728](https://doi.org/10.1038/nrm2728)
- Taymans J-M, Nkiliza A, Chartier-Harlin M-C. 2015. Deregulation of protein translation control, a potential game-changing hypothesis for parkinson's disease pathogenesis. *Trends in Molecular Medicine* **21**:466–472. doi: [10.1016/j.molmed.2015.05.004](https://doi.org/10.1016/j.molmed.2015.05.004)
- Vizcaíno JA, Deutsch EW, Wang R, Csordas A, Reisinger F, Ríos D, Dianas JA, Sun Z, Farrah T, Bandeira N, Binz P-A, Xenarios I, Eisenacher M, Mayer G, Gatto L, Campos A, Chalkley RJ, Kraus H-J, Albar JP, Martinez-Bartolomé S, Apweiler R, Omenn GS, Martens L, Jones AR, Hermjakob H. 2014. ProteomeXchange provides globally coordinated proteomics data submission and dissemination. *Nature Biotechnology* **32**:223–226. doi: [10.1038/nbt.2839](https://doi.org/10.1038/nbt.2839)
- Wandinger-Ness A, Zerial M. 2014. Rab proteins and the compartmentalization of the endosomal system. *Cold Spring Harbor Perspectives in Biology* **6**:a022616–a022616 doi: [10.1101/cshperspect.a022616](https://doi.org/10.1101/cshperspect.a022616)
- West AB, Moore DJ, Biskup S, Bugayenko A, Smith WW, Ross CA, Dawson VL, Dawson TM. 2005. From the cover: parkinson's disease-associated mutations in leucine-rich repeat kinase 2 augment kinase activity. *Proceedings of the National Academy of Sciences of the United States of America* **102**:16842–16847. doi: [10.1073/pnas.0507360102](https://doi.org/10.1073/pnas.0507360102)
- Westlake CJ, Baye LM, Nachury MV, Wright KJ, Ervin KE, Phu L, Chalouni C, Beck JS, Kirkpatrick DS, Slusarski DC, Sheffield VC, Scheller RH, Jackson PK. 2011. Primary cilia membrane assembly is initiated by Rab11 and transport protein particle II (tRAPP II) complex-dependent trafficking of Rabin8 to the centrosome. *Proceedings of the National Academy of Sciences of the United States of America* **108**:2759–2764. doi: [10.1073/pnas.1018823108](https://doi.org/10.1073/pnas.1018823108)
- Wiggin GR, Soloaga A, Foster JM, Murray-Tait V, Cohen P, Arthur JSC. 2002. MSK1 and MSK2 are required for the mitogen- and stress-induced phosphorylation of CREB and ATF1 in fibroblasts. *Molecular and Cellular Biology* **22**:2871–2881. doi: [10.1128/MCB.22.8.2871-2881.2002](https://doi.org/10.1128/MCB.22.8.2871-2881.2002)
- Wilson GR, Sim JCH, McLean C, Giannandrea M, Galea CA, Riseley JR, Stephenson SEM, Fitzpatrick E, Haas SA, Pope K, Hogan KJ, Gregg RG, Bromhead CJ, Wargowski DS, Lawrence CH, James PA, Churchyard A, Gao Y, Phelan DG, Gillies G, Salce N, Stanford L, Marsh APL, Mignogna ML, Hayflick SJ, Leventer RJ, Delatycki MB, Mellick GD, Kalscheuer VM, D'Adamo P, Bahlo M, Amor DJ, Lockhart PJ. 2014. Mutations in RAB39B cause x-linked intellectual disability and early-onset parkinson disease with  $\alpha$ -synuclein pathology. *The American Journal of Human Genetics* **95**:729–735. doi: [10.1016/j.ajhg.2014.10.015](https://doi.org/10.1016/j.ajhg.2014.10.015)
- Xiong Y, Yuan C, Chen R, Dawson TM, Dawson VL. 2012. ArfGAP1 is a GTPase activating protein for LRRK2: reciprocal regulation of ArfGAP1 by LRRK2. *Journal of Neuroscience* **32**:3877–3886. doi: [10.1523/JNEUROSCI.4566-11.2012](https://doi.org/10.1523/JNEUROSCI.4566-11.2012)
- Yao C, Johnson WM, Gao Y, Wang W, Zhang J, Deak M, Alessi DR, Zhu X, Mieyal JJ, Roder H, Wilson-Delfosse AL, Chen SG. 2013. Kinase inhibitors arrest neurodegeneration in cell and c. elegans models of LRRK2 toxicity. *Human Molecular Genetics* **22**:328–344. doi: [10.1093/hmg/dds431](https://doi.org/10.1093/hmg/dds431)
- Yun HJ, Kim H, Ga I, Oh H, Ho DH, Kim J, Seo H, Son I, Seol W. 2015. An early endosome regulator, Rab5b, is an LRRK2 kinase substrate. *Journal of Biochemistry* **157**:485–495. doi: [10.1093/jb/mvv005](https://doi.org/10.1093/jb/mvv005)
- Yun HJ, Park J, Ho DH, Kim H, Kim C-H, Oh H, Ga I, Seo H, Chang S, Son I, Seol W. 2013. LRRK2 phosphorylates snapin and inhibits interaction of snapin with SNAP-25. *Experimental & Molecular Medicine* **45**:e36. doi: [10.1038/emm.2013.68](https://doi.org/10.1038/emm.2013.68)
- Zhang Q, Pan Y, Yan R, Zeng B, Wang H, Zhang X, Li W, Wei H, Liu Z. 2015. Commensal bacteria direct selective cargo sorting to promote symbiosis. *Nature Immunology* **16**:918–926. doi: [10.1038/ni.3233](https://doi.org/10.1038/ni.3233)



---

## Figures and figure supplements

Phosphoproteomics reveals that Parkinson's disease kinase LRRK2 regulates a subset of Rab GTPases

**Martin Steger *et al***

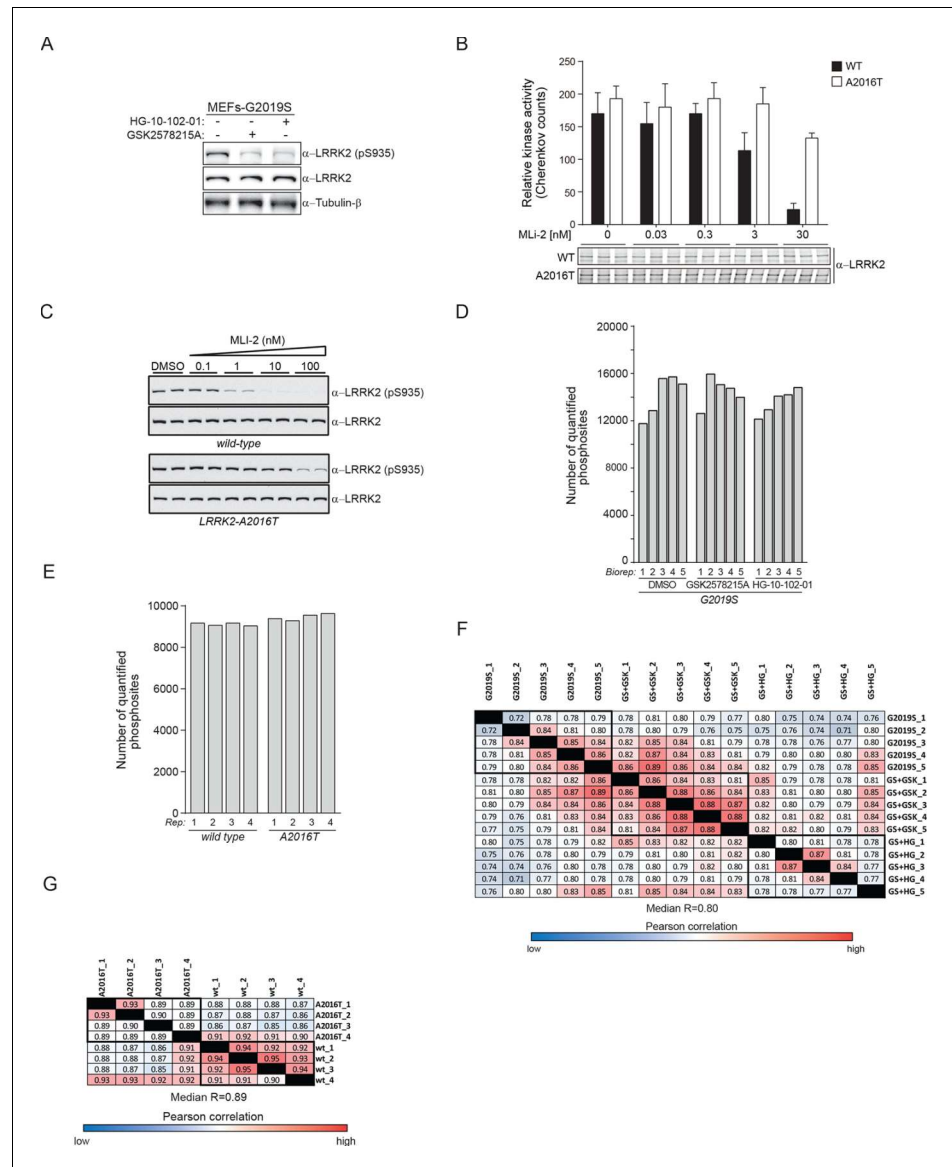


**Figure 1—figure supplement 1.** Two unbiased phosphoproteomic screens identify physiological LRRK2 targets. (A) Western blot analysis of wild type (wt) and LRRK2-G2019S<sup>GSK</sup> (G2019S) mouse embryonic fibroblasts (MEFs), treated with DMSO (-) or 1  $\mu$ M of GSK2578215A or HG-10-102-01 for 90 min. (B) In vitro kinase assay using LRRK2 immunoprecipitated from MEFs (wt and A2016T) in the presence of various concentrations of MLI-2. Phosphorylation of Nictide was quantified by liquid scintillation counting. The western blot below shows that similar levels of LRRK2 were used. Error bars are mean  $\pm$  SD (n=3). (C) Western blot analysis of pS935-LRRK2 and total LRRK2 levels in wt-LRRK2 MEFs and A2016T-LRRK2 MEFs treated for 60 min with the indicated concentrations of MLI-2. (D) Number of quantified class I phosphorylation sites of PS1 in five biological replicates (Biorep) per phenotype analyzed. (E) More than 9000 phosphorylation sites are identified in each of the four biological replicates (Biorep) of wild type and A2016T MEFs (PS2). (F) Pearson correlations for the phosphoproteomes of PS1 and PS2 (G). SD, standard deviation. DOI: 10.7554/eLife.12813.004

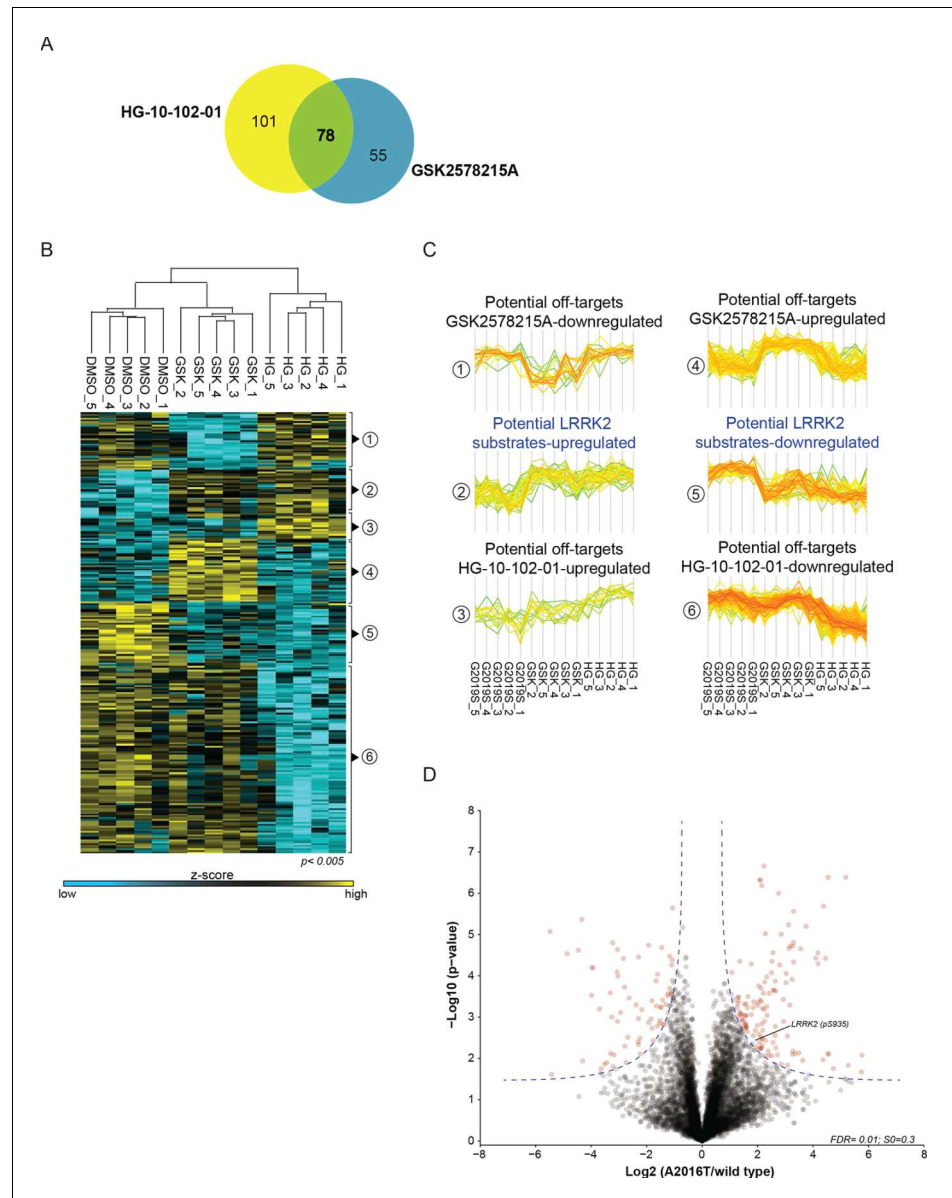


**Figure 1—figure supplement 2.** Two unbiased phosphoproteomic screens identify physiological LRRK2 targets. (A) Venn diagram of significantly regulated (ANOVA,  $p < 0.005$ ) sites with GSK2578215A and HG-10-102-01 in PS1. (B) Heat map of regulated phosphosites identified in five biological replicates of MEFs (LRRK2-G2019S<sup>GSK</sup> (DMSO), LRRK2-G2019S<sup>GSK</sup>+ GSK2578215A, and LRRK2-G2019S<sup>GSK</sup>+ HG-10-102-01). (C) Clusters identified in (B). (D) Volcano plot of all phosphosites of PS2. Significant sites are in blue and pS935 is indicated. ANOVA, analysis of variance.

DOI: 10.7554/eLife.12813.005

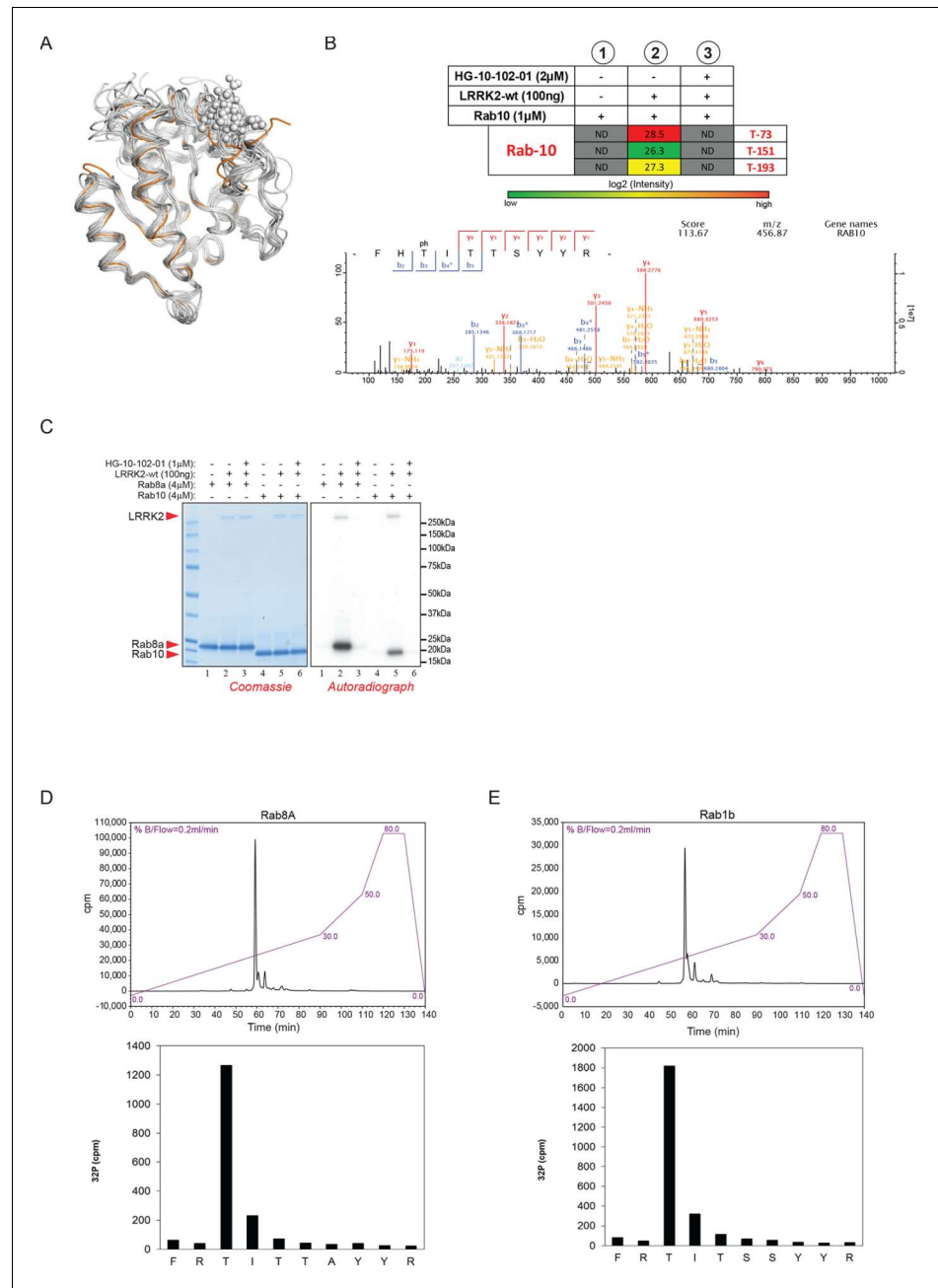


**Figure 2—figure supplement 1.** Phosphorylation of Rab GTPases by LRRK2 in vitro. (A) Superposition of the crystal structures of 14 Rab isoforms (Rab1a, 1b, 2, 3, 4, 6, 7, 9, 12, 18, 27, 30, 31, 43). All potential LRRK2 phosphorylation sites (in grey) cluster in the same region. (B) MS analysis of in vitro phosphorylated Rab10 identified three LRRK2-specific sites (note that phosphorylation is prevented completely by HG-10-102-01) and pT73 as the one with the highest intensity. The collision-induced dissociation (CID) fragmentation spectrum and the Andromeda score (score) (Cox et al., 2011) for the tryptic pT73-Rab10 peptide are shown. (C) Phosphorylation of Rab8a and Rab1b by LRRK2-wt. Inhibition of LRRK2 by HG-10-102-01 prevents phosphorylation. (D) HPLC trace of tryptic peptides of Rab8a and Rab1b (E) after in vitro phosphorylation by LRRK2-wt and Figure 2—figure supplement 1 continued on next page

Figure 2—figure supplement 1 continued

sequence analysis of tryptic peptides. Y axis units are relative Cherenkov counts per minute. MS, mass spectrometry; wt, wild type.

DOI: [10.7554/eLife.12813.007](https://doi.org/10.7554/eLife.12813.007)

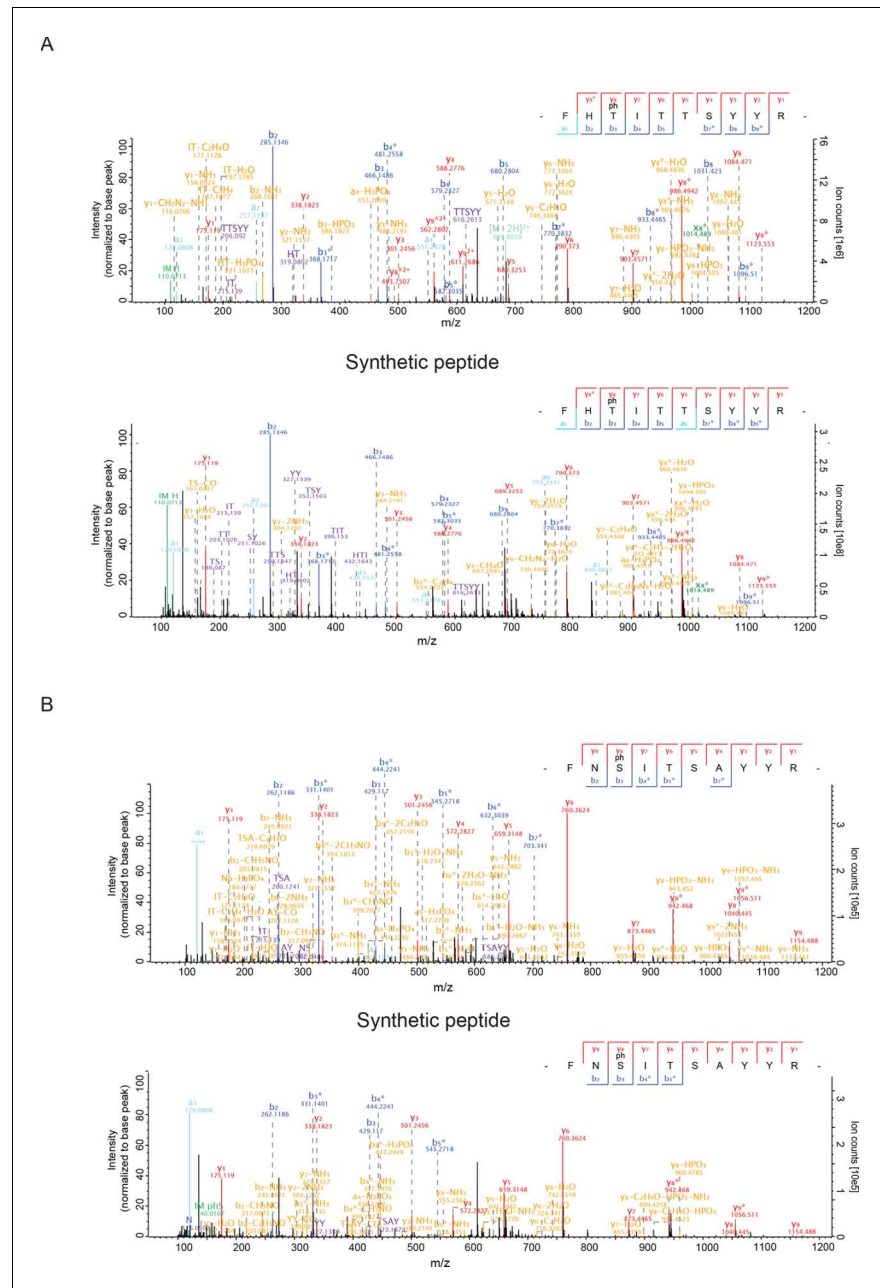


**Figure 3—figure supplement 1.** HCD MS/MS spectra of synthetic Rab peptides (A) Higher energy collision-induced dissociation (HCD) MS/MS spectra of the pT73-Rab10 peptide identified in PS2. The spectrum of the corresponding synthetic peptide is shown below. (B) Same as (A) but pS105-Rab12.  
DOI: 10.7554/eLife.12813.009

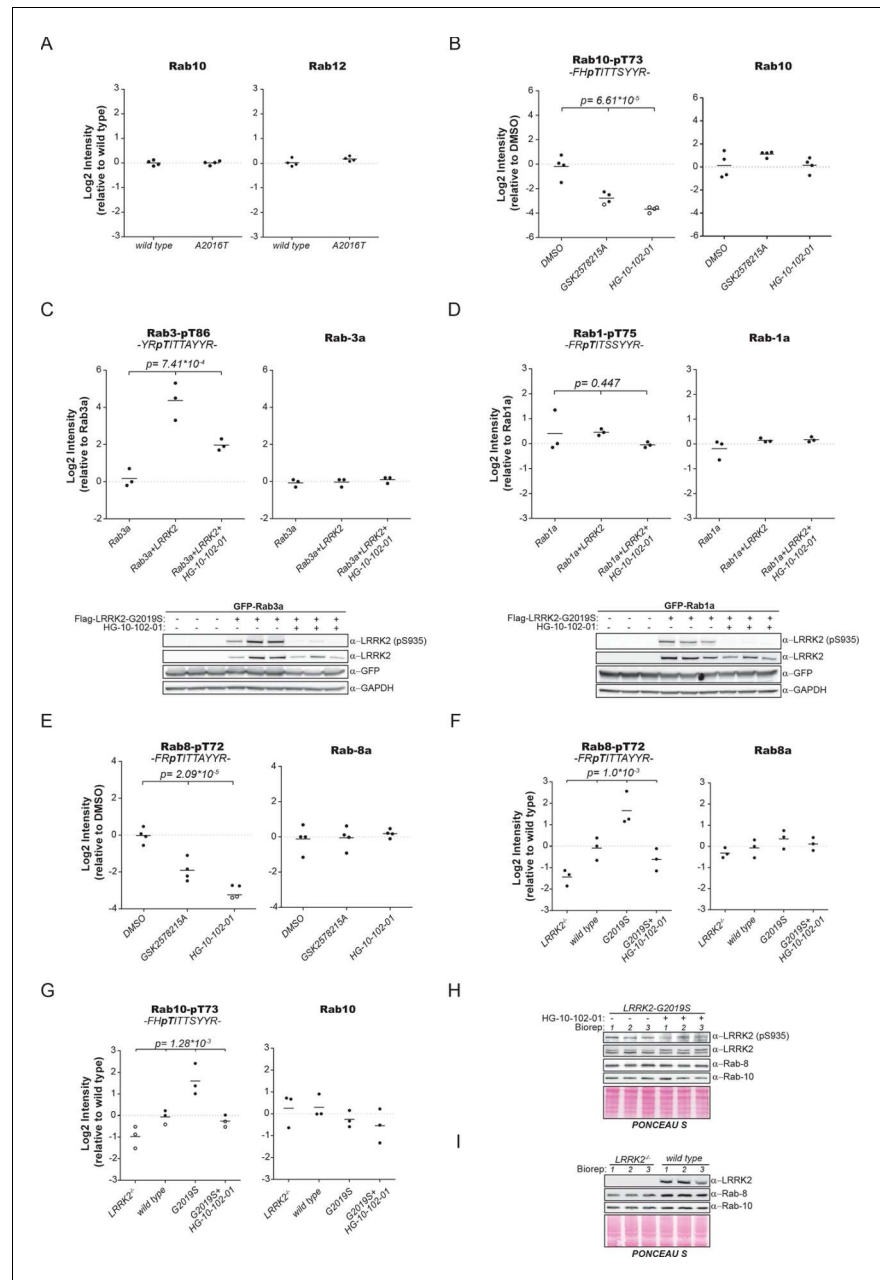


**Figure 3—figure supplement 2.** Quantification of Rab phosphorylation by mass spectrometry (MS). (A) MS-based label-free quantification (MaxLFQ, Cox et al., 2014) of the Rab10 and Rab12 protein intensities in PS2. (B) MS-based quantification of pT73-Rab10 (left) and total Rab10 (right) derived from HEK293 (trex flpIn) cells expressing GFP-LRRK2-G2019S after LRRK2 inhibition (n=4). (C) MS-quantified Rab3-pT86 peptide levels of ectopically expressed Rab3a alone or in combination with LRRK2-G2019S, in presence or absence of HG-10-102-01 (3 μM, 3 hr, n=3). A western blot of the same samples is shown below. (D) Same as (C) but Rab1a was expressed and pT75-Rab1a quantified. (E) Same as (B) with pT72-Rab8 (left) and total Rab8a (right). (F) Label-free quantification of pT72-Rab10 and (G) pT72-Rab8a from knockout, wt, G2019S, or G2019S treated with HG-10-102-01 (3 μM, 3 hr) MEFs. Total Rab10 and Rab8 protein levels were also quantified (n=3). (H) and (I) Western blot analyses of samples used in (F) and (G). Open circles indicate imputed values. MEFs, mouse embryonic fibroblasts; wt, wild type. DOI: 10.7554/eLife.12813.010

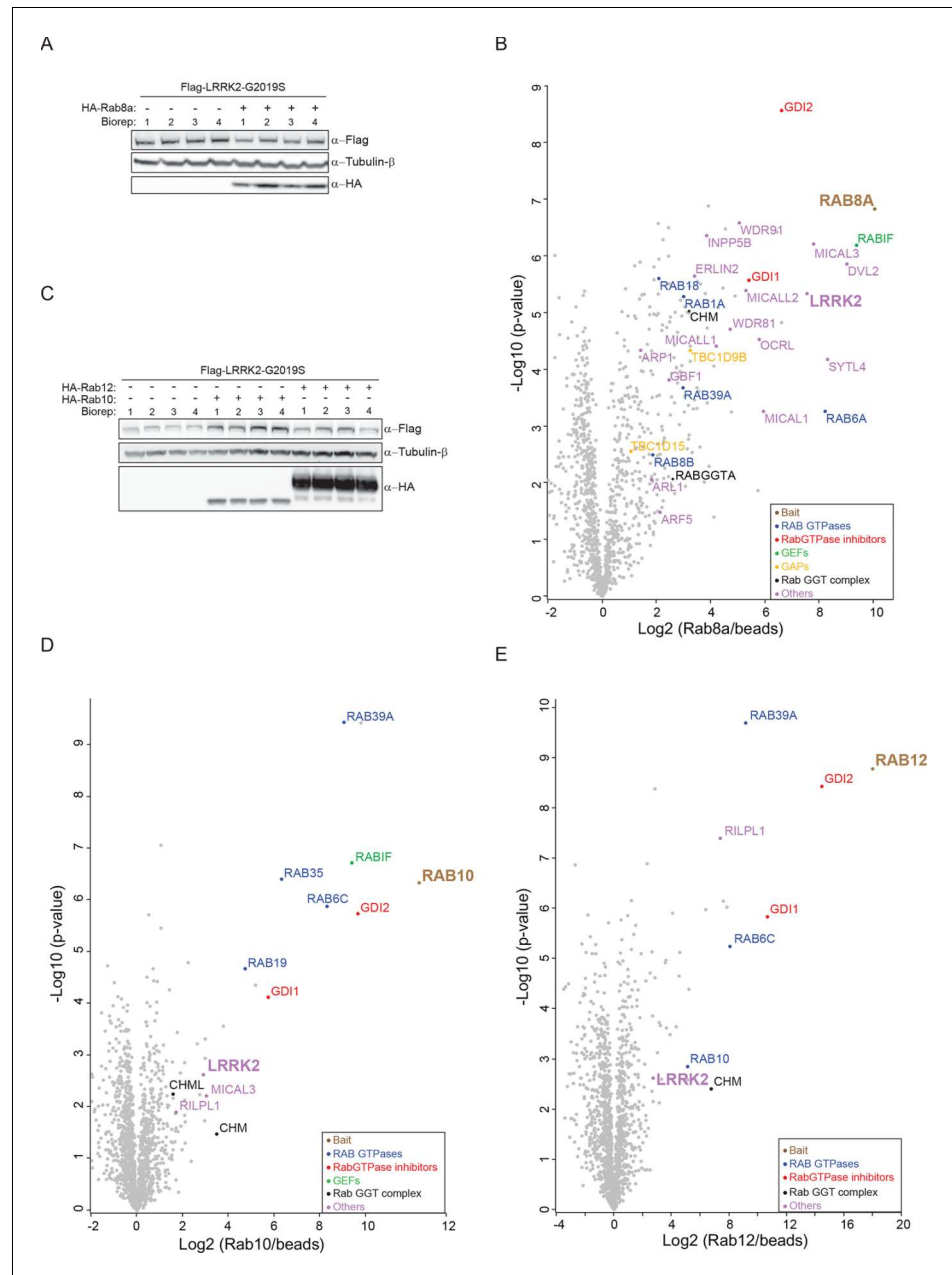


**Figure 3—figure supplement 3.** Several Rabs stably associate with LRRK2 in cells. (A) Western blot of HEK293 cells expressing flag-LRRK2-G2019S, either alone or in combination with HA-Rab8a. (B) Volcano plot of MS-quantified Rab8a interactors (n=4). (C) Same as (A) with HA-Rab10 or HA-Rab12. (D) and (E) Volcano plots of MS-quantified Rab10 and Rab12 interactors. MS, mass spectrometry.

DOI: [10.7554/eLife.12813.011](https://doi.org/10.7554/eLife.12813.011)

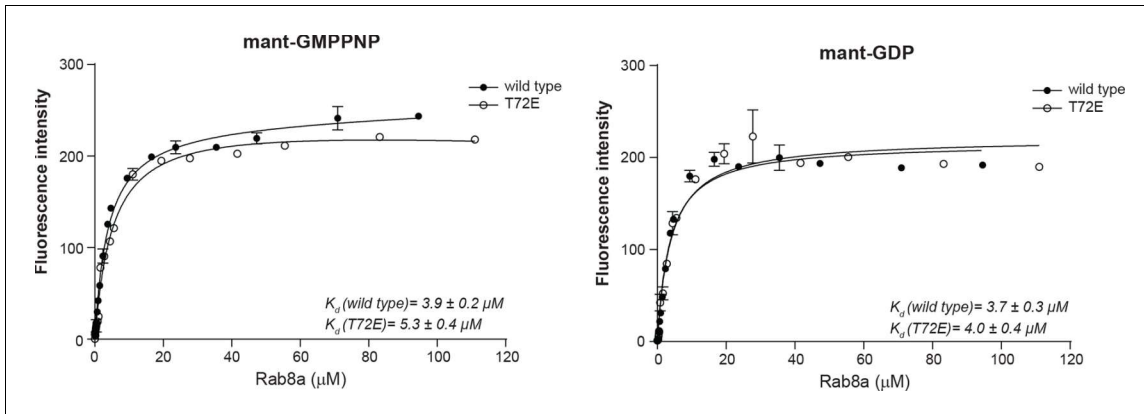


**Figure 5—figure supplement 1.** Rab8a nucleotide binding experiments. Titration experiment using Rab8a (wt and T72E) and fluorescently labeled non-hydrolysable GTP analog (mant-GMPPNP) or GDP (mant-GDP). The fluorescence signal is plotted as a function of Rab8a concentration. The dissociation constants ( $K_d$ )  $\pm$  SD are indicated. Error bars are mean  $\pm$  SD (n=3). SD, standard deviation; wt, wild type.

DOI: [10.7554/eLife.12813.014](https://doi.org/10.7554/eLife.12813.014)

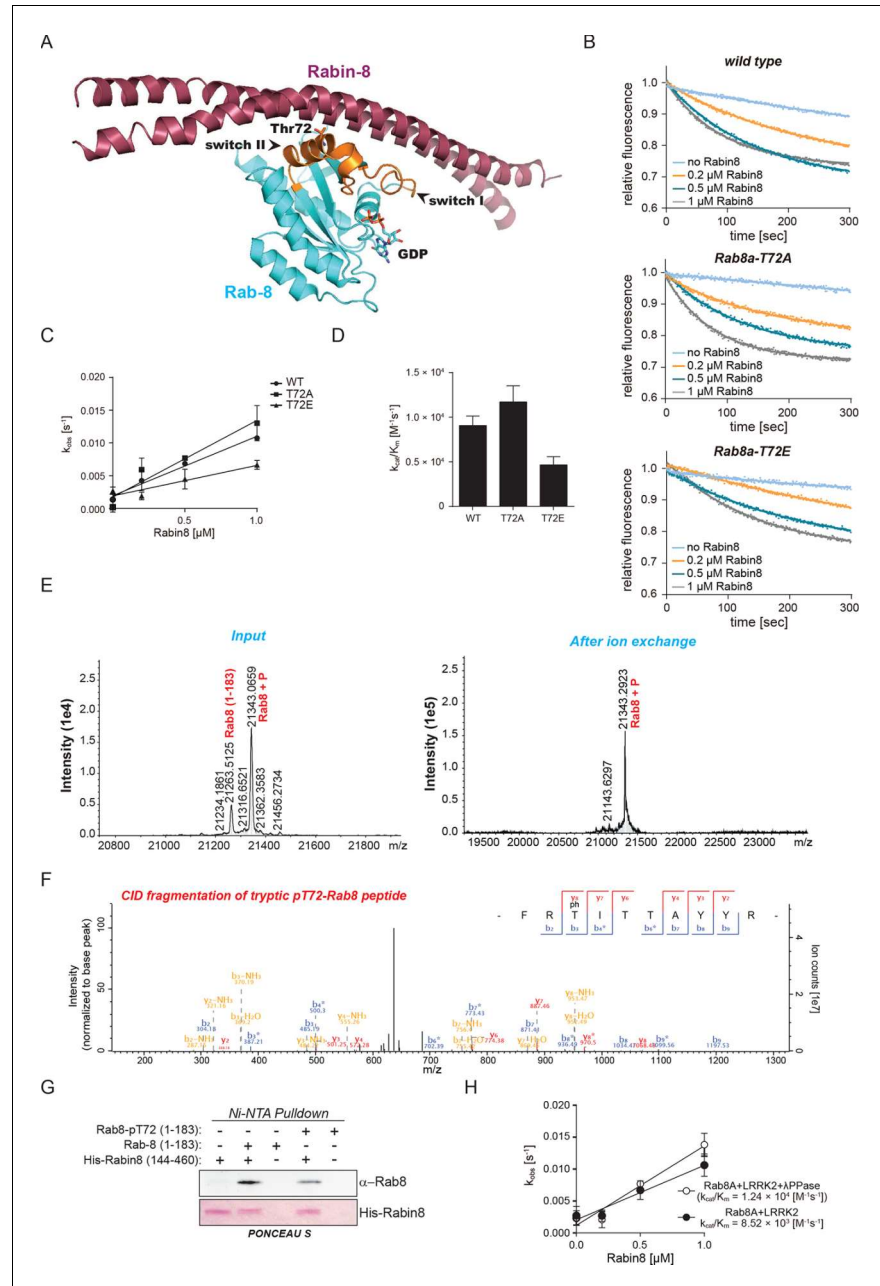


**Figure 5—figure supplement 2.** Rab8a guanine nucleotide exchange assays. (A) Ribbon structure of Rab8a in complex with Rabin8 (PDB: 4LHY). The LRRK2 phosphorylation site (T72) situated in the switch II region and forming close contact with Rabin8 is indicated. (B) Kinetics of mant-GDP dissociation from Rab8a (wt, T72A, and T72E) by Rabin8. (C) and (D) Representation of the observed rate constants ( $k_{obs}$ ) and catalytic efficiencies ( $k_{cat}/K_m$ ) for the same reactions. (E) ESI-TOF mass determination of Rab8a after in vitro phosphorylation by LRRK2-G2019S (left) and after enrichment of phosphorylated Rab8a by ion-exchange chromatography (right). (F) Collision-induced dissociation (CID) fragmentation spectrum of the tryptic pT72-Rab8a peptide, which was identified after phosphorylation of Rab8a by LRRK2 followed by enrichment of the phosphorylated form by ion exchange chromatography. (G)  $Ni^{2+}$ -NTA pull-down of Rab8a (non-phosphorylated or phosphorylated on T72) by HIS-Rabin8. *Figure 5—figure supplement 2 continued on next page*

Figure 5—figure supplement 2 continued

tagged Rabin8 using purified components. (H) Representation of the observed rate constants ( $k_{obs}$ ) and catalytic efficiencies ( $k_{cat}/K_m$ ) for the indicated reactions. Error bars are mean  $\pm$  SD (n=3).

DOI: [10.7554/eLife.12813.015](https://doi.org/10.7554/eLife.12813.015)

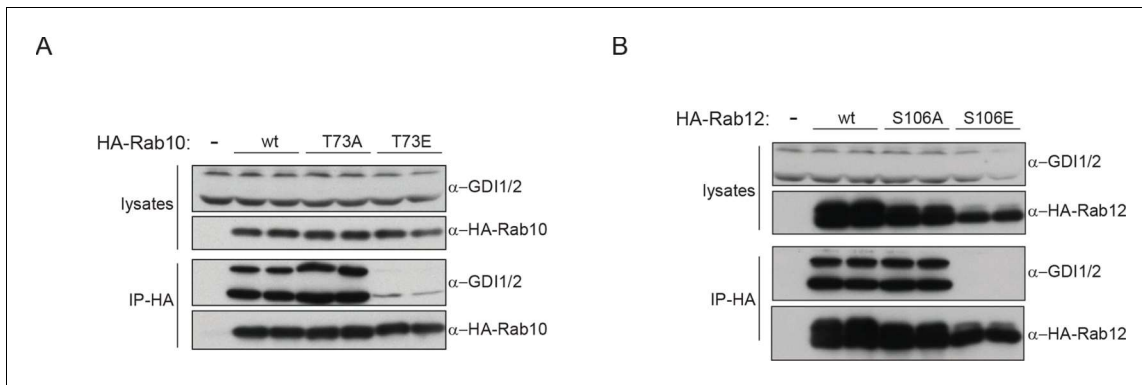


**Figure 6—figure supplement 1.** Rab10/12-GDI interactions. (A) HA-Rab10 constructs (wt, T73A, T73E) were expressed in HEK293 cells and lysates subjected to  $\alpha$ -HA immunoprecipitation before western blotting. (B) Same as (A) using HA-Rab12 (wt, S106A, S106E). wt, wild type.  
DOI: [10.7554/eLife.12813.017](https://doi.org/10.7554/eLife.12813.017)

# Extended discussion and perspectives

## 1 Towards a high-resolution structure of the IFT-B1 complex

The currently suggested composition of IFT-B1 consists of the 10 stably associated proteins IFT22/25/27/46/52/56/70/74/81/88, and extensive complex reconstitution studies using recombinant proteins led to a detailed interaction map of the individual components (Taschner et al. 2014) (see Fig. 9A). In the past years, a set of various high-resolution crystal structures of IFT-B1 proteins gave further insights into interaction surfaces and functions of individual domains. The novel IFT22/74/81 crystal structure obtained in this work represents the largest high-resolution structure (approximately 97 kDa) of an IFT subcomplex determined to date and the only structure of a trimeric assembly. The coiled-coil heterodimer IFT74/81 has previously been shown to provide a binding platform for several other IFT-B1 proteins (IFT22, IFT46/52 and IFT25/27), and forms an essential scaffold for IFT complex stability. Besides, it harbors an N-terminal tubulin-binding module and due to its elongated shape might as well function in other cargo interactions. The presented IFT22/74/81 structure covers more than 50 % and 60 % of the IFT74 and IFT81 sequences, respectively, and represents nearly 20 % of the whole IFT-B1 complex. It thus significantly supplements available structural information on IFT-B1 and provides a step towards a high-resolution model of the entire subcomplex. Currently available crystal structures including the one from this work thereby comprise about 50 % of the overall complex mass. This allows an updated view on the three-dimensional IFT-B1 model, as schematically depicted in Fig. 22. However, in order to correctly determine relative positions of individual linker-connected domains or map structurally uncharacterized binding sites (e. g. the IFT46/52-binding site on IFT74/81), further structural studies will be required using larger assemblies. In fact, in the course of this project reproducible crystals of a nearly full-length pentameric IFT22/25/27/74/81 complex could be obtained (data not shown), and yielded a full dataset at 3.8 Å resolution, but phasing with available crystal structures as molecular replacement models was not possible. The used constructs provide a promising basis for further crystallization and structure determination trials.

Apart from X-ray crystallography, cryo-EM as a prevalent method for structure determination of large macromolecular complexes will also be a useful tool for structural approaches on the IFT complex. Crystal structures of individual proteins and domains can then be modeled into obtained EM densities, producing a pseudo-atomic model of IFT-B1, IFT-B2 or even the whole IFT complex. Such three-dimensional models would certainly broaden our knowledge about ciliary transport complexes at the molecular level significantly, and might identify new potential cargo-binding sites or provide insights into IFT train formation.

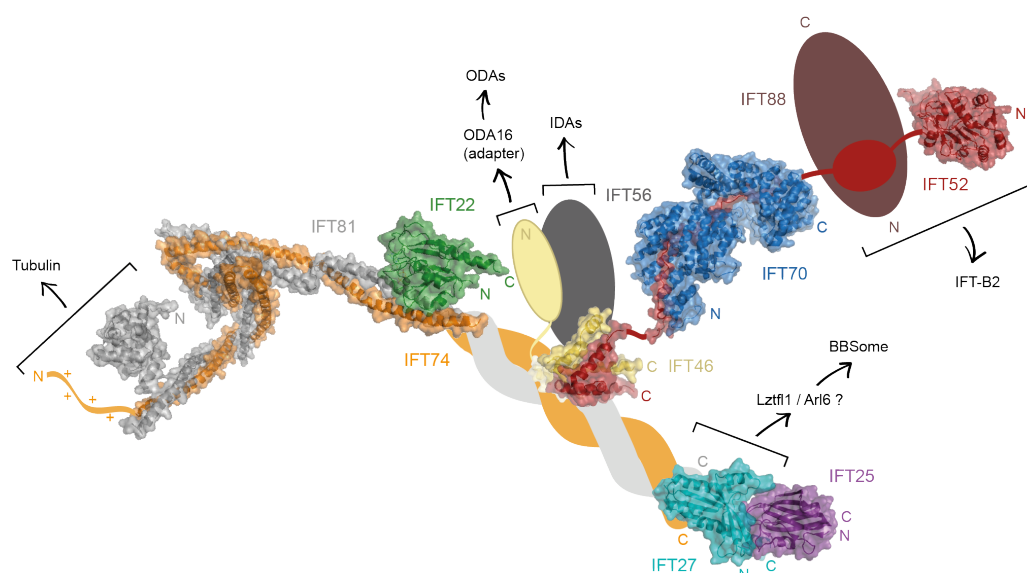


**Figure 22: Schematic interaction map of the IFT-B1 subcomplex with superposed available crystal structures**  
Structures are shown in surface representation and cargo interactions are indicated with arrows. (PDB IDs: 2yc2, 4uzz, 5fmr, 4uzy; IFT22/74/81: this work)

## 2 IFT74 could interact with IFT-A via a conserved N-terminal surface patch

As outlined in the introduction (section 2.2), different notions exist regarding the interplay of IFT-B and IFT-A subcomplexes. The initial characterization of IFT particle composition found that IFT-B and IFT-A interact at low ionic strength, but that they were easily separable at increasing salt concentrations (D G Cole et al. 1998). A recent publication on *in vivo* studies in *C. reinhardtii* reported that the N-terminal region of IFT74 is essential for IFT-A assembly into IFT trains at the ciliary base and import of IFT-A into the cilium (Brown et al. 2015). The authors showed that IFT74 is essential for overall IFT-B stability and that IFT74 null mutants fail to assemble cilia. This is in consistency with previously published interaction models from our lab (Taschner et al. 2014) and is further supported by the IFT22/74/81 crystal structure from this work. The structure demonstrates that IFT74 forms a tightly intertwined coiled-coil with IFT81, and depletion of either protein would certainly destabilize the tertiary structure of its partner. Besides, we showed that the binding site for IFT22 is of composite nature, involving both IFT74 and IFT81 residues (Fig. 14).

In the same study, Brown and colleagues performed rescue experiments and demonstrated that N-terminally truncated IFT74 versions lacking aa 1-130 and aa 1-196 were sufficient to stabilize IFT-B. However, only IFT74 $\Delta$ 130 enabled cilium assembly while expression of IFT74 $\Delta$ 196 severely disturbed ciliogenesis and led to short cilia filled with IFT aggregates, a typical retrograde IFT inactivation phenotype. Furthermore, the authors revealed that this is caused by defective IFT-A association with IFT particles and import of IFT-A into the ciliary organelle, and suggest that IFT-A is recruited to IFT-B at the basal body for ciliary import via aa 131-196 on IFT74 (D G Cole et al. 1998; Brown et al. 2015).

This residue range aligns to aa 82-147 of the *T. brucei* IFT74 homolog and contains residues visible in the presented crystal structure. To increase protein stability, we used an N-terminally truncated IFT74 version for crystallization, thus eliminating the unstructured N-terminal 79 residues while keeping the first coiled-coil part (cCl) intact. Interestingly, when analyzing the region hypothesized to be involved in direct or indirect IFT-A recruitment, we found two highly conserved sequence stretches in IFT74 sequence alignments (Fig. 23A). Stretch-1 is not completely visible in the crystal structure, but is spatially arranged N-terminally of the globular IFT81 CH domain and contains residues involved in stabilizing the IFT81 portion of cCl as well as residues previously suggested to bind tubulin E-hooks (Brown et al. 2015; Bhogaraju et al. 2013b). In contrast, stretch-2 forms a very conserved surface patch on cCl (Fig. 23B) and even the biggest continuous conserved area mapped onto the IFT22/74/81 crystal structure. Evolutionarily conserved surface areas are assumed to be good candidates for protein-protein interaction surfaces, and we suggest that this area might be involved in IFT-A binding. In addition, IFT81 contributes several conserved residues to this patch, consistent with the previously mentioned composite quality of other IFT interactions.

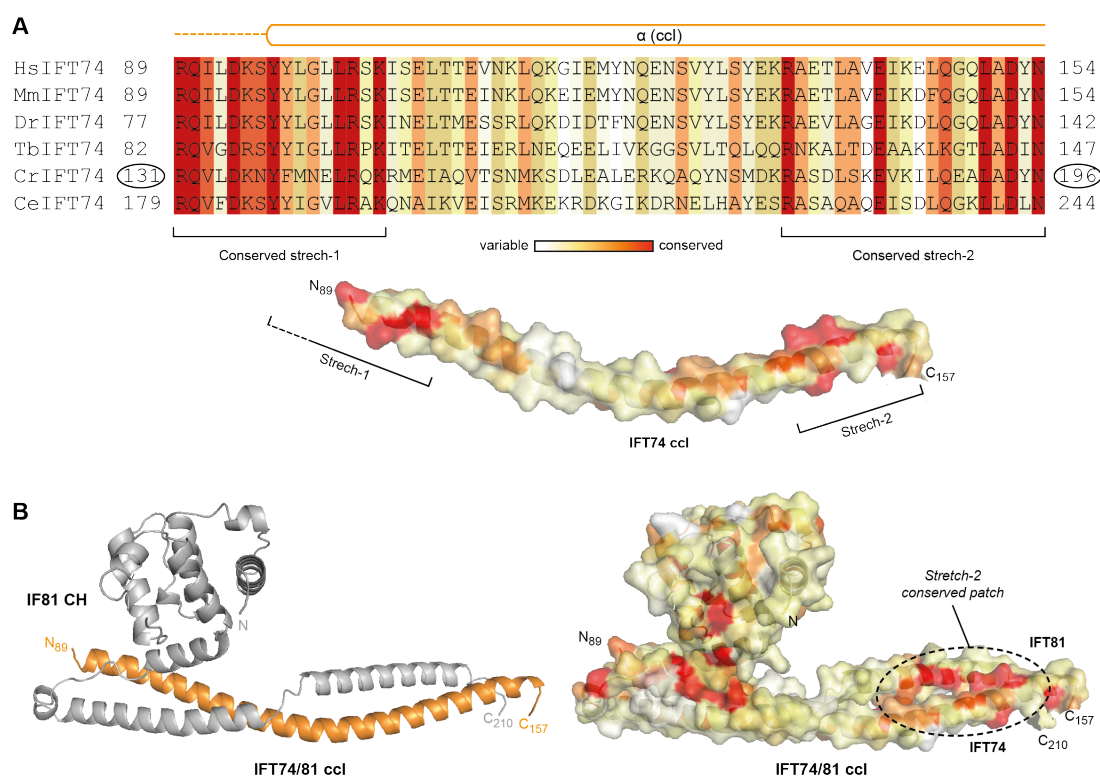


**Figure 23: The potential IFT-A binding site on IFT74**

**A.** Top: Multiple sequence alignment of IFT74 fragments from different species harboring the potential IFT-A binding region. Residue conservation is shown according to ConSurf grades and the position of secondary structure elements of *TbIFT74* is displayed above the sequence. Two conserved sequence stretches are indicated. Bottom: Corresponding region of the *TbIFT74* cCl crystal structure in surface representation with mapped conservation grades. (*Hs* = *Homo sapiens*, *Mm* = *Mus musculus*, *Dr* = *Danio rerio*, *Tb* = *Trypanosoma brucei*, *Cr* = *Chlamydomonas reinhardtii* and *Ce* = *Caenorhabditis elegans*) **B.** Relative position of stretch-2 in the *TbIFT22/74/81* crystal structure. Left: The N-terminal region in cartoon representation. Right: The same region in surface representation with mapped conservation grades. IFT81 contributes several residues to the conserved patch.

Taken together, the described observations will inspire future *in vivo* research to further investigate the biological function of IFT74 sequence stretch-2. Critical residues in the conserved patch will be

promising targets for point mutation studies in order to determine its biological function and to resolve if this patch indeed participates in IFT-A recruitment.

### 3 Analysis of the tubulin-binding CH domain

The IFT81 CH domain has been shown to bind both soluble  $\alpha/\beta$ -tubulin and MTs (Bhogaraju et al. 2013b). Structural comparison of the IFT81 CH domains with the CH domains of NDC80 and EB1, two other reported MT-binding CH domains (Slep & Vale 2007; Ciferri et al. 2008), reveals a significant difference in the C-terminal part of the domain, as already mentioned in Bhogaraju et al. 2013b (Supplementary Material). While NDC80 and EB1 possess one long, elongated C-terminal  $\alpha$ -helix (Fig. 24C and D), the corresponding part for both the *Cr* and *Tb*IFT81 CH domains is divided into two shorter helices ( $\alpha$ I and  $\alpha$ II) oriented almost perpendicular to each other (Fig. 24A, B). This unusual arrangement can be explained by the IFT22/74/81 crystal structure presented in this work. While  $\alpha$ I follows the direction of the conventional CH domain helix,  $\alpha$ II interacts with residues from ccl, thus fixing the position and orientation of the CH domain on the IFT74/81 scaffold (Fig. 24E).

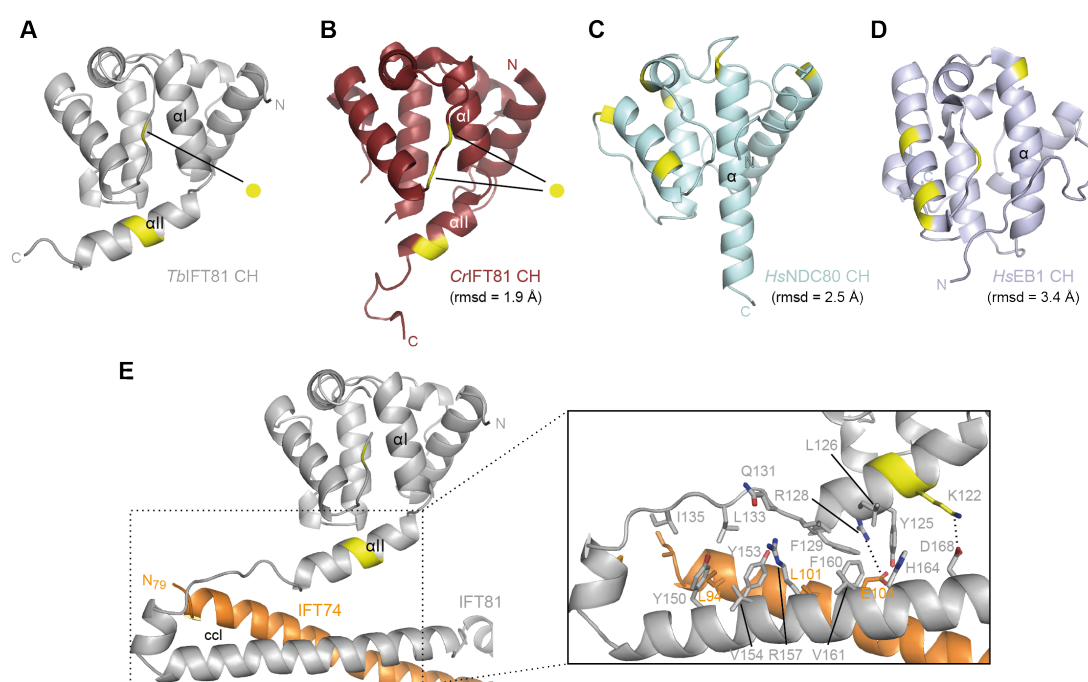


**Figure 24: Structural comparison of different microtubule-binding CH domains**

**A.** The *Tb*IFT81 CH domain presented in this work with labeled unusual C-terminal helices. **B.** Crystal structure of the *Cr*IFT81 CH domain (PDB ID: 4lvp) and CH domains of **C.** *Hs*NDC80 (PDB ID: 3iz0) and **D.** *Hs*EB1 (PDB ID: 3co1), two well-known MT-binding CH domains. All structures are shown in cartoon representation in the same orientation after superpositioning onto the *Tb*IFT81 CH structure. The rmsd for each superposition is indicated. Position of Tubulin/MT-interacting residues is shown in yellow. (MT = microtubule) **E.** Left: Relative position of the  $\alpha$ II helix to ccl in the *Tb*IFT22/74/81 structure (cartoon representation). Right: Interacting residues of  $\alpha$ II and ccl.

Interestingly,  $\alpha$ II harbors several of the basic conserved residues involved in tubulin binding. When comparing the potential IFT81 tubulin-binding residues with mapped MT-binding residues of NDC80 (Fig. 24, yellow residues), not much structural overlap could be found, indicating potentially different

binding modes. A cryo-EM structure of MT-bound NDC80 (Alushin et al. 2010) shows that individual tubulin modules are associated with the top part of the NDC80 CH domain (Fig. 25A, first orientation similar to the one in Fig. 24C), while the IFT81 CH domain crystal structures rather suggest binding on the front side of the orientation depicted in Fig. 24A. Differences in the position of tubulin-binding interfaces between NDC80 and IFT81 might be due to conformational differences of soluble and MT-bound  $\alpha/\beta$ -tubulin, but experimental evidence regarding the exact tubulin-binding mode of IFT81 is still missing. In contrast, MT-binding residues of the EB1 CH domain are positioned in a similar orientation to the ones of IFT81 (Fig. 24, yellow residues). A recent cryo-EM study of the EB1 yeast homolog Mal3 revealed that Mal3 indeed binds microtubules via this patch, however binding occurs between neighboring protofilaments and involves four individual  $\alpha/\beta$ -tubulin subunits (Fig. 25B) (Maurer et al. 2012). Therefore, the Mal3 tubulin-binding mode does not serve as a good model for IFT81 either. The constructs used for crystallization in this study provide a solid base for further structural approaches and co-crystallization trials with tubulin.

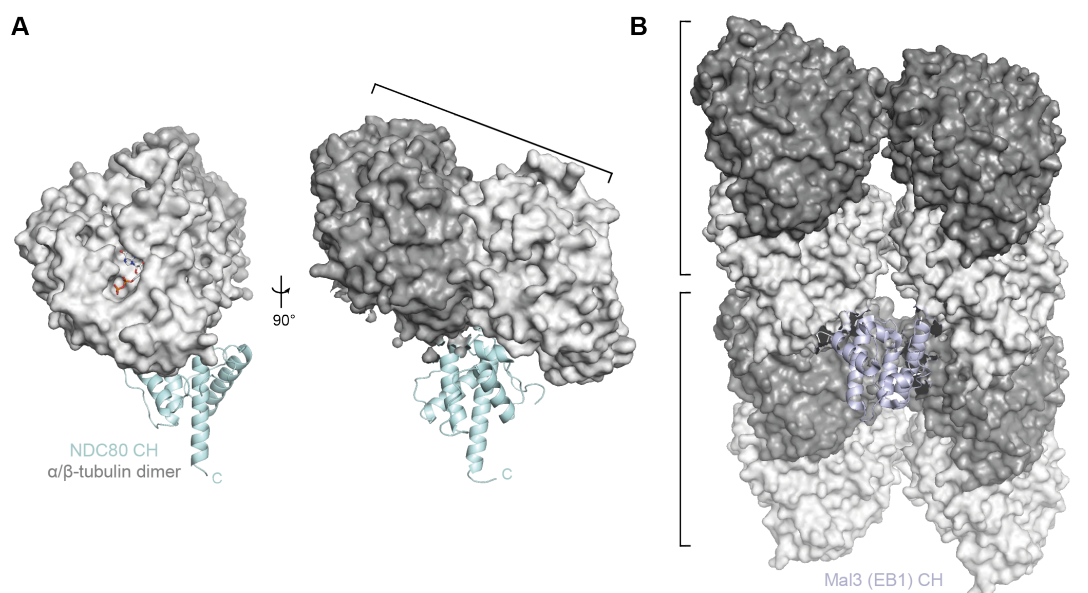


**Figure 25: Microtubule binding modes of NDC80 and Mal 3 (EB1) CH domains**

**A.** Cryo-EM structure of *Hs*NDC80 CH domain (PDB ID: 3iz0) bound to a  $\alpha/\beta$ -tubulin subunit of a microtubule. Left: Same orientation as depicted in Fig. 24C. Right: Orientation rotated by 90°. NDC80 binds in the cleft between  $\alpha$ - and  $\beta$ -tubulin. **B.** Cryo-EM structure of Mal3 CH domain (PDB ID: 4abo), the yeast EB1 homolog, bound to microtubule protofilaments. The orientation differs by 180° from the one depicted in Fig. 24D. Mal3 binds in the cleft between adjacent protofilaments and interacts with four different  $\alpha/\beta$ -tubulin subunits. NDC80/Mal3 are shown in cartoon and tubulin in surface representation.

## 4 IFT22 – a functional GTPase or not?

The results obtained in this work led to deeper insights into IFT22 biochemistry. The crystal structures of IFT22 revealed an overall Rab GTPase fold featuring an unusual nucleotide-binding mode. This new binding mode bypasses the conventional G4 motif by using an unusual Asp residue located in a different loop but positioned similarly to the Asp of the NKxD sequence, thus guaranteeing specificity for guanine over adenine nucleotides. We confirmed the base specificity experimentally and showed that

guanine nucleotide-binding is a conserved property amongst homologs from different species. IFT22 can therefore be considered a proper guanine nucleotide-binding protein, a notion that was not clear from previous sequence-based analysis (Schafer et al. 2006; Adhiambo et al. 2009). Binding affinities of IFT22 for GTP and GDP are in the low micromolar range, which is rather unusual for small Rab GTPases that normally possess nucleotide affinities several orders of magnitudes stronger (Simon et al. 1996). However, the measured affinities are similar to the ones reported for IFT27 (Bhogaraju et al. 2011), the other IFT-B1 GTPase, indicating that GEFs for GDP to GTP exchange are not required. Detected intrinsic GTP hydrolysis rates of IFT22 are low and are comparable to hydrolysis rates of other small GTPases (Simon et al. 1996; Scheffzek & Ahmadian 2005; Bhogaraju et al. 2011).

Structure-guided *in vivo* experiments in *T. brucei* showed that association of IFT22 with IFT-B1 and import into the organelle are essential for proper flagellum assembly, but expression of a GTP-binding mutant showed that GTP-binding is not necessarily required for association with the complex, ciliary entry and IFT trafficking under conditions of WT IFT22 depletion. Also, the IFT22 nucleotide state does not seem to influence its function in flagellar assembly. Therefore, we could not assign a specific phenotype-based cellular function to the IFT22 nucleotide state. However, biochemical *in vitro* experiments showed that the GTP-bound state of IFT22 shows significantly higher affinity for IFT74/81 than the nucleotide-free form. This is in accordance with results from an initial study in *C. elegans*, where the inactive IFT22 S to N mutant was restricted from the cilium (Schafer et al. 2006). It can therefore be stated that stable association of IFT22 to the IFT-B1 complex requires GTP-loading. Differences in the localization patterns of the mutants between the two organisms *in vivo* are likely due to slight differences in individual affinities for IFT74/81. One could assume that IFT22 is permanently GTP-loaded and the nucleotide is needed for stabilization of the switch regions and for stable binding to IFT74/81, but hydrolysis is not an intended functional feature of IFT22. However, to the best of our knowledge so far no Rab proteins have been reported to serve in functions that are GTPase cycle-independent. Despite the lack of experimental proof, there are several lines of evidence suggesting the presence of a functional GTPase cycle: 1) The IFT22 GTP-binding property is conserved amongst various organisms. If GTP-binding were only a stabilizing evolutionary remnant, it would likely have been lost in some species and replaced by other IFT22-stabilizing molecular interactions. 2) Functional Rab GTPases are characterized by an inactive cytosolic and membrane-targeted active state. Cellular localization and biochemistry of inactive IFT22 S to N mutant and WT IFT22 suggest a similar nucleotide-dependent localization pattern, with the active state being stably attached to IFT particles instead of membranes. 3) IFT22 shows low, but measurable GTPase activity. The detected intrinsic hydrolysis rate is comparable to that of other Rab GTPases, including IFT27, and solid turnover would require the presence of a yet to be identified GAP.

Although this work could not shed light on the role of the IFT22 GTPase cycle in *T. brucei*, the presented results might guide future research in the field. Since IFT22 was shown to have different functions in different species (Schafer et al. 2006; Adhiambo et al. 2009; Silva et al. 2012), it will be very interesting to also test the effect of nucleotide-binding mutants *in vivo* in other organisms such as mammalian cells.

## 5 The IFT74/81 heterodimer as a GTPase-binding platform

Both small GTPases IFT22 and IFT27 have been shown to bind to IFT-B1 via the IFT74/81 heterodimer (Taschner et al. 2014), with Rab12 being a transiently bound promising third candidate (Nishijima et al. 2017; Kanie et al. 2017). While the binding region of IFT22 has been mapped to a short sequence stretch and could be further narrowed down based on the presented IFT22/74/81 crystal structure, the exact binding sites for IFT27 and Rab12 remain uncertain, but were restricted to the C-terminal part of the coiled-coil, after the IFT22-binding site. The IFT74/81 coiled-coil protein can therefore be considered a binding platform for different Rab family GTPases. Interestingly, all three Rab-like GTPases of the IFT complex have been reported to preferentially or exclusively bind to IFT74/81 in their GTP-bound states (Schafer et al. 2006; Eguether et al. 2014; Huet et al. 2014; Nishijima et al. 2017; Kanie et al. 2017) (data from this study), thus making IFT74/81 a triple effector (Fig. 26). Results obtained from this study showed that IFT22 is mainly interacting with IFT74/81 via the switch regions, which is the usual effector-binding site of small GTPases. It is common that regulatory proteins of small GTPases (GAPs and GEFs) are multidomain proteins that combine several regulatory domains on one peptide chain (e. g. two GAP domains or a GAP and GEF domain within one protein) to provide efficient cross-talk between signaling processes (Bos et al. 2007). This characteristic also expands to several effector proteins. Rabin8 for example is both an effector of Rab11 and a GEF for Rab8, and FIP3 was shown to be a simultaneous effector of Arf4 and Rab11 (J. Wang & Deretic 2015) (see section 3.3). However, as an effector for three different GTPases, IFT74/81 represents a special case and is to our knowledge the first reported triple effector.

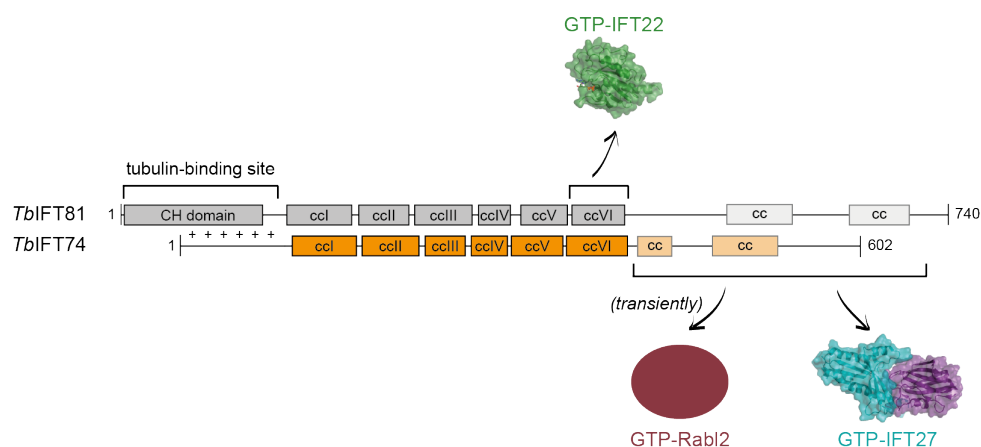


**Figure 26: The IFT74/81 triple effector complex**

Positions of ccl-ccVI are depicted according to their positions in the *TbIFT22/74/81* crystal structure. C-terminal cc regions are positioned according to PCOILS predictions. Binding regions of IFT22, IFT27 and Rab12 are indicated. IFT22 and IFT27 are shown in surface representation. (cc = coiled-coil; PDB ID of IFT25/27: 2yc2)

When compared to available 3D structures deposited in the protein data bank using the Dali server, both IFT22 and IFT27 show the lowest rmsd with Rab8 and Rab11 structures, two key regulators of vesicular ciliary trafficking. No structure is available for Rab12, but sequence homology searches detected the most

similar protein sequence to be Rab11 (66 % identity for human proteins). It is thus likely that several cilium-associated Rab proteins share a common ciliary Rab ancestor. Additionally, IFT22 and IFT27 share similar biochemical properties regarding nucleotide binding affinities and hydrolysis rates (Bhogaraju et al. 2011) (data from this study). Although no biochemical data on Rabl2 GTPase activity is available at present, conclusions drawn from *in vivo* experiments suggest different properties for Rabl2. The authors of two independent studies suppose high intrinsic GTP hydrolysis rates and therefore no need of a GAP for Rabl2 (Nishijima et al. 2017; Kanie et al. 2017). This is consistent with its reported transient association with IFT74/81 at the ciliary base. In contrast to IFT22 and IFT27, the Rabl2 sequence does still contain the catalytic Gln residue coordinating a water molecule that is needed for the hydrolysis reaction.

Given the high degree of surface conservation of the IFT22 binding site on IFT74/81, it is likely that binding sites for IFT27 and Rabl2 display similarly conserved patches in the C-terminal part of the heterodimer. It would be of great interest to obtain a high-resolution structure containing the IFT74/81 C-terminus with or without IFT27/Rabl2 in order to further map down their binding sites and potentially confirm binding of the small GTPases via the switch regions. Interestingly, we found that IFT74/81 residues interacting with IFT22 are conserved in *G. intestinalis* and *T. thermophila* sequences, two organisms that do not contain an IFT22 homolog. It is tempting to speculate that in these organisms other more distantly related small GTPases might potentially bind to the same surface patch on the IFT74/81 effector.

## **6 A potential role for IFT22 and the IFT74/81 effector complex in human disease**

As described in detail in the introduction, cellular functions of IFT22 are not entirely clear and vary significantly amongst species (see section 3.4.2). Apparently, IFT22 is not universally needed for cilium construction, eliminating the possibility of a regulatory role in one of the conserved IFT key steps, such as IFT train formation or IFT reassembly at the tip. However, knockout studies in *C. elegans* suggested a potential role for IFT22 in regulation of ciliary signaling cascades (Schafer et al. 2006). A function in certain signaling pathways could be species-dependent and lead to different phenotypes, although evidence for a signaling-related function in other organisms is lacking experimental evidence so far. Interestingly, a recent publication on clinical relevance of mutations in the IFT81 gene found an in-frame deletion of Leu435 to cause Short-Rib Polydactyly Syndrome (SRPS) (Duran et al. 2016). SRPS is a genetic skeletal disorder linked to disruption of retrograde IFT and abnormal Hh signaling. Leu435 corresponds to Leu443 in *T. brucei* IFT81 and is a well-conserved residue in the IFT22 binding site (Fig. 27B for conservation and Fig. 27A for residue position). When compared to another IFT81 mutation in the tubulin-binding CH domain in a second SRPS patient, the Leu435 deletion showed a more severe effect and the infant died shortly after birth (Duran et al. 2016). Since this study could not provide cultured cells for the Leu435 deletion mutant and thus lacks experimental data on expression levels and

stability of the IFT81 variant, conclusions remain speculative. However, possible explanations could be: 1) Either that Leu435 deletion leads to destabilization of the whole IFT81 protein and therefore affects IFT-B1 integrity, 2) or that the IFT74/81 coiled-coil interaction stays mostly intact, but IFT22-binding is impaired, leading to an IFT22-mediated phenotype. This could either be caused by disturbing the direct interaction between IFT81 and IFT22 or by loosening the coiled-coil interaction between IFT74 and IFT81 needed for stable IFT22-binding in that region.

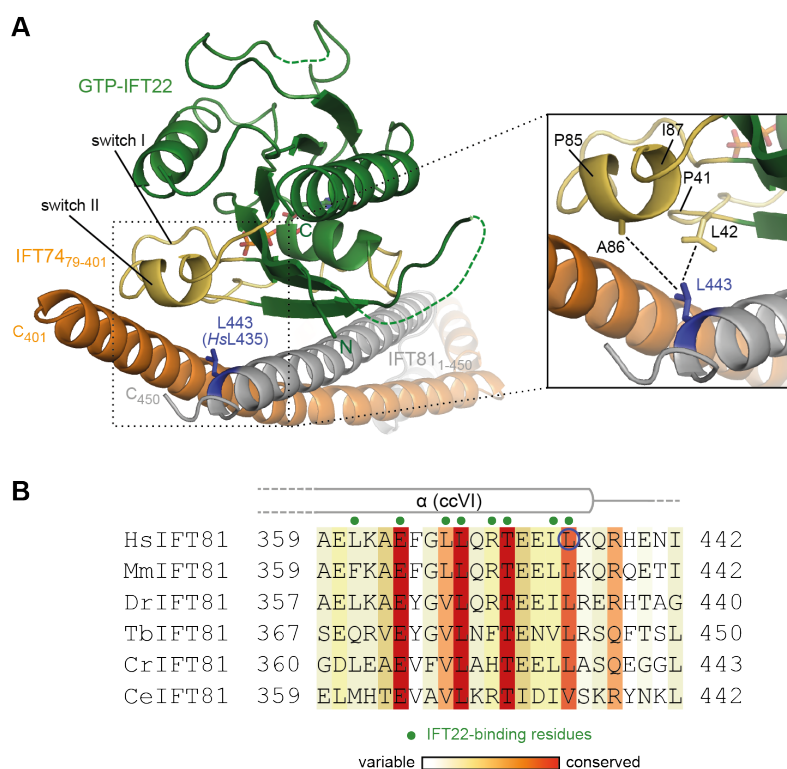


**Figure 27: Mutation of a conserved IFT81 Leu residue in the IFT22-binding region causes Short-Rib Polydactyly Syndrome**

**A.** Cartoon representation of the IFT22-binding region with the L443 (HsL435) disease mutation in IFT81 marked in blue. L443 interacts with hydrophobic residues from both switch I and switch II. **B.** Multiple sequence alignment of IFT81 fragments from different species harboring the IFT22-binding region with the conserved Leu residue (encircled in blue in the human sequence). Residues interacting with IFT22 are marked with green dots. Residue conservation is shown according to ConSurf grades and the position of secondary structure elements of TbIFT81 is displayed above the sequence. (Hs = *Homo sapiens*, Mm = *Mus musculus*, Dr = *Danio rerio*, Tb = *Trypanosoma brucei*, Cr = *Chlamydomonas reinhardtii* and Ce = *Caenorhabditis elegans*)

*In vitro* analysis of the reported IFT81 Leu435 deletion mutation could control if the mutation affects IFT81 stability, if it has an influence on IFT-B1 complex reconstitution, or if it influences IFT22-binding abilities of IFT74/81 $_{\Delta\text{Leu435}}$ , thus resolving which of the suggested scenarios is more likely.

# Abbreviations

Å	Ångström (1 Å = 0.1 nm)
aa	Amino acid
AMPPNP	5'-adenylyl-imido-triphosphate
ATP	Adenosine triphosphate
BB	Basal body
BBS	Bardet-Biedl syndrome
BiP	Binding immunoglobulin protein
BSA	Bovine serum albumin
cc	Coiled-coil
<i>Ce</i>	<i>Caenorhabditis elegans</i> , <i>C. elegans</i>
CH	Calponin homology
COPI	Coat protein complex I
<i>Cr</i>	<i>Chlamydomonas reinhardtii</i> , <i>C. reinhardtii</i>
CTS	Ciliary targeting sequences
DAPI	4',6-diamidino-2-phenylindole
Dsh	Dishevelled
<i>Dr</i>	<i>Danio rerio</i> , <i>D. rerio</i>
DRC	Dynein regulatory complex
DTT	Dithiothreitol
dsRNA	double-stranded RNA
<i>E. coli</i>	<i>Escherichia coli</i>
EDTA	Ethylenediaminetetraacetic acid
EM	Electron microscopy
ER	Endoplasmic reticulum
FL	Full-length
Fz	Frizzled
G domain	GTPase domain
G protein	GTP-binding protein
GAP	GTPase activating protein
GDF	GDI-displacement factor
GDI	Rab GDP-dissociation inhibitor
GEF	Guanine nucleotide exchange factor
GFP	Green fluorescent protein
<i>Gi</i>	<i>Giardia intestinalis</i> , <i>G. intestinalis</i>
Gli	Glioma
GMPPNP	5'-guanylyl-imido-triphosphate

GPCR	G protein-coupled receptor
GTP	Guanosine triphosphate
HEPES	4-(2-hydroxyethyl)-1-piperazineethanesulfonic acid
Hh	Hedgehog
HPLC	High-performance liquid chromatography
<i>Hs</i>	<i>Homo sapiens, H. sapiens</i>
IDA	Inner dynein arms
IFA	Immunofluorescence assay
IFT	Intraflagellar transport
Inv	Inversin
IPTG	isopropyl $\beta$ -D-1-thiogalactopyranoside
ITC	Isothermal titration calorimetry
$K_d$	Dissociation constant
mant	2',3'-O-(N-methyl-anthraniloyl)
<i>Mm</i>	<i>Mus musculus, M. musculus</i>
MR	Molecular replacement
MT	Microtubule
MW	Molecular weight
NTA	Nitrilotriacetic acid
OD	Optical density
ODA	Outer dynein arms
P loop	Phosphate-binding loop
PAGE	Polyacrylamide gel electrophoresis
PBS	Phosphate-buffered saline
PBST	PBS-Tween
PC1/2	Polycystin1/2
PCD	Primary cilia dyskinesia
PDGFR $\alpha$	Platelet-derived growth factor receptor- $\alpha$
PEG	Polyethylene glycol
PFR	Paraflagellar rod
$P_i$	Inorganic phosphate
PKD	Polycystic kidney disease
PM	Plasma membrane
PMSF	Phenylmethanesulfonyl fluoride
Ptch-1	Patched-1
PTM	Post-translational modification
Rab1	Rab-like
rmsd	Root mean square deviation
ROI	Region of interest
RS	Radial spokes

## Abbreviations

---

SAP	Shrimp alkaline phosphatase
SDS	Sodium dodecyl sulfate
SEC	Size-exclusion chromatography
Smo	Smoothened
SRPS	Short-rib Polydactyly Syndrome
<i>Tb</i>	<i>Trypanosoma brucei</i> , <i>T. brucei</i>
TEM	Transmission electron microscopy
TEV	Tobacco Etch Virus
TGN	Trans Golgi network
TPR	Tetratricopeptide repeat
Tris	Tris(hydroxymethyl)aminomethane
<i>Tt</i>	<i>Tetrahymena thermophila</i> , <i>T. thermophila</i>
TULP	Tubby-like protein
TZ	Transition zone
Wnt	Wingless
WT	Wild type

# List of Figures

1	Scanning electron microscopy images of different ciliated cell types . . . . .	12
2	Schematic overview of the ciliary ultrastructure . . . . .	13
3	Schematic illustration of various sensory cilia . . . . .	17
4	The role of cilia in different signaling pathways . . . . .	18
5	Simplified overview of the trypanosome life cycle . . . . .	21
6	Overview of the intraflagellar transport key steps . . . . .	22
7	Schematic overview of IFT-A complex components . . . . .	24
8	Domain architecture of IFT-B complex components . . . . .	25
9	Schematic overview of the IFT-B complex . . . . .	26
10	Structure and features of small Rab GTPases . . . . .	30
11	Schematic representation of ciliary membrane trafficking . . . . .	32
12	IFT22 is an unusual guanine specific Rab GTPase . . . . .	44
13	Overall structure of the N-terminal IFT22/74/81 complex . . . . .	47
14	IFT74/81 shows effector binding for IFT22 . . . . .	49
15	Analysis of different IFT22 mutants . . . . .	51
16	The IFT22 A86R protein does not sustain IFT and cannot rescue the absence of IFT22 .	52
17	The inactive GTPase mutant only shows a mild phenotype <i>in vivo</i> . . . . .	54
18	Multiple sequence alignment of IFT22 homologs . . . . .	68
19	Additional IFT22 data . . . . .	69
20	Additional IFT22/74/81 complex data . . . . .	70
21	IFT22 D175A undergoes normal IFT and can rescue the absence of endogenous IFT22 .	71
22	Schematic interaction map of the IFT-B1 subcomplex with superposed available crystal structures . . . . .	115
23	The potential IFT-A binding site on IFT74 . . . . .	116
24	Structural comparison of different microtubule-binding CH domains . . . . .	117
25	Microtubule binding modes of NDC80 and Mal 3 (EB1) CH domains . . . . .	118
26	The IFT74/81 triple effector complex . . . . .	120
27	Mutation of a conserved IFT81 Leu residue in the IFT22-binding region causes Short-Rib Polydactyly Syndrome . . . . .	122

# References

- Absalon, Sabrina et al. (2008): Intraflagellar transport and functional analysis of genes required for flagellum formation in trypanosomes. *Molecular biology of the cell*, 19(3): 929–944.
- Adams, Paul D et al. (2010): PHENIX: a comprehensive Python-based system for macromolecular structure solution. *Acta crystallographica. Section D, Biological crystallography*, 66(Pt 2): 213–221.
- Adhiambo, Christine, Thierry Blisnick, Géraldine Toutirais, Emmanuelle Delannoy & Philippe Bastin (2009): A novel function for the atypical small G protein Rab-like 5 in the assembly of the trypanosome flagellum. *Journal of cell science*, 122(Pt 6): 834–841.
- Afzelius, Björn A (1976): A human syndrome caused by immotile cilia. *Science (New York, N.Y.)* 193(4250): 317–319.
- Ahmed, Noveera T & David R Mitchell (2005): ODA16p, a Chlamydomonas flagellar protein needed for dynein assembly. *Molecular biology of the cell*, 16(10): 5004–5012.
- Aldahmesh, Mohammed A et al. (2014): IFT27, encoding a small GTPase component of IFT particles, is mutated in a consanguineous family with Bardet-Biedl syndrome. *Human molecular genetics*, 23(12): 3307–3315.
- Altschul, Stephen F, Warren Gish, Webb Miller, Eugene W Myers & David J Lipman (1990): Basic local alignment search tool. *Journal of molecular biology*, 215(3): 403–410.
- Alushin, Gregory M et al. (2010): The Ndc80 kinetochore complex forms oligomeric arrays along microtubules. *Nature*, 467(7317): 805–810.
- Alva, Vikram, Seung-Zin Nam, Johannes Söding & Andrei N Lupas (2016): The MPI bioinformatics Toolkit as an integrative platform for advanced protein sequence and structure analysis. *Nucleic acids research*, 44(W1): W410–5.
- Andrae, Johanna, Radosa Gallini & Christer Betsholtz (2008): Role of platelet-derived growth factors in physiology and medicine. *Genes & development*, 22(10): 1276–1312.
- Arts, Heleen H et al. (2011): C14ORF179 encoding IFT43 is mutated in Sensenbrenner syndrome. *Journal of medical genetics*, 48(6): 390–395.
- Aslett, Martin et al. (2010): TriTrypDB: a functional genomic resource for the Trypanosomatidae. *Nucleic acids research*, 38(Database issue): D457–62.
- Baczynska, Agata et al. (2007): Morphology of human Fallopian tubes after infection with Mycoplasma genitalium and Mycoplasma hominis—in vitro organ culture study. *Human reproduction (Oxford, England)*, 22(4): 968–979.
- Badano, Jose L, Norimasa Mitsuma, Phil L Beales & Nicholas Katsanis (2006): The ciliopathies: an emerging class of human genetic disorders. *Annual review of genomics and human genetics*, 7: 125–148.
- Baker, Sheila A, Katie Freeman, Katherine Luby-Phelps, Gregory J Pazour & Joseph C Besharse (2003): IFT20 links kinesin II with a mammalian intraflagellar transport complex that is conserved in motile flagella and sensory cilia. *The Journal of biological chemistry*, 278(36): 34211–34218.
- Bangs, James D, Lyle Uyetake, Marla J Brickman, Andrew E Balber & John C Boothroyd (1993): Molecular cloning and cellular localization of a BiP homologue in Trypanosoma brucei. Divergent ER retention signals in a lower eukaryote. *Journal of cell science*, 105 (Pt 4): 1101–1113.

- Baniz, Boglarka et al. (2005): Dysfunctional cilia lead to altered ependyma and choroid plexus function, and result in the formation of hydrocephalus. *Development (Cambridge, England)*, 132(23): 5329–5339.
- Bastin, Philippe, Keith R Matthews & Keith Gull (1996): The paraflagellar rod of kinetoplastida: solved and unsolved questions. *Parasitology today (Personal ed.)* 12(8): 302–307.
- Bastin, Philippe, Trevor Sherwin & Keith Gull (1998): Paraflagellar rod is vital for trypanosome motility. *Nature*, 391(6667): 548.
- Behal, Robert H et al. (2012): Subunit interactions and organization of the *Chlamydomonas reinhardtii* intraflagellar transport complex A proteins. *The Journal of biological chemistry*, 287(15): 11689–11703.
- Beisson, Janine & Michel Wright (2003): Basal body/centriole assembly and continuity. *Current opinion in cell biology*, 15(1): 96–104.
- Benmerah, Alexandre (2013): The ciliary pocket. *Current opinion in cell biology*, 25(1): 78–84.
- Benmerah, Alexandre et al. (2015): The more we know, the more we have to discover: an exciting future for understanding cilia and ciliopathies. *Cilia*, 4: 5.
- Berbari, Nicolas F, Andrew D Johnson, Jacqueline S Lewis, Candice C Askwith & Kirk Mykytyn (2008): Identification of ciliary localization sequences within the third intracellular loop of G protein-coupled receptors. *Molecular biology of the cell*, 19(4): 1540–1547.
- Bhogaraju, Sagar, Benjamin D Engel & Esben Lorentzen (2013a): Intraflagellar transport complex structure and cargo interactions. *Cilia*, 2(1): 10.
- Bhogaraju, Sagar, Michael Taschner, Michaela Morawetz, Claire Basquin & Esben Lorentzen (2011): Crystal structure of the intraflagellar transport complex 25/27. *The EMBO journal*, 30(10): 1907–1918.
- Bhogaraju, Sagar, Kristina Weber, Benjamin D Engel, Karl-Ferdinand Lechtreck & Esben Lorentzen (2014): Getting tubulin to the tip of the cilium: one IFT train, many different tubulin cargo-binding sites? *BioEssays : news and reviews in molecular, cellular and developmental biology*, 36(5): 463–467.
- Bhogaraju, Sagar et al. (2013b): Molecular basis of tubulin transport within the cilium by IFT74 and IFT81. *Science (New York, N.Y.)* 341(6149): 1009–1012.
- Blacque, Oliver E & Michel R Leroux (2006): Bardet-Biedl syndrome: an emerging pathomechanism of intracellular transport. *Cellular and molecular life sciences : CMLS*, 63(18): 2145–2161.
- Blacque, Oliver E, Noemie Scheidel & Stefanie Kuhns (2017): Rab GTPases in cilium formation and function. *Small GTPases*, 1–19.
- Blacque, Oliver E et al. (2006): The WD repeat-containing protein IFTA-1 is required for retrograde intraflagellar transport. *Molecular biology of the cell*, 17(12): 5053–5062.
- Bos, Johannes L, Holger Rehmann & Alfred Wittinghofer (2007): GEFs and GAPs: critical elements in the control of small G proteins. *Cell*, 129(5): 865–877.
- Bredrup, Cecilie et al. (2011): Ciliopathies with skeletal anomalies and renal insufficiency due to mutations in the IFT-A gene WDR19. *American journal of human genetics*, 89(5): 634–643.
- Breslow, David K, Elena F Koslover, Federica Seydel, Andrew J Spakowitz & Maxence V Nachury (2013): An in vitro assay for entry into cilia reveals unique properties of the soluble diffusion barrier. *The Journal of cell biology*, 203(1): 129–147.
- Brown, Jason M, Deborah A Cochran, Branch Craige, Tomohiro Kubo & George B Witman (2015): Assembly of IFT trains at the ciliary base depends on IFT74. *Current biology : CB*, 25(12): 1583–1593.

- Brun, Reto & Myriam Schönenberger (1979): Cultivation and in vitro cloning or procyclic culture forms of *Trypanosoma brucei* in a semi-defined medium. Short communication. *Acta tropica*, 36(3): 289–292.
- Buck, Linda & Richard Axel (1991): A novel multigene family may encode odorant receptors: a molecular basis for odor recognition. *Cell*, 65(1): 175–187.
- Buisson, Johanna et al. (2013): Intraflagellar transport proteins cycle between the flagellum and its base. *Journal of cell science*, 126(Pt 1): 327–338.
- Burkard, Gabriela, Cristina M Fragoso & Isabel Roditi (2007): Highly efficient stable transformation of bloodstream forms of *Trypanosoma brucei*. *Molecular and biochemical parasitology*, 153(2): 220–223.
- Cherfils, Jacqueline & Mahel Zeghouf (2013): Regulation of small GTPases by GEFs, GAPs, and GDIs. *Physiological reviews*, 93(1): 269–309.
- Christensen, Søren Tvorup, Stine F Pedersen, Peter Satir, Iben R Veland & Linda Schneider (2008): The primary cilium coordinates signaling pathways in cell cycle control and migration during development and tissue repair. *Current topics in developmental biology*, 85: 261–301.
- Ciferri, Claudio et al. (2008): Implications for kinetochore-microtubule attachment from the structure of an engineered Ndc80 complex. *Cell*, 133(3): 427–439.
- Clevers, Hans (2006): Wnt/beta-catenin signaling in development and disease. *Cell*, 127(3): 469–480.
- Cole, D G et al. (1998): Chlamydomonas kinesin-II-dependent intraflagellar transport (IFT): IFT particles contain proteins required for ciliary assembly in *Caenorhabditis elegans* sensory neurons. *The Journal of cell biology*, 141(4): 993–1008.
- Cole, Douglas G et al. (1993): Novel heterotrimeric kinesin-related protein purified from sea urchin eggs. *Nature*, 366(6452): 268–270.
- Cooper, Geoffrey M (2000): “The Mechanism of Vesicular Transport.” *The Cell: A Molecular Approach. 2nd edition*. Sunderland Sinauer Associates.
- Corbit, Kevin C et al. (2005): Vertebrate Smoothed functions at the primary cilium. *Nature*, 437(7061): 1018–1021.
- Craft, Julie M, J Aaron Harris, Sebastian Hyman, Peter Kner & Karl F Lehtreck (2015): Tubulin transport by IFT is upregulated during ciliary growth by a cilium-autonomous mechanism. *The Journal of cell biology*, 208(2): 223–237.
- Dabdoub, Alain & Matthew W Kelley (2005): Planar cell polarity and a potential role for a Wnt morphogen gradient in stereociliary bundle orientation in the mammalian inner ear. *Journal of neurobiology*, 64(4): 446–457.
- Dagoneau, Nathalie et al. (2009): DYNC2H1 mutations cause asphyxiating thoracic dystrophy and short rib-polydactyly syndrome, type III. *American journal of human genetics*, 84(5): 706–711.
- Deane, James A, Douglas G Cole, Scott Seeley, Dennis R Diener & Joel L Rosenbaum (2001): Localization of intraflagellar transport protein IFT52 identifies basal body transitional fibers as the docking site for IFT particles. *Current biology : CB*, 11(20): 1586–1590.
- Delling, Markus, Paul G DeCaen, Julia F Doerner, Sebastien Febvay & David E Clapham (2013): Primary cilia are specialized calcium signalling organelles. *Nature*, 504(7479): 311–314.
- Deretic, Dusanka (1998): Post-Golgi trafficking of rhodopsin in retinal photoreceptors. *Eye (London, England)*, 12 ( Pt 3b): 526–530.

- Duchateau, Guus S, Kees Graamans, Jelle Zuidema & Frans W Merkus (1985): Correlation between nasal ciliary beat frequency and mucus transport rate in volunteers. *The Laryngoscope*, 95(7 Pt 1): 854–859.
- Duran, Ivan et al. (2016): Destabilization of the IFT-B cilia core complex due to mutations in IFT81 causes a Spectrum of Short-Rib Polydactyly Syndrome. *Scientific reports*, 6: 34232.
- Eathiraj, Sudharshan, Xiaojing Pan, Christopher Ritacco & David G Lambright (2005): Structural basis of family-wide Rab GTPase recognition by rabenosyn-5. *Nature*, 436(7049): 415–419.
- Efimenko, Evgeni et al. (2006): Caenorhabditis elegans DYF-2, an orthologue of human WDR19, is a component of the intraflagellar transport machinery in sensory cilia. *Molecular biology of the cell*, 17(11): 4801–4811.
- Eguether, Thibaut et al. (2014): IFT27 links the BBSome to IFT for maintenance of the ciliary signaling compartment. *Developmental cell*, 31(3): 279–290.
- Eliáš, Marek, Vladimír Klimeš, Romain Derelle, Romana Petrželková & Jan Tachezy (2016): A paneukaryotic genomic analysis of the small GTPase RABL2 underscores the significance of recurrent gene loss in eukaryote evolution. *Biology direct*, 11(1): 5.
- Eliasson, Rune, Björn Mossberg, Per Camner & Björn A Afzelius (1977): The immotile-cilia syndrome. A congenital ciliary abnormality as an etiologic factor in chronic airway infections and male sterility. *The New England journal of medicine*, 297(1): 1–6.
- Emmer, Brian T, Danijela Maric & David M Engman (2010): Molecular mechanisms of protein and lipid targeting to ciliary membranes. *Journal of cell science*, 123(Pt 4): 529–536.
- Emsley, Paul, Bernhard Lohkamp, William G Scott & Kevin Cowtan (2010): Features and development of Coot. *Acta crystallographica. Section D, Biological crystallography*, 66(Pt 4): 486–501.
- Engel, Benjamin D et al. (2012): The role of retrograde intraflagellar transport in flagellar assembly, maintenance, and function. *The Journal of cell biology*, 199(1): 151–167.
- Espinosa, Eric J, Monica Calero, Khambhampaty Sridevi & Suzanne R Pfeffer (2009): RhoBTB3: a Rho GTPase-family ATPase required for endosome to Golgi transport. *Cell*, 137(5): 938–948.
- Fan, Zhen-Chuan et al. (2010): Chlamydomonas IFT70/CrDYF-1 is a core component of IFT particle complex B and is required for flagellar assembly. *Molecular biology of the cell*, 21(15): 2696–2706.
- Fliegauf, Manfred, Thomas Benzing & Heymut Omran (2007): When cilia go bad: cilia defects and ciliopathies. *Nature reviews. Molecular cell biology*, 8(11): 880–893.
- Follit, John A, Lixia Li, Yvonne Vucica & Gregory J Pazour (2010): The cytoplasmic tail of fibrocystin contains a ciliary targeting sequence. *The Journal of cell biology*, 188(1): 21–28.
- Follit, John A, Richard A Tuft, Kevin E Fogarty & Gregory J Pazour (2006): The intraflagellar transport protein IFT20 is associated with the Golgi complex and is required for cilia assembly. *Molecular biology of the cell*, 17(9): 3781–3792.
- Follit, John A, Fenghui Xu, Brian T Keady & Gregory J Pazour (2009): Characterization of mouse IFT complex B. *Cell motility and the cytoskeleton*, 66(8): 457–468.
- Foster, Kenneth W (2009): Analysis of the ciliary/flagellar beating of Chlamydomonas. *Methods in cell biology*, 91: 173–239.
- Franco, Brunella & Christel Thauvin-Robinet (2016): Update on oral-facial-digital syndromes (OFDS). *Cilia*, 5: 12.
- Franklin, Joseph B & Elisabetta Ullu (2010): Biochemical analysis of PIFTC3, the Trypanosoma brucei orthologue of nematode DYF-13, reveals interactions with established and putative intraflagellar transport components. *Molecular microbiology*, 78(1): 173–186.

- Fredriksson, Linda, Hong Li & Ulf Eriksson (2004): The PDGF family: four gene products form five dimeric isoforms. *Cytokine & growth factor reviews*, 15(4): 197–204.
- Fukuda, Terunobu et al. (2014): Aberrant cochlear hair cell attachments caused by Nectin-3 deficiency result in hair bundle abnormalities. *Development (Cambridge, England)*, 141(2): 399–409.
- Geng, Lin et al. (2006): Polycystin-2 traffics to cilia independently of polycystin-1 by using an N-terminal RVxP motif. *Journal of cell science*, 119(Pt 7): 1383–1395.
- Gibbons, Ian R & Arthur J Rowe (1965): Dynein: A Protein with Adenosine Triphosphatase Activity from Cilia. *Science (New York, N.Y.)* 149(3682): 424–426.
- Gilissen, Christian et al. (2010): Exome sequencing identifies WDR35 variants involved in Sensenbrenner syndrome. *American journal of human genetics*, 87(3): 418–423.
- Gilula, Norton B & Peter Satir (1972): The ciliary necklace. A ciliary membrane specialization. *The Journal of cell biology*, 53(2): 494–509.
- Goetz, Sarah C & Kathryn V Anderson (2010): The primary cilium: a signalling centre during vertebrate development. *Nature reviews. Genetics*, 11(5): 331–344.
- Grati, M'hamed et al. (2015): A missense mutation in DCDC2 causes human recessive deafness DFNB66, likely by interfering with sensory hair cell and supporting cell cilia length regulation. *Human molecular genetics*, 24(9): 2482–2491.
- Hao, Limin & Jonathan M Scholey (2009): Intraflagellar transport at a glance. *Journal of cell science*, 122(Pt 7): 889–892.
- Hao, Limin et al. (2011): Intraflagellar transport delivers tubulin isoforms to sensory cilium middle and distal segments. *Nature cell biology*, 13(7): 790–798.
- Haycraft, Courtney J et al. (2005): Gli2 and Gli3 localize to cilia and require the intraflagellar transport protein polaris for processing and function. *PLoS genetics*, 1(4): e53.
- Heuser, Thomas, Milen Raytchev, Jeremy Krell, Mary E Porter & Daniela Nicastro (2009): The dynein regulatory complex is the nexin link and a major regulatory node in cilia and flagella. *The Journal of cell biology*, 187(6): 921–933.
- Hirokawa, Nobutaka, Yosuke Tanaka, Yasushi Okada & Sen Takeda (2006): Nodal flow and the generation of left-right asymmetry. *Cell*, 125(1): 33–45.
- Hollyfield, Joe G, Joseph C Besharse & Mary E Rayborn (1977): Turnover of rod photoreceptor outer segments. I. Membrane addition and loss in relationship to temperature. *The Journal of cell biology*, 75(2 Pt 1): 490–506.
- Holm, Liisa & Chris Sander (1993): Protein structure comparison by alignment of distance matrices. *Journal of molecular biology*, 233(1): 123–138.
- Horst, Cynthia J, Lincoln V Johnson & Joseph C Besharse (1990): Transmembrane assemblage of the photoreceptor connecting cilium and motile cilium transition zone contain a common immunologic epitope. *Cell motility and the cytoskeleton*, 17(4): 329–344.
- Hou, Yuqing, Gregory J Pazour & George B Witman (2004): A dynein light intermediate chain, D1LIC, is required for retrograde intraflagellar transport. *Molecular biology of the cell*, 15(10): 4382–4394.
- Hou, Yuqing et al. (2007): Functional analysis of an individual IFT protein: IFT46 is required for transport of outer dynein arms into flagella. *The Journal of cell biology*, 176(5): 653–665.
- Huangfu, Danwei et al. (2003): Hedgehog signalling in the mouse requires intraflagellar transport proteins. *Nature*, 426(6962): 83–87.
- Hudspeth, Albert J (1985): The cellular basis of hearing: the biophysics of hair cells. *Science (New York, N.Y.)* 230(4727): 745–752.

- Huet, Diego, Thierry Blisnick, Sylvie Perrot & Philippe Bastin (2014): The GTPase IFT27 is involved in both anterograde and retrograde intraflagellar transport. *eLife*, 3: e02419.
- Hughes, Louise, Samantha Borrett, Katie Towers, Tobias Starborg & Sue Vaughan (2017): Patterns of organelle ontogeny through a cell cycle revealed by whole-cell reconstructions using 3D electron microscopy. *Journal of cell science*, 130(3): 637–647.
- Ibañez-Tallon, Inés, Svetlana Gorokhova & Nathaniel Heintz (2002): Loss of function of axonemal dynein Mdnah5 causes primary ciliary dyskinesia and hydrocephalus. *Human molecular genetics*, 11(6): 715–721.
- Iomini, Carlo, Linya Li, Jessica M Esparza & Susan K Dutcher (2009): Retrograde intraflagellar transport mutants identify complex A proteins with multiple genetic interactions in *Chlamydomonas reinhardtii*. *Genetics*, 183(3): 885–896.
- Ishikawa, Hiroaki & Wallace F Marshall (2011): Ciliogenesis: building the cell's antenna. *Nature reviews. Molecular cell biology*, 12(4): 222–234.
- Ishikawa, Hiroaki & Wallace F Marshall (2015): Efficient live fluorescence imaging of intraflagellar transport in mammalian primary cilia. *Methods in cell biology*, 127: 189–201.
- Ishikawa, Hiroaki et al. (2014): TTC26/DYF13 is an intraflagellar transport protein required for transport of motility-related proteins into flagella. *eLife*, 3: e01566.
- Itzen, Aymelt & Roger S Goody (2011): GTPases involved in vesicular trafficking: structures and mechanisms. *Seminars in cell & developmental biology*, 22(1): 48–56.
- Jékely, Gáspár & Detlev Arendt (2006): Evolution of intraflagellar transport from coated vesicles and autogenous origin of the eukaryotic cilium. *BioEssays : news and reviews in molecular, cellular and developmental biology*, 28(2): 191–198.
- Johnson, Karl A & Joel L Rosenbaum (1992): Polarity of flagellar assembly in *Chlamydomonas*. *The Journal of cell biology*, 119(6): 1605–1611.
- Julkowska, Daria & Philippe Bastin (2009): Tools for analyzing intraflagellar transport in trypanosomes. *Methods in cell biology*, 93: 59–80.
- Kabsch, Wolfgang (2010): XDS. *Acta crystallographica. Section D, Biological crystallography*, 66(Pt 2): 125–132.
- Kanie, Tomoharu et al. (2017): The CEP19-RABL2 GTPase Complex Binds IFT-B to Initiate Intraflagellar Transport at the Ciliary Base. *Developmental cell*, 42(1): 22–36.e12.
- Katoh, Yohei et al. (2016): Overall Architecture of the Intraflagellar Transport (IFT)-B Complex Containing Cluap1/IFT38 as an Essential Component of the IFT-B Peripheral Subcomplex. *The Journal of biological chemistry*, 291(21): 10962–10975.
- Keady, Brian T et al. (2012): IFT25 links the signal-dependent movement of Hedgehog components to intraflagellar transport. *Developmental cell*, 22(5): 940–951.
- Kobayashi, Tetsuo, Keiko Gengyo-Ando, Takeshi Ishihara, Isao Katsura & Shohei Mitani (2007): IFT-81 and IFT-74 are required for intraflagellar transport in *C. elegans*. *Genes to cells : devoted to molecular & cellular mechanisms*, 12(5): 593–602.
- Kohl, Linda, Derrick Robinson & Philippe Bastin (2003): Novel roles for the flagellum in cell morphogenesis and cytokinesis of trypanosomes. *The EMBO journal*, 22(20): 5336–5346.
- Kohl, Linda, Trevor Sherwin & Keith Gull (1999): Assembly of the paraflagellar rod and the flagellum attachment zone complex during the *Trypanosoma brucei* cell cycle. *The Journal of eukaryotic microbiology*, 46(2): 105–109.
- Kozminski, Keith G, Peter L Beech & Joel L Rosenbaum (1995): The *Chlamydomonas* kinesin-like protein FLA10 is involved in motility associated with the flagellar membrane. *The Journal of cell biology*, 131(6 Pt 1): 1517–1527.

- Kozminski, Keith G, Karl A Johnson, Paul Forscher & Joel L Rosenbaum (1993): A motility in the eukaryotic flagellum unrelated to flagellar beating. *Proceedings of the National Academy of Sciences of the United States of America*, 90(12): 5519–5523.
- Kulaga, Heather M et al. (2004): Loss of BBS proteins causes anosmia in humans and defects in olfactory cilia structure and function in the mouse. *Nature genetics*, 36(9): 994–998.
- Kunitomo, Hirofumi & Yuichi Iino (2008): Caenorhabditis elegans DYF-11, an orthologue of mammalian Traf3ip1/MIP-T3, is required for sensory cilia formation. *Genes to cells : devoted to molecular & cellular mechanisms*, 13(1): 13–25.
- Landau, Meytal et al. (2005): ConSurf 2005: the projection of evolutionary conservation scores of residues on protein structures. *Nucleic acids research*, 33(Web Server issue): W299–302.
- Langousis, Gerasimos & Kent L Hill (2014): Motility and more: the flagellum of Trypanosoma brucei. *Nature reviews. Microbiology*, 12(7): 505–518.
- Langousis, Gerasimos et al. (2016): Loss of the BBSome perturbs endocytic trafficking and disrupts virulence of Trypanosoma brucei. *Proceedings of the National Academy of Sciences of the United States of America*, 113(3): 632–637.
- Lechtreck, Karl-Ferdinand, Scott Luro, Junya Awata & George B Witman (2009a): HA-tagging of putative flagellar proteins in Chlamydomonas reinhardtii identifies a novel protein of intraflagellar transport complex B. *Cell motility and the cytoskeleton*, 66(8): 469–482.
- Lechtreck, Karl-Ferdinand et al. (2009b): The Chlamydomonas reinhardtii BBSome is an IFT cargo required for export of specific signaling proteins from flagella. *The Journal of cell biology*, 187(7): 1117–1132.
- Leung, Daisy W & Michael K Rosen (2005): The nucleotide switch in Cdc42 modulates coupling between the GTPase-binding and allosteric equilibria of Wiskott-Aldrich syndrome protein. *Proceedings of the National Academy of Sciences of the United States of America*, 102(16): 5685–5690.
- Li, Yujie & Jinghua Hu (2011): Small GTPases and cilia. *Protein & cell*, 2(1): 13–25.
- Liang, Yinwen et al. (2014): FLA8/KIF3B phosphorylation regulates kinesin-II interaction with IFT-B to control IFT entry and turnaround. *Developmental cell*, 30(5): 585–597.
- Liew, Gerald M et al. (2014): The intraflagellar transport protein IFT27 promotes BBSome exit from cilia through the GTPase ARL6/BBS3. *Developmental cell*, 31(3): 265–278.
- Lo, Jennifer C Y et al. (2012): RAB-like 2 has an essential role in male fertility, sperm intraflagellar transport, and tail assembly. *PLoS genetics*, 8(10): e1002969.
- Logan, Catriona Y & Roel Nusse (2004): The Wnt signaling pathway in development and disease. *Annual review of cell and developmental biology*, 20: 781–810.
- Lucker, Ben F et al. (2005): Characterization of the intraflagellar transport complex B core: direct interaction of the IFT81 and IFT74/72 subunits. *The Journal of biological chemistry*, 280(30): 27688–27696.
- Lynn, Denis (2008): *The Ciliated Protozoa*. Characterization, Classification, and Guide to the Literature. Springer Science & Business Media.
- Lyons, Ronan A, Ertan Saridogan & Ovrang Djahanbakhch (2006): The reproductive significance of human Fallopian tube cilia. *Human reproduction update*, 12(4): 363–372.
- Marszalek, Joseph R et al. (2000): Genetic evidence for selective transport of opsin and arrestin by kinesin-II in mammalian photoreceptors. *Cell*, 102(2): 175–187.
- Maurer, Sebastian P, Franck J Fourniol, Gergő Bohner, Carolyn A Moores & Thomas Surrey (2012): EBs recognize a nucleotide-dependent structural cap at growing microtubule ends. *Cell*, 149(2): 371–382.

- Mazelova, Jana et al. (2009): Ciliary targeting motif VxPx directs assembly of a trafficking module through Arf4. *The EMBO journal*, 28(3): 183–192.
- McEwen, Dyke P, Paul M Jenkins & Jeffrey R Martens (2008): Olfactory cilia: our direct neuronal connection to the external world. *Current topics in developmental biology*, 85: 333–370.
- McMahon, Andrew P, Philip W Ingham & Clifford J Tabin (2003): Developmental roles and clinical significance of hedgehog signaling. *Current topics in developmental biology*, 53: 1–114.
- Ménasché, Gaël et al. (2000): Mutations in RAB27A cause Griscelli syndrome associated with haemophagocytic syndrome. *Nature genetics*, 25(2): 173–176.
- Milburn, Michael V et al. (1990): Molecular switch for signal transduction: structural differences between active and inactive forms of protooncogenic ras proteins. *Science (New York, N.Y.)* 247(4945): 939–945.
- Mill, Pleasantine et al. (2011): Human and mouse mutations in WDR35 cause short-rib polydactyly syndromes due to abnormal ciliogenesis. *American journal of human genetics*, 88(4): 508–515.
- Molla-Herman, Anahi et al. (2010): The ciliary pocket: an endocytic membrane domain at the base of primary and motile cilia. *Journal of cell science*, 123(Pt 10): 1785–1795.
- Morga, Benjamin & Philippe Bastin (2013): Getting to the heart of intraflagellar transport using Trypanosoma and Chlamydomonas models: the strength is in their differences. *Cilia*, 2(1): 16.
- Mourão, André, Søren Tvorup Christensen & Esben Lorentzen (2016): The intraflagellar transport machinery in ciliary signaling. *Current opinion in structural biology*, 41: 98–108.
- Mourão, André, Andrew R Nager, Maxence V Nachury & Esben Lorentzen (2014): Structural basis for membrane targeting of the BBSome by ARL6. *Nature structural & molecular biology*, 21(12): 1035–1041.
- Mukhopadhyay, Saikat et al. (2010): TULP3 bridges the IFT-A complex and membrane phosphoinositides to promote trafficking of G protein-coupled receptors into primary cilia. *Genes & development*, 24(19): 2180–2193.
- Müller, Roman-Ulrich, Sibylle Zank, Francesca Fabretti & Thomas Benzing (2011): Caenorhabditis elegans, a model organism for kidney research: from cilia to mechanosensation and longevity. *Current opinion in nephrology and hypertension*, 20(4): 400–408.
- Munro, Neil C et al. (1994): Fertility in men with primary ciliary dyskinesia presenting with respiratory infection. *Thorax*, 49(7): 684–687.
- Nachury, Maxence V, E Scott Seeley & Hua Jin (2010): Trafficking to the ciliary membrane: how to get across the periciliary diffusion barrier? *Annual review of cell and developmental biology*, 26: 59–87.
- Nachury, Maxence V et al. (2007): A core complex of BBS proteins cooperates with the GTPase Rab8 to promote ciliary membrane biogenesis. *Cell*, 129(6): 1201–1213.
- Nagao, Shizuko et al. (2008): Calcium channel inhibition accelerates polycystic kidney disease progression in the Cy/+ rat. *Kidney international*, 73(3): 269–277.
- Nauli, Surya M et al. (2003): Polycystins 1 and 2 mediate mechanosensation in the primary cilium of kidney cells. *Nature genetics*, 33(2): 129–137.
- Nishijima, Yuya et al. (2017): RABL2 interacts with the intraflagellar transport-B complex and CEP19 and participates in ciliary assembly. *Molecular biology of the cell*, 28(12): 1652–1666.
- Nonaka, Shigenori, Hidetaka Shiratori, Yukio Saijoh & Hiroshi Hamada (2002): Determination of left-right patterning of the mouse embryo by artificial nodal flow. *Nature*, 418(6893): 96–99.
- Nottingham, Ryan M & Suzanne R Pfeffer (2014): Mutant enzymes challenge all assumptions. *eLife*, 3: e02171.

- Nussdorfer, Petra, Ines Cilenšek, Branko Zorn & Daniel Petrovič (2018): Adapted methods for scanning electron microscopy (SEM) in assessment of human sperm morphology. *Bosnian journal of basic medical sciences*, 18(1): 43–48.
- Okada, Yasushi et al. (1999): Abnormal nodal flow precedes situs inversus in iv and inv mice. *Molecular cell*, 4(4): 459–468.
- Olbrich, Heike et al. (2002): Mutations in DNAH5 cause primary ciliary dyskinesia and randomization of left-right asymmetry. *Nature genetics*, 30(2): 143–144.
- O'Toole, Eileen T, Thomas H Giddings & Susan K Dutcher (2007): Understanding microtubule organizing centers by comparing mutant and wild-type structures with electron tomography. *Methods in cell biology*, 79: 125–143.
- Ou, Guangshuo, Hongmin Qin, Joel L Rosenbaum & Jonathan M Scholey (2005): The PKD protein qilin undergoes intraflagellar transport. *Current biology : CB*, 15(11): R410–1.
- Overath, Peter & Markus Engstler (2004): Endocytosis, membrane recycling and sorting of GPI-anchored proteins: *Trypanosoma brucei* as a model system. *Molecular microbiology*, 53(3): 735–744.
- Paduch, Marcin, Filip Jeleń & Jacek Otlewski (2001): Structure of small G proteins and their regulators. *Acta biochimica Polonica*, 48(4): 829–850.
- Parnell, Stephen C et al. (2002): Polycystin-1 activation of c-Jun N-terminal kinase and AP-1 is mediated by heterotrimeric G proteins. *The Journal of biological chemistry*, 277(22): 19566–19572.
- Pasca di Magliano, Marina & Matthias Hebrok (2003): Hedgehog signalling in cancer formation and maintenance. *Nature reviews. Cancer*, 3(12): 903–911.
- Pastural, Elodie et al. (1997): Griscelli disease maps to chromosome 15q21 and is associated with mutations in the myosin-Va gene. *Nature genetics*, 16(3): 289–292.
- Pazour, Gregory J, Nathan Agrin, John Leszyk & George B Witman (2005): Proteomic analysis of a eukaryotic cilium. *The Journal of cell biology*, 170(1): 103–113.
- Pazour, Gregory J, Bethany L Dickert & George B Witman (1999): The DHC1b (DHC2) isoform of cytoplasmic dynein is required for flagellar assembly. *The Journal of cell biology*, 144(3): 473–481.
- Pazour, Gregory J, Jovenal T San Agustin, John A Follit, Joel L Rosenbaum & George B Witman (2002a): Polycystin-2 localizes to kidney cilia and the ciliary level is elevated in orpk mice with polycystic kidney disease. *Current biology : CB*, 12(11): R378–80.
- Pazour, Gregory J, Curtis G Wilkerson & George B Witman (1998): A dynein light chain is essential for the retrograde particle movement of intraflagellar transport (IFT). *The Journal of cell biology*, 141(4): 979–992.
- Pazour, Gregory J et al. (2000): *Chlamydomonas* IFT88 and its mouse homologue, polycystic kidney disease gene tg737, are required for assembly of cilia and flagella. *The Journal of cell biology*, 151(3): 709–718.
- Pazour, Gregory J et al. (2002b): The intraflagellar transport protein, IFT88, is essential for vertebrate photoreceptor assembly and maintenance. *The Journal of cell biology*, 157(1): 103–113.
- Pedersen, Lotte B et al. (2005): *Chlamydomonas* IFT172 is encoded by FLA11, interacts with CrEB1, and regulates IFT at the flagellar tip. *Current biology : CB*, 15(3): 262–266.
- Pereira-Leal, José B & Miguel C Seabra (2000): The mammalian Rab family of small GTPases: definition of family and subfamily sequence motifs suggests a mechanism for functional specificity in the Ras superfamily. *Journal of molecular biology*, 301(4): 1077–1087.

- Perrone, Catherine A et al. (2003): A novel dynein light intermediate chain colocalizes with the retrograde motor for intraflagellar transport at sites of axoneme assembly in chlamydomonas and Mammalian cells. *Molecular biology of the cell*, 14(5): 2041–2056.
- Piperno, Gianni & Kara Mead (1997): Transport of a novel complex in the cytoplasmic matrix of Chlamydomonas flagella. *Proceedings of the National Academy of Sciences of the United States of America*, 94(9): 4457–4462.
- Piperno, Gianni et al. (1998): Distinct mutants of retrograde intraflagellar transport (IFT) share similar morphological and molecular defects. *The Journal of cell biology*, 143(6): 1591–1601.
- Porter, Mary E, Raqual Bower, Julie A Knott, Pamela Byrd & William Dentler (1999): Cytoplasmic dynein heavy chain 1b is required for flagellar assembly in Chlamydomonas. *Molecular biology of the cell*, 10(3): 693–712.
- Pradel, Lydie C, Mélanie Bonhivers, Nicolas Landrein & Derrick R Robinson (2006): NIMA-related kinase TbNRKC is involved in basal body separation in Trypanosoma brucei. *Journal of cell science*, 119(Pt 9): 1852–1863.
- Prevo, Bram, Pierre Mangeol, Felix Oswald, Jonathan M Scholey & Erwin J G Peterman (2015): Functional differentiation of cooperating kinesin-2 motors orchestrates cargo import and transport in C. elegans cilia. *Nature cell biology*, 17(12): 1536–1545.
- Qin, Hongmin, Dennis R Diener, Stefan Geimer, Douglas G Cole & Joel L Rosenbaum (2004): Intraflagellar transport (IFT) cargo: IFT transports flagellar precursors to the tip and turnover products to the cell body. *The Journal of cell biology*, 164(2): 255–266.
- Qin, Hongmin, Zhaohui Wang, Dennis R Diener & Joel L Rosenbaum (2007): Intraflagellar transport protein 27 is a small G protein involved in cell-cycle control. *Current biology : CB*, 17(3): 193–202.
- Rajagopalan, Vidyalakshmi et al. (2009): Analysis of properties of cilia using Tetrahymena thermophila. *Methods in molecular biology (Clifton, N.J.)* 586: 283–299.
- Ralston, Katherine S, Zakayi P Kabututu, Jason H Melehan, Michael Oberholzer & Kent L Hill (2009): The Trypanosoma brucei flagellum: moving parasites in new directions. *Annual review of microbiology*, 63: 335–362.
- Reiter, Jeremy F, Oliver E Blacque & Michel R Leroux (2012): The base of the cilium: roles for transition fibres and the transition zone in ciliary formation, maintenance and compartmentalization. *EMBO reports*, 13(7): 608–618.
- Reiter, Jeremy F & Michel R Leroux (2017): Genes and molecular pathways underpinning ciliopathies. *Nature reviews. Molecular cell biology*, 18(9): 533–547.
- Rensland, Hans et al. (1995): Substrate and product structural requirements for binding of nucleotides to H-ras p21: the mechanism of discrimination between guanosine and adenosine nucleotides. *Biochemistry*, 34(2): 593–599.
- Richey, Elizabeth A & Hongmin Qin (2012): Dissecting the sequential assembly and localization of intraflagellar transport particle complex B in Chlamydomonas. *PloS one*, 7(8): e43118.
- Rohatgi, Rajat, Ljiljana Milenkovic & Matthew P Scott (2007): Patched1 regulates hedgehog signaling at the primary cilium. *Science (New York, N.Y.)* 317(5836): 372–376.
- Rohatgi, Rajat & William J Snell (2010): The ciliary membrane. *Current opinion in cell biology*, 22(4): 541–546.
- Rosenbaum, Joel L, Douglas G Cole & Dennis R Diener (1999): Intraflagellar transport: the eyes have it. *The Journal of cell biology*, 144(3): 385–388.
- Rosenbaum, Joel L & George B Witman (2002): Intraflagellar transport. *Nature reviews. Molecular cell biology*, 3(11): 813–825.

- Rual, Jean-François et al. (2005): Towards a proteome-scale map of the human protein-protein interaction network. *Nature*, 437(7062): 1173–1178.
- Salinas, Raquel Y et al. (2017): Photoreceptor discs form through peripherin-dependent suppression of ciliary ectosome release. *The Journal of cell biology*, 216(5): 1489–1499.
- San Agustin, Jovenal T, Gregory J Pazour & George B Witman (2015): Intraflagellar transport is essential for mammalian spermiogenesis but is absent in mature sperm. *Molecular biology of the cell*, 26(24): 4358–4372.
- Satir, Peter & Søren Tvorup Christensen (2007): Overview of structure and function of mammalian cilia. *Annual review of physiology*, 69: 377–400.
- Satir, Peter, David R Mitchell & Gáspár Jékely (2008): How did the cilium evolve? *Current topics in developmental biology*, 85: 63–82.
- Schafer, Jenny C et al. (2006): IFTA-2 is a conserved cilia protein involved in pathways regulating longevity and dauer formation in *Caenorhabditis elegans*. *Journal of cell science*, 119(Pt 19): 4088–4100.
- Scheffzek, Klaus & Mohammad R Ahmadian (2005): GTPase activating proteins: structural and functional insights 18 years after discovery. *Cellular and molecular life sciences : CMLS*, 62(24): 3014–3038.
- Schietroma, Cataldo et al. (2017): Usher syndrome type 1-associated cadherins shape the photoreceptor outer segment. *The Journal of cell biology*, 216(6): 1849–1864.
- Schipper, Ori (2017): *Das Erbgut entrümpeln*. URL: <https://www.horizonte-magazin.ch/2017/09/20/das-erbgut-entruempeln/>.
- Schneider, Linda et al. (2005): PDGFR $\alpha$  signaling is regulated through the primary cilium in fibroblasts. *Current biology : CB*, 15(20): 1861–1866.
- Schwarz, Jason S, Tobias Reichenbach & Albert J Hudspeth (2011): A hydrodynamic sensory antenna used by killifish for nocturnal hunting. *The Journal of experimental biology*, 214(Pt 11): 1857–1866.
- Seabra, Miguel C, Michael S Brown & Joseph L Goldstein (1993): Retinal degeneration in choroideremia: deficiency of rab geranylgeranyl transferase. *Science (New York, N.Y.)* 259(5093): 377–381.
- Seo, Seongjin et al. (2011): A novel protein LZTFL1 regulates ciliary trafficking of the BBSome and Smoothed. *PLoS genetics*, 7(11): e1002358.
- Serricchio, Mauro et al. (2015): Flagellar membranes are rich in raft-forming phospholipids. *Biology open*, 4(9): 1143–1153.
- Sherwin, Trevor & Keith Gull (1989): The cell division cycle of *Trypanosoma brucei brucei*: timing of event markers and cytoskeletal modulations. *Philosophical transactions of the Royal Society of London. Series B, Biological sciences*, 323(1218): 573–588.
- Sievers, Fabian et al. (2011): Fast, scalable generation of high-quality protein multiple sequence alignments using Clustal Omega. *Molecular systems biology*, 7: 539.
- Signor, Dawn et al. (1999): Role of a class DHC1b dynein in retrograde transport of IFT motors and IFT raft particles along cilia, but not dendrites, in chemosensory neurons of living *Caenorhabditis elegans*. *The Journal of cell biology*, 147(3): 519–530.
- Silva, David A, Xiaomeng Huang, Robert H Behal, Douglas G Cole & Hongmin Qin (2012): The RABL5 homolog IFT22 regulates the cellular pool size and the amount of IFT particles partitioned to the flagellar compartment in *Chlamydomonas reinhardtii*. *Cytoskeleton (Hoboken, N.J.)* 69(1): 33–48.

- Simon, Iris, Marino Zerial & Roger S Goody (1996): Kinetics of interaction of Rab5 and Rab7 with nucleotides and magnesium ions. *The Journal of biological chemistry*, 271(34): 20470–20478.
- Simons, Kai & Robert Ehehalt (2002): Cholesterol, lipid rafts, and disease. *The Journal of clinical investigation*, 110(5): 597–603.
- Singer, Emily (2009): *Cellular Wonders*. URL: <https://www.technologyreview.com/s/416669/cellular-wonders/>.
- Sivars, Ulf, Dikran Aivazian & Suzanne R Pfeffer (2003): Yip3 catalyses the dissociation of endosomal Rab-GDI complexes. *Nature*, 425(6960): 856–859.
- Slep, Kevin C & Ronald D Vale (2007): Structural basis of microtubule plus end tracking by XMAP215, CLIP-170, and EB1. *Molecular cell*, 27(6): 976–991.
- Snow, Joshua J et al. (2004): Two anterograde intraflagellar transport motors cooperate to build sensory cilia on *C. elegans* neurons. *Nature cell biology*, 6(11): 1109–1113.
- Sorokin, Sergei P (1968): Reconstructions of centriole formation and ciliogenesis in mammalian lungs. *Journal of cell science*, 3(2): 207–230.
- Stenmark, Harald (2009): Rab GTPases as coordinators of vesicle traffic. *Nature reviews. Molecular cell biology*, 10(8): 513–525.
- Stenmark, Harald & Vesa M Olkkonen (2001): The Rab GTPase family. *Genome biology*, 2(5): REVIEWS3007.
- Stepanek, Ludek & Gaia Pigino (2016): Microtubule doublets are double-track railways for intraflagellar transport trains. *Science (New York, N.Y.)* 352(6286): 721–724.
- Storoni, Laurent C, Airlie J McCoy & Randy J Read (2004): Likelihood-enhanced fast rotation functions. *Acta crystallographica. Section D, Biological crystallography*, 60(Pt 3): 432–438.
- Stroupe, Christopher & Axel T Brunger (2000): Crystal structures of a Rab protein in its inactive and active conformations. *Journal of molecular biology*, 304(4): 585–598.
- Tam, Beatrice M, Orson L Moritz, Lawrence B Hurd & David S Papermaster (2000): Identification of an outer segment targeting signal in the COOH terminus of rhodopsin using transgenic *Xenopus laevis*. *The Journal of cell biology*, 151(7): 1369–1380.
- Taschner, Michael, Sagar Bhogaraju & Esben Lorentzen (2012): Architecture and function of IFT complex proteins in ciliogenesis. *Differentiation; research in biological diversity*, 83(2): S12–22.
- Taschner, Michael, Sagar Bhogaraju, Melanie Vetter, Michaela Morawetz & Esben Lorentzen (2011): Biochemical mapping of interactions within the intraflagellar transport (IFT) B core complex: IFT52 binds directly to four other IFT-B subunits. *The Journal of biological chemistry*, 286(30): 26344–26352.
- Taschner, Michael, Fruzsina Kotsis, Philipp Braeuer, Wolfgang Kuehn & Esben Lorentzen (2014): Crystal structures of IFT70/52 and IFT52/46 provide insight into intraflagellar transport B core complex assembly. *The Journal of cell biology*, 207(2): 269–282.
- Taschner, Michael & Esben Lorentzen (2016a): Recombinant Reconstitution and Purification of the IFT-B Core Complex from *Chlamydomonas reinhardtii*. *Methods in molecular biology (Clifton, N.J.)* 1454: 69–82.
- Taschner, Michael & Esben Lorentzen (2016b): The Intraflagellar Transport Machinery. *Cold Spring Harbor perspectives in biology*, 8(10).
- Taschner, Michael, André Mourão, Mayanka Awasthi, Jerome Basquin & Esben Lorentzen (2017): Structural basis of outer dynein arm intraflagellar transport by the transport adaptor protein ODA16 and the intraflagellar transport protein IFT46. *The Journal of biological chemistry*, 292(18): 7462–7473.

- Taschner, Michael et al. (2016): Intraflagellar transport proteins 172, 80, 57, 54, 38, and 20 form a stable tubulin-binding IFT-B2 complex. *The EMBO journal*, 35(7): 773–790.
- Taylor, Paige et al. (2015): Mutations in DYNC2LI1 disrupt cilia function and cause short rib polydactyly syndrome. *Nature communications*, 6: 7092.
- Tran, Pamela V et al. (2008): THM1 negatively modulates mouse sonic hedgehog signal transduction and affects retrograde intraflagellar transport in cilia. *Nature genetics*, 40(4): 403–410.
- Trépout, Sylvain, Anne-Marie Tassin, Sergio Marco & Philippe Bastin (2018): STEM tomography analysis of the trypanosome transition zone. *Journal of structural biology*, 202(1): 51–60.
- Tsao, Che-Chia & Martin A Gorovsky (2008): Different effects of Tetrahymena IFT172 domains on anterograde and retrograde intraflagellar transport. *Molecular biology of the cell*, 19(4): 1450–1461.
- Ullrich, Oliver et al. (1993): Rab GDP dissociation inhibitor as a general regulator for the membrane association of rab proteins. *The Journal of biological chemistry*, 268(24): 18143–18150.
- Uthaiyah, Revathy C, Gerrit J Praefcke, Jonathan C Howard & Christian Herrmann (2003): IIGP1, an interferon-gamma-inducible 47-kDa GTPase of the mouse, showing cooperative enzymatic activity and GTP-dependent multimerization. *The Journal of biological chemistry*, 278(31): 29336–29343.
- Van Dam, Teunis J P et al. (2013): Evolution of modular intraflagellar transport from a coatomer-like progenitor. *Proceedings of the National Academy of Sciences of the United States of America*, 110(17): 6943–6948.
- Van Leeuwenhoek, Antonie (1677): *Observations ... Concerning Little Animals by Him Observed in Rain-well-sea and Snowwater ; as Also in Water Wherein Pepper Has Lain Insused*.
- Veeman, Michael T, Jeffrey D Axelrod & Randall T Moon (2003): A second canon. Functions and mechanisms of beta-catenin-independent Wnt signaling. *Developmental cell*, 5(3): 367–377.
- Veleri, Shobi et al. (2014): Ciliopathy-associated gene Cc2d2a promotes assembly of subdistal appendages on the mother centriole during cilia biogenesis. *Nature communications*, 5: 4207.
- Vetter, Ingrid R & Alfred Wittinghofer (2001): The guanine nucleotide-binding switch in three dimensions. *Science (New York, N.Y.)* 294(5545): 1299–1304.
- Vetter, Melanie, Ralf Stehle, Claire Basquin & Esben Lorentzen (2015): Structure of Rab11-FIP3-Rabin8 reveals simultaneous binding of FIP3 and Rabin8 effectors to Rab11. *Nature structural & molecular biology*, 22(9): 695–702.
- Vieira, Otilia V et al. (2006): FAPP2, cilium formation, and compartmentalization of the apical membrane in polarized Madin-Darby canine kidney (MDCK) cells. *Proceedings of the National Academy of Sciences of the United States of America*, 103(49): 18556–18561.
- Walther, Zenta, Malini Vashishtha & John L Hall (1994): The Chlamydomonas FLA10 gene encodes a novel kinesin-homologous protein. *The Journal of cell biology*, 126(1): 175–188.
- Wandinger-Ness, Angela & Marino Zerial (2014): Rab proteins and the compartmentalization of the endosomal system. *Cold Spring Harbor perspectives in biology*, 6(11): a022616.
- Wang, Jing & Dusanka Deretic (2015): The Arf and Rab11 effector FIP3 acts synergistically with ASAP1 to direct Rabin8 in ciliary receptor targeting. *Journal of cell science*, 128(7): 1375–1385.
- Wang, Jing, Yoshiko Morita, Jana Mazelova & Dusanka Deretic (2012): The Arf GAP ASAP1 provides a platform to regulate Arf4- and Rab11-Rab8-mediated ciliary receptor targeting. *The EMBO journal*, 31(20): 4057–4071.

- Wang, Zefeng, James C Morris, Mark E Drew & Paul T Englund (2000): Inhibition of Trypanosoma brucei gene expression by RNA interference using an integratable vector with opposing T7 promoters. *The Journal of biological chemistry*, 275(51): 40174–40179.
- Wang, Zhaohui, Zhen-Chuan Fan, Shana M Williamson & Hongmin Qin (2009): Intraflagellar transport (IFT) protein IFT25 is a phosphoprotein component of IFT complex B and physically interacts with IFT27 in Chlamydomonas. *PloS one*, 4(5): e5384.
- Warner, Fred D & Peter Satir (1974): The structural basis of ciliary bend formation. Radial spoke positional changes accompanying microtubule sliding. *The Journal of cell biology*, 63(1): 35–63.
- Waters, Aoife M & Philip L Beales (2011): Ciliopathies: an expanding disease spectrum. *Pediatric nephrology (Berlin, Germany)*, 26(7): 1039–1056.
- Wei, Qing et al. (2012): The BBSome controls IFT assembly and turnaround in cilia. *Nature cell biology*, 14(9): 950–957.
- Williams, Corey L et al. (2014): Direct evidence for BBSome-associated intraflagellar transport reveals distinct properties of native mammalian cilia. *Nature communications*, 5: 5813.
- Winn, Martyn D et al. (2011): Overview of the CCP4 suite and current developments. *Acta crystallographica. Section D, Biological crystallography*, 67(Pt 4): 235–242.
- Wittinghofer, Alfred (2014): *Ras Superfamily Small G Proteins: Biology and Mechanisms 1. General Features, Signaling*. Springer.
- Wittinghofer, Alfred & Ingrid R Vetter (2011): Structure-function relationships of the G domain, a canonical switch motif. *Annual review of biochemistry*, 80: 943–971.
- Wloga, Dorota, Ewa Joachimiak, Panagiota Louka & Jacek Gaertig (2017): Posttranslational Modifications of Tubulin and Cilia. *Cold Spring Harbor perspectives in biology*, 9(6).
- Yoshimura, Shin-Ichiro, Johannes Egerer, Evelyn Fuchs, Alexander K Haas & Francis A Barr (2007): Functional dissection of Rab GTPases involved in primary cilium formation. *The Journal of cell biology*, 178(3): 363–369.
- Zhang, Qihong et al. (2013): BBS7 is required for BBSome formation and its absence in mice results in Bardet-Biedl syndrome phenotypes and selective abnormalities in membrane protein trafficking. *Journal of cell science*, 126(Pt 11): 2372–2380.
- Zimmermann, Karl Wilhelm (1898): *Beiträge zur Kenntnis einiger Drüsen und Epithelien*.